LUND UNIVERSITY

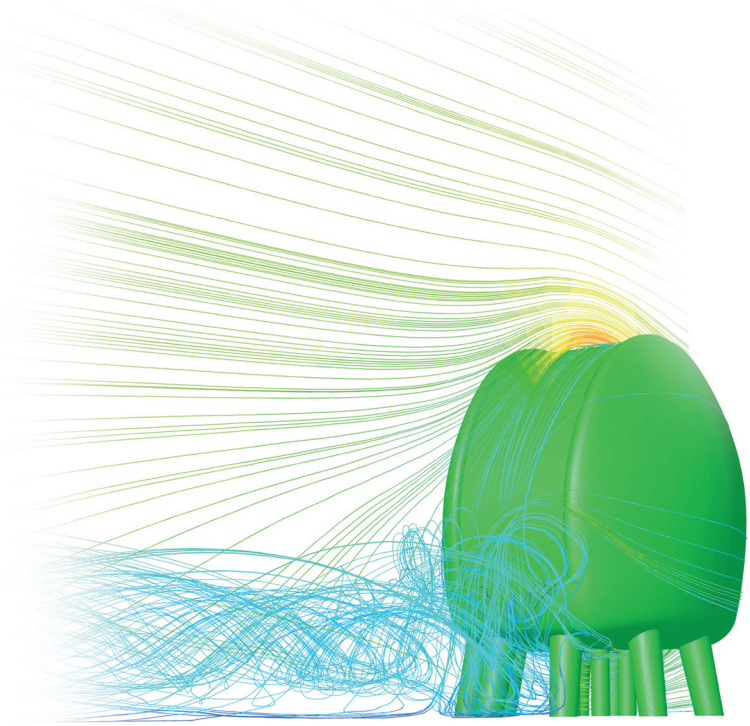

Proceedings of the 19TH NORDIC SEMINAR ON COMPUTATIONAL MECHANICS Lund, 20-21 October, 2006

O. Dahlblom, L. Fuchs, K. Persson, M. Ristinmaa, G. Sandberg and I. Svensson (editors)

Department of Construction Sciences
Structural Mechanics

ISSN 0281-6679

Proceedings of the 19TH NORDIC SEMINAR ON COMPUTATIONAL MECHANICS Lund, 20-21 October, 2006

O. Dahlblom, L. Fuchs, K. Persson,
M. Ristinmaa, G. Sandberg and I. Svensson
(editors)

Printed by KFS I Lund AB, Lund, Sweden, October 2006.

For information, address:
Division of Structural Mechanics, LTH, Lund University, Box 118, SE-221 00 Lund, Sweden.
Homepage: http://www.byggmek.lth.se

Preface

These proceedings contain the papers presented at the Nineteenth Nordic Seminar on Computational Mechanics, held at Lund University, Lund, Sweden, 20-21 October 2006. The Nordic Seminars on Computational Mechanics represent the major activity of the Nordic Association for Computational Mechanics (NoACM). The NoACM was founded in 1988 with the objective to stimulate and promote research and practice in computational mechanics, to foster the interchange of ideas among the various fields contributing to computational mechanics, and to provide forums and meetings for dissemination of knowledge in computational mechanics. Younger researchers, including doctorate students etc., are especially encouraged to take part at these seminars. The member countries of NoACM are the Nordic countries (Denmark, Finland, Iceland, Norway and Sweden) and the Baltic countries (Estonia, Latvia and Lithuania). NoACM is a subchapter of the International Organization for Computational Mechanics (IACM) and the European Community on Computational Methods in Applied Sciences (ECCOMAS).

The responsibility for organizing this year's seminar was assigned by NoACM to the Division of Structural Mechanics, Lund University. This year's seminar contains four invited lectures and 53 contributed presentations divided into 14 sessions. In the present volume, all the invited lectures are placed first, followed by the contributed papers in the order of appearance. New this year is the announcement of mini sessions suggested by members of the community; Biomechanics, multiscale modelling, fracture mechanics.

On behalf of the organizers, sincere appreciations are extended to all contributors at the seminar, not least to the invited lecturers and to the other speakers for their efforts in preparing talks and papers.

Lund, 11 October 2006

The editors

Local Organizing Committee

Ola Dahlblom
Lazlo Fuchs
Kent Persson
Matti Ristinmaa
Göran Sandberg (chair)
Ingrid Svensson

Program Committee

Kjell Magne Mathisen & Trond Kvamsdal *Norway*
Anders Eriksson & Göran Sandberg *Sweden*
Roland Rikards *Latvia (Baltic countries)*
Juha Paavola & Jouni Freund *Finland*
Niels Olhoff & Jens Sørensen *Denmark*

NSCM16 Secretariat

Christina Glans

Phone: +46 46 2227421
E-mail: Christina.Glans@bekon.lth.se
Lund University, Faculty of Engineering,
Department of Construction Sciences

Göran Sandberg

Phone: +46 46 2228146
E-mail: goran.sandberg@byggmek.lth.se
Lund University, Faculty of Engineering,
Department of Construction Sciences

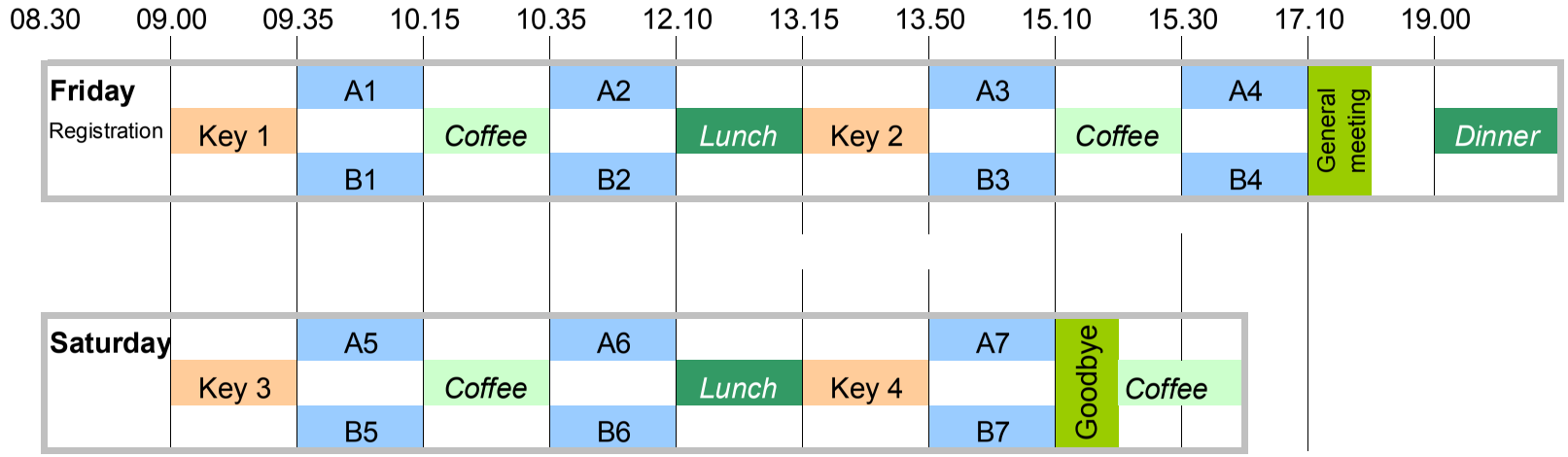

Key 1

Professor Gerhard Holzapfel
Rupture Analysis for Human Atherosclerotic Plaques

Key 2

Professor Henrik Myhre Jensen
Numerical Calculation of Interface Bond Fracture

Key 3

Professor Einar M. Rønquist
The reduced basis element method

Key 4

Professor Reijo Kouhia
Some Observations on the Integration of Inelastic Constitutive Models with Damage

	Sessions	**No. of papers**
A1	Biomechanics	2
A2	Biomechanics	4
A3	Material	4
A4	Products	5
A5	CFD	2
A6	CFD	4
A7	Products	4
		25
B1	Fracture Mechanics	2
B2	Multiscale modelling	4
B3	Multiscale + fracture	4
B4	Fracture Mechanics	5
B5	Misc.	2
B6	Optimization	5
B7	Material	5
		27

Key Sessions

	Title	Author		Co-author	Organisation
Key Sessions					
	Rupture Analysis for Human Atherosclerotic Plaques	Holzapfel	Gehard	Gasser, Sommer	KTH, Dept of Solid Mechanics
	Numerical Calculation of Interface Bond Fracture	Jensen	Henrik Myhre		Aalborg University
	The reduced basis element method	Rönquist	Einar M		Dept of Mathematical Sciences, NTNU
	Some Observations on the Integration of Inelastic Constitutive Models with Damage	Kouhia	Reijo	Eirola, Hartikainen, and Manninen	Inst of Mathematics and Lab of Struc Mech, Helsinki Univ of Tech

A Sessions

	Title	Author		Co-author	Organisation
Session A1, Biomechanics					
	Kinematic Analysis of Over-determinate Systems	Andersen	Michael Skippe	Damsgaard, Christensen, Rasmussen	Aalborg University
	Optimal simulations for human androbotic movements	Kaphle	Manindra	Eriksson	KTH, Engineering Sciences
Session A2, Biomechanics					
	Computational Modelling of Plate-gap Biosensors with a Porous Inert Membrane	Baronas	Romas	Ivanauskas	Vilnius university
	Finite Element Analyses of the Influence of the Chordae on the Mitral Valve Response	Prot	Victorien	Skallerud	Norwegian University of Science and Technology
	Spatial Differences in Cardiac Strains During Filling	Kindberg	Katarina	Karlsson	Linköping University, IMT
	Fluid dynamics of mechanical aortic valves	Hellevik	Leif Rune	Leinan, Skallerud	NTNU Norway, Div of Biomechanics, Dep of Struc Eng
	Temporal Changes in Sheet Architecture During Systole	Oom	Charlotte	Kindberg, Karlsson	Linköping University, IMT
Session A3, Material					
	A sorption hysteresis model for cellulosic materials	Frandsen	Henrik	Damkilde	Aalborg University, Dept of Civil Engineering
	Time-Sequential Error Control and Adaptivity in Space-Time for Poro-mechanics Problems	Runesson	Kenneth	Larsson	Chalmers University of Technology
	A Spatial Formulation of Anisotropic Material at Large Strains with Application to Cubic Material Symmetry	Harrysson	Magnus	Harrysson, Ristinmaa	Lund University, LTH, Div of Solid Mechanics
	An integration algorithm for elasto-plastic damage	Wallin	Mathias	Ristinmaa	Lund University, LTH, Dept of Solid Mechanics
Session A4, Products					
	Design of Multiple Tuned mass Dampers on Flexible Structures	Krenk	Steen	Högsberg	DTU, Dept of Mecanical Engineering
	On optimal control of hydraulic cranes	Ekevid	Torbjörn		Växjö University
	Modelling the Dynamic Properties of Rubber in Rolling Contact	Olsson	A K	Austrell	Lund University, LTH, Div of Structural Mechanics
	Conceptual design of the enclosure of an extremely large telescope - 1	Persson	Kent	Sandberg, Revstedt	Lund University, Div of Structural Mechanics
	Conceptual design of the enclosure of an extremely large telescope - 2	Revstedt	Johan		Lund University, LTH, Dept of Energy Sciences
Session A5, CFD					
	A new collocation method for solving the nonstationary Navier …	Zapomel	Jaroslav		VSB - Technical university of Ostrava
	Use of Richardson Extrapolation in Error Estimation of LES	Brandt	Tellervo		Laboratory of Aerodynamics, Helsinki University of Technology TKK
Session A6, CFD					
	Direct numerical simulation of non-isothermal turbulent wall-jets	Ahlman	Daniel	Brethouwer, Johasson	KTH, Dept of Mechanics
	POD analysis of the acoustic field in a gas turbine combustion chamber	Szasz	Robert Zoltan	Fuchs	Lund University, LTH, Dept of Energy Sciences
	Simulation of the Acoustics Behind a Barrier Generated by Periodically Passing Vehicles	Åberg	Magnus	Szasz	Lund University, LTH, Dept of Energy Sciences
	Large Eddy Simulation and Proper Orthogonal Decomposition of a swirling turbulent flow.	Duwig	Christophe	Fuchs	Lund University, LTH, Dept of Energy Sciences
Session A7, Products					
	Equivalent Diagonal Strut Width Computation for Infill Frame with Central Window Opening	Høiseth	Karl Vincent	Pradham, Murty, Aryal	NTNU Norway, Dept of Science and Technology
	Numerical simulations of RC beams with corroded rebars	Sæther	Irina	Horrigmoe, Sand	Norut Technology Ltd.
	Parameterization and Contact analysis of an Offshore Saddle Tapping Tee System	Kristensen	Anders	Larsen, Bay, Jepsen	Alborg University, Esbjerg Inst of Technology
	Optimal Modules in Conceptual Design of Car Product Families	Torstenfelt	Bo	Klarbring	Linköping University, Dept of Mechanical Engineering

B Sessions

	Title	Author		Co-author	Organisation
Session B1, Fracture Mechanics					
	A Conservative Integral for Piezoelectric Ceramics with Impermeable Crack Face Conditions	Banks-Sills	Leslie	Motola, Shemesh	Lund University, LTH, Div of Solid Mechanics
	Crack Tip Singularity in a Buckling Thin Sheet	Ståhle	Per	Li, Bjerkén	Lund University, LTH, Div of Solid Mechanics
Session B2, Multiscale modelling					
	Adaptive Variational Multiscale Methods	Larsson	Mats G.		Umåe University, Dept of Mathematics
	Aspects on Error Controlled Concurrent Muliscale Modeling Based on RVE Computations - The Power of Duality	Larsson	Fredrik	Runesson	Chalmers University of Technology, Dept of Applied Mechanics
	Adaptive Finite Element Simulation of Coupled Flow - Transport	Bengzon	Fredrik	Larson and Söderlund	Umeå University, Department of Mathematics, Sweden
	Estimation of model and discretization errors in parameter identification problems	Johansson	Håkan	Larsson, Runesson	Department of Mathematics, Umeå University, Sweden
Session B3, Multiscale modelling and Fracture mechanics					
	Computational Aspects on Multiscale Modeling of Polycrystallines with Gradient Crystal Plasticity	Ekh	Magnus	Grymer, Runesson	Chalmers University of Technology
	On the Implementation of Plane Stress in Computational Multiscale Modeling	Lillbacka	Robert	Runesson, Larsson	SP, Swedish National Testing and Research Institute
	An experimental method to determine compliance curves close to the crack tip …	Jacobsson	Lars		Lund University, LTH, Division of Materials Engineering
	Fracture of Zr-alloy pressure tubes due to hydride blister formation	Singh	Ram		Malmö University, Div of Materials Science
Session B4, Fracture Mechanics					
	Crack branching - Experiment and Simulation of Strain Assisted Corrosion Cracking	Hejman	Ulf	Bjerkén	Malmö University, Dept of Solid Mechanics
	Dislocation modelling of short fatigue cracks	Hansson		Melin	
	Dissolution Driven Fracture - Simulation of Crack Growth	Bjerkén	Christina		Malmö University, Div of Materials Science
	Micromechanical Modeling of Rupture in Combined Tension and Shear	Barsoum	Imad	Faleskog	KTH, Dept oft Solid Mechanics
	Mixed mode energy release rate analysis by a beam theory applied to timber beams with a hole	Gustafsson	Per Johan		Lund University
Session B5, Misc.					
	Teaching Principal Stresses by Truss Analogies	Tibert	Gunnar	Krantz	KTH Engineering Sciences, Dept of Mechanics
	A Lightweight Application Portal for the Grid	Lindemann	Jonas	Sandberg	Lund University, LTH, Div of Structural Mechanics
Session B6, Optimization					
	Application of an adaptive response surface approach for efficients tructural reliability analysis	Most	Thomas	Bucher	Institute of Structural Mechanics, Bauhaus-University Weimar
	A parallel method for solving discrete topology design problems	Rasmussen	Marie-Louise	Stolpe	Technical University of Denmark, Dept of Mathematics
	Topology optimization - Improved checker-board filtering with sharp contours	Damkilde	Lars	Pedersen, Lund, Kristensen	Aalborg University Esbjerg
	Vibration reduction of structures using global and local optimization techniques	Movaffaghi	Hamid		Chalmers University of Technology, Applied Mechanic
	Optimal design of inelastic spherical caps with cracks	Lellep	Jaan	Tungel	Tartu University
Session B7, Material					
	Crack-growth in a strain gradient Dept ofendent plasticity model	Mikkelsen	Lars Pilgaard		Risø National Laboratorium
	A simple and efficient FEM-implementation of the Modified Mohr-Coulomb criterion	Clausen	Johan	Damkilde	Aalborg University Esbjerg
	Simulation of Martensitic Phase Transformation in Austenitic Steel	Hallberg	Håkan	Håkansson, Ristinmaa	Dept of Solid Mechanics, Lund University
	Continuum Mixture theory as an approach to Fluid-Structure Interaction	Strömberg	Lena		KTH, Dept of Solid Mechanics
	Simulation of a Friction Stir Welding process using FE technique	Ahadi	Aylin	Gagner	Lund University, LTH, Div of Mechanics

Rupture Analysis for Human Atherosclerotic Plaques

G.A. Holzapfel, C.T. Gasser, G. Sommer

Department of Solid Mechanics
Royal Institute of Technology (KTH)
Osquars backe 1, SE-100 44 Stockholm
E-mail: gh@hallf.kth.se

Recent results on the anisotropic dissection properties of human arterial tissues are presented. They serve as a basis for the material and numerical modeling of plaque rupture which may occur spontaneously or traumatic. A patient-specific biomechanical analysis of plaque rupture during balloon-angioplasty is shown. The lecture closes by pointing out some multi-disciplinary future challenges in the field of tissue biomechanics with academia, industry and clinical importance.

Numerical Calculation of Interface Bond Fracture

Henrik Myhre Jensen

Department of Civil Engineering
Aalborg University, Aalborg, Denmark
e-mail: hmj@civil.aau.dk

Summary A description of two methods for numerical prediction of crack propagation through an adhesive layer is presented. The first method is based on a fracture mechanical approach where the edge of the bond region is treated as an interface crack front. Along the front, the energy release rate and the mode I, II and III stress intensity factors are calculated. A method for predicting quasi-static crack growth is presented by introducing a crack growth criterion. The shape of the crack front and the critical applied load to propagate the crack is obtained. The second method is based on a cohesive zone description of the adhesive layer. Comparisons of results based on the two approaches are shown.

Introduction

Examples of plate or shell structures, which are adhesively bonded, include composite structures applied in the aeroplane, automotive and the wind turbine blade industry. Traditional methods for calculating the failure strength of adhesive bonds include the model of Volkersen [1] and the model of Goland and Reissner [2]. Both models are stress based and they are used as simple design tools for dimensioning single lap joints. The theory has later been expanded to other geometries as described by Adams [3].

Fracture mechanical models for predicting bond failure have been developed more recently. Fracture mechanical solutions for initiation of failure in spot welds have been formulated in Radaj [4] and Zhang [5] and in Jensen [6], [7] for initiation and propagation of fracture in adhesive joints. A thin adhesive layer can be analyzed as an external interface crack front. Assuming linear elastic fracture mechanics, the energy release rate G at the crack front is given by the effective crack tip loads. The fracture mechanical model uses a mixed mode interface fracture criterion coupled with a propagation formulation, embedded in an outer finite element model.

In the cohesive zone model, the adhesive bond region is represented by non-linear springs used to model the fracture process. The cohesive zone is embedded in a finite element model of the adherends. Cohesive zone models have been applied to model fracture in elastic–plastic solids in *e.g.* Tvergaard and Hutchinson [8]. Plastically deforming adhesive joints in Modes 1 and 2 loading conditions have been modeled using a cohesive zone representation of the bond region in Wei and Hutchinson [9] and Yang and Thouless [10]. In Feraren and Jensen [11] the cohesive zone model predictions were compared to fracture mechanical predictions of the crack front shape during the process of interface bond failure.

The basic joint geometry considered consists of two partly overlapping shells, bonded along a thin adhesive layer. In this case the thickness of the adherends are required to be significantly higher than that of the adhesive layer, and it is assumed that the fracture process is limited to the bond region. The significance of fracture process zone parameters is investigated.

Fracture mechanics

The edge of the bond zone is regarded as an interface crack front, which is subject to combined mode I, II and III loading. The energy release rate, G, and the mode I, II and III contributions to G

can be calculated by the coupling of an inner, fracture mechanics based solution close to the crack tip with an outer solution for the stress state in the adherends.

The relation between the energy release rate and the stress intensity factors K_I, K_{II} and K_{III} is given by

$$G = \frac{1}{\cosh^2(\pi\varepsilon)}\frac{1}{2}\left(\frac{1}{\bar{E}}+\frac{1}{\bar{E}_s}\right)\left(K_I^2+K_{II}^2\right)+\frac{1}{2}\left(\frac{1+\nu}{E}+\frac{1+\nu_s}{E_s}\right)K_{III}^2 \tag{1}$$

The subscript $(\,)_s$ refers to the lower plate, which may have elastic properties E_s and ν_s different from those of the top plate. In (1) ε denotes the bimaterial index.

A family of interface fracture criteria formulated in Jensen *et al.* [12] is applied in the form

$$G_I+\lambda_2 G_{II}+\lambda_3 G_{III} = G_{1c} \tag{2}$$

where λ_2 and λ_3 denote parameters between 0 and 1 adjusting the relative contributions of mode II and III to the fracture criterion, and G_{1c} is the mode I fracture toughness of the bond.

The criterion (2) has been applied to thin film debonding problems in *e.g.* Jensen *et al.* [12] and Jensen and Thouless [13]. The fracture criterion captures the mixed mode dependence of interface fracture toughness due to plastic deformation at the crack tip [8] or rough crack faces contacting under mode II and III dominant loading conditions (Evans and Hutchinson [14] and Jensen [15]).

The application of (2) requires a separation of the energy release rate into mode I, II and III components, This follows from the definitions of the phase angles of loading ψ and ϕ introduced in Jensen *et al.* [12]

$$\tan\psi = \frac{\mathrm{Im}\left((K_I+iK_{II})h^{i\varepsilon}\right)}{\mathrm{Re}\left((K_I+iK_{II})h^{i\varepsilon}\right)}\ ,\ \cos\phi = \sqrt{\frac{G_{III}}{G}} \tag{3}$$

where i is the imaginary unit ($i = \sqrt{-1}$), ε is the bimaterial constant and h is the thickness of the top plate. The results below are presented for the case of a large difference in bottom and top plate thickness but this is not a restriction on the method.

The fracture mechanical approach to interface crack propagation works by increasing the load incrementally until (2) is exceeded. A crack growth criterion point wise along the crack front during further incremental loading is assumed of the type

$$C_{i+1} = C_i + \mathscr{G}\mathbf{n}\left(G\left(1+(1-\lambda_2)\sin^2\psi\sin^2\phi+(1-\lambda_3)\cos^2\phi\right)-G_{1c}\right)^p \tag{4}$$

Here, C_i denotes the crack front curve at increment number i, which has the unit normal vector $\mathbf{n}$ and $\mathscr{G}$ and p are parameters chosen so that during incremental loading the fracture criterion is satisfied along the propagating part of the crack front, and the fracture criterion is not exceeded elsewhere.

Results and discussion

Results are presented below for the case of planar plates subject to in-plane loads. The following parameters are introduced

$$k = \frac{2\lambda_3}{(1-\nu)\left(1+(\lambda_2-1)\sin^2\omega\right)}$$

$$\sigma_c = \left(\frac{2EG_{1c}}{(1-\nu^2)h\left(1+(\lambda_2-1)\sin^2\omega\right)}\right)^{1/2} \tag{5}$$

The angle ω is a weak function of the elastic mismatch in the system. It has been tabulated in Suo and Hutchinson [16] and for most systems $40^o < \omega < 60^o$.

The stress, σ_c , has the interpretation as being the critical stress required to propagate a plane strain edge crack under steady-state conditions.

In Fig. 1 shapes of initially circular bond regions during fracture are shown. Results are presented for three values of parameters in the fracture criterion (2) characterised by k in (5).

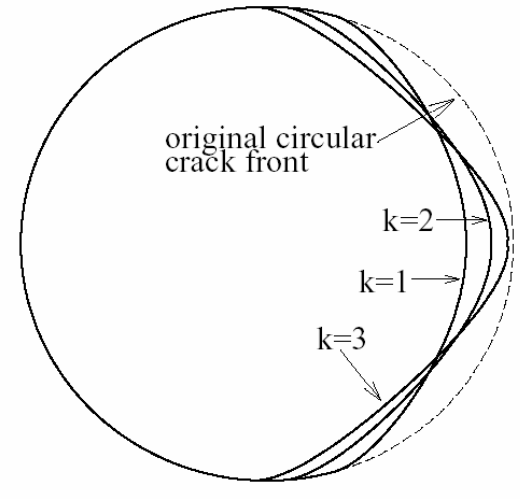

Fig. 1. Shapes of circular bond during failure for three different fracture criteria.

Initial stable crack propagation in the bond region is predicted indicating a significant residual strength of the bond after initial failure. The failure strength of the bond is denoted by σ_0 and is obtained as part of the numerical predictions. The initial stable crack propagation following initiation is illustrated in Fig. 2 where the stress required to propagate the crack is shown as a function of the relative area change of the bond region, which is introduced as a measure of the amount of crack growth.

The bond strength, σ_0 , is written as

$$\sigma_0 = \frac{1}{\sqrt{hF_p}}\sqrt{\frac{2EG_{1c}}{(1-\nu^2)\left(1+(\lambda_2-1)\sin^2\omega\right)}} \tag{6}$$

where F_p denotes the peak value of the left hand side of (2) along the crack front for a given applied external load.

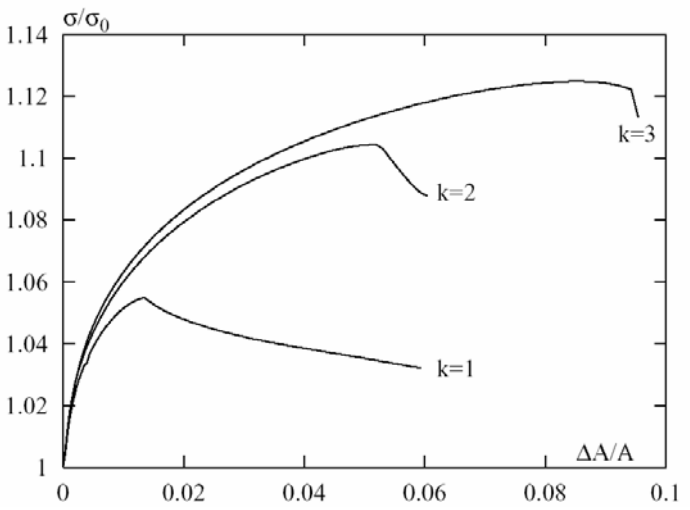

Fig. 2. Stress for crack propagation as a function of relative area change of bond region.

As seen in Fig. 2 the residual strength of the bond is sensitive to the interface fracture criterion. The classical mode independent Griffith fracture criterion corresponds to $k = 3$.

As described, the cohesive zone model assumes the bond region to be described by non-linear springs. A tri-linear relationship between crack surface tractions and crack opening displacements is assumed (Feraren and Jensen [11]). A measured traction separation law is shown in Fig. 3 for a glass fibre epoxy beam.

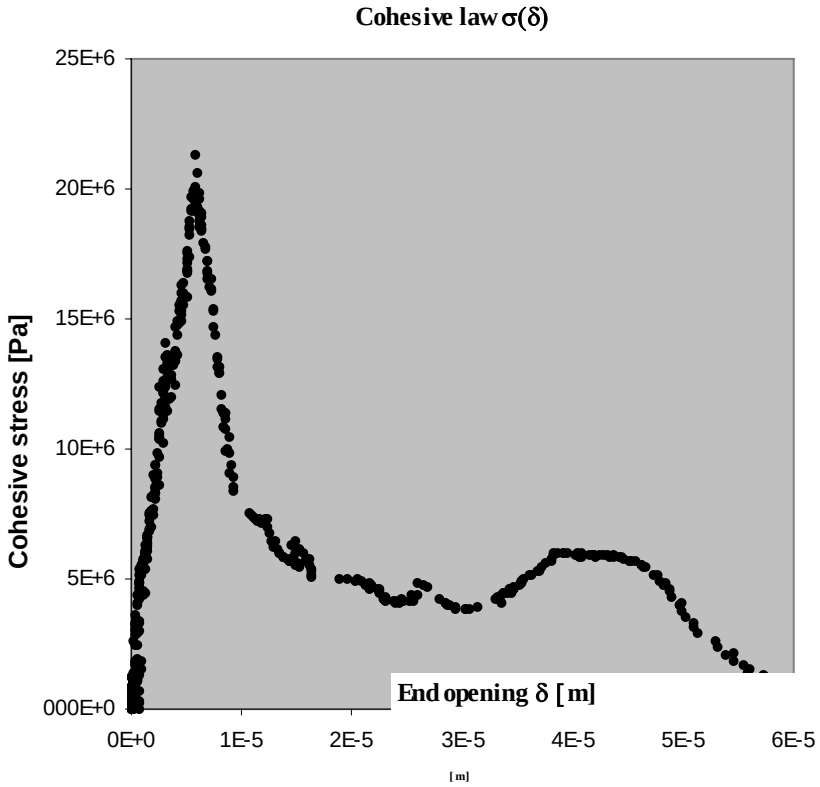

Fig. 3. Measured traction vs. separation law.

A comparison between calculated shapes of the crack front based of the fracture mechanics approach and the cohesive zone model is shown in Fig. 4. A good agreement is observed.

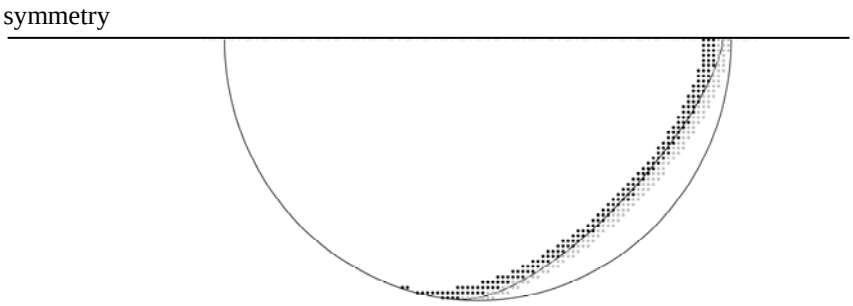

Fig. 4. Crack front predicted by fracture mechanics and cohesive zone model.

The advantage of the cohesive zone model over the fracture mechanical model is that large curvature of the crack front is allowed for. Also plastic deformation in large scale in the adherends can be taken into account. A realistic situation in adhesive bond problems is the occurrence of trapped air-bubbles or flaws, which reduces the strength of the bond. In Fig. 5 the shape of a crack propagating at an interface and interacting with a circular flaw is shown.

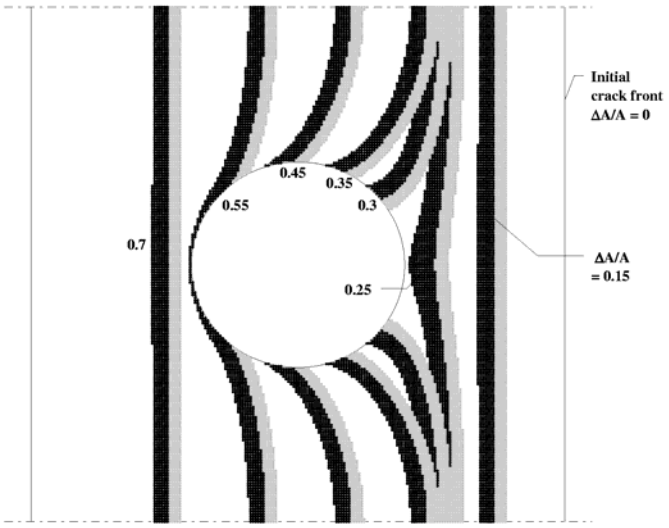

Fig. 5. Predicted crack front shape around a circular interface flaw.

The stress vs. relative area change prediction corresponding to Fig. 5 are shown in Fig. 6 by which the reduction in bond strength can be predicted. The three curves in Fig. 6 denoted A, B and C correspond to three cohesive laws with the same toughness but different strength.

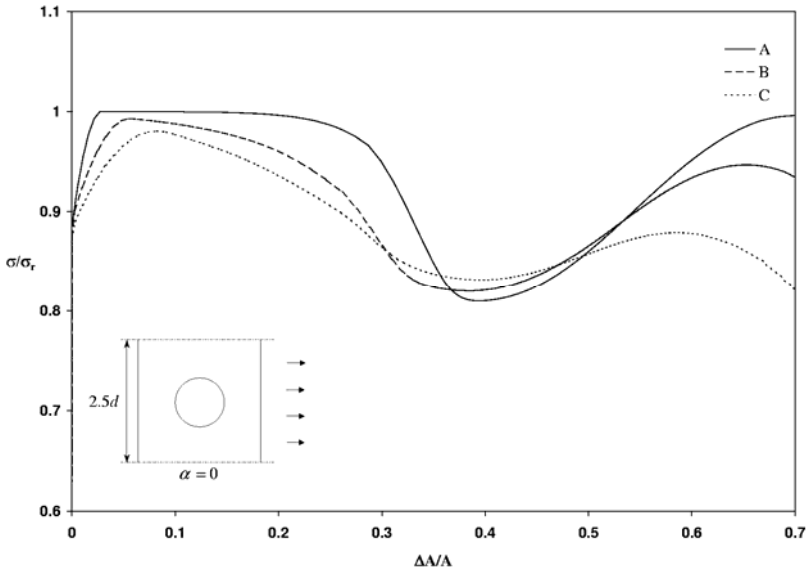

Fig. 6. Stress vs. relative area change for three cohesive laws.

Acknowledgements Support from the Danish Technical Research Council through the Framework Programme "Interface Design of Composite Materials" (STVF fund no. 26-03-0160) is gratefully acknowledged.

References

[1] O. Volkersen. Die nietkraftverteilung in zugbeanspruchten nietverbindungen mit konstanten laschenquerschnitten. *Luftfahrtforschung* **15**, 41–47 (1938).

[2] M. Goland and E. Reissner. The stresses in cemented joints. *Journal of Applied Mechanics* **66,** A17–27 (1944).

[3] R.D. Adams. Theoretical stress analysis of adhesively bonded joints. *Joining Fibre Reinforced Plastics*, 185–226 (1987).

[4] D. Radaj. Local fatigue strength characteristic values for spot welded joints. *Engineering Fracture Mechanics* **37**, 245-250 (1990).

[5] S. Zang. Fracture mechanics solutions to spot welds. *International Journal of Fracture* **112**, 247–274 (2001).

[6] H.M. Jensen. Three-dimensional numerical investigation of brittle bond fracture. *International Journal of Fracture* **114**, 153–165 (2001).

[7] H.M. Jensen. Crack initiation and growth in brittle bonds. *Engineering Fracture Mechanics* **70**, 1611–1621 (2003).

[8] V. Tvergaard and J.W. Hutchinson. The relation between crack growth resistance and fracture process parameters in elastic–plastic solids. *Journal of the Mechanics and Physics of Solids* **40**, 1377–1397 (1992).

[9] Y. Wei and J.W. Hutchinson. Interface strength, work of adhesion and plasticity in the peel test. *International Journal of Fracture* **93**, 315–333 (1989).

[10] Q.D. Yang and M.D. Thouless. Mixed-mode fracture analyses of plastically-deforming adhesive joints. *International Journal of Fracture* **110**, 175–187 (2001).

[11] P. Feraren and H.M. Jensen, Cohesive Zone Modelling of Interface Fracture near Flaws in Adhesive Bonds. *Engineering Fracture Mechanics* **71**, 2125-2142, (2004).

[12] H.M. Jensen, J.W. Hutchinson and K.-S. Kim. Decohesion of a cut prestressed film on a substrate. *International Journal of Solids and Structures* **26**, 1099–1114 (1990).

[13] H.M. Jensen and M.D. Thouless. Effects of residual stresses in the blister test. *International Journal of Solids and Structures* **30**, 779-795 (1993).

[14] A.G. Evans and J.W. Hutchinson. Effects of non-planarity on the mixed mode fracture resistance of bimaterial interfaces. *Acta Materialia* **37**, 909-916 (1989).

[15] H.M. Jensen. Mixed mode interface fracture criteria. *Acta Materialia* **38**, 2637-2644 (1990).

[16] Z. Suo and J.W. Hutchinson. Interface crack between two elastic layers. *International Journal of Fracture* **43**, 1-18 (1990).

The reduced basis element method

Einar M. Rønquist
Department of Mathematical Sciences
Norwegian University of Science and Technology (NTNU)
email: ronquist@math.ntnu.no

Abstract

The reduced basis element method is a new approach for approximating the solution of problems described by partial differential equations. The method takes its roots in domain decomposition methods and reduced basis discretizations [1–5].

The basic idea is to first decompose the computational domain into a series of subdomains that are similar to a few reference domains (or generic computational parts). Associated with each reference domain are precomputed solutions corresponding to the same governing partial differential equation, and the same boundary conditions, but solved for different choices of some underlying parameter. In this work, the parameters are representing the geometric shape associated with a computational part. The approximation corresponding to a new shape is then taken to be a linear combination of the precomputed solutions, mapped from the reference domain for the part to the actual domain [6].

We discuss the basic ideas related to the construction of the basis functions and to "gluing" the local approximations together in the multidomain case. We also discuss the computational cost associated with this approach, as well as *a posteriori* error bounds in order to certify the quality of the reduced basis approximations. Finally, we present application of the method to a thermal fin problem [7], and to simulating hierarchical flow systems [8, 9].

This is joint work with Professor Yvon Maday at Laboratoire Jacques-Louis Lions, Université Pierre et Marie Curie, and with Dr. Alf Emil Løvgren at Department of Mathematical Sciences, Norwegian University of Science and Technology.

References

[1] J. P. Fink and W. C. Rheinboldt. On the error behaviour of the reduced basis technique in nonlinear finite element approximations. *Z. Angew. Math. Mech.*, **63**, 21–28, 1983.

[2] A. K. Noor and J. M. Peters. Reduced basis technique for nonlinear analysis of structures. *AIAA J.*, **18**(4), 455–462, 1980.

[3] C. Prud'homme, D. V. Rovas, K. Veroy, L. Machiels, Y. Maday, A. T. Patera, and G. Turinici. Reliable real-time solution of parametrized partial differential equations: Reduced basis output bound methods. *J. Fluids Engineering*, **124**, 70–80, 2002.

[4] N.N. Cueong, K. Veroy, and A.T. Patera. Certified real-time solution of parameterized partial differential equations. In *Handbook of Materials Modeling*, Edited by S. Yip, Springer, 1523-1558 (2005).

[5] M. Barrault, Y. Maday, N. C. Nguyen, and A. T. Patera. An 'empirical interpolation' method: Application to efficient reduced-basis discretization of partial differential equations. *C. R. Acad. Sci. Paris, Serie I*, **339**, 667–672, 2004.

[6] Y. Maday and E. M. Rønquist. A reduced-basis element method. *J. Sci. Comput.*, **17**, 447–459, 2002.

[7] Y. Maday and E. M. Rønquist. The reduced-basis element method: Application to a thermal fin problem. *SIAM J. Sci. Comput.*, **26**(1), 240–258, 2004.

[8] A.E. Løvgren, Y. Maday, and E.M. Rønquist. A reduced basis element method for the steady Stokes problem. M2AN, **40**(3), 529–552, 2006.

[9] A.E. Løvgren, Y. Maday and E.M. Rønquist. A reduced basis element method for the steady Stokes problem: application to hierarchical flow systems, *Modeling, Identification and Control*, **27**(2), 79–94, 2006.

Some Observations on the Integration of Inelastic Constitutive Models with Damage

Timo Eirola[1], Juha Hartikainen[2], Reijo Kouhia[2*] and Timo Manninen[2]
[1]Institute of Mathematics
[2]Laboratory of Structural Mechanics
Helsinki University of Technology, Finland
e–mail: firstname.lastname@tkk.fi

Summary Accurate integration of inelastic constitutive models including damage is a challenging task due to the different nature of plastic/viscous and damage evolution processes. Stability of the integration scheme is guaranteed if all the eigenvalues of the stability matrix have modulus less than unity. For standard implicit schemes this is automatically satisfied for plastic and viscous models, since all the eigenvalues of the system's Jacobian matrix are negative. However, for damaging materials the notion of stability is not relevant, due to the unstable character of the damage process. Therefore, strongly dissipative implicit algorithms, like backward Euler, do not perform well in integrating inelastic constitutive models with damage. Application of discontinuos Galerkin type methods will be discussed.

Introduction

There are many different algorithms for the integration of inelastic constitutive models. However, the fully implicit backward Euler scheme seems to be the most popular, although it is only first-order accurate [1, 2, 3]. In practical problems, especially in those of creep and viscoplasticity, the time steps are often large, several magnitudes larger than the critical time step of some explicit methods, e.g. the forward Euler method. Therefore, the integrator should be unconditionally stable and sufficiently accurate for large time steps.

As shown in [4], the asymptotic convergence rate does not necessarily reflect high accuracy outside the asymptotic range, which usually means step sizes smaller than the critical time step of the explicit Euler method. For large time steps, the first-order accurate backward Euler method seems to be more accurate than many higher-order schemes. Therefore, an integrator for inelastic constitutive models should be at least [4, 5]:

- L-stable
- and for $\dot{\sigma} + \lambda\sigma = 0$, λ = constant, the stability function should be
  - strictly positive, and
  - monotonous with respect to time step.

It is obvious that the standard backward Euler scheme fulfills these requirements.

When damage is included in the constitutive model, behaviour of the solution of the governing evolution equations is completely different from that of viscous and plastic solutions. Solutions of problems in creep, plasticity and viscoplasticity are diffusive and decay exponentially with time whereas damage produces reactive type of solutions growing exponentially with time.

To demonstrate the difference of the solution types, a simple uniaxial Maxwell type creep model is considered first. The inelastic strain rate is defined as $\dot{\epsilon}_{\mathrm{i}} = \tau_{\mathrm{vp}}^{-1}(\sigma/\sigma_{\mathrm{r}})$, where τ_{vp} is the viscosity parameter and σ_{r} is an arbitrary reference stress. The resulting evolution equation for the stress is the following simple first order ordinary differential equation with constant coefficients

$$\dot{\sigma} + \frac{E}{\tau_{\mathrm{vp}}}\frac{\sigma}{\sigma_{\mathrm{r}}} = E\dot{\epsilon} \tag{1}$$

where E is the Young's modulus and $\dot{\epsilon}$ is the total strain rate. With the initial condition $\sigma(t_0) = \sigma_0$,

the nondimensional form of the problem is

$$\dot{y} + \frac{1}{\tau_{\rm vp}\epsilon_{\rm r}} y = \frac{\dot{\epsilon}}{\epsilon_{\rm r}}, \qquad y(t_0) = y_0 \tag{2}$$

where $y = \sigma/\sigma_{\rm r}$, $y_0 = \sigma/\sigma_0$ and $\epsilon_{\rm r} = \sigma_{\rm r}/E$. Typically, in non-linear finite element codes the strain rate is constant over an increment ($\dot{\epsilon} = \dot{\epsilon}_{\rm c}$), in which case the solution of problem (2) can be expressed in a closed form as follows

$$y(t) = \tau_{\rm vp}\dot{\epsilon}_{\rm c}\left[1 + \left(\frac{y_0}{\tau_{\rm vp}\dot{\epsilon}_{\rm c}} - 1\right)\exp\left(-\frac{t - t_0}{\tau_{\rm d}\epsilon_{\rm r}}\right)\right]. \tag{3}$$

Notice that $y(t) \longrightarrow \tau_{\rm d}\dot{\epsilon}_{\rm c}$ as $t \longrightarrow \infty$.

For a damage, if a slightly modified Kachanov/Rabotnov type evolution equation is chosen, the constitutive model can be written in the form

$$\sigma = (1 - D)E\epsilon, \qquad \text{and} \qquad \dot{D} = \frac{1 + D}{\tau_{\rm d}}\left(\frac{Y}{Y_{\rm r}}\right)^r, \tag{4}$$

where D is the nondimensional scalar damage variable, Y is the thermodynamic force, conjugate to the damage rate $\dot{D}$ and has the expression $Y = \frac{1}{2}E\epsilon^2$. The reference value $Y_{\rm r}$ is chosen as

$$Y_{\rm r} = \tfrac{1}{2}{\sigma_{\rm r}}^2/E. \tag{5}$$

For a constant strain rate loading, $\epsilon(t) = \dot{\epsilon}_{\rm c}t$, and initial condition $D(t_0) = D_0$, the solution of the damage evolution equation $(4)_2$ is

$$D = (1 + D_0)\exp\left\{\frac{\epsilon_{\rm r}}{(2r+1)\tau_{\rm d}\dot{\epsilon}_{\rm c}}\left[\left(\frac{\dot{\epsilon}_{\rm c}t}{\epsilon_{\rm r}}\right)^{2r+1} - \left(\frac{\dot{\epsilon}_{\rm c}t_0}{\epsilon_{\rm r}}\right)^{2r+1}\right]\right\} - 1. \tag{6}$$

Performance of different time integrators for the model evolution equations (1) and (4) is shown in Fig. 1 for single time step computation as a function of the nondimensional time step, normalized with respect to the relaxation times $\tau_{\rm vp}\epsilon_{\rm r}$ and $\tau_{\rm d}\epsilon_{\rm r}$. In creep analysis, conditionally stable explicit methods are not feasible due to the restricting critical time step. The implicit backward Euler method in turn seems to be the most popular integrator for inelastic constitutive models. This is probably due to its good accuracy properties when time steps are large [4]. An intepretation by Alberty and Carstensen [6] is that the backward Euler scheme has "additional exactness properties in some examples". The discontinuous Galerkin method with linear interpolation, dG(1), is integrated using either the the two point Gauss-Legendre or the two point Gauss-Lobatto quadratures. When the integrals in the dG(1) scheme are underintegrated by using the two-point Gauss-Lobatto scheme (endpoint rule) the dG(1) scheme is identical to the Lobatto IIIC type implicit Runge-Kutta method, see Ref. [7], which also exhibits good accuracy properties for large time steps [4, 5].

Unfortunately, the good behaviour of the simple backward Euler scheme for plasticity and viscoplasticity computations is not inherited for damage models. The backward Euler scheme even blows up when $\Delta t/\tau_{\rm d} = (\epsilon_{\rm r}/\epsilon)^{2r}$. The fundamental difference of models (1) and $(4)_2$, when written in a generic form $\dot{y} = f(y)$, is that the eigenvalues of the Jacobian $\partial f/\partial y$ are negative for the creep model and positive for the damage model. Solutions are either "diffusive", exponentially decaying, Eq. (3), or "reactive", exponentially growing, Eq. (6).

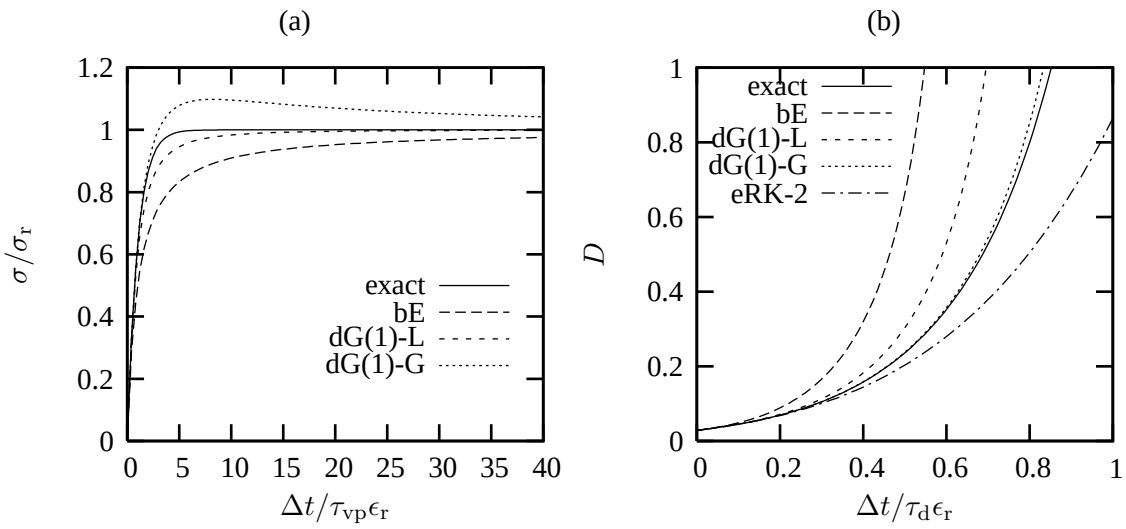

Figure 1: Performance of different integrators in a single step computation under uniaxial constant strain-rate loading. (a) Creep model (1) with $\tau_{\rm vp}\dot{\epsilon}_{\rm c} = 1$ and $t_0 = 0$, (b) damage model (4) with $\tau_{\rm d}\dot{\epsilon}_{\rm c} = 1$ and $t_0 = 2\tau_{\rm d}\epsilon_{\rm r}$. Abbreviation dG(1)-L denotes the dG(1)-scheme with two point Gauss-Lobatto integration, while dG(1)-G stands for the dG(1)-scheme with two point Gauss-Legendre integration and eRK-2 for the explicit two stage Runge-Kutta scheme.

Due to the unstable character of the damage process, there is no limiting critical time-steps for explicit methods. Even the most simple time-integrator, the explicit forward Euler scheme, performs better than its implicit counterpart. As it can be seen from the Fig.1b, the second order accurate explicit two-stage Runge-Kutta scheme (eRK-2) performs well. In this simple example, the dG(1)-scheme is clearly the best, both in asymptotic convergence rate and accuraty when time steps are large.

Constitutive model

In this paper, the integration schemes are tested for a model which describes the strain-rate dependent ductile-to-brittle transition [8]. The ductile behavior is considered as a viscoplastic feature, whereas the strain softening behaviour, after reaching the transition strain-rate, is dealt with a continuum damage model.

Thermodynamic formulation

The constitutive model is derived using a thermodynamic formulation, in which the material behaviour is described completely through the Helmholz free energy and the dissipation potential in terms of the variables of state and dissipation and considering that the Clausius-Duhem inequality is satisfied [9].

The Helmholtz free energy

$$\psi = \psi(\epsilon_{\rm e}, \omega) \tag{7}$$

is assumed to be a function of the elastic strains, $\epsilon_{\rm e}$, and the scalar integrity parameter, ω, describing damage $\omega = 1 - D$. For undamaged material $\omega = 1$ and $D = 0$, whereas the material is fully damaged when $\omega = 0$ and $D = 1$. Restricting the discussion to linear kinematics, the infinitesimal strain tensor, ϵ, can be additively decomposed into elastic and inelastic parts as

$$\epsilon = \epsilon_{\rm e} + \epsilon_{\rm i}. \tag{8}$$

As usual in the solid mechanics, the dissipation potential

$$\varphi = \varphi(\sigma, Y) \tag{9}$$

is expressed in terms of the thermodynamic forces σ and Y dual to the fluxes $\dot{\epsilon}_{\mathrm{i}}$ and $\dot{\omega}$, respectively. The dissipation potential is associated with the power of dissipation, γ, such that

$$\gamma = \frac{\partial \varphi}{\partial \sigma} : \sigma + \frac{\partial \varphi}{\partial Y} Y. \tag{10}$$

Convexity is not a prerequisite for the dissipation potential but the condition that the product $(\partial\varphi/\partial\sigma) : \sigma + (\partial\varphi/\partial Y)Y$ is non-negative.

The Clausius-Duhem inequality, in the absence of thermal effects, is formulated as

$$\gamma \geq 0, \quad \gamma = -\rho\dot{\psi} + \sigma : \dot{\epsilon}, \tag{11}$$

where ρ is the material density. Using decomposition (8) and defining that $\partial\psi/\partial\omega = Y$, the definition (10) and expression $(11)_2$ results in equation

$$\left(\sigma - \rho\frac{\partial \psi}{\partial \epsilon_{\mathrm{e}}}\right) : \dot{\epsilon}_{\mathrm{e}} + \left(\dot{\epsilon}_{\mathrm{i}} - \frac{\partial \varphi}{\partial \sigma}\right) : \sigma + \left(-\dot{\omega} - \frac{\partial \varphi}{\partial Y}\right) Y = 0. \tag{12}$$

Then, if eq. (12) holds for any evolution of $\dot{\epsilon}_{\mathrm{e}}$, σ and Y, inequality (11) is satisfied and the following relevant constitutive relations are obtained:

$$\sigma = \rho\frac{\partial \psi}{\partial \epsilon_{\mathrm{e}}}, \qquad \dot{\epsilon}_{\mathrm{i}} = \frac{\partial \varphi}{\partial \sigma}, \qquad \dot{\omega} = -\frac{\partial \varphi}{\partial Y}. \tag{13}$$

Particular model

A particular expression for the free energy, describing the elastic material behaviour with the reduction effect due to damage, is given by

$$\rho\psi = \frac{1}{2}\omega\epsilon_{\mathrm{e}} : C_{\mathrm{e}} : \epsilon_{\mathrm{e}} \tag{14}$$

where C_{e} is the elasticity tensor.

To model the ductile-to-brittle transition due to increasing strain-rate, the dissipation potential is decomposed into the brittle damaging part, φ_{d}, and the ductile viscoplastic part, φ_{vp}, as

$$\varphi(\sigma, Y) = \varphi_{\mathrm{d}}(Y)\varphi_{\mathrm{tr}}(\sigma) + \varphi_{\mathrm{vp}}(\sigma), \tag{15}$$

where the transition function, φ_{tr}, deals with the change in the mode of deformation when the strain-rate $\dot{\epsilon}_{\mathrm{i}}$ increases. Applying an overstress type of viscoplasticity [10, 11, 12] and the principle of strain equivalence [13, 14], the following choices are made to characterize the inelastic material behaviour:

$$\varphi_{\mathrm{d}} = \frac{1}{r+1}\frac{Y_{\mathrm{r}}}{\tau_{\mathrm{d}}\omega}\left(\frac{Y}{Y_{\mathrm{r}}}\right)^{r+1}, \tag{16}$$

$$\varphi_{\mathrm{tr}} = \frac{1}{pn}\left[\frac{1}{\tau_{\mathrm{vp}}\eta}\left(\frac{\bar{\sigma}}{\omega\sigma_{\mathrm{r}}}\right)^{p}\right]^{n}, \tag{17}$$

$$\varphi_{\mathrm{vp}} = \frac{1}{p+1}\frac{\sigma_{\mathrm{r}}}{\tau_{\mathrm{vp}}}\left(\frac{\bar{\sigma}}{\omega\sigma_{\mathrm{r}}}\right)^{p+1}, \tag{18}$$

where parameters $\tau_{\rm d}$, r and n are associated with the damage evolution, and parameters $\tau_{\rm vp}$ and p with the visco-plastic flow. In addition, η denotes the inelastic transition strain-rate. The pseudo relaxation times $\tau_{\rm d}$ and $\tau_{\rm vp}$ have the dimension of time and the exponents $r, p \geq 0$ and $n \geq 1$ are dimensionless. $\bar{\sigma}$ is a scalar function of stress, e.g. the effective stress $\sigma_{\rm eff} = \sqrt{3J_2}$, where J_2 is the second invariant of the deviatoric stress. The reference values $Y_{\rm r}$ and $\sigma_{\rm r}$ can be chosen arbitrarily, and they are used to make the expressions dimensionally reasonable.

Making use of Eqs. (8) and (13), choices (14)-(18) yield the following constitutive equations:

$$\sigma = \omega C_{\rm e} : (\epsilon - \epsilon_{\rm i}) \,, \tag{19}$$

$$\dot{\epsilon}_{\rm i} = \left[\frac{\varphi_{\rm d}}{(\tau_{\rm vp}\eta)^n \omega \sigma_{\rm r}} \left(\frac{\bar{\sigma}}{\omega \sigma_{\rm r}} \right)^{np-1} + \frac{1}{\tau_{\rm vp}\omega} \left(\frac{\bar{\sigma}}{\omega \sigma_{\rm r}} \right)^{p} \right] \frac{\partial \bar{\sigma}}{\partial \sigma} = g(\bar{\sigma}, \omega) \frac{\partial \bar{\sigma}}{\partial \sigma}, \tag{20}$$

$$\dot{\omega} = -\frac{\varphi_{\rm tr}}{\tau_{\rm d}\omega} \left(\frac{Y}{Y_{\rm r}} \right)^{r} . \tag{21}$$

Moreover,

$$Y = \rho \frac{\partial \psi}{\partial \omega} = \frac{1}{2} \left(\epsilon - \epsilon_{\rm i} \right) : C_{\rm e} : \left(\epsilon - \epsilon_{\rm i} \right) = \frac{1}{2\omega^2} \sigma : C_{\rm e}^{-1} : \sigma. \tag{22}$$

Properties of this model are discussed in [8]. However, it should be mentioned that the Clausius-Duhem inequality (11) is satisfied *a priori* for any admissible isothermal process. In addition, the constraint for the integrity ω that $\omega \in [0, 1]$ is satisfied automatically, since $\omega(x, 0) = 1$, $\dot{\omega} \leq 0$ and $\dot{\omega} \to 0$ as $\omega \to 0$.

Algorithmic treatment

Using matrix notation, the constitutive model (19)-(21) is rewritten in the form

$$\dot{\boldsymbol{\sigma}} = \boldsymbol{f}_{\sigma}(\boldsymbol{\sigma}, \omega), \tag{23}$$

$$\dot{\omega} = f_{\omega}(\boldsymbol{\sigma}, \omega) \tag{24}$$

where

$$\boldsymbol{f}_{\sigma}(\boldsymbol{\sigma}, \omega) = \omega \boldsymbol{C}_{\rm e}(\dot{\boldsymbol{\epsilon}} - \dot{\boldsymbol{\epsilon}}_{\rm i}) + \frac{f_{\omega}}{\omega}\boldsymbol{\sigma} = \omega \boldsymbol{C}_{\rm e} \left(\dot{\boldsymbol{\epsilon}} - g(\bar{\sigma}, \omega) \frac{\partial \bar{\sigma}}{\partial \boldsymbol{\sigma}} \right) + \frac{f_{\omega}}{\omega}\boldsymbol{\sigma}, \tag{25}$$

$$f_{\omega}(\boldsymbol{\sigma}, \omega) = -\frac{\varphi_{\rm tr}}{\tau_{\rm d}\omega} \left(\frac{Y}{Y_{\rm r}} \right)^{r} . \tag{26}$$

The backward Euler method

Applying the backward Euler scheme and the Newton's linearisation method to the evolution equations (23) and (24) results in the linear system of equations[1]

$$\begin{bmatrix} \boldsymbol{H}_{11} & \boldsymbol{h}_{12} \\ \boldsymbol{h}_{21}^T & H_{22} \end{bmatrix} \begin{Bmatrix} \delta\boldsymbol{\sigma} \\ \delta\omega \end{Bmatrix} = \Delta t \begin{Bmatrix} \boldsymbol{f}_{\sigma} \\ f_{\omega} \end{Bmatrix} - \begin{Bmatrix} \Delta\boldsymbol{\sigma} \\ \Delta\omega \end{Bmatrix}, \tag{27}$$

where

$$\boldsymbol{H}_{11} = \boldsymbol{I} - \Delta t \frac{\partial \boldsymbol{f}_{\sigma}}{\partial \boldsymbol{\sigma}}, \qquad \boldsymbol{h}_{12} = -\Delta t \frac{\partial \boldsymbol{f}_{\sigma}}{\partial \omega}, \tag{28}$$

$$\boldsymbol{h}_{21}^T = -\Delta t \frac{\partial f_{\omega}}{\partial \boldsymbol{\sigma}}, \qquad H_{22} = 1 - \Delta t \frac{\partial f_{\omega}}{\partial \omega}. \tag{29}$$

[1]The symbols Δ and δ refer to incremental and iterative values, $\boldsymbol{\sigma}_n^{i+1} = \boldsymbol{\sigma}_n^i + \delta\boldsymbol{\sigma}_n^i$, $\Delta\boldsymbol{\sigma}_n^i = \boldsymbol{\sigma}_n^i - \boldsymbol{\sigma}_{n-1}$, where the sub- and superscripts refer to step- and iteration numbers, respectively.

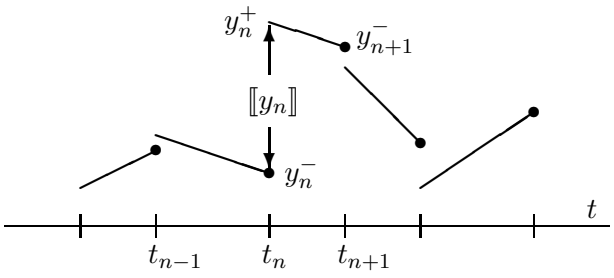

Figure 2: Discontinuous Galerkin method, dG(1); notation.

The algorithmic tangent matrix, i.e. the Jacobian of the algorithmic stress-strain relation, has the simple form

$$\boldsymbol{C} = \omega \widetilde{\boldsymbol{H}}_{11}^{-1} \boldsymbol{C}_{\mathrm{e}}, \tag{30}$$

where

$$\widetilde{\boldsymbol{H}}_{11} = \boldsymbol{H}_{11} - \boldsymbol{h}_{12} H_{22}^{-1} \boldsymbol{h}_{21}^T. \tag{31}$$

Due to the damage the Jacobian matrix is in general nonsymmetric. The Jacobian matrix is a necessity for the Newton's method to obtain asymptotically quadratic rate of convergence of the global equilibrium iterations. Notice that the Jacobian (30) can be ill-conditioned when $H_{22} \approx 0$.

The discontinuous Galerkin method

Denoting the evolution equations (23) as

$$\dot{\boldsymbol{y}} = \boldsymbol{f}(\boldsymbol{y}), \tag{32}$$

where $\boldsymbol{y} = [\boldsymbol{\sigma}, \omega]^T$ and $\boldsymbol{f} = [\boldsymbol{f}_\sigma, f_\omega]^T$. The discontinuous Galerkin method of degree q can be stated as follows[15]. For a given time interval $I_n = (t_n, t_{n+1}]$ find $\boldsymbol{y}$ (polynomial of degree q) such that

$$\int_{I_n} (\dot{\boldsymbol{y}} - \boldsymbol{f}(\boldsymbol{y}))^T \hat{\boldsymbol{y}} \, \mathrm{d}t + [\![\boldsymbol{y}_n]\!]^T \hat{\boldsymbol{y}}_n^+ = 0. \tag{33}$$

For the test functions $\boldsymbol{y}$, polynomials of degree q are used. The notations $\boldsymbol{y}_n^+$ and $\boldsymbol{y}_n^-$ are the limits $\boldsymbol{y}_n^\pm = \lim_{\epsilon \to 0} \boldsymbol{y}(t_n \pm |\epsilon|)$, $[\![\boldsymbol{y}_n]\!] = \boldsymbol{y}_n^+ - \boldsymbol{y}_n^-$. These notations are illustrated in Fig. 2.

After the Newton's linearisation step, the following system of linear equations is obtained

$$\begin{aligned} &\begin{bmatrix} A_{11}\boldsymbol{I} - \boldsymbol{M}_{11} & A_{12}\boldsymbol{I} - \boldsymbol{M}_{12} \\ A_{21}\boldsymbol{I} - \boldsymbol{M}_{21} & (1 + A_{22})\boldsymbol{I} - \boldsymbol{M}_{22} \end{bmatrix}^i \begin{Bmatrix} \delta \boldsymbol{y}^- \\ \delta \boldsymbol{y}^+ \end{Bmatrix} \\ &\qquad = \begin{Bmatrix} \boldsymbol{r}_1 \\ \boldsymbol{r}_2 \end{Bmatrix}^i - \begin{bmatrix} A_{11}\boldsymbol{I} & A_{12}\boldsymbol{I} \\ A_{21}\boldsymbol{I} & A_{22}\boldsymbol{I} \end{bmatrix} \begin{Bmatrix} \boldsymbol{y}^- \\ \boldsymbol{y}^+ \end{Bmatrix}^i - \begin{Bmatrix} \boldsymbol{0} \\ \boldsymbol{y}_n^{+i} - \boldsymbol{y}_n^- \end{Bmatrix}, \end{aligned} \tag{34}$$

where

$$A_{ij} = \int_{I_n} N_i \dot{N}_j \, \mathrm{d}t, \qquad \boldsymbol{M}_{ij} = \int_{I_n} N_i \frac{\partial \boldsymbol{f}}{\partial \boldsymbol{y}} N_j \, \mathrm{d}t, \qquad \boldsymbol{r}_i = \int_{I_n} N_i \boldsymbol{f} \, \mathrm{d}t, \tag{35}$$

and N_i's are the linear interpolation functions $N_1 = (t - t_n)/\Delta t, N_2 = 1 - (t - t_n)/\Delta t$, which can be collected into a row vector $\boldsymbol{N} = [N_1, N_2]$.

Partitioning the unknows in the vector $\boldsymbol{y}$ as $\boldsymbol{y} = \left[(\boldsymbol{\sigma}^-)^T, (\boldsymbol{\sigma}^+)^T, \boldsymbol{\omega}^T\right]^T$, where $\boldsymbol{\omega} = [\omega^-, \omega^+]^T$, the coefficient matrix on the right hand side of Eq. (34) can be written as

$$\boldsymbol{J}_{\mathrm{dG}(1)} = \begin{bmatrix} \boldsymbol{B}_{11} & \boldsymbol{B}_{12} & \boldsymbol{G}_{1\omega} \\ \boldsymbol{B}_{21} & \boldsymbol{I} + \boldsymbol{B}_{22} & \boldsymbol{G}_{2\omega} \\ \boldsymbol{G}_{\omega 1} & \boldsymbol{G}_{\omega 2} & \boldsymbol{G}_{\omega\omega} \end{bmatrix}, \tag{36}$$

where

$$\boldsymbol{B}_{ij} = A_{ij}\boldsymbol{I} - \boldsymbol{M}_{\sigma ij}, \qquad \boldsymbol{M}_{\sigma ij} = \int_{I_n} N_i \frac{\partial \boldsymbol{f}_\sigma}{\partial \boldsymbol{\sigma}} N_j \, \mathrm{d}t, \tag{37}$$

$$\boldsymbol{G}_{i\omega} = -\int_{I_n} N_i \frac{\partial \boldsymbol{f}_\sigma}{\partial \omega} \boldsymbol{N} \, \mathrm{d}t, \qquad \boldsymbol{G}_{\omega i} = -\int_{I_n} \boldsymbol{N}^T \frac{\partial f_\omega}{\partial \boldsymbol{\sigma}} N_i \, \mathrm{d}t, \tag{38}$$

$$\boldsymbol{G}_{\omega\omega} = \widetilde{\boldsymbol{A}} - \int_{I_n} \boldsymbol{N}^T \frac{\partial f_\omega}{\partial \omega} \boldsymbol{N} \, \mathrm{d}t, \qquad \widetilde{\boldsymbol{A}} = \begin{bmatrix} A_{11} & A_{12} \\ A_{21} & 1 + A_{22} \end{bmatrix}. \tag{39}$$

The Jacobian of the algorithmic stress-strain relation for the dG(1)-method has the form

$$\boldsymbol{C} = \omega(\widetilde{\boldsymbol{B}}_{11} - \widetilde{\boldsymbol{B}}_{12}\widetilde{\boldsymbol{B}}_{22}^{-1}\widetilde{\boldsymbol{B}}_{21})^{-1}(\boldsymbol{I} - \widetilde{\boldsymbol{B}}_{12}\widetilde{\boldsymbol{B}}_{22}^{-1})\boldsymbol{C}_{\mathrm{e}}, \tag{40}$$

where

$$\widetilde{\boldsymbol{B}}_{ij} = \boldsymbol{B}_{ij} - \boldsymbol{G}_{i\omega}\boldsymbol{G}_{\omega\omega}^{-1}\boldsymbol{G}_{\omega j}. \tag{41}$$

Explicit-implicit split

From the results of the subsequent section, it seems that the dG(1)-method performs well in computing inelastic material behaviour with damage. The only drawback is that the method is twice as laborous as the backward Euler scheme. One alternative strategy could be an explicit-implicit split strategy, where the reactive like damage component is integrated by explicit schemes, like two-stage explicit Runge-Kutta method, and the diffusive part using an implicit scheme. The split can be performed when there exists at least one positive eigenvalue in the Jacobian matrix $\boldsymbol{J} = \partial \boldsymbol{f}/\partial \boldsymbol{y}$. At that state use of a similarity transformation, $\boldsymbol{J} = \boldsymbol{T}\boldsymbol{\Lambda}\boldsymbol{T}^{-1}$, where $\boldsymbol{\Lambda}$ is a diagonal matrix containing the eigenvalues of $\boldsymbol{J}$, and the coordinate transformation $\boldsymbol{z} = \boldsymbol{T}\boldsymbol{y}$ will result in

$$\dot{\boldsymbol{z}} = \boldsymbol{T}\boldsymbol{f}(\boldsymbol{T}^{-1}\boldsymbol{z}). \tag{42}$$

Now, the vector $\boldsymbol{z}$ can be divided into two parts $\boldsymbol{z}_-$ and $\boldsymbol{z}_+$, corresponding to negative and positive eigenvalues of the Jacobian, respectively. The components $\boldsymbol{z}_+$ is then integrated with an explicit scheme keeping the component $\boldsymbol{z}_-$ fixed after which the component $\boldsymbol{z}_-$ is integrated with an implicit scheme keeping the new values of $\boldsymbol{z}_+$ fixed.

Numerical example

Performance of the integrators is tested for the coupled viscous-damage model (19)-(21). For simplicity the transition function is assumed to be unity in this example, i.e. $\varphi_{\mathrm{tr}} \equiv 1$. The accuracy properties, when sufficiently large time steps are used, is of primary interest. The following material parameters are used: Young's modulus E = 40 GPa, reference stress σ_{r} = 20 Mpa, the viscocity parameters τ_{vp} = 1000 s, τ_{d} = 0.2 s and the exponents $p = r$ = 4. The reference value Y_{r} is chosen as in Eq. 5.

The stress-strain curves for an uniaxial constant strain rate $\dot{\epsilon}_{\mathrm{c}} = 5 \cdot 10^{-4}$ s^{-1} are shown in Fig. 3, where the true dG(1) solution, i.e. discontinuous, piecewise linear approximation is

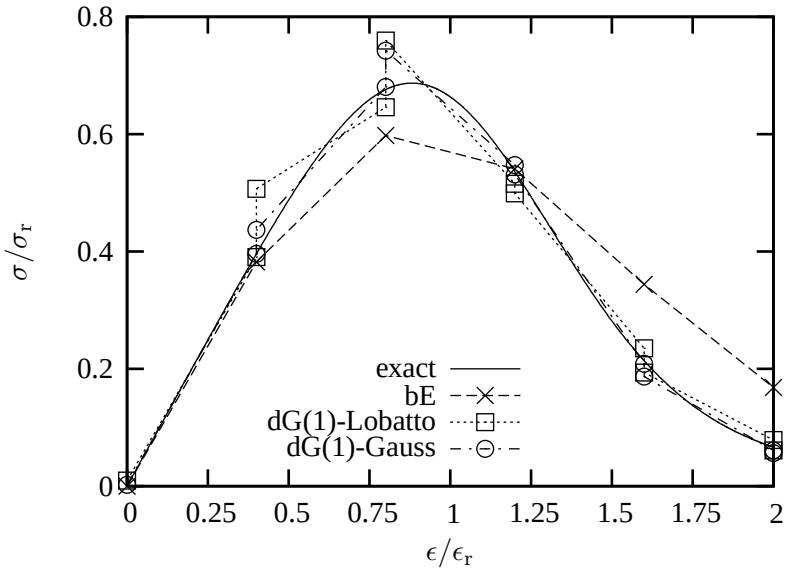

Figure 3: Uniaxial constant strain-rate loading.

depicted. To keep the figure readable, the endpoint solution valus for the dG(1) methods are connected in Fig. 4, where the stress, damage and inelastic strain are shown as a function of strain. Ten equal time steps are used for strain up to $4\epsilon_{\rm r}$, thus $\Delta t = 0.4$ s. Inability of the backward Euler scheme to capture the damage evolution well is clearly visible in these figures. The "exact" solution shown in Figs. 3 and 4 is obtained by using the dG(1)-method with time step $\Delta t = 8{\cdot}10^{-4}$ s, resulting in 5000 steps in the range shown in Fig. 4. Estimated relative error for this solution is less than 10^{-5}.

Concluding remarks

Behaviour of some time-integrators has been investigated for damaging inelastic material models. Due to the unstable nature of damage, the conventional backward Euler method does not perform well. Oscillations in the damage variable can result in convergence problems in the local Newton iteration at the integration point level. The discontinuous piecewise linear Galerkin method seems to perform well. It is third order method, but it has also good accuracy properties for large time steps. If purely plastic/viscoplastic problems are to be solved, the classical backward Euler method is a good choise. Evaluating the integrals in the dG(1)-scheme by the two point Gauss-Lobatto quadrature, results in a asymptotically second order method which gives accurate solutions also for large time steps. However, when combining the inelastic deformation with damage, the dG(1) scheme with two point Gauss-Legendre quadrature is better both in the asymptotic range and for large time steps.

Future work will include implementation of the explicit-implicit split method.

Acknowledgments

This research has been supported in part by Tekes - the National Technology Agency of Finland (project KOMASI, decision number 40288/05) and in part by the Academy of Finland, (decision numbers 210622 and 107290).

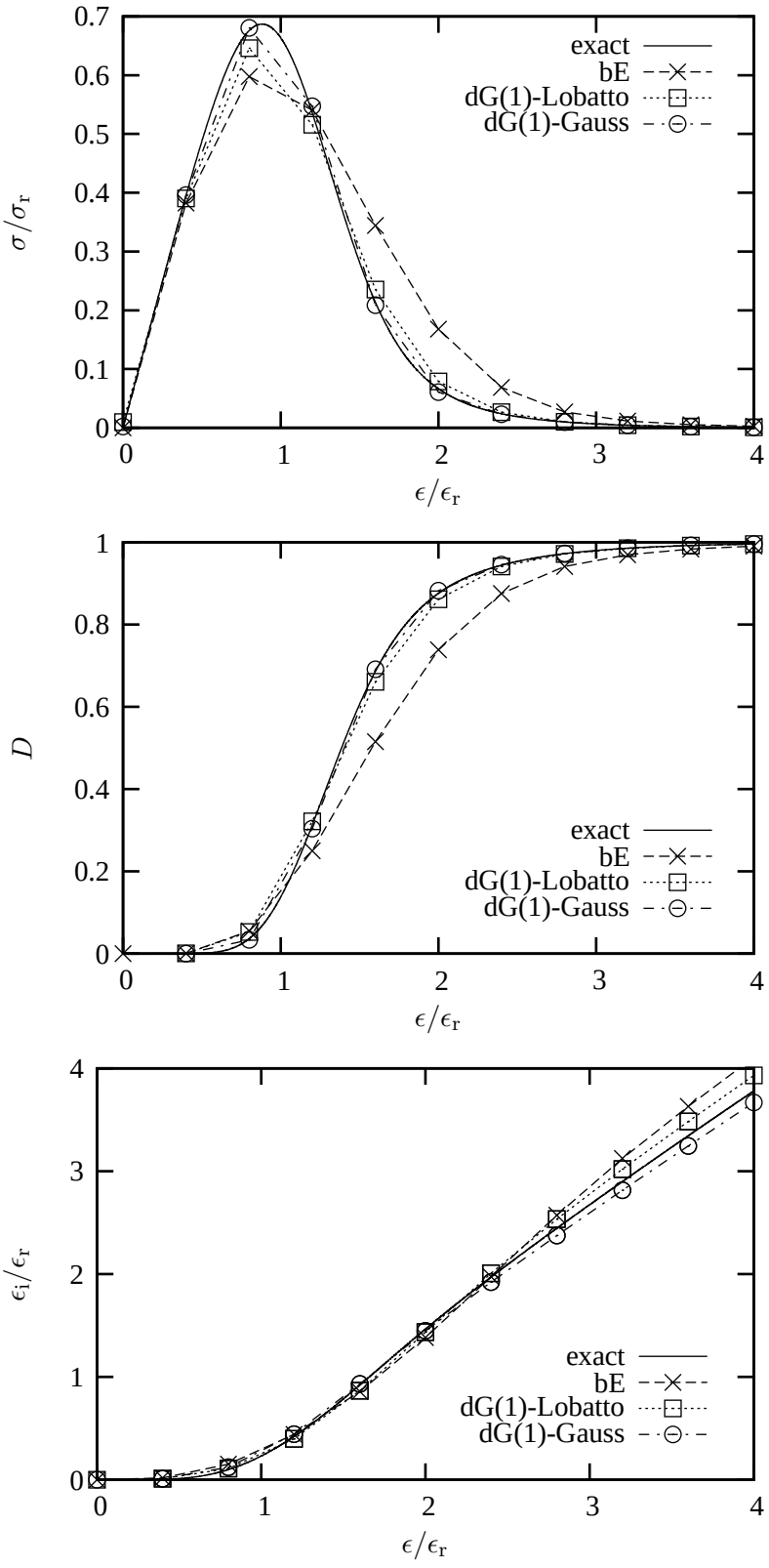

Figure 4: Uniaxial constant strain-rate loading. For the dG(1)-schemes, only the endpoints are connected.

References

[1] J.C. Simo and T.J.R. Hughes. *Computational Inelasticity*. Springer: New York, 1998.

[2] M. Wallin and M. Ristinmaa. Accurate stress updating algorithm based on constant strain rate assumption. *Comp. Meth. Appl. Mech. Eng.* **190** (42), 5583–5601 (2001)

[3] K. Runesson, S. Sture, K. Willam. Integration in computational plasticity. *Comp. Struct.*, **30** (1/2), 119–130 (1988).

[4] R. Kouhia, P. Marjamäki, J. Kivilahti. On the implicit integration of rate-dependent inelastic constitutive models, *Int. J. Numer. Meth. Engng.*, **62**, 1832–1856 (2005).

[5] R. Kouhia. A time discontinuous Petrov-Galerkin method for the integration of inelastic constitutive equations, In *ECCOMAS 2004 CD-ROM proceedings*, P. Neittaanmäki, T. Rossi, K. Majava and O. Pironneau (eds.).

[6] J. Alberty, C. Carstensen. Discontinuous Galerkin time discretization in elastoplasticity: motivation, numerical algorithms, and applications. *Comp. Meth. Appl. Mech. Eng.*, **191**, 4949–4969 (2002).

[7] E. Hairer, G. Wanner. *Solving Ordinary Differential Equations II, Stiff and Differential-Algebraic Problems*. Springer, second ed., 1991.

[8] S. Fortino, J. Hartikainen, K. Kolari, R. Kouhia, T. Manninen, A constitutive model for strain-rate dependent ductile-to-brittle transition, In *Proceedings of the IX Finnish Mechanics Days*, R. von Herzen and T. Halme (eds.), Lappeenranta University of Technology, Department of Mechanical Engineering, Report 17, 652–662 (2006).

[9] M. Frémond. *Non-Smooth Thermomechanics*, Springer, Berlin, 2002.

[10] P. Perzyna. Fundamental problems in viscoplasticity, *Advances in Applied Mechanics*, **9**, 243–377 (1966).

[11] G. Duvaut and L.J. Lions. *Inequalities in Mechanics and Physics*, Springer, Berlin, 1972.

[12] M. Ristinmaa and N.S. Ottosen. Consequences of dynamic yield surface in viscoplasticity, *Int. J. Solids Structures*, **37**, 4601–4622 (2000).

[13] J. Lemaitre, J.-L. Chaboche. *Mechanics of Solid Materials*, Cambridge University Press, 1990.

[14] J. Lemaitre. *A Course on Damage Mechanics*, Springer-Verlag, Berlin, 1992.

[15] K. Eriksson, D. Estep, P. Hansbo, C. Johnsson. *Computational Differential Equations*. Studentlitteratur, 1996.

Kinematic Analysis of Over-determinate Systems

Michael Skipper Andersen[1*] **and Michael Damsgaard**[2]

[1]Department of Mechanical Engineering
Aalborg University, Aalborg, Denmark
e–mail: msa@ime.aau.dk

[2]AnyBody Technology A/S, Denmark
e–mail: md@anybodytech.com

Søren Tørholm Christensen[1] **and John Rasmussen**[2]

[1]AnyBody Technology A/S, Denmark
e–mail: stc@anybodytech.com

[2]Department of Mechanical Engineering
Aalborg University, Aalborg, Denmark
e–mail: jr@ime.aau.dk

Summary This paper proposes a general solution to the well-known problem of kinematic over-determinacy when driving a mechanical model from measured data in the form of marker tracjectories. The proposed solution is based on solving an appropriate constrained weighted least-squares optimization problem for each discrete time step with the system coordinates as unknowns. The method is demonstrated on a 12 degree-of-freedom 3-D rigid-body model of gait.

Introduction

When it is desired to drive a musculo-skeletal model from motion capture data for inverse dynamics analysis, it is very often the case that the resulting set of equations will be over-determinate, i.e. the measurement results in more measured degrees-of-freedom (DOF) than the DOF of the model. As these measurements are affected by skin-artifacts, which is the primary source-of-error, noise, and small modeling errors, kinematic analysis remains a difficult task.

Several solutions to this problem have been posed in the literature. They are essentially split into two groups: 1) methods that work on a segment-to-segment basis [1, 2], and 2) methods that use model information, such as joint constraints, to reduce the effects of skin-artifacts [3, 4, 5]. However, none of these methods are in a form that can be used in a general purpose computer-aided analysis system, where both forward and inverse kinematic analysis may be desired.

Kinematic Analysis - An Optimization-Based Approach

The first step in inverse dynamics is always to perform kinematic analysis to find the positions, velocities and acceleration of the time-dependent system coordinates, $q(t) \in \mathcal{Q}$, i.e. given some system description we wish to find $q(t)$, $\dot{q}(t)$ and $\ddot{q}(t)$. We shall define the dimension of $q(t)$ as n. In the rest of the paper, we shall only write q and leave it understood that it is a time-dependent variable.

For systems with holonomic constraints, the position analysis can be formulated as solving a set of m equations [6]:

$$\Upsilon \equiv \Upsilon(q,t) = 0 \tag{1}$$

These independent constraint equations are usually composed of constraints describing joints and constraints that describe the motion. We shall assume that these equations are differentiable sufficiently many times.

If there are as many constraint equations, m, as unknowns, n, this set of equations can be solved numerically using methods like the Newton-Raphson method [6]. Additionally, the linear velocity and acceleration equations can also be derived using the chain rule on equation (1). However, in this paper we shall only focus on the case where $m \geq n$, i.e the system is either determinate or over-determinate and there may not exist a q that solves equation (1) for some or all time steps.

Position Analysis

To accommodate this over-determinacy, we shall presume that it is possible to split equation (1) into two sets:

$$\Upsilon(q,t) = \begin{bmatrix} \Psi(q,t) \\ \Phi(q,t) \end{bmatrix} \tag{2}$$

where $\Psi \equiv \Psi(q,t)$ is a set of equations that only have to be solved "as well as possible" in some sense and the remaining $\Phi \equiv \Phi(q,t)$ equations have to be fulfilled exactly. For instance when driving a musculo-skeletal model from motion capture data, a reasonable choice of these sets would be that the experimental data belongs to Ψ and joint constraints and additional driver equations to Φ.

In other words, we want to solve the following optimization problem:

$$\begin{aligned} \min_{q} \quad & G(\Psi(q,t)) \\ \text{s.t.} \quad & \Phi(q,t) = 0 \end{aligned} \tag{3}$$

One reasonable choice of G would be a weighted least-square:

$$G(\Psi(q,t)) = \Psi(q,t)^T W(t) \Psi(q,t) \tag{4}$$

where $W(t)$ is a differentiable, time-dependent weight matrix.

This optimization problem is in general nonlinear and non-convex, which implies that for large-scale systems, such as a full human body model, only local minimization is feasible.

Velocity Analysis

Having solved the optimization problem in equation (3), the system coordinates, q, will be known for the discrete time steps where the optimization problem is solved. However, it still remains to find the velocities and accelerations. Although an approximation of the velocities and accelerations could be found by finite differences, it is indeed possible to derive exact equations for these as we shall show in the following.

From local optimization theory, it is known that the Karush-Kuhn-Tucker (KKT) conditions are the necessary conditions for optimality:

$$\begin{aligned} G_q^T + \Phi_q^T \lambda &= 0 \\ \Phi &= 0 \end{aligned} \tag{5}$$

where λ is known as the Lagrange multipliers and the subscript q denotes the partial derivative with respect to q. It is important to remember that this equation will hold for any time step the optimization problem is solved.

As all involved functions are assumed to be differentiable, the velocity equations can be derived by differentiation of equation (5) with respect to time using the chain rule and re-writing to matrix form:

$$\begin{bmatrix} G_{qq}^T + \left(\Phi_q^T \lambda\right)_q & \Phi_q^T \\ \Phi_q & 0 \end{bmatrix} \begin{bmatrix} \dot{q} \\ \dot{\lambda} \end{bmatrix} = \begin{bmatrix} -G_{qt}^T - \Phi_{qt}^T \lambda \\ -\Phi_t \end{bmatrix} \tag{6}$$

Acceleration Analysis

Similarly to the velocity analysis, the acceleration equations can be derived by differentiation once again with respect to time:

$$\begin{bmatrix} G_{qq}^T + \left(\Phi_q^T \lambda\right)_q & \Phi_q^T \\ \Phi_q & 0 \end{bmatrix} \begin{bmatrix} \ddot{q} \\ \ddot{\lambda} \end{bmatrix} = \begin{bmatrix} \gamma_1 \\ \gamma_2 \end{bmatrix} \tag{7}$$

where:

$$\begin{aligned} \gamma_1 =& -2\left(\Phi_q^T \dot{\lambda}\right)_q \dot{q} - 2\Phi_{qt}^T \dot{\lambda} - \left(G_{qq}^T \dot{q}\right)_q \dot{q} - 2G_{qqt}^T \dot{q} - G_{qtt}^T - 2\left(\Phi_{qt}^T \lambda\right)_q \dot{q} - \Phi_{qtt}^T \lambda \\ & - \left(\left(\Phi_q^T \lambda\right)_q \dot{q}\right)_q \dot{q} \\ \gamma_2 =& -\left(\Phi_q \dot{q}\right)_q \dot{q} - 2\Phi_{qt} \dot{q} - \Phi_{tt} \end{aligned} \tag{8}$$

Examples and Results

The method has been applied to a 12 DOF, 3-D, rigid-body gait model comprised of four segments (pelvis, thigh, shank, and foot) and driven using measured marker trajectories from the Hip98 cd [7]. An illustration of the leg and the trajectories of the markers are given in Figure 1.

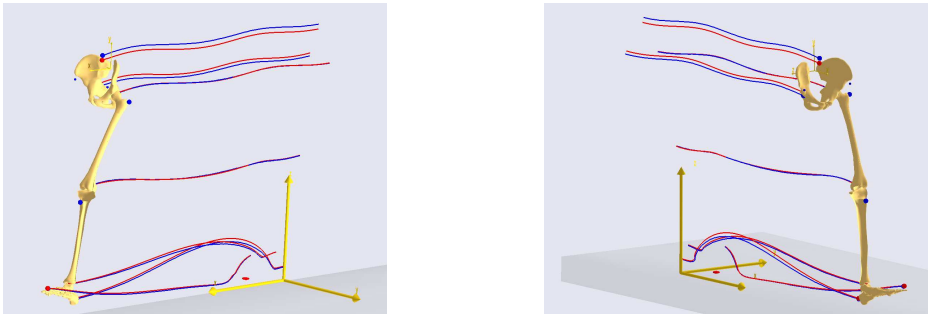

(a) (b)

Figure 1: An illustration of the leg model. The red curves are the trajectories of the measured markers and the blue curves are the trajectories of the corresponding points in the model calculated from the analysis.

The kinematics of the model is formulated using the so-called full Cartesian formulation where q is composed of translational and rotational coordinates for each segment [6]. We use Euler parameters as the rotational coordinates. The hip joint is modeled as a spherical joint, the knee as a revolute joint, and the ankle as a universal joint. These joints are put in $\Phi(q,t)$ together with the constraints on the Euler parameters. The difference between the 7 measured marker trajectories and their corresponding point in the model is used in the objective function, i.e in $\Psi(q,t)$ in equation (4). This amounts to 37 equations and 28 unknowns.

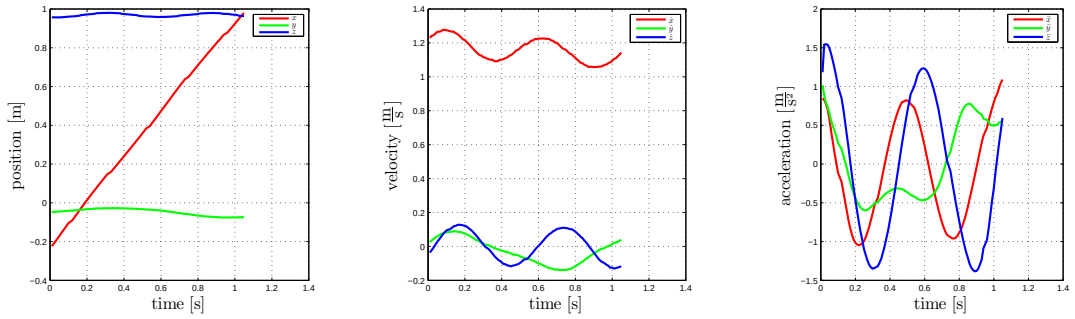

(a) (b) (c)

Figure 2: Trajectory of the translational coordinates of pelvis. (a) Position. (b) Velocity. (c) Acceleration.

When solving the optimization problem for position analysis, the weight matrix in equation (4) is set to the identity matrix for all time steps. The resulting marker trajectories can be seen together with the leg illustration in Figure 1. Hereafter, velocity and acceleration analysis is carried out and the result for the translation of pelvis can be seen in Figure 2.

As seen in Figure 1, the resulting motion closely resembles the measured motion. Additionally, the solution of the velocity and acceleration equations give the expected result (see Figure 2).

Conclusion

In this paper we presented a new method for analysis of kinematically over-determinate systems using optimization. Not only does the method allow us to handle practical over-determinate systems, it also provides methods for finding exact velocities and accelerations of the involved coordinates.

The presented formulation holds for both forward kinematics, inverse kinematics and any possible combination of those. Actually, the same model has been produced using generalized joint coordinates in q as verification and the two models produce exactly the same motion of the bodies.

References

[1] L. Cheze, B. J. Fregly and J. Dimnet. A Solidification Procedure to Facilitate Kinematic Analysis Based on Video System Data *J. Biomechanics.*, Vol. 28, No. 7, 879–884, (1995).

[2] A. Cappozzo, A. Cappello, U. D. Croce and F. Pensalfini. Surface-Marker Cluster Design Criteria for 3-D Bone Movement Reconstruction. *IEEE Transactions on Biomedical Engineering*, Vol. 44, No. 11 (1997).

[3] T.-W. Lu and J. J. O'Connor. Bone Position Estimation from Skin Marker Co-ordinates using Global Optimization with Joint Constraints. *J. Biomechanics*, Vol. 32, 129–134, (1999).

[4] S. Jung and K. Wohn. Tracking and Motion Estimation of the Articulated Object: a Hierarchical Kalman Filter Approach. *Real-Time Imaging*, Vol. 3, 415–432, (1997).

[5] P. Cerveri, A. Pedotti, and G. Ferrigno. Kinematic Models to Reduce the Effects of Skin Artifacts on Marker-based Human Motion Estimation. *J. Biomechanics*, Vol. 38, 2228–2236, (2005).

[6] P. E. Nikravesh. Computer-aided Analysis of Mechanical Systems. *Prentice-Hall International, Inc.*, (1988).

[7] G. Bergmann. Hip98: Loading of the Hip Joint: Contact forces, Gait Patterns, Muscle Forces, Activities. *J, Biomechanics*, Vol. 34, No. 7, cd-rom attachment, (2001).

Optimal simulations for human and robotic movements

Manindra Kaphle* **and Anders Eriksson**
KTH Engineering Sciences
Department of Mechanics, Stockholm, Sweden
e–mail: anderi@kth.se

Summary This paper discusses the simulation of forces creating motion in robotic and musculoskeletal systems. Main focus is put on the treatment of dynamic equilibrium for a redundant force system. The dynamic equilibrium during movement is solved through a temporal finite element form for treatment of target-controlled movements. Different criteria for optimality can be introduced. It is concluded that this method is able to describe the optimal movements, and that the criteria affect the resulting movements. With respect to musculoskeletal simulations, it can be concluded that existing numerical descriptions for muscular behavior are missing some important aspects.

Introduction

Computational modeling of load-carrying structures is a conventional tool in mechanical, structural and robotic engineering. These modeling possibilities are more or less general in their representation of the behavior of the structures and components, when subjected to load. Many such tools have also been used for bio-mechanical problems, in the form of special simulation packages, such as the Danish project AnyBody (http://anybody.auc.dk), as specialized additions to general simulation programs for rigid mechanisms, e.g. ADAMS (MSC Software, Santa Ana, CA, USA), or as components in e.g. car crash simulations with general elasto-dynamic programs, [1]. In order to allow for these extremely complex simulation models, significant simplifications of the real behavior of the biological systems are often necessary. These simplifications thereby often represent the human body parts as rigid, undeformable links, connected by perfect hinges and affected by very simplified muscle models — 'rubber-band' or at best 'Hill-type', [2]. The created bio-mechanical models can be subjected to active or passive forces, and predict with some accuracy the expected response of the modeled object, at least for rather common situations of, primarily, repetitive movements at reasonable loading levels.

The musculoskeletal system is, in contrast to a robotic system with well-defined actuators, a highly redundant force system for most loading cases, [3]. The indeterminacy in force distribution is related to the high number of alternative components over most joints. The redundancy allows very complex movements under neural control, but causes computational difficulties when simulating the behavior. The control system must be modeled in simulations of any will-controlled movements, [4], when evaluating the response to external forces. It is, however, not always easily represented, as it consists of several levels of learnt and instant control, [5].

The exact functioning of the control system is not fully known, but a common approach is to assume that the forces are distributed between the muscles following some optimization rule: minimum forces, nominal efforts, activation, energy consumption, maximum smoothness, *etc.* In simulations, these can be formulated as mathematical rules, and solutions thereby obtained. Several investigations have, however, pointed to the fact that there is probably no universal rule for this distribution of forces, [6]. A special aspect of this is the distribution of forces between synergistic muscles, [7], which is often seen as a static or dynamic optimization problem, [8]; several methods and criteria for static optimization can easily be set in a common algorithm, [9]. An interesting question is related to the similarities and differences obtained with different criteria for

optimality, and also the possibilities to introduce kinematical and strength restrictions in the search for optimal movements. Rapid dynamic situations emphasize the problems.

Numerical formulation of dynamics

With N_d displacement coordinates describing the current configuration, the dynamic problem is governed by $N_e \equiv N_d$ equilibrium equations. Allowing very general formulations, these are for a specific time instance t collected as, [10]:

$$\mathbf{M}\boldsymbol{a}(t) + \boldsymbol{f}(\boldsymbol{q}(t), \boldsymbol{v}(t)) - \boldsymbol{p}(t) - \mathbf{E}_c\boldsymbol{c}(t) = \mathbf{0} \tag{1}$$

using the mass matrix $\mathbf{M}$ together with the coordinates $\boldsymbol{q}(t)$, velocities $\boldsymbol{v}(t)$ and accelerations $\boldsymbol{a}(t)$. The vector $\boldsymbol{f}$ describes all internal forces and displacement affected loads. Known external force variations are described by $\boldsymbol{p}(t)$, and the effects of N_c control forces $\boldsymbol{c}(t)$ by an action description matrix $\mathbf{E}_c$, of size $N_d \times N_c$. With these assumptions, a time instance residual form is written:

$$\boldsymbol{e}(t) \equiv \boldsymbol{e}(\boldsymbol{q}(t), \boldsymbol{v}(t), \boldsymbol{a}(t), \boldsymbol{p}(t), \boldsymbol{c}(t); t) = \mathbf{0} \tag{2}$$

for a specific structural system.

In the simulation, the whole movement is described by a collection of time stations:

$$\boldsymbol{Q} = \left[\boldsymbol{Q}^{0\,\mathrm{T}}, \boldsymbol{Q}^{1\,\mathrm{T}}, \boldsymbol{Q}^{2\,\mathrm{T}}, \ldots, \boldsymbol{Q}^{N_t\,\mathrm{T}}\right]^{\mathrm{T}} \tag{3}$$

where

$$\boldsymbol{Q}^j = \boldsymbol{Q}(t^j) \equiv \left(q_1(t^j), \dot{q}_1(t^j), q_2(t^j), \ldots, \dot{q}_{N_d}(t^j)\right)^{\mathrm{T}} \tag{4}$$

when a time interval T is discretized by $N_t + 1$ equally spaced time stations: $t^j = j \cdot \frac{T}{N_t}$ $(0 \leq j \leq N_t)$; $\boldsymbol{Q}$ is a vector of length $2\,N_d(N_t + 1)$.

The whole set of unknown control force components is collected as:

$$\boldsymbol{C} = \left[\boldsymbol{C}^{1\,\mathrm{T}}, \boldsymbol{C}^{2\,\mathrm{T}}, \ldots, \boldsymbol{C}^{N_k\,\mathrm{T}}\right]^{\mathrm{T}} \tag{5}$$

where

$$\boldsymbol{C}^{j\,T} = \boldsymbol{c}(\tau^j) \equiv \left[c_1(\tau^j)\,,\, c_2(\tau^j)\,,\, \ldots\,,\, c_{N_c}(\tau^j)\right] \tag{6}$$

for $0 \leq \tau^j \leq T$, and $1 \leq j \leq N_k$, a set of control time instances.

Through a Hermitian third-order interpolation of the displacement coordinates, and a linear for the controls, a global system of equilibrium equations can be formulated:

$$\boldsymbol{E}(\boldsymbol{Q}, \boldsymbol{C}, \boldsymbol{P}) = \mathbf{0} \tag{7}$$

A set of N_b linear boundary conditions on the discrete coordinates are introduced by:

$$\boldsymbol{B}(\boldsymbol{Q}) \equiv \mathbf{B}_Q\,\boldsymbol{Q} - \boldsymbol{b}_Q = \mathbf{0} \tag{8}$$

In addition, the displacements and control forces are restricted by mechanical, anatomical or physiological limits. These can be described as:

$$\mathbf{B}_G \begin{pmatrix} \boldsymbol{Q} \\ \boldsymbol{C} \end{pmatrix} - \boldsymbol{b}_G \geq \mathbf{0} \tag{9}$$

obtained from a repetition of time instance restrictions.

Optimization problem

With excessive control force components available, an optimal solution can be sought. This needs a 'cost' or 'performance' function to minimize: one class measures some aspect of the needed control forces, another class the displacements. Of the latter class, seeking an optimally smooth movement, a jerkiness 'cost' can be formulated, based on the idea in [11]. This leads to an optimization problem, [12]:

$$\begin{aligned} \text{mimimize} \quad & \Pi_z \equiv \Pi(\boldsymbol{z}) \\ \text{under equality constraints} \quad & \boldsymbol{b}_1(\boldsymbol{z}) = 0 \\ \text{and inequalities} \quad & \boldsymbol{b}_2(\boldsymbol{z}) \geq 0 \end{aligned} \tag{10}$$

where the unknown $\boldsymbol{z}$ contains both the displacements and the control forces:

$$\boldsymbol{z} = \begin{pmatrix} \boldsymbol{Q} \\ \boldsymbol{C} \end{pmatrix} \tag{11}$$

The equalities are the non-linear equilibrium equations and the linear boundary value conditions, whereas the restrictions lead to, normally linear, inequalities

An in-house optimization function based on sequential linear programming was developed for the stated problem, [10, 13]. In a more general, but also more computationally expensive, approach, a standard package for constrained optimization was used. The function 'fmincon' included in the 'Optimization toolbox' of Matlab offers a suitable format for solving the stated problem; it uses a sequential quadratic programming approach. An estimate of the Hessian of the Lagrangian is updated in each iteration using a BFGS method, [12]. A line search is performed in each iterative step.

Demonstration example

As one example, a specified movement of a sagittal model of an upper limb was studied. Given anatomical and physiological data, a set of results were obtained, clearly indicating the effects of the optimal movement strategies as a function of, e.g., the restrictions on muscular forces and joint movement ranges, as well as on the time defined for the specified movement. Numerical conclusions on the used optimization method, and the time discretization were also drawn. Performed experiments also verify the importance of correctly specifying the time variation of displacements at the initial and final stages.

Concluding remarks

The present paper discusses the treatment of dynamics of a redundant robotic or musculoskeletal system through optimizations methods. Discussed basic formulations were shown to give good tools for the analysis of postures and movements. It was concluded that the mechanical formulations strongly affect the results, but also that the criteria behind an assumed neural optimization criterion are very important for the simulated behavior.

As a description of real human movements, the descriptions of course have some shortcomings, as they are not closely enough related to physiological behavior. In addition to not considering the neural control of movement, the muscular descriptions are over-simplified. The demands for a better representation of the history dependence in muscular force production is emphasized by the examples.

As the used algorithms establish very large systems of equations, computational efficiency is essential. In the present context, good use can be made of a sparse matrix solvers, but it is believed to be possible and important to develop other solution methods, where the full matrix is never needed. Efforts are presently devoted to a partial inversion of the stated problem in Eq. (10), aiming at usage of a 'CCSA' optimization algorithm, [14].

References

[1] A. Wittek, J. Kajzer, E. Haug, Hill-type muscle model for analysis of mechanical effect of muscle tension on the human body response in a car collision using an explicit finite element code, *JSME int. j. ser. A – Sol. Mech. Mat. Engng.*, **43**, 8–18, (2000).

[2] A. Hill, The heat of shortening and the dynamic constants of muscle, *Proc. Royal Soc. London*, **B 126**, 136–195, (1938).

[3] A. Eriksson, A. G. Tibert, Redundant and force-differentiated systems in engineering and nature, *Comput. Methods Appl. Mech. Engrg.*, **195**, 5437–5453, (2006).

[4] D. A. Hawkins, M. L. Hull, A computer-simulation of muscle tendon mechanics, *Comp. Biol. Med.*, **21**, 369–382, (1991).

[5] J. Duysens, H. W. A. A. V. de Crommert, B. C. M. Smits-Engelsman, F. C. T. V. der Helm, A walking robot called human: lessons to be learnt from neural control of locomotion, *J. Biomech.*, **35**, 447–453, (2002).

[6] T. Phanindra, S. Majumdar, Selection of the cost function for determination of muscle forces, in: B. H. V. Topping, C. A. Mota Soares (Eds.), *Proc. 7th Int. Conf. Comp. Struct. Techn.*, Civil-Comp Press, Stirling, U.K., 2004.

[7] P. Binding, A. Jinha, W. Herzog, Analytic analysis of the force sharing among synergistic muscles in one- and two-degree-of-freedom models, *J. Biomech.*, **33**, 1423–1432, (2000) .

[8] F. C. Anderson, M. G. Pandy, Static and dynamic optimization solutions for gait are practically equivalent, *J. Biomech.*, **34**, 153–161, (2001).

[9] S. Heintz, E. Gutierrez-Farewik, A. Eriksson, Evaluation of load-sharing and load capacity in force-limited muscle systems, *Comp. Meth. Biomech. Biomed. Eng.* (submitted 2006).

[10] A. Eriksson, Analysis methodology based on temporal FEM for bio-mechanical simulations, in: M. Ursino, C. A. Brebbia, G. Pontrelli, E. Magosso (Eds.), *Modelling in Medicine and Biology VI*, WIT Press, Southampton, 2005.

[11] T. Flash, N. Hogan, The coordination of arm movements: an experimentally confirmed mathematical model, *J. Neurosci.*, **5**, 1688–1703, (1985).

[12] J. Nocedal, S. J. Wright, *Numerical optimization*, Springer, (1999).

[13] A. Eriksson, Temporal finite elements for target control dynamics of mechanisms, *Comp. Struct.* (in press).

[14] K. Svanberg, A class of globally convergent optimization methods based on conservative convex separable approximations, *SIAM J. Optim.*, **12**, 555–573, (2002).

A CONSERVATIVE INTEGRAL FOR PIEZOELECTRIC CERAMICS WITH IMPERMEABLE CRACK FACE CONDITIONS

Leslie Banks-Sills[†,§], Yael Motola[†] and Lucy Shemesh[†]

[†]The Dreszer Fracture Mechanics Laboratory,
Department of Solid Mechanics, Materials and Systems, Faculty of Engineering,
Tel Aviv University, Ramat Aviv 69978, Israel.

[§]Division of Solid Mechanics, Faculty of Engineering, Lund University,
22100 Lund, Sweden.

As a result of their wide use in the form of sensors and actuators, much interest has been focused on the reliability and failure behavior of piezoelectric materials. This leads to the need to develop techniques for predicting crack growth under monotonic and fatigue loading (both mechanical and electric). To this end, accurate methods are required for calculating stress and electric flux density intensity factors in these materials. The solution is affected by the mechanical and electrical coupling, as well as material anisotropy in its poled state.

In this study, a conservative integral is derived for calculating the intensity factors associated with piezoelectric material for an impermeable crack. This is an extension of the M-integral or interaction energy integral for mode separation in mechanical problems. In addition, the method of displacement extrapolation is extended for this application as a check on results obtained with the conservative integral**.** The crack is assumed along the *x*-axis in the *xy* – plane. Poling is at an arbitrary angle with respect to the crack plane with poling within the $z = 0$ plane. These methods were extended in this study in order to calibrate specimens for carrying out fracture tests in piezoelectric materials.

To obtain the M-integral, use is made of the relation between the energy release rate and the J-integral. The former is given by

$$G = \frac{1}{2}\mathbf{k}^T\mathbf{L}^{-1}\mathbf{k} \tag{1}$$

where $\mathbf{k}$ is the intensity factor vector, namely $\mathbf{k}^T = [K_{II}, K_I, K_{III}, K_{IV}]$, and $\mathbf{L}$ is one of the Barnett-Lothe tensors. The path independent *J*-integral is given by [1]

$$J = \int_\Gamma \left(hn_1 - T_i u_{i,1} + D_i n_i E_1 \right) ds \tag{2}$$

where Γ is a path beginning at the lower crack face and ending at the upper crack face, h is the electric enthalpy density given by

$$h = \frac{1}{2} C_{ijks} \varepsilon_{ij} \varepsilon_{ks} - \frac{1}{2} \kappa_{ij} E_i E_j - e_{sij} E_s \varepsilon_{ij} \tag{3}$$

$\mathbf{n}$ is the unit outward normal to Γ, $T_i = \sigma_{ij} n_j$ is the traction, u_i and D_i are the displacement and electric flux density fields, and E_1 is the electric field in the x_1-direction. The material properties consist of the stiffness tensor C_{ijks} which is measured with the electric field held constant, κ_{ij} is the permittivity tensor measured with the strain held constant and e_{sij} is the array of piezoelectric coupling coefficients. Indicial notation is used with $i, j, k, s = 1,2,3$ and the comma represents differentiation.

To obtain the M-integral, two equilibrium solutions are assumed and superposed; this is possible since the material behaves linearly. Thus, the expressions for the stress, strain, displacement, electric fields, the electric flux density and the intensity factors are written as a combination of two solutions. The first solution is the sought after solution; the fields are obtained by means of a finite element calculation. The second solution consists of four auxiliary solutions which are derived from the first term of the asymptotic solution. By the usual manipulation, two expressions for the M-integral are derived and equated.

Several problems are analyzed by means of the finite element method with the program ANSYS [2]. Eight noded quadrilateral coupled field elements are employed. Quarter-point elements are used at the crack tip, so that the square-root singularity is well modeled. In order to accurately calculate the stress and electric fields at the crack tip, the mesh density is increased in that region. Several benchmark problems are examined to demonstrate the accuracy of the method. Numerical difficulties encountered resulting from multiplication of large and small numbers is solved by normalizing the variables. Since an analytical solution exists, a finite length crack in an infinite body is also considered. In addition, a four point bend specimen subjected to both an applied load and an electric field is presented for a crack at an angle to the poling direction. It is seen that neglecting the piezoelectric effect in calculating stress intensity factors may lead to errors.

References

1. Suo, Z., Kuo, C.-M., Barnett, D.M. and Willis, J.R., *J Mech Phys Solids*, **40**, 739-765, 1992.
2. ANSYS, Release 8.1, Ansys, Inc., Canonsburg, Pennsylvania, 2004.

Crack Tip Singularity in a Buckling Thin Sheet

Per Ståhle* **and Chong Li**
Division of Solid Mechanics
Lund University, Lund, Sweden
e–mail: per.stahle@solid.lth.se

Christina Bjerkén
Division of Materials Science
Malm University, Malm, Sweden

Summary The effect of buckling on stress distribution in the crack tip vicinity is explored. The computed stress state reveal that the buckling leads to a weaker crack tip singularity than the one of linear elastic fracture mechanics. The change of the singularity has been studied in this work by post-buckling analysis using FE method. The weaker singularity has been taken into account in a modified fracture mechanical theory. The implications for fracture mechanical predictions are discussed.

Introduction

When thin cracked plates are subjected to tensile loading in a direction perpendicular to the crack surface buckling is observed when the load exceed a critical limt. Experimental data by Dixon and Strannigan [1], shows that the maximum stress at a crack tip was about 30 % for a buckled sample in comparison to a sample where buckling was artificially held back. Li *et al.* [2] suggests that the asymptotic stresses are singular but the singularity is weaker that the square root stress singularity of linear fracture mechanics. The change of the singularity implies that the stress intensity factor become undefined after buckling.

The buckling of thin plates containing cracks has been studied in previous works although most investigators address prediction of the critical buckling load for various crack orientations (cf. Markström and Storåkers [3] and Sih and Lee [4]). Recently Brighenti [5] also conducted an investigation of postbuckled cracked plates using nonlinear FE analyses although the work mainly focus on the critical buckling load.

Problem formulation

Consider a thin and rectangular shaped plate containing a crack. The plate consists of a homogeneous, isotropic elastic material described by the modulus of elasticity E and Poissons ratio ν. The bending stiffness of the plate is $D = Et^3/[12(1-\nu^2)]$. One of two studied geometries, an edge crack is given in Fig. 1. The other geometry is a centred cracked panel. The right half of that geometry is defined also by Fig. 1.

The in plane stresses are divided into a membrane part given as a force per unit of thickness N_{xx}, N_{yy} and N_{xy} and bending moment per unit of thickness M_{xx}, M_{yy} and M_{xy}.

For the centered crack, the applied displacement on the constrained opposed edges $v = v_\infty$, $u = w = 0$ and $dw/dy = 0$ on $0 \leq x \leq b$ ($|x| \leq b$ for the centre cracked plate) and $|y| = h$. All other boundaries are traction free.

Because of the symmetric geometry and load across x = 0 and across y = 0 only one quarter of the plate is studied. Plausible buckling modes are symmetry and antisymmetry for the out of plane displacement w. The lowest buckling mode is obtained for $w(x,y) = w(x,-y) = w(-x,y)$

meaning that the plate moves either strictly toward $z > 0$ or to $z < 0$ (cf. Markström and Storåkers [3]).

For low load, in the vicinity of the crack tip, stresses are assumed to be singular as expected for linear fracture mechanics

$$\sigma_{yy} = \frac{K_I}{\sqrt{2\pi r}} f_{yy}(\theta), \tag{1}$$

where the polar coordinates $r = \sqrt{x^2 + y^2}$ and $\theta = tan^{-1}(y/x)$ are used. The angular function $f_{yy}(\theta)$ is known. Straight ahead of the crack tip $f_{yy}(0)$ equals unity.

At post buckling loads it is assumed that the crack tip stresses may be written as

$$\sigma_{yy} = K(2\pi r)^s g_{yy}(\theta), \tag{2}$$

where $g_{yy}(\theta)$ is chosen to be unity straight ahead of the crack tip.

Numerical method

To perform the buckling and the post-buckling analysis, the finite element method is utilized through the commercial software ABAQUS [6]. With regard to the symmetry, the calculations are performed using one quarter of the central cracked plate and one half of the edge cracked plate. The following dimensions are used to describe the model: $h/w = 1.5$ and $t/w = 0.0001$. Two different crack lengths are modeled for the centre cracked plate, i.e. $a/w = 0.1$ and 0.2, respectively, and for the edge cracked plate a crack with $a/w = 0.1$ is investigated. The size of the plate is assumed sufficient to represent very large plates. The relation between bending stiffness and tensile stiffness enters the equations only through the ratio t/a, which is very small.

The element net uses 6-node triangular thin shell elements with five degrees of freedom per node. Quadratic shape functions are used. The mesh region near crack tip is made denser as the distance to the tip decreases. A denser element net is also used, where the number of nodes is doubled on the edges and the distribution is kept the same as for the coarser case. The coarser case consists of approximately 10 000 elements and the denser case up to approximately 37 000 elements. The length of shortest side of the elements for the entire model is $1.310^{-6}a$ for the coarser case and $6.510^{-7}a$ for the denser case.

To obtain the post buckling responses a modified Riks method was used. This method appears to be most successful among some suggested methods solving unstable problems Ramm [7] and Crisfield [8]. It is able to obtain static equilibrium solutions for unstable problem where the load magnitude is determined by one single scalar parameter. To be able to analyze the post-buckling response the problem needs to be converted into a continuous response instead of bifurcation. A geometric imperfection is introduced as a superimposed displacement field of a buckling mode from the eigenvalue estimation and a scale factor is applied to the field to scale the applied imperfection. The basic of the modified Riks method is the Newton-Raphson method (cf. Riks [9], [10]). The load magnitude taken into consideration as an additional unknown thus the method solves both the load and the displacement at the same time on the equilibrium path. The implemented Riks method by ABAQUS [6] uses an arc length to designate the progress of the calculation, Riks [11]. The choice of the size of the arc length is governed by the convergence rate-dependent, automatic

incrementation algorithm for static cases within the Abaqus standard solver. The finite element implementation of the modification of Riks method is known to suffer from an inability to deal with wrongly chosen direction of integration path along the response curve, thus the solution occasionally get stuck in a loop (Silver et al. [12]; ABAQUS [6]).

Results

The analysis for the central cracked plate could be carried out to an extent of where the applied load reached 100 times for the corresponding buckling load while for the edge cracked plate only about 2 times the corresponding buckling load was reached.

The critical load is expected to increase with increasing thickness in proportion to t^2. For dimensional reasons the critical buckling stress may therefore be written: $\sigma_k = \lambda E(t/a)^2$, where λ is a geometry and load case dependent dimensionless parameter. For the central crack with $a/w = 0.1, 0.2$ and for the edge crack with $a/w = 0.1$ the result is 2.2883, 2.674 and 28.1835 respectively.

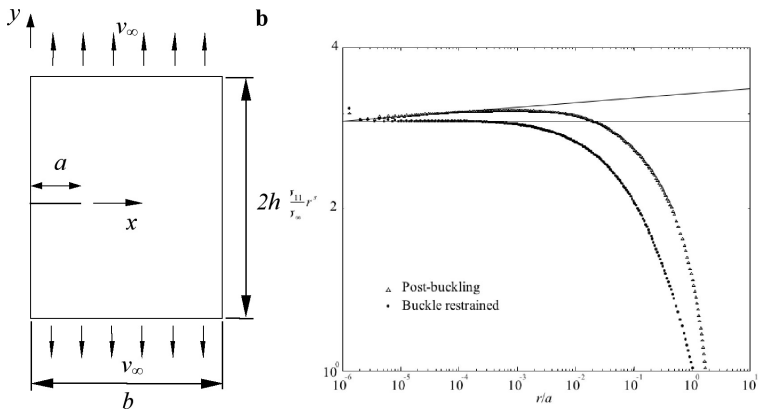

Figure 1: Comparison of stresses normalized by the applied stresses and scaled by the $r_{|s|}-$dependence of the unbuckled case straight ahead of the crack tip between pre- and post-buckling for the edge crack with $a/w = 0.1$

Stresses in the x direction straight ahead of the crack tip normalized with the applied stresses and the r-dependence of the unbuckled case are plotted against the distance from the crack tip normalized with the crack length in a log-log diagram in Fig. 2. The comparison is made between the last steps of the post-buckling analyses versus a buckle restrained case. The stress responses of the buckle restrained case should maintain the characteristics of a case where linear fracture mechanism is valid; therefore the slope of the curve should correspond to the square-root singularity in a region close to the crack tip. By selecting the region between $10^{-5} < r/a < 10^{-4}$ an exponent $|s|$ in the $r^{|s|}$ depending stresses, is less than 1% below the theoretical value, -1/2. A difference of inclination between the buckled case and the buckle restrained case indicates that a different crack tip singularity is at play after the occurrence of buckling. To clearly identify the differences of the singularity the normalized stress response is rescaled with r^s where $s = -0.505$, is plotted against r/a in Fig. 5, where s is the singularity calculated from the buckle restrained cases. The result shows that the singularity is weaker in a post-buckled state. This result is in accordance with the preliminary calculations by Li *et al.* [2].

Conclusions

A thin plate containing a central crack or an edge crack under tensile load in the direction perpendicular to the crack surface was studied. FEM calculations of the post-buckling behaviour using non-linear geometries have been conducted. The post-buckling calculation was performed by the modified Riks method where the plate is considered as imperfect prior buckling.

The post-buckling analyses have shown that within a region of $0.0001a$ ahead of the crack tip the stress field is found to be of the form $r^{-s}f(\theta)$

The field possesses a weaker singularity than a square root singularity that is found for in-plane deformation. Already when the buckling load is exceeded by 100 times the singularity decreases from -0.5 to -0.49, this applied load that causes a 2% drop of the singularity may seem quite small. However, maximum stress in a sheet of paper containing a crack of the length of 20% of the width at the moment of fracture is several thousand times larger than its buckling load and the drop of singularity could be of considerably larger as load of such magnitude is reached.

Different a/w relations for the central cracks appears to have little influence on the weakening of singularity. As a result by the presented data it can be concluded that if the apply load remain below 100 times the buckling load of the specimen then fracture criteria by linear fracture mechanics should retain validity for a central crack. References

References

[1] J. R. Dixon and J. S. Strannigan. Stress distribution and buckling in thin sheets with central slits. *2nd International Conference on Fracture*, Brighton, 105-118, (1969)

[2] C, Li, R. Espinosa and P. Ståhle. Fracture mechanics for membranes. *The 15th Europan Conference of Fracture*, Stocholm, (2004)

[3] K. Markström and B. Storåkers. Buckling of cracked members under tension. *nternational Journals of Solid Mechanics*, **16**, 217-229 (1980)

[4] G. C. Sih and Y. D. Lee. Tensile and compressive buckling of plates weakened by cracks. *Theoretical and Applied Fracture Mechanics*,**6**, 129-138, (1986)

[5] R. Brighenti. Buckling of cracked thin-plates under tension or compression. *Thin-walled Structures*, 1-16, (2004)

[6] ABAQUS. Analysis Users Manual ver. 6.4. Hibbit, Karlsson & Sorensen Inc., (2003)

[7] E. Ramm. Strategies for Tracing the Nonlinear Response Near Limit Points. *Nonlinear Finite Element Analysis in Structural Mechanics*, Edited by E. Wunderlich, E. Stein, and K. J. Bathe, Springer-Verlag, Berlin, (1981)

[8] M. A. Crisfield. A fast incremental/iterative solution procedure that handles snap-through. *Computers & Structures*, **13**, 55-62, (1981)

[9] E. Riks. The application of Newtons method to the problem of elastic stability. *Journal of Applied Mechanics*, **39**, 1060-1066, (1972)

[10] E. Riks. An incremental approach to the solution of snapping and buckling problems. *International Journal of Solids and Structures*, **15**, 529-551, (1979)

[11] E. Riks, C. C. Rankin and F. A. Brogan An incremental approach to the solution of snapping and buckling problems. *International Journal of Solids and Structures*, **15**, 529-551, (1979)

[12] M. J. Silver, J. D. Hinkle and L. D. Peterson. The buckling behavior of a central crack in a plate under tension. *Engineering Fracture Mechanics,* **43***, no. 4, 529-548, (1992)*

Computational Modelling of Plate-gap Biosensors with a Porous Inert Membrane

Romas Baronas*
Faculty of Mathematics and Informatics
Vilnius University, Vilnius, Lithuania
e–mail: romas.baronas@maf.vu.lt

Feliksas Ivanauskas
Institute of Mathematics and Informatics,
Vilnius University, Vilnius, Lithuania
e–mail: feliksas.ivanauskas@maf.vu.lt

Summary This paper presents a two-dimensional-in-space mathematical model of a plate-gap biosensor with a porous inert membrane acting under internal and external diffusion limitations. The model is based on non-linear reaction-diffusion equations. The problem was solved numerically using finite-difference technique. Using numerical simulation the influence of the geometry of the porous membrane as well as of the external diffusion region on the biosensor response was investigated.

Introduction

Biosensors are sensing devices made up of a combination of a specific biological entity, usually the enzyme, that recognizes a specific analyte and the transducer that translates the changes in the biomolecule into an electrical signal [1]. The signal is proportional to the concentration of the analyte. The biosensors are classified according to the nature of the physical transducer. The amperometric biosensors measure the faradic current that arises on a working indicator electrode by direct electrochemical oxidation or reduction of the product. The amperometric biosensors are known to be reliable, cheap and highly sensitive for environment, clinical and industrial purposes [2].

Very recently a plate-gap model of a porous electrode was proposed and successfully applied to carbon paste based biosensors [3, 4]. The purpose of this work was to enhance the mathematical model of the plate-gap biosensors with the external diffusion limiting region. The model is based on reaction-diffusion equations containing a non-linear term related to Michaelis-Menten kinetics of the enzymatic reaction. The model involves four regions: the enzyme layer where enzyme reaction as well as mass transport by diffusion take place, inert membrane and external diffusion regions where only a mass transport by diffusion takes place, and a convective region, where the analyte concentration is maintained constant.

Using numerical simulation of the biosensor action, the influence of the geometry of the porous membrane as well as of the external diffusion region on the biosensor response was investigated. The behaviour of the plate-gap biosensor was compared with that of a flat mono-layer biosensor [5]. The simulation was carried out using the finite difference technique [6].

Mathematical model

Fig. 1a shows a profile of a biosensor, where enzyme filled gaps are modelled by right quadrangular prisms of base $2a_1$ by c distributed uniformly so, that the distance between adjacent prisms equals to $2(a_2 - a_1)$, a is the half width of the gaps, c is the gap depth and d is the thickness of the inert membrane. Due to the uniform distribution of the gaps, it is reasonable to consider only a

unit consisting of a single gap together with the regions between adjacent gaps. Because of the symmetry and the relatively great length of the gaps we consider only a half of the unit.

Fig. 1b shows the profile of a unit cell to be considered in mathematical modelling of a plate-gap biosensor. $c = b_1$ is the depth of the gaps, $d = b_2 - b_1$ is the thickness of the porous membrane and $\delta = b_3 - b_2$ is the thickness of the external diffusion layer.

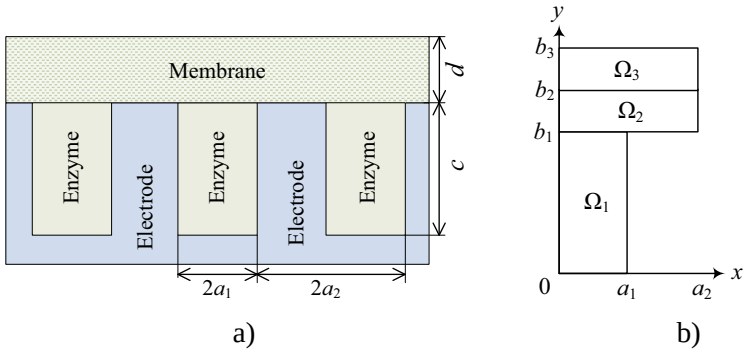

Figure 1: Profiles of a plate-gap biosensor and the unit cell.

Let Ω_1, Ω_2, Ω_3 be open regions corresponding to the enzyme-filled gaps, porous membrane and diffusion layer, respectively, Γ_1 - the electrode border and Γ_2 is the inert membrane/bulk solution boundary

$$\begin{aligned} &\Omega_1 = (0, a_1) \times (0, b_1), \quad \Omega_2 = (0, a_2) \times (b_1, b_2), \quad \Omega_3 = (0, a_2) \times (b_2, b_3), \\ &\Gamma_1 = ([0, a_1] \times \{0\}) \cup (\{a_1\} \times [0, b_1]) \cup ([a_1, a_2] \times \{b_1\}), \quad \Gamma_2 = [0, a_2] \times \{b_2\}. \end{aligned} \tag{1}$$

The biosensor action is described by the following reaction - diffusion system ($t > 0$):

$$\frac{\partial S_1}{\partial t} = D_1 \Delta S_1 - \frac{V_{max} S_1}{K_M + S_1}, \quad \frac{\partial P_1}{\partial t} = D_1 \Delta P_1 + \frac{V_{max} S_1}{K_M + S_1}, \ (x, y) \in \Omega_1, \tag{2}$$

$$\frac{\partial S_j}{\partial t} = D_j \Delta S_j, \quad \frac{\partial P_j}{\partial t} = D_j \Delta P_j, \ (x, y) \in \Omega_j, \quad j = 2, 3, \tag{3}$$

where Δ is the Laplacian, $S_i(x, y, t)$ is the concentration of the substrate in Ω_i, $P_i(x, y, t)$ is the concentration of the reaction product in Ω_i, $i = 1, 2, 3$, V_{max} is the maximal enzymatic rate and K_M is the Michaelis constant.

Let $\overline{\Omega}_i$ be the closure of the corresponding open region Ω_i, $i = 1, 2, 3$. The biosensor operation starts when the substrate of concentration S_0 appears over the surface of the inert membrane. This is used in the initial conditions ($t = 0$):

$$\begin{aligned} &S_1(x, y, 0) = 0, \quad (x, y) \in \overline{\Omega}_1, \\ &S_2(x, y, 0) = 0, \quad (x, y) \in \overline{\Omega}_2 \setminus \Gamma_2, \quad S_2(x, y, 0) = S_0, \ (x, y) \in \Gamma_2, \\ &S_3(x, y, 0) = S_0, \ (x, y) \in \overline{\Omega}_3, \\ &P_i(x, y, 0) = 0, \quad (x, y) \in \overline{\Omega}_i, \quad i = 1, 2, 3. \end{aligned} \tag{4}$$

Assuming $b_0 = 0$, the following boundary conditions express the symmetry of the biosensor ($t > 0$):

$$\frac{\partial P_i}{\partial x}\Big|_{x=0} = \frac{\partial S_i}{\partial x}\Big|_{x=0} = 0, \quad y \in [b_{i-1}, b_i], \quad i = 1, 2, 3, \tag{5}$$

$$\frac{\partial P_j}{\partial x}\Big|_{x=a_2} = \frac{\partial S_j}{\partial x}\Big|_{x=a_2} = 0, \quad y \in [b_{j-1}, b_j], \quad j = 2, 3. \tag{6}$$

The following boundary condition on the electrode border Γ_1 defines the electrochemical process:

$$\frac{\partial S_k}{\partial n}\Big|_{\Gamma_1} = 0, \quad P_k = 0, \quad (x, y) \in \Gamma_1, \quad k = 1, 2, \tag{7}$$

where n stands for the normal direction.

If the bulk solution is well-stirred and in powerful motion then the diffusion layer remains at a constant thickness ($t > 0$),

$$S_3(x, b_3, 0) = S_0, \quad P_3(x, b_3, 0) = S_0, \quad x \in [0, a_2]. \tag{8}$$

On the boundary between adjacent regions $\overline{\Omega}_k$ and $\overline{\Omega}_{k+1}$ we define the matching conditions, k = 1, 2 ($t > 0$),

$$\begin{aligned} &D_k \frac{\partial S_k}{\partial y}\Big|_{y=b_k} = D_{k+1} \frac{\partial S_{k+1}}{\partial y}\Big|_{y=b_k}, \; S_k(x, b_k, t) = S_{k+1}(x, b_k, t), \\ &D_k \frac{\partial P_k}{\partial y}\Big|_{y=b_k} = D_{k+1} \frac{\partial P_{k+1}}{\partial y}\Big|_{y=b_k}, \; P_k(x, b_k, t) = P_{k+1}(x, b_k, t), \quad (x, y) \in \overline{\Omega}_k \cap \overline{\Omega}_{k+1}. \end{aligned} \tag{9}$$

The measured current is accepted as a response of a biosensor in a actual experiment. The current depends upon the flux of the reaction product at the electrode surface, i.e. on the border Γ_1. The density $i(t)$ of the current at time t is obtained explicitly from Faraday's and Fick's laws,

$$i(t) = \frac{n_e F}{a_2} \left(D_1 \int_0^{a_1} \frac{\partial P_1}{\partial y}\Big|_{y=0} dx + D_1 \int_0^{b_1} \frac{\partial P_1}{\partial x}\Big|_{x=a_1} dy + D_2 \int_{a_1}^{a_2} \frac{\partial P_2}{\partial y}\Big|_{y=b_1} dx \right), \tag{10}$$

where n_e is a number of electrons involved in a charge transfer and F is Faraday constant. We assume, that the system (2)-(9) approaches steady - state when $t \to \infty$, $i_\infty = \lim\limits_{t\to\infty} i(t)$.

The problem was solved numerically using the finite difference technique [6]. We introduced a non-uniform discrete grid in all three directions: x, y and t. Using the alternating direction method, an implicit finite difference scheme was built as a result of the difference approximation of the model. The resulting systems of linear algebraic equations were solved efficiently because of the tridiagonality of their matrices.

Results of calculations

The thickness $\delta = b_3 - b_2$ of the external diffusion layer depends upon stirring of the solution and is inversely proportional to the intensity of solution stirring [5]. To investigate the effect of the external diffusion on the biosensor response we calculated the normalized steady-state current,

$$i_N(\delta) = \frac{i_\infty(\delta)}{i_\infty(0)}, \quad \delta = b_3 - b_2, \; \delta \geq 0, \tag{11}$$

where $i_\infty(\delta)$ is the steady-state biosensor current at given thickness δ of the diffusion layer. Fig. 2 shows the results of calculations.

One can see in Fig. 2, that I_N is a monotonous decreasing function of the thickness δ of the diffusion layer in the cases of high enzymatic rate, $V_{max} \geq 1$ mM/s. Due to the external diffusion the biosensor current can vary even several times. In the case of relatively low enzymatic rates, the biosensor response practically does not depend upon the thickness δ of the diffusion layer. This property is valid for wide rages of the substrate concentration S_0 and the thickness d of the porous inert membrane.

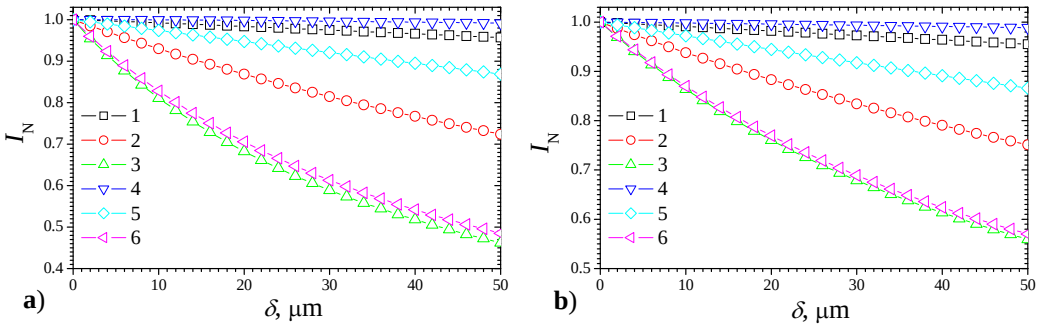

Figure 2: The normalized steady-state current i_N versus the thickness δ of the diffusion layer for two values of the thickness $d = b_2 - b_1$ of the inert membrane: 1 **(a)**, 2 **(b)** μm, S_0: 0.01 (1-3), 1 (3-4) mM, V_{max}: 0.1 (1, 4), 1 (2, 5), 10 (3, 6) mM/s, $a_1 = 1$, $a_2 = 2$, $b_1 = 4$, $b_2 = 6$ μm, $b_3 = b_2 + \delta$, $D_1 = 100$, $D_2 = 10$ μm^2/s, $D_3 = 2D_1$, $K_M = 1$ mM, $n_e = 2$.

Concluding remarks

The mathematical model (2)-(9) of the operation of the amperometric plate-gap biosensors with a porous inert membrane can be used to investigate peculiarities of the biosensor response in stirred and non stirred analytes.

In the case of relatively high rate V_{max} of the enzymatic reaction, the steady-state current is a monotonous decreasing function of the thickness of the external diffusion layer and that layer should be taken into consideration when modelling the biosensor action (Fig. 2).

In the case of relatively low values of V_{max} the biosensor response practically does not depend upon the intensity of stirring of analyte (Fig. 2), and the external diffusion layer may be neglected to model the operation of biosensors with inert membrane.

Acknowledgement

This research was supported by Lithuanian State Science and Studies Foundation, project No. C-03048.

References

[1] F. Scheller and F. Schubert. *Biosensors*. Elsevier, Amsterdam, (1992).

[2] U. Wollenberger, F. Lisdat and F.W. Scheller. *Frontiers in Biosensorics 2. Practical Applications*. Birkhauser Verlag, Basel, (1997).

[3] F. Ivanauskas, I. Kaunietis, V. Laurinavicius, J. Razumiene and R. Simkus. Computer simulation of the steady state currents at enzyme doped carbon paste electrode. *J. Math. Chem.*, **38**, 355–366, (2005).

[4] R.Baronas, F.Ivanauskas, I. Kaunietis and V. Laurinavicius. Mathematical modeling of plate-gap biosensors with an outer porous membrane. *Sensors*, **6**, 727–745, (2006).

[5] R. Baronas, F. Ivanauskas and J. Kulys. Computer simulation of the response of amperometric biosensors in stirred and non stirred solution. *Nonlinear Analysis: Modelling and Control*, **8**, 3–18, (2003).

[6] A.A. Samarskii. *The Theory of Difference Schemes*. Marcel Dekker, New York-Basel, (2001).

Finite Element Analyses of the Influence of the Chordae on the Mitral Valve Response

V. Prot and B. Skallerud
Department of Structural Engineering
Norwegian University of Science and Technology, Trondheim, Norway
e–mail: victorien.prot@ntnu.no, bjorn.skallerud@ntnu.no

Summary The mitral valve is a very important valve between the left atrium and left ventricle of the heart. During the systole the mitral apparatus prevents blood from flowing back into the atrium when the ventricle contracts. Hence, it is of major importance in order to avoid regurgitation. The purpose of this study is to develop a three-dimensional finite element model of the mitral valve in order to understand its function and its behaviour using a transversely isotropic material model for the mitral valve leaflets.

Introduction

The mitral valve is one of the four valves of the heart. It consists of two leaflets: the anterior, and posterior. The anterior leaflet is much larger than the posterior leaflet. Both leaflets are attached to the annulus and to the chordae tendinae. The chordae tendinae are further attached to the papillary muscles. The mitral valve combined with the mitral annulus, the chordae, and the papillary muscles are often referred to as the mitral apparatus, see Figure 1. In this study, we present a

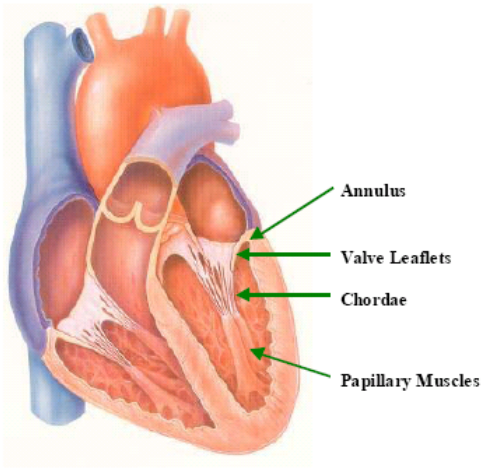

Figure 1: Mitral apparatus

three-dimensional finite element model of the porcine mitral valve that simulates a part of the heart cycle: starting at end of diastole and ending at the maximum pressure in the left ventricle. Three finite element analyses were performed in order to investigate the role of the chordae on the mitral valve response. The first one considered the marginal chordae attached to the free edge of the leaflets only (pathological state). The second one considered marginal chordae and strut chordae (i.e, chordae attached beyond the free edge). In the healthy mitral valve these two types of chordae are present. In the last simulation, the mitral apparatus was modeled with too soft chordae. This last case corresponds to the Marfan's syndrome.

Methods

Geometry and boundary conditions

The dimensions of the porcine mitral valve were measured during the autopsy of a pig on which 3D ultrasound measurements had been carried out. These dimensions are reported in Figure 2. The annulus was assumed to be flat and the commissures of the mitral valve were neglected. Then some

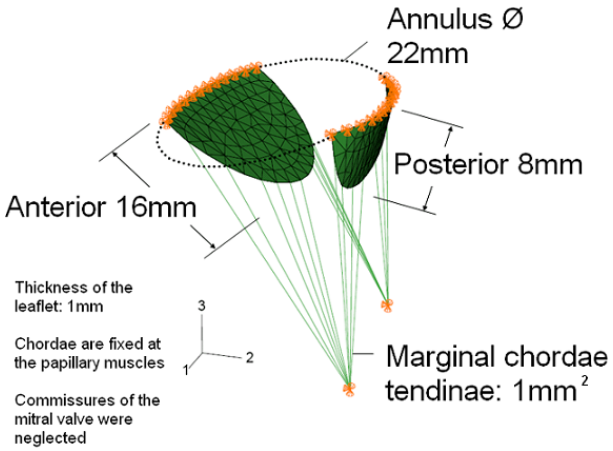

Figure 2: Initial geometry of the valve at the beginning of systole with related boundary conditions

additional simulations were conducted with a saddle annulus and accounting for the commissural area of the mitral valve.

The leaflets were meshed with triangular membrane elements M3D3 (ABAQUS element) and the chordae tendinae with truss elements T3D2 (ABAQUS element). The leaflets were allowed to rotate at the annular attachment. The translations were constrained at the attachment between the chordae and the papillary muscles. We assumed fixed boundary conditions for the papillary muscles. In order to prevent the leaflets from interpenetrating each other upon closure, a contact condition was set between the two surfaces. The measured blood pressure in the left ventricle of the pig during the isovolumetric contraction phase up to the maximum pressure in the left ventricle in the ejection phase was applied as load history.

Material models

The leaflets were modeled with an incompressible hyperelastic transversely isotropic material model. The formulation of transversely isotropic hyperelasticity is based on the account provided by Holzapfel [1], and the constitutive model was derived from the strain-energy function proposed by Holzapfel et al. [2],

$$\Psi(I_1, I_4) = c_0[\exp^{c_1(I_1-3)^2+c_2(I_4-1)^2} - 1] + p(J-1), \tag{1}$$

where, c_i, $i = 0, 1, 2$, are material parameters, $\sqrt{I_4}$ represensents the stretch of the collagen fibers and the scalar p serves as an inderteminate Lagrange multiplier.

The material parameters were determined from the experimental data provided by May-Newman

and Yin [4]. The expression of the spatial elasticity tensor derived from relation (1) is,

$$\begin{aligned}\mathbb{c} &= 4\psi_{11}\mathbf{B}\otimes\mathbf{B} + 4\psi_{14}(\mathbf{B}\otimes\mathbf{a}\otimes\mathbf{a} + \mathbf{a}\otimes\mathbf{a}\otimes\mathbf{B}) + 4\psi_{44}\mathbf{a}\otimes\mathbf{a}\otimes\mathbf{a}\otimes\mathbf{a} \\ &\quad +2\,\mathbf{1}\otimes\left(\mathbf{F}\frac{\partial p}{\partial \mathbf{C}}\mathbf{F}^T\right) - 2p\mathbb{I}, \qquad (2) \\ &\quad \text{where} \quad \psi_{ij} = \frac{\partial^2\Psi}{\partial I_i \partial I_j} \quad (i,j = 1,4)\end{aligned}$$

The material model was implemented into ABAQUS/standard by using the user-defined subroutine UMAT. The details of the material model are given in [3]. The comparison between the analytical Cauchy stresses and those obtained from the FE analysis on a displacement controlled single membrane element equibiaxial test is presented in Figure 3 for the posterior leaflet.

For the chordae, an isotropic incompressible hyperelastic material model was implemented into

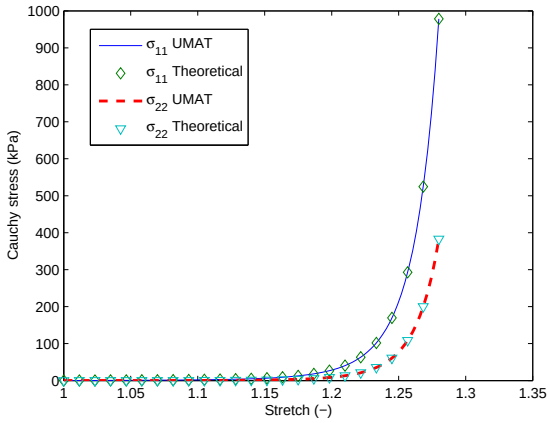

Figure 3: Equibiaxial test on the posterior leaflet ($c_0 = 0.171$ kPa, $c_1 = 5.28$, $c_2 = 6.46$)

the ABAQUS/Standard user-defined subroutine UHYPER. The material model was derived from the following strain-energy function U,

$$U(I_1) = a_1(I_1 - 3) + a_2[\exp^{a_3(I_1-3)} - 1], \qquad (3)$$

where a_1, a_2 and a_3 are the material parameters determined from experiemental tensile tests published by Kunzelman and Cochran [5].

Results

The first simulation considered only marginal chordae, i.e related to a pathological state. In Figure 4, it appears for this case that the displacement in the 3-direction (see Figure 2) is approximatively 2 mm larger than the displacement obtained from the ultrasound measurement. Thus, in order to reduce the displacement of the anterior leaflet in the 3-direction, strut chordae (i.e chordae attached beyond the free edge of the leaflet) were attached to the anterior leaflet in addition to the marginal chordae already attached. Hence, a FE analysis with six strut chordae, i.e. related to a healthy state, was performed.

Finally, a third simulation with softer chordae was performed, i.e related to a pathological case. In this last case, the displacement in the 3-direction of the anterior leaflet is much larger than for the two first cases.

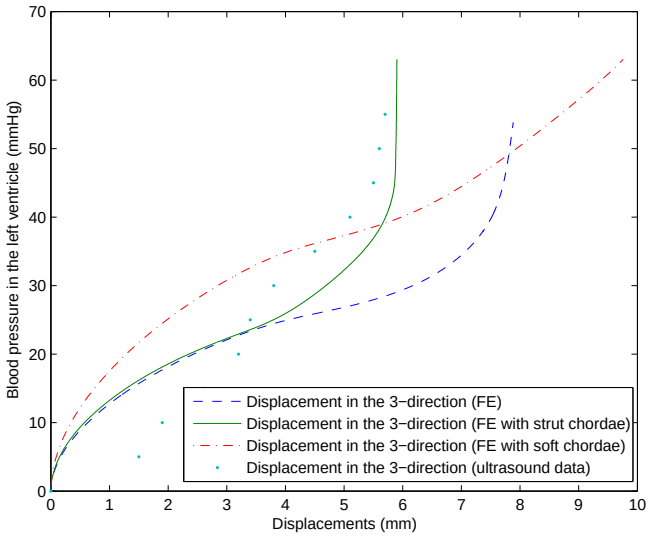

Figure 4: Left ventricle blood pressure versus the computed displacements in the 3-direction for a node located at the middle of the anterior leaflet. The dashed curve shows the pressure-displacement relationship for the model with marginal chordae (pathological state), while the solid curve shows the pressure-displacement relationship for the model with marginal and strut chordae (healthy state). The dashdot curve shows the pressure-displacement relationship for the model with softer chordae. The dots show the measured data of the corresponding node obtained from the ultrasound measurements carried out on the pig.

Concluding remarks

This study shows the importance of the chordae to prevent the leaflets from collapsing into the left atrium.

In additions, these simulations were performed with realistic material models for both mitral leaflets and chordae tendinae. This three-dimensional finite element model allows the simulation of mitral valve response for both healthy and diseased conditions.

References

[1] G. A. Holzapfel. *Nonlinear Solid Mechanics. A Continuum Approach for Engineering* . John Wiley & Sons, Chichester, 2000.

[2] G. A. Holzapfel, G. Sommer, C. T. Gasser, and P. Regitnig. Determination of the layer-specific mechanical properties of human coronary arteries with non-atherosclerotic intimal thickening, and related constitutive modelling. *Am. J. Physiol. Heart Circ. Physiol.*, 289:H2048–2058, 2005.

[3] V. Prot, B. Skallerud , G. A. Holzapfel. Transversely isotropic membrane shells with application to mitral valve mechanics. Constitutive modeling and finite element implementation. Submitted 2006.

[4] K. May-Newman and F. C. P. Yin. A constitutive law for mitral valve tissue. *J. Biomech. Eng.*, 120:38–47, 1998.

[5] K. S. Kunzelman and R. P. Cochran. Mechanical properties of basal and marginal mitral valve chordae tendineae. *ASAIO Trans.*, 36:M405–408, 1990.

Fluid dynamics of mechanical aortic valves

Leif Rune Hellevik*, Paul Roger Leinan and Bjørn Skallerud
Division of Biomechanics
Department of Structural Engineering
The Norwegian University of Science and Technology, Trondheim, Norway
e–mail: leif.r.hellevik@ntnu.no

Summary Mechanical prosthetic heart valves are an important option in surgical treatment of human pathological heart valves. In the design of a mechanical heart valve, at least three design criteria are of importance: a) the prosthesis should mimic the function of a physiological valve as closely as possible, b) the shear stresses in the blood flow through the valve should be minimized to reduce risk of thrombosis, and c) the risk of structural failure must be low.
In this paper we report results from work in progress on numerical and experimental modeling of mechanical heart valves. A strongly coupled fluid structure interaction scheme was utilized for the numerical simulations. Experiments have been carried out in a pulsatile flow loop for a Björk-Shilely Convexo-Concave heart valve prosthesis. Discrepancies were found between experimental and numerical predictions of the valve opening angle. However, by employing a moment of inertia yielding dynamical similarity for the 2D simulations, improved time-stepping scheme and boundary conditions, we believe that better agreement will be obtained.

Introduction

Mechanical prosthetic heart valves have been used in surgical treatment of pathological valves for the last fifty years. The design of mechanical heart valves have improved greatly in this period. The aim has been to mimic the function of a physiological valve as best as possible, at the same time as the blood flow around the valve must be controlled to ensure low flow velocities and shear stresses. High shear stresses damage the blood, mainly by destroying the red blood cells and also contribute to thrombus initiation. Durability is also a major concern, as mechanical valves must able to withstand the stresses inflicted from millions of heart beats.

Fluid structure interaction (FSI) simulations has recently emerged as a promising approach, which alongside experiments, may be used to study the hemodynamic of prosthetic heart valves.

In this paper we employ an arbitrary Lagrangian-Eulerian (ALE) coupling procedure, where the valve motion, is strongly coupled with the solution of the flow field, inspired by [1]. A backward Euler-scheme was used for the valve motion, rather than the Newmark scheme[1]. The dynamic mesh model in the commercial CFD-package FLUENT 6.2 was used for the ALE-simulations. The coupling procedure was implemented as a user-defined function in FLUENT.

A Björk-Shiley Convexo-Concave (BSCC) valve was chosen as the specific valve for the experimental work, as it was readily available to us.

Method

Experimental setup

In the pulsatile flow loop, a fluid reservoir were connected to a tube leading to the mitral entrance of the ventricular chamber. A second tube representing the aorta leaves the ventricular chamber at a 90° angle, to the mitral entrance and completes the loop back to the reservoir (see Fig. 1).

The ventricular chamber, the first part of the aorta and the mitral entrance are all made of Plexiglas. The ventricular chamber is square box connected to a bellow pump. The first part of the aorta and

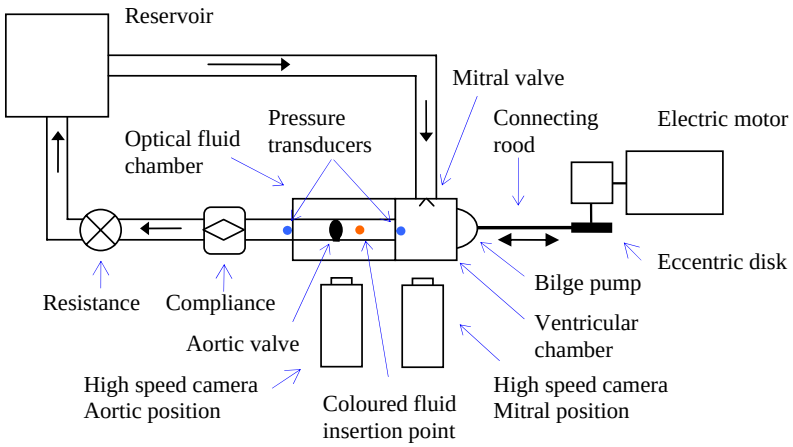

Figur 1: A schematic diagram of the pulsatile flow loop with the positions of the pressure transducers and the high speed camera positions.

the mitral ventricular entrance are made of Plexiglas tubes with an inner diameter of 28 mm, and lengths of 250 and 100mm, respectively. The volume change over time in is control by a rood connected to the pump and an eccentric disk. The profile of the disk combined with the rotational velocity controls the volume rate time in the ventricular chamber.

A high speed video camera (Phantom Vision) was used to allow for visualization of the flow field (BXXX and water mixture inserted by a needle), investigation of the opening and closing behavior of the valve, and measurements of the valve closing time (see Fig. 1).

Pressures were measured (BD DTX Plus Blood Pressure Transducers) at two locations; the ventricular chamber upstream of the valve, and in the tube representing the aorta, 200 mm downstream of the ventricle (see Fig. 1).

The average volume flow and the ventricular ejection volume were by collecting the return flow in a graduated flask and average over the time period and the number of strokes, respectively.

Numerical simulations

The numerical simulations were performed using the dynamic mesh model in FLUENT 6.2, a commercial software package. All simulations were performed in 2D to reduce the computational costs in this initial study. The Navier-Stokes equations, in a conservative ALE formulation, were solved with time-varying pressure boundary conditions.

The valve was modeled as a rigid body, rotating around a given axis of rotation, with the equation of motion:

$$M = I \cdot \ddot{\theta} \tag{1}$$

where M is the net moment of forces acting on the valve, I the moment of inertia and θ the angular position of the valve. To obtain geometric similarity between experiments and simulations, the valve length in the 2D simulations l, were taken as the diameter of the valve in the experiments. For the moment of inertia around the axis of rotation, the value for a thin rectangular plate was used:

$$I = \frac{m\ l^2}{3} \tag{2}$$

where m denotes the mass of the valve.

To provide a better coupling between the fluid and structural solvers, and a higher degree of implicity, subiterations are used (denoted by subscript k), with a Newton-type correction of the moment:

$$M_k + \frac{\partial M}{\partial \ddot{\theta}} \left(\ddot{\theta}_{k+1} - \ddot{\theta}_k \right) \approx I \cdot \ddot{\theta}_{k+1} \tag{3}$$

$$\ddot{\theta}_{k+1} = \frac{M_k - \frac{\partial M}{\partial \ddot{\theta}} \cdot \ddot{\theta}_k}{I - \frac{\partial M}{\partial \ddot{\theta}}} \tag{4}$$

The $\frac{\partial M}{\partial \ddot{\theta}}$ may be considered as a Jacobian, which must be estimated numerically:

$$\frac{\partial M}{\partial \ddot{\theta}} \approx \frac{M_k - M_{k-1}}{\ddot{\theta}_k - \ddot{\theta}_{k-1}} \tag{5}$$

To start the sub-iteration scheme an initial perturbation of $\ddot{\theta}$ must be provided. For more details see [1]. The convergence criterion for the sub-iterations is:

$$\| M_k - I \cdot \ddot{\theta}_k \| < \epsilon \tag{6}$$

The equation of motion is integrated with a backward Euler scheme:

$$\dot{\theta}^{n+1} = \dot{\theta}^n + \ddot{\theta}^{n+1} \Delta t \tag{7}$$

$$\theta^{n+1} = \theta^n + \dot{\theta}^{n+1} \Delta t \tag{8}$$

Results

Measurements on the closure time for both the inline and angular displacement of the valve were carried out. The experimental fluid was water and experiments were performed with and without an aortic compliance to be better able to compare the experiments, to the numerical simulation which do not include an aortic compliance.The aortic compliance in the pulsatile flow loop was incorporated to make the model more realistic physiologically and to produce results for suitable for comparison with results from other experimental flow loops.

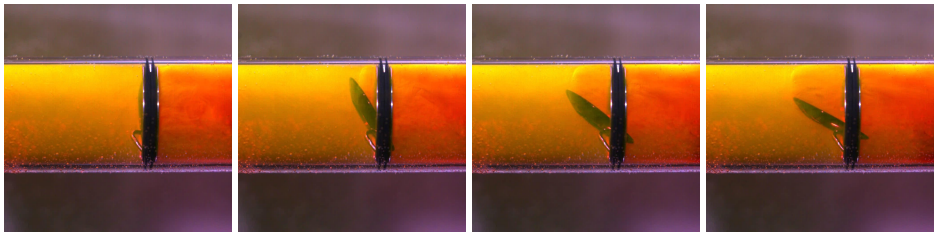

Figur 2: High speed video camera recordings of the opening av the valve.

The high speed video camera recordings allowed for both visualization of the flow field (Fig. 2) and for experimental estimates of the inline and angular displacements of the valve as a function of time.

In all the numerical simulations the thermodynamic properties of water were used for the fluid. The FSI simulations provide estimates of the velocity, pressure, vorticity during the simulated

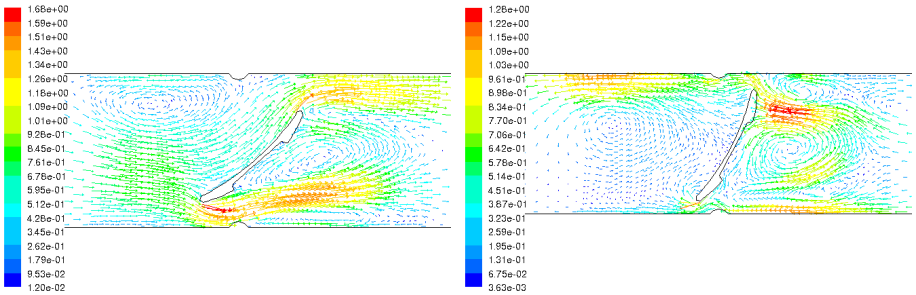

Figur 3: Velocity vectors during closure of the valve.

cycle as illustrated in Fig. 3. Time-varying pressure boundary conditions were imposed, with the intention to mimic the pressures recorded in the experiments. However, a shorter fundamental frequency was used in the pressure boundary conditions, corresponding to a shorter diastole, to save computational time.

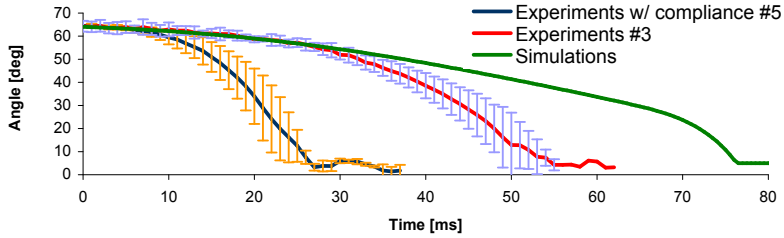

Figur 4: Comparison of the valve angle during closure between experiments with and without compliance and simulations.

Preliminary comparison between experimental measurements and FSI predictions of BSCC angle as a function of time are illustrated in Fig. 4. The measurements were done by examining high speed photos from the experiments, and recording the angle per time by using computer software accompanying the high speed camera. This software included the possibility to store coordinates from each frame captured by the high speed camera.

Discussion

In this paper we have presented work in progress on the fluid dynamics mechanical aortic valves. In particular, the BSCC valve have been investigated experimetally and numerically. Substantial discrepancies were found between experiments and simulations for the prediction of the opening angle of the valve as a function of time, in particular for the compliant case. However, by employing a moment of inertia which provides dynamical similarity (i.e. for a circular disc), a higher order time-stepping scheme, using the full cycle of the pressures obtained experimentally as boundary conditions, and simulating for several cycles, we believe that better agreement will be obtained.

References

[1] Jan Vierendeels, Kris Dumont, Erik Dick, and Pascal Verdonck. Stabilization of a fluid-structure coupling procedure for rigid body motion. In *33rd AIAA Fluid Dynamics Conference and Exhibit*, pages AIAA 2003–3720, Orlando, Florida, June 2003.

Spatial Differences in Cardiac Strains During Filling

Katarina Kindberg* **and Matts Karlsson**
Department of Biomedical Engineering
Linköping University, Linköping, Sweden
e–mail: katki@imt.liu.se

Summary Radiopaque marker technology provides data for detailed studies of cardiac kinematics. We developed a strain estimation method tailored for data from a transmural myocardial bead array. This method is accurate and robust and reveals interesting transmural discrepancies in the relationship between circumferential strain and percentage filling volume during diastole in the lateral equatorial left ventricular wall of the ovine heart.

Introduction

Knowledge of normal cardiac mechanics is important when attempting to understand the mechanisms that impair the contractile function of the heart in the setting of disease. Although ventricular pressures and volumes are valuable for assessing the global pumping performance of the heart, suitable measures of the regional kinematics of the myocardium are needed to understand the underlying structural basis of ventricular function. The scope of this project was the detailed study of cardiac strain during diastole, i.e. during left ventricular filling.

Method

The global heart kinematics can be studied by radiopaque markers that are surgically implanted to silhouette the walls of the heart chambers. Three-dimensional coordinates of the markers are acquired by merging two simultaneously acquired two-dimensional X-ray video images from two different views [1]. To study strain of the heart wall, three transmural columns of close-spaced radiopaque beads can be inserted in a dense region through the left ventricular wall. The three-dimensional bead coordinates are acquired in the same manner as the marker coordinates [1].

To estimate the Lagrangian strain tensor, defined by $\mathbf{E} = \frac{1}{2}\left(\mathbf{F}^T\mathbf{F} - \mathbf{I}\right)$ where $\mathbf{F}$ is the deformation gradient tensor and $\mathbf{I}$ is the identity tensor, in the region of the beads, the position field as a function of the position in the reference configuration could be determined. Different ways of doing this has been presented [2, 3]. The method of Waldman et al. [2] assumes strain to be constant within tetrahedral regions bordered by the beads, and computes the constant strain within these regions. The finite element method presented by McCulloch et al. [3] greatly improves the strain estimations. Instead of assuming constant strain within regions, a bilinear-cubic or a bilinear-quadratic displacement field is fitted to the bead positions.

We developed a method for strain estimation tailored for coordinate data from a transmural myocardial bead array that fits a polynomial forthright without isoparametric formulation to the bead coordinates, without loss in accuracy [4]. The number of beads in each column of the bead array is subjected to surgical and acquiremental limitations. A benefit with this polynomial method for strain estimation is its ability to avoid loss of accuracy for the case of a missing bead [4].

Material

Ovine marker coordinate data

Marker and bead coordinate data, acquired without interventions eight weeks after marker implantation, from seven closed-chest sheep have been used in this project. Details about the surgery and

data acquisition are to be found in [1]. Briefly, 13 radiopaque markers were surgically implanted to silhouette the left ventricular chamber, along with three transmural columns of four beads each in the lateral equatorial left ventricular wall in a region equally-spaced between the papillary muscles. The marker and bead arrays used in this project are shown in Figure 1. The Lagrangian strain

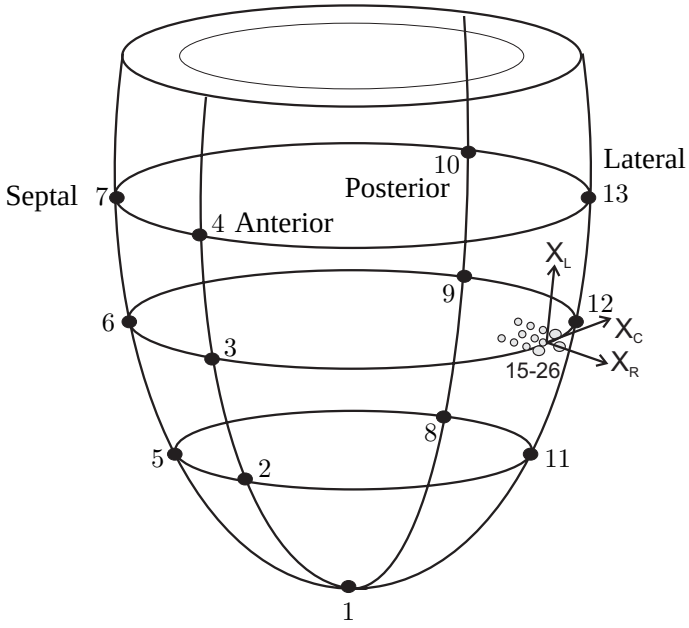

Figure 1: Left ventricular chamber silhouette markers (#1-13) and the transmural bead array (#15-26) as well as the local cartesian cardiac coordinate system $(\mathbf{X}_C, \mathbf{X}_L, \mathbf{X}_R)$. There are three columns of beads: #15-18, #19-22 and #23-26.

tensor was estimated at subepicardium (20% of wall thickness below the epicardial surface) and subendocardium (80% of wall thickness) at each time increment during left ventricular filling using a linear-quadratic polynomial assumption, with filling onset used as the reference configuration [5].

Analytical model

An analytical model of the left ventricle can be used to predict the theoretical relationship between circumferential strain at endo- and epicardium and relative left ventricular filling volume during diastole. The model is implemented as a thick-walled incompressible cylinder with appropriate dimensions of the ovine left ventricle. The theoretical endo- and epicardial circumferential strain and relative left ventricular filling volume during diastole can be computed by increasing the inner radius linearly from $R_1 = 2.0$ cm to $r_1 = 2.2$ cm while the height $h = 8.0$ cm of the cylinder is kept constant and thereby increasing the volume inside the cylinder (Figure 2). The outer radius is set to $R_2 = 3.0$ cm at filling onset. This deformation is given by

$$\begin{aligned} r &= \sqrt{R^2 - R_1^2 + r_1} \\ \theta &= \Theta \\ z &= Z \end{aligned} \tag{1}$$

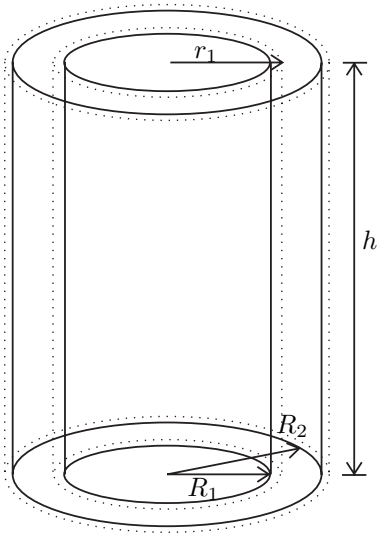

Figure 2: Analytical model of the left ventricle. Diastolic deformation with dimensions of the cylinder at filling onset (solid lines) and ED (dashed lines).

where upper-case letters denote reference configuration (filling onset) and lower-case letters denote deformed configuration.

The analytical solution for the deformation gradient tensor of the cylinder is given by

$$\mathbf{F} = \mathbf{R}^T \begin{pmatrix} \frac{\partial r}{\partial R} & \frac{1}{R}\frac{\partial r}{\partial \Theta} & \frac{\partial r}{\partial Z} \\ r\frac{\partial \theta}{\partial R} & \frac{r}{R}\frac{\partial \theta}{\partial \Theta} & r\frac{\partial \theta}{\partial Z} \\ \frac{\partial z}{\partial R} & \frac{1}{R}\frac{\partial z}{\partial \Theta} & \frac{\partial z}{\partial Z} \end{pmatrix} \mathbf{R}_0 \tag{2}$$

where the parenthesized expression is the deformation gradient tensor of components of $\mathbf{F}$ referred to cylindrical coordinates [6]. The rotation matrices $\mathbf{R}$ and $\mathbf{R}_0$ are introduced to transform the deformation gradient tensor from the cylindrical coordinate system to the cartesian coordinate system and are defined as

$$\mathbf{R} = \begin{pmatrix} \sin\theta & 0 & \cos\theta \\ \cos\theta & 0 & -\sin\theta \\ 0 & 1 & 0 \end{pmatrix}, \qquad \mathbf{R}_0 = \begin{pmatrix} \sin\Theta & 0 & \cos\Theta \\ \cos\Theta & 0 & -\sin\Theta \\ 0 & 1 & 0 \end{pmatrix} \tag{3}$$

Results

The theoretical relationships between percentage filling volume and circumferential strain (E_{CC}) at the inner and outer surfaces of the analytical cylinder model are linear (Figure 3, open symbols), but left ventricular volume increase is more sensitive to changes in epicardial circumference than to endocardial circumferential strain [5]. Figure 3 compares subendocardial and subepicardial theoretical strains with the experimentally measured group mean circumferential strains from the lateral equatorial left ventricular wall of the ovine heart. There is a close relationship in the subendocardium between theoretically predicted and experimentally measured values, but the subepicardium shows a significant divergence from the theoretical values. Subepicardial circumferential

expansion is virtually complete after about one third of the filling interval, which clearly is not the behaviour of a simple linear system acted on only by left ventricular inflow.

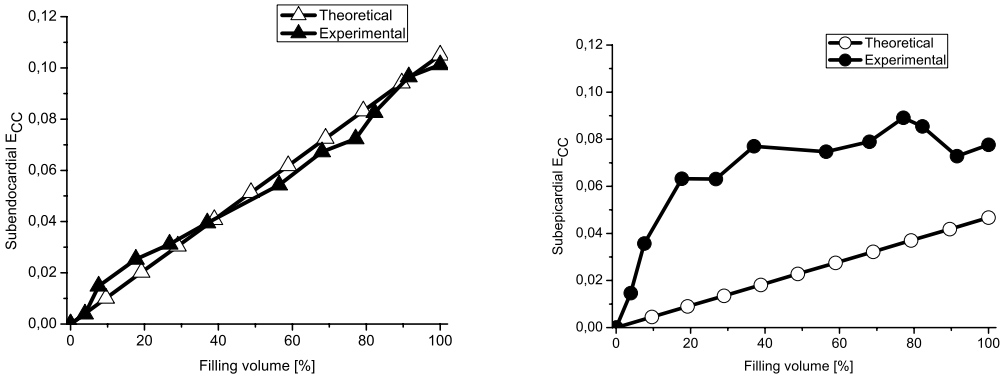

(a) Subendocardium (b) Subepicardium

Figure 3: Theoretical and mean experimental circumferential strain versus percentage filling volume.

Concluding remarks

The polynomial method for strain estimation is accurate and robust and suitable for a transmural myocardial bead array. The experimental relationship between circumferential strain and percentage filling volume is close to the theoretical relationship at the subendocardium, but diverges significantly from the theoretical values at the subepicardium. This calls for further research taking the myocardial fiber and sheet architecture into account in order to understand the mechanisms that underlie the rapid increase in subepicardial circumferential strain during early left ventricular filling.

References

[1] A. Cheng, F. Langer, F. Rodriguez, J. C. Criscione, G. T. Daughters, D. C. Miller, and Ingels, N. B. Jr. Transmural cardiac strains in the lateral wall of the ovine left ventricle. *Am J Physiol Heart Circ Physiol*, 288(4):H1546–56, 2005.

[2] L. K. Waldman, Y. C. Fung, and J. W. Covell. Transmural myocardial deformation in the canine left ventricle. normal in vivo three-dimensional finite strains. *Circ Res*, 57(1):152–63, 1985.

[3] A. D. McCulloch and J. H. Omens. Non-homogeneous analysis of three-dimensional transmural finite deformation in canine ventricular myocardium. *J Biomech*, 24(7):539–48, 1991.

[4] K. Kindberg, M. Karlsson, N.B. Ingels Jr and J.C. Criscione. Non-homogeneous strain from sparse marker arrays for analysis of transmural myocardial mechanics. *Submitted*

[5] K. Kindberg, A. Cheng, F. Langer, F. Rodriguez, G. T. Daughters, D. C. Miller, N. B. Ingels and M. Karlsson. Spatial and temporal inhomogeneity of left ventricular myocardial transmural strains during diastole. *In manuscript*

[6] A. J. M. Spencer. *Continuum mechanics*. Longman mathematical texts. Longman, London, 1980.

Temporal Changes in Sheet Architecture During Systole

Charlotte Oom*, Katarina Kindberg and Matts Karlsson
Department of Biomedical Engineering
Linköping University, Linköping, Sweden
e–mail: chaoo@imt.liu.se

Summary The end-diastolic (ED) orientations of muscle fibers and sheets in the myocardium can be directly measured using quantitative histology by terminating an ovine heart at ED. The ED architecture as well as myocardial strains during the cardiac cycle may be used for determining fiber and sheet orientations at any time during the cardiac cycle. This paper aims to describe the method and to give a brief analysis of the temporal changes in myocardial architecture from ED to end-systole (ES).

Introduction

Left ventricular (LV) myofibers are connected by an extensive extracellular collagen matrix to form myolaminar sheets. The sheet architecture and deformation are thought to underlie LV mechanics during systole and diastole. Sheet structure at end-diastole (ED) has previously been shown to be transmurally inhomogeneous and it has been suggested that a laminar deformation during the cardiac cycle could create an "accordion-like" wall thickening mechanism with a temporal change in sheet directions [1]. The orientations of muscle fibers and sheets in the myocardium can be directly measured using quantitative histology after terminating an ovine heart. However, since a heart can only be terminated once, only the myocardial structure at that particular configuration is obtained. With the use of continuum mechanics theory, the fiber and sheet orientation at any time during the cardiac cycle can be determined [2]. In this paper the method for determining sheet orientations will be described and a brief analysis of temporal changes in myocardial architecture at different depths of the myocardium will be given.

Materials and Methods

The cardiac wall kinematics were studied using biplane videofluoroscopic images of myocardial markers and two bead arrays implanted in the left ventricle according to figure 1 [3]. Bead array coordinates were acquired at 60 Hz during two cardiac cycles eight weeks after surgery and the sheet angle, β, was measured at end-diastolic pressure in the arrested hearts at approximately 20% (subepicardium), 50% (midwall) and 80% (subendocardium) of wall depth [3]. The 3D coordinates of all markers were transformed from their reference coordinate system to a Cartesian cardiac coordinate system (X_1, X_2, X_3), where X_1 is the circumferential axis, directed clockwise in a short-axis view seen from apex, X_2 is the longitudinal axis with positive direction apex-to-base, and X_3 is the radial axis, directed outwards from the ventricle. The local Cartesian fiber coordinate system has the coordinate directions of the muscle fiber axis (X_f), the myofiber sheet axis (X_s) and the axis normal to the sheets (X_n). The fiber angle, α, is defined as the angle between the fiber axis (X_f) and the cardiac circumferential axis (X_1) and the sheet angle, β, as the angle between the sheet axis (X_s) and the cardiac radial axis (X_3) according to figure 1. X_c is the cross-fiber axis, perpendicular to X_f within the X_1,X_2-plane.

The configuration at ED was used as reference state and strains in the cardiac wall were characterized by a continuous polynomial position field with quadratic dependence in X_3 and linear dependence in both X_1 and X_2 using least-squares fitting [4]. The Lagrangian strain tensor ($\mathbf{E}^k$)

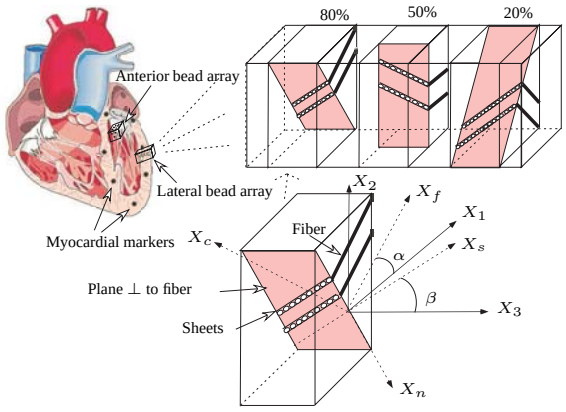

Figure 1: The fiber and sheet architecture at three transmural depths of the lateral equatorial left ventricular myocardium.

was then calculated at each time frame k during the cardiac cycle, in the subendocardium, midwall and subepicardium. It can be shown that for the radial strain component, E_{33}, it holds that [5]

$$E_{33} = \cos^2\beta\, E_{ss} + \sin 2\beta\, E_{sn} + \sin^2\beta\, E_{nn} \tag{1}$$

which indicates that the strain in radial direction depends on the sheet angle only and is independent of the fiber angle. Hence, since we are interested in changes in myocardial architecture as the wall thickness changes we will focus on temporal changes in β.

Sheet rearrangement

Figure 2 depicts a transmural section of LV free wall cut perpendicular to the local muscle fiber axis before and after deformation. The fiber axis (X_f/x_f) points into the page, the radial axis (X_3/x_3) is the local normal to the epicardial tangent plane and the cross-fiber axis (X_c/x_c) is perpendicular to the fiber axis and the radial axis and parallel to the epicardial tangent plane. The sheet axis (X_s/x_s) is oriented perpendicular to the fiber axis. The sheet angle (β/β') is the angle between the sheet and the radial axes.

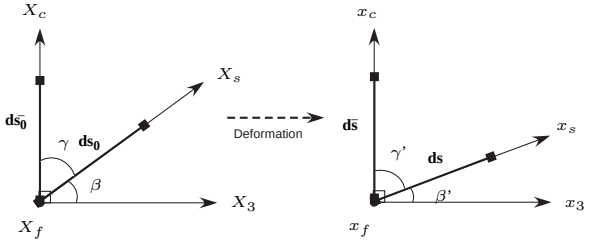

Figure 2: Deformation of the sheet angle, β. Left: Reference state. The line segments $\mathbf{ds_0}$ and $\mathbf{d\bar{s}_0}$ (starting and ending in black squares) are located in X_s and X_c direction respectively. The angle between them is γ. X_c, X_3 and X_s lie in the same plane, orthogonal to X_f which points into the page. Right: Deformed state. The line segments $\mathbf{ds_0}$ and $\mathbf{d\bar{s}_0}$ have become $\mathbf{ds}$ and $\mathbf{d\bar{s}}$. The angle between them is γ'.

In order to find the angle β' the scalar product between $\mathbf{ds}$ and $\mathbf{d\bar{s}}$ was calculated. By substituting $dx_i = \frac{\partial x_i}{\partial X_j}\, dX_j$ and $d\bar{x}_i = \frac{\partial x_i}{\partial X_j}\, d\bar{X}_j$ the scalar product may be written

$$ds\,\bar{ds}\,cos\gamma' = (\frac{\partial x_k}{\partial X_c}\frac{\partial x_k}{\partial X_c}\cos\gamma + \frac{\partial x_k}{\partial X_c}\frac{\partial x_k}{\partial X_3}\sin\gamma)\cdot ds_0\,d\bar{s_0} \tag{2}$$

The Lagrangian *strain tensor* is defined as [6]

$$E_{ij} = \frac{1}{2}\left(\frac{\partial x_m}{\partial X_i}\frac{\partial x_m}{\partial X_j} - \delta_{ij}\right) \tag{3}$$

where δ_{ij} is the Kronecker Delta. Thus from (2) and (3) we get

$$cos\,\gamma' = \frac{(2\,(E_{cc}+1)\,\cos\gamma + 2E_{c3}\,\sin\,\gamma)\;ds_0\,d\bar{s_0}}{ds\,d\bar{s}} \tag{4}$$

The stretches (Λ_i) of the line segments in X_c- and X_s-directions are defined as

$$\begin{array}{lll} \Lambda_c = \frac{ds - ds_0}{ds_0} & \Rightarrow & ds = (1+\Lambda_c)\,ds_0 \\ \Lambda_s = \frac{d\bar{s} - d\bar{s_0}}{d\bar{s_0}} & \Rightarrow & d\bar{s} = (1+\Lambda_s)\,d\bar{s_0} \end{array} \tag{5}$$

Λ_c and Λ_s may then be computed by using the change in the squares of the length elements during deformation [6], i.e.

$$\begin{array}{c} ds^2 - ds_0^2 = 2\,E_{ij}\,dX_i\,dX_j \\ d\bar{s}^2 - d\bar{s_0}^2 = 2\,E_{ij}\,d\bar{X_i}\,d\bar{X_j} \end{array} \tag{6}$$

The final equation for γ' is obtained by combining (4), (5) and (6) and the expression for β' is obtained by substituting γ=π-β and γ'=π-β'.

$$sin\,\beta' = \frac{(2\,(E_{cc}+1)\,\sin\beta + 2E_{c3}\,\cos\,\beta)}{(\sqrt{2\,E_{cc}+1})\,(\sqrt{2\,(E_{cc}\,\sin^2\beta + E_{33}\,\cos^2\beta + 2\,E_{c3}\,\sin\beta\,\cos\beta)+1})} \tag{7}$$

where E_{cc} and E_{c3} are obtained by rotating the X_1, X_2, X_3 - system through an angle α around the X_3-axis

$$\begin{array}{lcl} E_{cc} & = & \sin^2\alpha\,E_{11} - 2\,\cos\alpha\,\sin\alpha\,E_{12} + \cos^2\alpha\,E_{22} \\ E_{c3} & = & \cos\alpha\,E_{23} - \sin\alpha\,E_{13} \end{array} \tag{8}$$

Results

Table 1 shows that there are temporal variations in sheet architecture in the midwall (50%) and in the subendocardium (80%), but not in the subepicardium (20%).

Table 1: Temporal changes in sheet angle, β, from ED to ES. Reference angles measured at ED at lateral and anterior site compared with calculated angles at ES. Students paired t-test were performed between ED and ES. Values are means $\pm$ SE, N=7 for lateral site, N=6 for anterior site and *=p$<$0.05, **=p$<$0.01.

	Lateral Site		Anterior Site	
Wall depth	ED	ES	ED	ES
20%	37.3$\pm$12.5	38.5$\pm$11.7	- 8.3$\pm$20.1	- 3.7$\pm$16.6
50%	-37.1$\pm$2.3	-26.6$\pm$3.3**	40.3$\pm$4.3	29.7$\pm$4.2**
80%	62.3$\pm$4.7	55.5$\pm$5.8*	-30.3$\pm$14.0	-22.9$\pm$11.5

Conclusion

The magnitude of the sheet angle decreased from ED to ES at midwall and subendocardium, hence suggesting an "accordion-like" [1] movement of the sheets in the two inner thirds of the myocardium as the wall thickness changes. The principle is illustrated in figure 3.

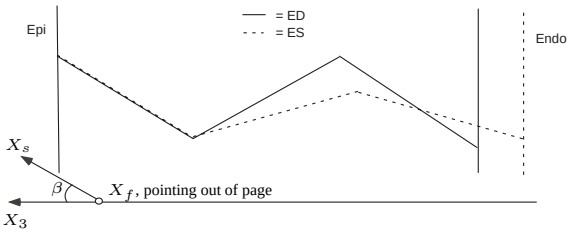

Figure 3: Two-dimensional representation of the positions of the lateral subepicardial, midwall and subendocardial sheets at ED and ES. An "accordion-like" movement of the sheets is observed in the inner two thirds of the cardiac wall as the wall thickness changes.

References

[1] K.B. Harrington and F. Rodriguez and A. Cheng and F. Langer and H. Ashikaga and G.T. Daughters and J.C. Criscione and N.B. Ingels and D.C. Miller. Direct measurement of transmural laminar architecture in the anterolateral wall of the ovine left ventricle: new implications for wall thickening mechanics. *American Journal of Physiology 288 (Heart Circ. Physiol.)*. H1324-H1330, (2005).

[2] Y. Takayama and K.D. Costa and J.W. Covell. Contribution of laminar myofiber architecture to load-dependent changes in mechanics of LV myocardium. *American Journal of Physiology 282 (Heart Circ. Physiol.)*. H1510-H1520, (2002).

[3] A. Cheng and F. Langer and F. Rodriguez and J.C. Criscione and G.T. Daughters and D.C. Miller and N.B.Jr. Ingels. Transmural sheet strains in the lateral wall of the ovine left ventricle. *American Journal of Physiology 289 (Heart Circ. Physiol.)*. H1234-H1241, (2005).

[4] K. Kindberg and M. Karlsson and N.B. Ingels Jr. and J.C. Criscione. Non-homogeneous strain from sparse marker arrays for analysis of transmural myocardial mechanics. Submitted.

[5] K.D. Costa and Y. Takayama and A.D. McCulloch and J.W. Cowell. Laminar fiber architecture and three-dimensional systolic mechanics in canine ventricular myocardium. *American Journal of Physiology 276 (Heart Circ. Physiol.)*. H595-H607, (1999).

[6] Y.C. Fung. *A first course in continuum mechanics*. Prentice-Hall, Inc, Englewood Cliffs, N.J. USA. (1969).

Adaptive Variational Multiscale Methods

Mats G. Larson
Department of Mathematics
Umeå University, Lund, Sweden
e–mail: mats.larson@math.umu.se

Summary
Recent multiscale algorithms are based on solution of a combination of global and local problems, where the global problem captures the coarse scale behavior of the system and the local problems resolve fine scale behavior and are used to compute feedback from fine to coarse scales.
In this talk we present a framework for systematic construction of the subgrid problems in a variational setting, see [1]. The subgrid problems are used to compute the effects of fine scales on coarse scales and to resolve the fine scale details of the solution. We also discuss extensions including several levels of subgrid problems and subgrid problems which contain other types of physics than the global model. The subgrid problems are solved numerically on localized patches with individually adapted mesh size and patch size.
We develop a posteriori error estimates for automatic adaptive tuning of the size of the patches and the subgrid meshes. The adaptive tuning of the discretization parameters is essential to guarantee overall accuracy in these complex methods where errors interact over several scales and to optimize the use of computing resources.
We discuss several applications involving materials with microstructure coefficients.

References

[1] M.G. Larson and A. Malqvist. Adaptive Variational Multiscale Methods Based on A Posteriori Error Estimates: Energy Norm Estimates for Elliptic Problems. To appear in Comput. Methods Appl. Mech. Engrg. Preprint available at www.femcenter.org.

Aspects on Error Controlled Concurrent Multiscale Modeling Based on RVE Computations – The Power of Duality

Fredrik Larsson* **and Kenneth Runesson**
Department of Applied Mechanics
Chalmers University of Technology, Göteborg, Sweden
e–mail: fredrik.larsson@chalmers.se

Summary The basic ingredient in concurrent multiscale modeling (CMM) is the calculation of the macroscale stress, for given macroscale deformation, via computations on a representative volume element (RVE). In this paper CMM-computations are carried out subjected to combined model and discretization error control, while a condition of (macroscale) plane stress is imposed. A particular measure of model error is considered: The subscale discretization. This type of two-scale error computation requires access to the corresponding dual solutions on the subscale (RVE-solution) as well as the macroscale. As a new result, it is shown how the same dual solutions can be conveniently used in computing the algorithmic tangent stiffness tensor for the macroscale plane stress condition, thereby demonstrating the "power of duality".

Introduction

Based on the assumption of complete scale separation, one may account for the effect of the material substructure in constitutive modeling by Concurrent Multiscale Modeling (CMM). The key ingredient is thereby to compute macroscale stresses from homogenization on a Representative Volume Element (RVE) subjected to the constraint of macro-homogeneity, cf. Miehe and coworkers [1, 2]. This means that the subscale and macroscale quantities must be chosen such that the equivalence of subscale and macroscale virtual work is satisfied. To obtain representative results, the size of the RVE must be sufficiently larger than the characteristic length of the meso-scale structure, e.g. the particle spacing in a particle-reinforced composite.

Apart from the basic assumption on scale separation, a number of other model assumptions are (implicitly or explicitly) made as part of the computations in practice. One such model assumption, valid for thin structures (such as metal sheets) is "macroscale plane stress", which was discussed extensively by Lillbacka et al. [3]. Another type of assumptions relate to the choice of substructure modeling (constitutive moddeling of constituents, size and type of boundary conditions of the RVE, discretization of the RVE, to mention the most important assumptions. Hence, it is inevitable that model errors are introduced, and they should be quantified in addition to the standard discretization errors on the macroscale. Methods for estimating the model error estimators have been developed by, for instance, Stein and coworkers [4], Oden and coworkers [5], and Larsson and Runesson [6, 7].

The purpose of this paper is to discuss various aspects on the fully adaptive two-scale CMM computations, whereby the appropriate dual solutions on the subscale (RVE solution), as well as on the macroscale, are exploited. Moreover, the dual method is adopted for computing the macroscale ATS-tensor (with a brief remark on the primal method), which is an added bonus in terms of increased efficiency.

Computational results

In order to investigate the performance of a fully adaptive procedure, we consider the coupled meso-macro-scale computation for Cook's membrane, as illustrated in Figure 1(b). The overall

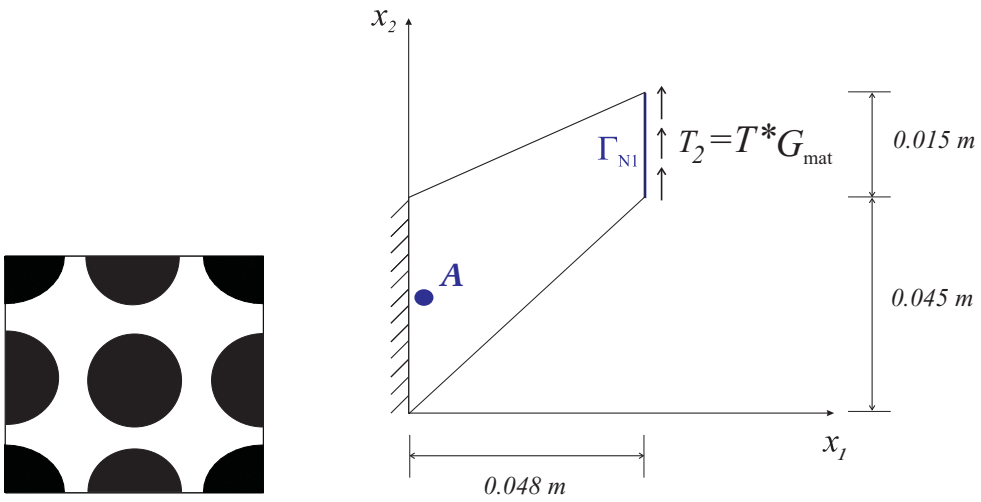

Figure 1: (a) RVE with periodic meso-scale arrangement of particles in matrix (2×2 unit cells shown in the figure), (b) Cook's membrane used in computational example of adaptive modeling.

dimension of the membrane is $48 \times 60\, mm^2$. The periodic meso-structure is depicted in Figure 1(a). The stiffness ratio particle/matrix is chosen as: $G_{\mathrm{par}}/G_{\mathrm{mat}} = 5$ and $K_{\mathrm{par}}/K_{\mathrm{mat}} = 2$. Moreover, the volume fraction of particles is $V_{\mathrm{par}}/V = 4\pi/25 \approx 50\%$. The membrane, which is assumed to be subjected to plane strain (in the present calculations), is loaded at its right end with a conservative shear loading defined by the nominal traction

$$\boldsymbol{t}_0(\bar{\boldsymbol{X}}) = T^* G_{\mathrm{mat}} \boldsymbol{e}_2 \quad \text{for} \quad \bar{\boldsymbol{X}} \in \bar{\Gamma}_{\mathrm{N1}}, \tag{1}$$

where G_{mat} is the shear modulus, $\boldsymbol{e}_2$ is the unit base vector and T^* is a loading factor.

As the goal functional we choose the macro-scale displacement gradient component $\bar{H}_{11}$ in point A, shown in Figure 1(b).

In Figure 2, we show the adapted mesh and model distribution obtained after 6 adaptive remeshing/remodelling steps corresponding to an estimated error $E^{\mathrm{rel}} \approx 5.8\%$. Finally, examples of adaptively meshed RVEs using different tolerence levels for the subscale discretization (defining the model hierarchy) are shown in Figure 3 for $q = 1$, $q = 2$ and $q = 3$, where the tolerance is defined as $TOL(q) = 10^{-(q+1)/2}$. In particular, we note that the required mesh refinement also resolves the substructure of the composite in terms of the boundary between the particles and the matrix.

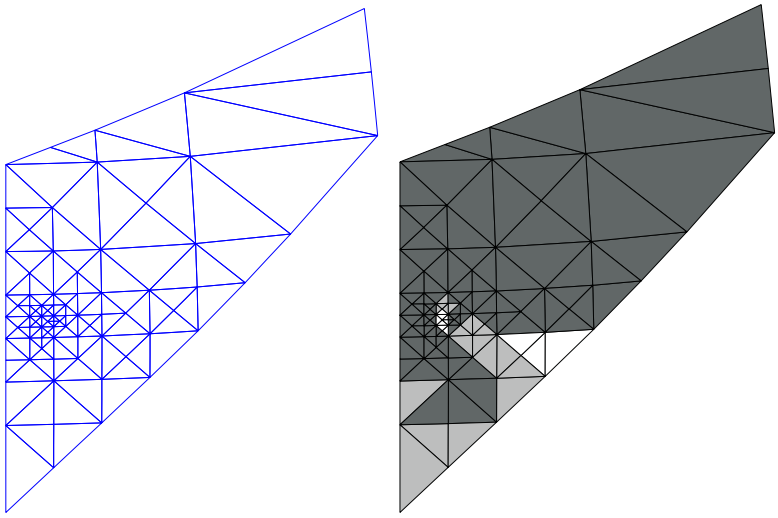

Figure 2: Adapted mesh (left) and model distribution (right), $q \in \{1, 2, 3\}$ (dark–light), for $T^* = 0.1$. 6th iteration corresponding to $E^{\mathrm{rel}} = 5.8\%$ is shown.

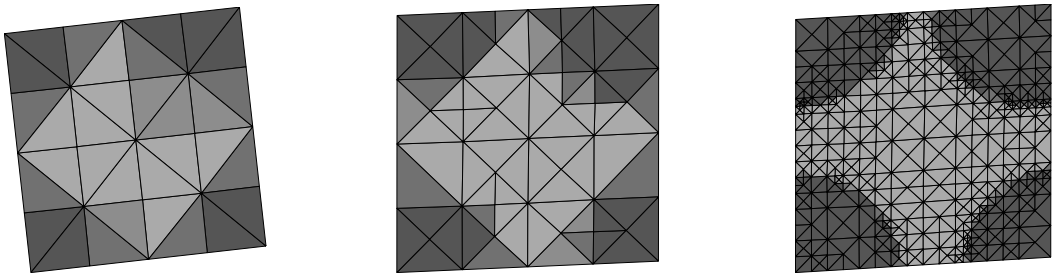

Figure 3: Examples of RVEs deformed according to the actual $\bar{\boldsymbol{H}}$ for different tolerance levels ($q = 1, 2, 3$).

References

[1] C. Miehe, J. Schröder and J. Schotte. Computational homogenization analysis in finite plasticity simulation of texture development in polycrystalline materials. *Computer Methods in Applied Mechanics and Engineering*, **171**, 387–418, 1999.

[2] C. Miehe and A. Koch. Computational micro-to-macro transitions of discretized microstructures undergoing small strains. *Archive of Applied Mechanics*, **72**, 300–317, 2002.

[3] R. Lillbacka, F. Larsson and K. Runesson. On the implementation of plane stress in computational multiscale modeling. Submitted to *International Journal for Multiscale Computational Engineering*.

[4] E. Stein and S. Ohnimus. Coupled model- and solution-adaptivity in the finite-element method. *Computer Methods in Applied Mechanics and Engineering*, **150**, 327–350, 1997.

[5] J. T. Oden and K. S. Vemaganti. Estimation of local modeling error and goal-oriented adaptive modeling of heterogeneous materials. *Journal of Computational Physics*, **164**, 22–47, 2000.

[6] F. Larsson and K. Runesson. Modeling and discretization errors in hyperelasto-(visco-)plasticity with a view to hierarchical Modeling. *Computer Methods in Applied Mechanics and Engineering*, **193**, 5283–5300, 2004.

[7] F. Larsson, and K. Runesson. RVE computations with error control and adaptivity - The power of duality. *Computational Mechanics*, DOI 10.1007/s0466-006-0108-z

Adaptive Finite Element Simulation of Coupled Flow-Transport Problems

Fredrik Bengzon, Mats G. Larson and Robert Söderlund
Department of Mathematics
Umeå University, Lund, Sweden
e–mail: fredrik.bengzon@math.umu.se

Summary
In this talk we present an adaptive finite element method for solution of coupled flow and transport problems. We present applications to cooling processes and filters. The flow may be governed by a pressure equation or the Navier-Stokes equations.
The method is based on adaptive finite element solution of the flow equation followed by solution of the transport equation and builds on an a posteriori error estimate for the quantity of interest in the transport equation, for instance the total integrated heat flux through the boundary of a hot object. The a posteriori error estimate is derived using duality techniques involving two duals one for the transport and one for the flow problem. The proper dual for the flow equation is determined in the analysis and takes the specific coupling between the two problems into account.
The resulting estimate is of weighted residual type and can be used to guide individual adaptive mesh refinement in the two problems. Furthermore, the dual problems may also be solved on separate meshes.

Estimation of model and discretization errors in parameter identification problems

Håkan Johansson*, Fredrik Larsson and Kenneth Runesson
Department of Applied Mechanics
Chalmers University, Göteborg, Sweden
e–mail: hakan.johansson@chalmers.se

Summary Parameter identification is essentially a non-linear least squares fit of predicted model response to experimental data. In this short paper we describe how a goal-oriented a posteriori error estimation can be used to assess errors introduced by finite element discretization of the underlying model. Moreover, it turns out that the same procedure can be used to assess errors introduced by the particular model we seek to calibrate.

Introduction

The calibration of constitutive models is an optimization problem, where the parameter values are sought to minimize the discrepancy between the predicted response (which depends on the sought parameters) and the observed response in a least-squares sense. In the present situation the underlying equation of state is solved using a finite element method, and consequently, discretization errors will be introduced such that the optimal parameter values will be perturbed. In order to ensure good quality of the parameter values, the errors (perturbations) of the parameters arising from the FE-discretization are estimated *a posteriori* using the solution of an appropriate dual problem. The general framework for calibration with sensitivity assessments and error computation can be found in [1] and [2].

In this paper, we seek to investigate the effects of calibrating a more inclusive model compared to choosing a simple one. In particular, we strive to estimate the outcome without actually having to carry out the full calibration of the more inclusive model. In fact, it turns out that model errors can be perceived as a special kind of discretiztion error. It is believed that such information can be vital in the subsequent task of validating the calibrated model.

Identification problem

We consider the *calibration* of a model describing some physical phenomenon in space-time as the task of finding values of a parameter set p such that minimal discrepancy is achieved between experimental observations s^{obs} and predicted response $s(p,u)$. The predicted response is a function of the variable u, which is the solution of a *state problem*, typically a partial differential equation. We thus wish to solve the optimization problem: Find $p \in \mathbb{P}$ such that the objective function(al) of least-squares type,

$$\mathcal{F}(p,u) = \frac{1}{2}||s(p,u(p)) - s^{\text{obs}}||^2 \tag{1}$$

is minimized under the constraint that p and $u \in \mathbb{U}$ satisfy the appropriate equation of state given on abstract form as

$$a(p,u,v) = l(p,v) \qquad \forall v \in \mathbb{U}^0 \tag{2}$$

The Lagrangian function(al) pertinent to the minimization problem defined by (1) and (2) is defined as

$$\mathcal{L}(p,u,\lambda) = \mathcal{F}(p,u) + a(p,u,\lambda) - l(p,\lambda) \tag{3}$$

where $p \in \mathbb{P}$, $u \in \mathbb{U}$ and the costate variable $\lambda \in \mathbb{U}^0$ are considered as independent variables. The costate (or adjoint) solution plays the role of the lagrangian multiplier in the optimality conditions characterizing a stationary point $z \stackrel{\text{def}}{=} (p, u, \lambda)$ of $\mathcal{L}$. Thus, we seek $z \in \mathbb{Z} \stackrel{\text{def}}{=} \mathbb{P} \times \mathbb{U} \times \mathbb{U}^0$ such that the Gâteaux-derivative of $\mathcal{L}$ with respect to z is zero, i.e.

$$\mathcal{L}'_z(z; \delta z) = 0 \quad \forall \delta z \in \mathbb{Z}^0 \stackrel{\text{def}}{=} \mathbb{P} \times \mathbb{U}^0 \times \mathbb{U}^0 \tag{4}$$

In order to be more explicit, we keep in mind that (4) consists of three components

$$\mathcal{L}'_p(z; \delta p) = \mathcal{F}'_p(p, u; \delta p) + a'_p(p, u, \lambda; \delta p) - l'_p(p, \lambda; \delta p) = 0 \quad \forall \delta p \in \mathbb{P} \tag{5}$$

$$\mathcal{L}'_u(z; \delta u) = \mathcal{F}'_u(p, u; \delta u) + a'_u(p, u, \lambda; \delta u) = 0 \quad \forall \delta u \in \mathbb{U}^0 \tag{6}$$

$$\mathcal{L}'_\lambda(z; \delta \lambda) = a'_\lambda(p, u, \lambda; \delta \lambda) - l'_\lambda(p, \lambda) = a(p, u, \delta \lambda) - l(p, \delta \lambda) = 0 \quad \forall \delta \lambda \in \mathbb{U}^0 \tag{7}$$

where we denote (6) the costate equation and (7) is the state equation.

For the numerical solution of (4), we introduce a Finite Element discretization. Firstly, the state space $\mathbb{U}$ is replaced by a finite-dimensional counterpart $\mathbb{U}_h \subset \mathbb{U}$ in which the FE-solution u_h resides. Consequently, we have $\lambda_h \in \mathbb{U}^0_h$. Furthermore, we will consider the situation where we make a restriction (not necessarily of FE type) in the parameter space $\mathbb{P}_h \subset \mathbb{P}$ with the "discrete" parameter set p_h. We write the FE-discretized version of (4) as follows: Find $z_h = (p_h, u_h, \lambda_h) \in \mathbb{Z}_h \subset \mathbb{Z}$ such that

$$\mathcal{L}'_z(z_h; \delta z_h) = 0 \quad \forall \delta z_h \in \mathbb{Z}^0_h \stackrel{\text{def}}{=} \mathbb{P}_h \times \mathbb{U}^0_h \times \mathbb{U}^0_h \tag{8}$$

A natural choice of how to solve the nonlinear set of equations (8) is by Newton's method involving the Hessian $\mathcal{L}''_{zz}$, which in principle reads as follows: Find a better solution $z_h^{(k+1)} = z_h^{(k)} + \Delta z_h$ where the update Δz_h is solved from the linear Newton system

$$\mathcal{L}''_{zz}(z_h^{(k)}; \delta z_h, \Delta z_h) = -\mathcal{L}'_z(z_h^{(k)}; \delta z_h) \quad \forall \delta z_h \in \mathbb{Z}^0_h \tag{9}$$

The practical implementation and solution scheme is omitted here.

We consider parametric models that are *hierarchial* in the sense that from a given model a coarser (or simpler) version is obtained by prescribing some parameters to fixed values. One example of such a hierarchy is Plasticity as a special type of Viscoplasticity (where "pure" plasticity is retrieved if the relaxation time is set to zero). Another example is the Neo-Hooke hyperelastic model, which is a simplified version of the Mooney-Rivlin model which, in turn, is a special choice of Ogden model.

The model hierarchy allows a specific model to be represented by a suitable restriction in the parameter space $\mathbb{P}$. This important property allows us to treat model errors in exactly the same manner as discretization errors, since this restriction is in complete analogy to the restriction made in the state space $\mathbb{U}$ by the introduction of the FE-space $\mathbb{U}_h$.

A posteriori error estimation

Upon introducing the discrete counterpart of the optimality condition in (8) above, discretization errors arise. These errors are denoted as $e = z - z_h$, and we assume that there is an error in each component, $e_p = p - p_h$, $e_u = u - u_h$ and $e_\lambda = \lambda - \lambda_h$. In order to estimate the effect of these errors we will employ goal-oriented *a posteriori* error estimations, as described in [1]. As a point

of departure we define a goal quantity $\mathcal{Q}(z)$ of engineering interest, in which we wish to estimate the error. Here, we focus on the analysis of the errors in the parameters, i.e. $\mathcal{Q}(z) = p_i$. In order to estimate the error in the goal quantity, we define the error measure as $\mathcal{E}(z, z_h) \stackrel{\text{def}}{=} \mathcal{Q}(z) - \mathcal{Q}(z_h)$ measuring the effect of computing $\mathcal{Q}$ using the discrete solution z_h rather than the actual solution z. The secant form of the error measure and the linear approximation of the secant form can be written as

$$\begin{aligned} \mathcal{E}(z, z_h) &= \mathcal{Q}(z) - \mathcal{Q}(z_h) = \int_0^1 \mathcal{Q}'_z(z_h + s(z - z_h); e)\mathrm{d}s \stackrel{\text{def}}{=} \hat{\mathcal{Q}}'_z(z, z_h; e) \\ &\approx \hat{\mathcal{Q}}'_z(z_h, z_h; e) = \mathcal{Q}'_z(z_h; e) \end{aligned} \tag{10}$$

In a similar way, we define the residual $\mathcal{R}$ and its secant form as

$$\begin{aligned} \mathcal{R}(z_h; \delta z) &\stackrel{\text{def}}{=} \underbrace{\mathcal{L}'_z(z; \delta z)}_{=0} - \mathcal{L}'_z(z_h; \delta z) \\ &= \int_0^1 \mathcal{L}''_{zz}(z_h + s(z - z_h); \delta z, e)\mathrm{d}s \stackrel{\text{def}}{=} \hat{\mathcal{L}}''_{zz}(z, z_h; \delta z, e) \\ &\approx \hat{\mathcal{L}}''_{zz}(z_h, z_h; \delta z, e) = \mathcal{L}''_{zz}(z_h; \delta z, e) \quad \forall \delta z \in \mathbb{Z}^0 \end{aligned} \tag{11}$$

By the introduction of the dual variable $z^* \in \mathbb{Z}$ as the solution to the *dual* problem

$$\hat{\mathcal{L}}''_{zz}(z, z_h; z^*, \delta z) = \hat{\mathcal{Q}}'_z(z, z_h; \delta z) \qquad \forall \delta z \in \mathbb{Z}^0 \tag{12}$$

we may (formally) obtain the exact error representation, by utilizing $e \in \mathbb{Z}^0$, as

$$\mathcal{E}(z, z_h) = \left[\hat{\mathcal{Q}}'_z(z, z_h; e) = \hat{\mathcal{L}}''_{zz}(z, z_h; z^*, e)\right] = \mathcal{R}(z_h; z^*) \tag{13}$$

Unfortunately, it is not possible to solve the dual problem (12) exactly, since it requires knowledge of the unknown solution z. Instead, we may utilize the approximations in (10) and (11) to arrive at the linearized dual problem, which itself is discretized; we seek $\tilde{z}_h^* \in \tilde{\mathbb{Z}}_h^0$ such that

$$\mathcal{L}''_{zz}(z_h; \tilde{z}_h^*, \delta \tilde{z}_h) = \mathcal{Q}'_z(z_h; \delta \tilde{z}_h) \qquad \forall \delta \tilde{z}_h \in \tilde{\mathbb{Z}}_h^0 \tag{14}$$

By subtracting an interpolant $\pi_h \tilde{z}_h^* \in \mathbb{Z}_h^0$ of the dual solution the error representation (13) is split into two terms, as

$$\mathcal{E}(z, z_h) \simeq \tilde{\mathcal{E}}(z, z_h) \stackrel{\text{def}}{=} \mathcal{R}(z_h; \tilde{z}_h^*) = \mathcal{R}(z_h; \tilde{z}_h^* - \pi_h \tilde{z}_h^*) + \mathcal{R}(z_h; \pi_h \tilde{z}_h^*) \tag{15}$$

The first term in (15) estimates the error from the discretization whereas the second term estimates the solution errors which arise in practice, typically from a termination criterion for the Newton iterations.

From (5)-(7) it is natural to also split the residual $\mathcal{R}$, and consequently the error representation, into $p, u-$ and $\lambda-$components. We can thus express (15) as

$$\begin{aligned} \mathcal{E}(z, z_h) \simeq\ & \mathcal{R}(z_h, \tilde{z}_h^* - \pi_h \tilde{z}_h^*) + \mathcal{R}(z_h, \pi_h \tilde{z}_h^*) \\ =\ & \overbrace{\mathcal{R}_p(z_h; \tilde{p}_h^* - \pi_h \tilde{p}_h^*)}^{\text{Model error}} + \overbrace{\mathcal{R}_u(z_h; \tilde{u}_h^* - \pi_h \tilde{u}_h^*) + \mathcal{R}_\lambda(z_h; \tilde{\lambda}_h^* - \pi_h \tilde{\lambda}_h^*)}^{\text{Discretization error}} \\ & + \underbrace{\mathcal{R}_p(z_h; \pi_h \tilde{p}_h^*)}_{\text{Residual error}} + \underbrace{\mathcal{R}_u(z_h; \pi_h \tilde{u}_h^*) + \mathcal{R}_\lambda(z_h; \pi_h \tilde{\lambda}_h^*)}_{\text{Solution error}} \end{aligned} \tag{16}$$

Note here that the decomposition in (16) is chosen such that the components correspond to different special cases. In order to illustrate this, we now disregard the solution and residual errors, and consider the model and disretization errors. If we have made no enrichment of the parameter space, i.e. $\tilde{\mathbb{P}}_h = \mathbb{P}_h$, the model error component vanishes and we estimate only discretization errors. Analogously, if we make no refinement of the state space, i.e. $\tilde{\mathbb{U}}_h^0 = \mathbb{U}_h^0$, we measure only model errors. In the case where both $\tilde{\mathbb{P}}_h$ and $\tilde{\mathbb{U}}_h^0$ are enriched both sources of errors interact.

Example

In order to give an example of the underlying problem, we consider the calibration of the evolution law for the Norton viscoelasticity. The model is characterized by the parameter set $p = \{E,\ \tau,\ n_{\mathrm{c}}\}$, which are, the E-modulus, relaxation time and creep exponent, respectively. The simple model in this case is Maxwell's viscoelasticity model that is obtained by restricting the exponent n_{c} to unity. For given synthetic data we consider four cases, a coarse mesh and Maxwell model, whose optimal parameter set is $p_{50}^{\mathrm{Max}} = \{10.0589,\ 43.619,\ 1\}$, a coarse mesh but the Norton model, $p_{50}^{\mathrm{Nort}} = \{10.6142,\ 0.97599,\ 1.97444\}$, a very fine mesh and the Maxwell model $p_{\mathrm{ref}}^{\mathrm{Max}} = \{9.6585,\ 45.5588,\ 1\}$ and, finally, a fine mesh and the Norton model $p_{\mathrm{ref}}^{\mathrm{Nort}} = \{10.0005,\ 1.0835,\ 1.9793\}$. Also, another synthetic data set constructed to give smaller errors was tested.

Although we do not give the detailed results here, in the case of large model errors (τ and n_{c} varies more than one magnitude) it was found that the error estimation gives poor precision (effectivity indices $\eta = 0.4-3$) while, in the case of moderate model errors (τ and n_{c} varies more 10-40%), we obtain better precision ($\eta = 0.5 - 1.2$) of the error estimations. A graphical interpretation is given in Figure 1. Since we make use of a linearization around p_{50}^{Max} for the error estimation, we can only expect to estimate the parts $p_{50}^{\mathrm{Nort}} - p_{50}^{\mathrm{Max}}$ and $p_{\mathrm{ref}}^{\mathrm{Max}} - p_{50}^{\mathrm{Max}}$ although we really seek to determine $p_{\mathrm{ref}}^{\mathrm{Nort}} - p_{50}^{\mathrm{Max}}$. Thus, a good precision in the error estimations requires that the discretization and model errors are independent of each other, i.e. the four solutions should form a parallelogram in $\mathbb{P}$-space. In the case of large model errors, it can be seen that the discretization errors change quite a bit between the Maxwell and Norton models compared to the case of moderate model errors.

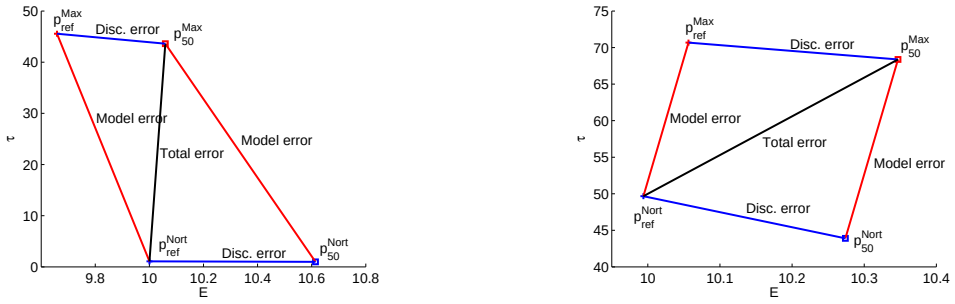

Figure 1: True error in $\mathbb{P}$ ($E - \tau$-plane) for large model error *(left)* and for moderate model error *(right)*.

References

[1] H. Johansson and K. Runesson. Parameter identification in constitutive models via optimization with a posteriori error control *Int. J. Num. Meth. Eng.*, **62**, 1315–1340, (2005).

[2] R. Becker and B. Vexler. Mesh refinement and numerical sensitivity analysis for parameter calibration of partial differential equations. *J. Comput. Phys.*, **206**, 95–110, (2005).

A sorption hysteresis model for cellulosic materials

Henrik Lund Frandsen
Department of Civil Engineering
Aalborg University, Aalborg, Denmark
e–mail: hlf@civil.aau.dk

Lars Damkilde
Esbjerg Institute of Technology
Aalborg University, Esbjerg, Denmark
e–mail: ld@aaue.dk

Summary The equilibrium concentration of adsorbed water in cellulosic materials is dependent on the history of the variations of vapor pressure in the ambient air, i.e. sorption hysteresis. Existing models to describe this phenomenon such as the independent domain theory have numerical drawbacks and/or imply accounting for the entire history variations of every material point. This paper presents a sorption hysteresis model based on a state formulation and expressed in closed-form solutions, which makes it suitable for implementation into a numerical method.

Introduction

Cellulosic materials adsorb water from the ambient air by binding of the water molecules to hydroxyl groups on cellulose. The amount of adsorbed water is dependent on the relative humidity of the air and on the amount of hydroxyl groups available, which again is dependent on the variation of the relative humidity. Hence, at a given relative humidity a cellulosic material may contain more or less water dependent on the preceding path of the relative humidity variations, see figure 2. During adsorption the material swells and more hydroxyl groups become available for adsorption. Since water occupies the hydroxyl groups, hydrogen bonds between the cellulose molecules are prevented from re-establishment during desorption. Thus, more hydroxyl groups are available during desorption than during adsorption. For an arbitrary variation of the relative humidity, more or less hydroxyl groups may be available leading to conditions between pure adsorption and pure desorption on so-called scanning curves.

In figure 1 the terminology is presented by the variation of relative humidity in the ambient air, h, and moisture content in wood, m (=concentration of water /dry density of cellulosic material).

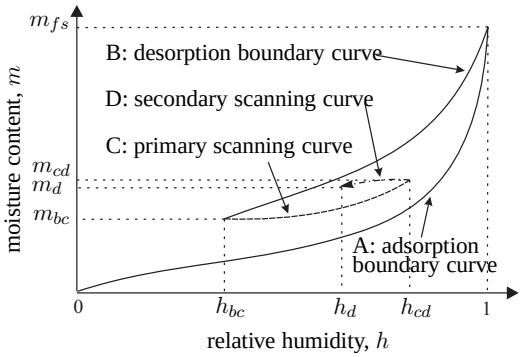

Figure 1: The terminology of sorption hysteresis.

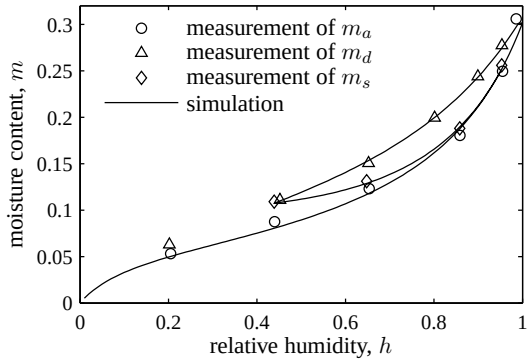

Figure 2: Measurements of boundary and an adsorption scanning curve in Norway Spruce [1].

Existing models

A classical approach for modeling sorption hysteresis is the independent domain model developed by Everett et al. [2], refined to require less calibration measurements by Mualem [3], and applied

to wood and paper by Peralta [4] and Chatterjee [5], respectively. The independent domain theory involves complicated accounting for a volume integral of a function over a varying 2D-domain for each point in a material to obtain the moisture content. Additionally it implicitly involves singularities of the function over the domain, as shown in [6].

A simpler model by Pedersen [7], stated as a set of differential equations, provides a good alternative. Though, the differential equation in h and m must be solved numerically in the vicinity of the actual state for each step in time.

The proposed model

The proposed sorption hysteresis model has the following advantages:

- Formulated in terms of current state, thus no accounting for the history of the relative humidity variations is required.
- Formulated as closed-form expressions enabling easy time integration.
- Generalizes the scanning curves to be independent of the temperature dependent boundary curves by a normalization .

Uniqueness of scanning curves

In [6] it is argued that adsorption scanning curves origining at different points will not intersect and likewise for the desorption scanning curves, see figure 3. Hence, a state within the boundary curves are uniquely defined by the origin of the scanning curve leading to the state, i.e. $z_a^0 = \{h_a^0, m_a^0\}$ and $z_d^0 = \{h_d^0, m_d^0\}$, see figure 4.

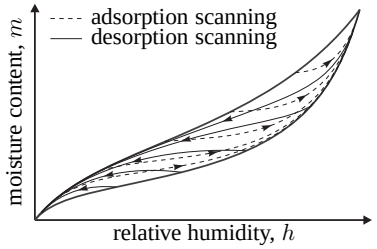

Figure 3: Grid of non-intersecting adsorption scanning curves and non-intersecting desorption scanning curves.

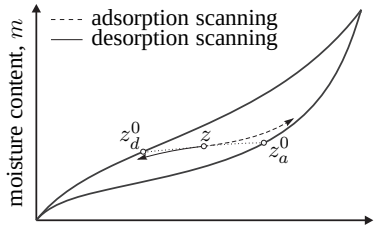

Figure 4: Definition of a state z from the scanning curves origin states z_a^0 and z_d^0.

Generalization of scanning curves

The expression for the scanning curves will be stated in the normalized parameter $s(h)$, which is the fractional amount of exploited hydroxyl groups at the given relative humidity

$$s(h) = \frac{m(h) - m_a(h)}{m_d(h) - m_a(h)} \tag{1}$$

Hereby the material-, species- and temperature-dependent boundary curves $m_a(h)$ and $m_d(h)$ are excluded from the expression for the scanning curves. In figures 5 and 6, some scanning curves from the different measurements are presented in the 1 by 1 normalized domain.

The mathematical model

As seen in figures 5 and 6, the slope of the desorption scanning curves originating at the adsorption boundary curve ($h = h_a^0$, $s = 0$) will approach the desorption boundary curve ($s = 1$) asymptotically, i.e. $\partial s/\partial h \rightarrow 0^-$. Similar observations are made for the adsorption scanning curves originating at the desorption boundary curve ($h = h_d^0$, $s = 1$), i.e. $\partial s/\partial h \rightarrow 0^+$ for $s \rightarrow 0$.

The mathematical model in equation (2) implicitly fulfills these requirements and implies the scanning curves to be uniquely defined by their origins h_a^0 and h_d^0, see figure 4

$$s = \begin{cases} -1 + 2^{\left(\frac{1-h}{1-h_d^0}\right)^{\left(\frac{d_1}{\ln(d_2(1-h_d^0))}\right)}} & \dot{h} > 0 \quad \wedge \quad s_0 > 0 \\ 2 - 2^{\left(\frac{h}{h_a^0}\right)^{\left(\frac{d_1}{\ln(d_2\, h_a^0)}\right)}} & \dot{h} < 0 \quad \wedge \quad s_0 < 1 \\ 0 & \dot{h} > 0 \quad \wedge \quad s_0 = 0 \\ 1 & \dot{h} < 0 \quad \wedge \quad s_0 = 1 \end{cases} \tag{2}$$

where d_1 and d_2 are shape parameters. Equations (2a) and (2b) model the scanning curves during adsorption ($\dot{h} > 0$) and during desorption ($\dot{h} < 0$), respectively. Equation (2c) simply states that a state with origin on the adsorption boundary curve ($s = 0$) will follow the adsorption boundary curve if adsorption is taking place ($\dot{h} > 0$) and similarly for desorption in equation (2d). Since the scanning curves are known to trail through the initial state $z_0 = \{h_0, m_0\}$, the expressions for h_a^0 and h_d^0 can be obtained by solving (2a) and (2b) for h_a^0 and h_d^0, respectively

$$h_a^0 = h_0(d_2 h_0)^{q_1} \qquad , \qquad h_d^0 = 1 - (1 - h_0)(d_2(1 - h_0))^{q_2} \tag{3}$$

where

$$q_1 = -\frac{\ln(\ln(2)) - \ln(\ln(2 - s_0))}{\ln(\ln(2)) - \ln(\ln(2 - s_0)) - d_1} \quad , \quad q_2 = -\frac{\ln(\ln(2)) - \ln(\ln(1 + s_0))}{\ln(\ln(2)) - \ln(\ln(1 + s_0)) - d_1} \tag{4}$$

The result in terms of $m(h)$ can be obtained by the reverse mapping $m(h) = (m_d(h) - m_a(h))s(h) + m_a(h)$. An analytical expression for the derivative for time integration into a numerical method is also easily obtained.

Fitting of the model

In figures 5, 7 and 2, measurements of scanning curves for sorption in Yellow Poplar by Peralta [8] and Norway Spruce by Ahlgren [1] are simulated by the proposed model. The scanning curves for sorption in a bleached-kraft paperboard measured by Chatterjee [5] are simulated in figures 6 and 8. The applied shape parameters d_1 and d_2 for wood and paper are shown in table 1.

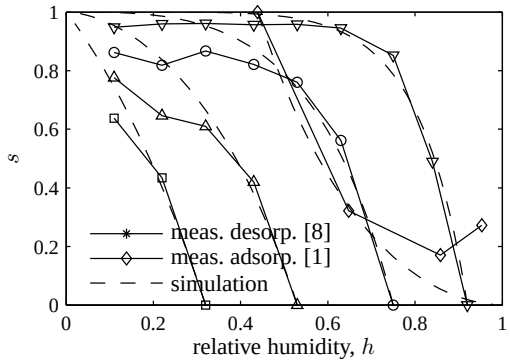

Figure 5: Scanning curves from sorption in Norway Spruce [1] and Yellow Poplar [8].

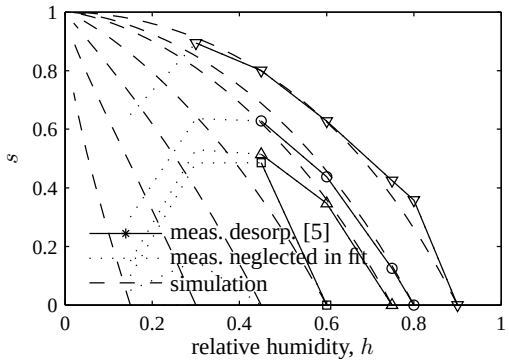

Figure 6: Desorption scanning curves from sorption in bleached-kraft paperboard [5].

In figures 5 and 6 at $h \to 0$ and at $h \to 1$, the deviations of the measurements displayed with s as a function of h appear larger, since the denominator of s approaches zero ($m_a \approx m_d$).

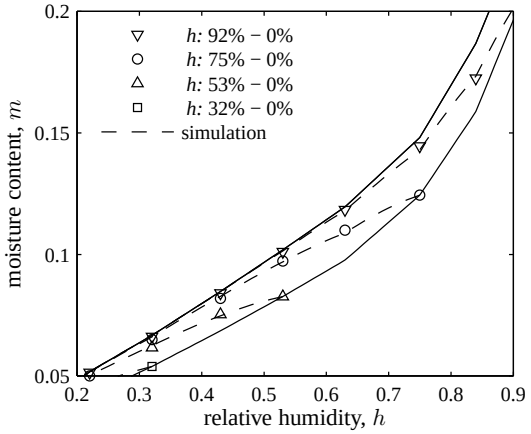

Figure 7: Desorption scanning curves from sorption in Yellow Poplar [8].

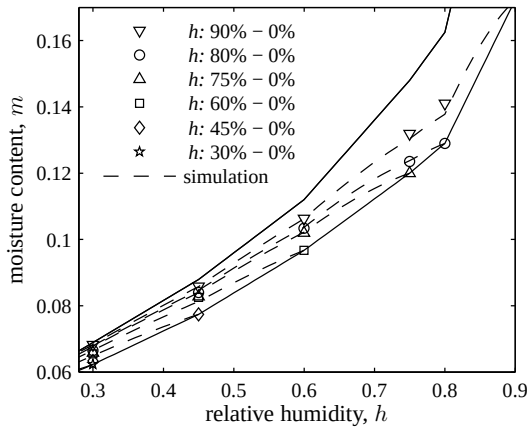

Figure 8: Desorption scanning curves from sorption in bleached-kraft paperboard [5].

	Wood	Paper
d_1	-1.32	-1.28
d_2	0.88	0.57

Table 1: Shape parameters of the scanning curves

Conclusion

The present paper proposes a sorption hysteresis model, which offers advantages for implementation in a numerical method. Easy time integration is obtained by expressing the scanning curves in closed-form solutions with the current state as the only input parameter. General applicability is provided by excluding the material, wood-species and temperature dependent boundary curves boundary curves from the hysteresis scanning curves.

References

[1] L. Ahlgren. *Moisture fixation in porous building materials*. Division Of Building Technology, The Lund Institute Of Technology, 1972.

[2] D. H. Everett. A general approach to hysteresis. part 4. an alternative formulation of the domain model. *In: Trans. Faraday Soc.*, 51:1551–1557, 1955.

[3] Y. Mualem. Conceptual model of hysteresis. *Water Resources*, 10(3):514–520, 1974.

[4] P. N. Peralta and A. P. Bangi. Modeling wood moisture sorption hysteresis based on similarity hypothesis. part ii. capillary-radii approach. *Wood and Fiber Science*, 30(2):148–154, 1998.

[5] S. G. Chatterjee, B. V. Ramarao, and C. Tien. Water-vapour sorption equilibria of a bleached-kraft paperboard - a study of the hysteresis region. *Jour. of Pulp and Paper Science*, 23(8):366–373, 1997.

[6] H. L. Frandsen, S. Svensson, and L. Damkilde. A hysteresis model suitable for numerical simulation of moisture content in wood. *Submitted to Holzforschung*.

[7] C. R. Pedersen. Combined heat and moisture transfer in build constructions. Technical report, Thermal Insulation Laboratory, Technical University of Denmark, 1990.

[8] P. N. Peralta. Sorption of moisture by wood within a limited range of relative humidities. *Wood and Fiber Science*, 27(1):13–21, 1995.

Time-Sequential Error Control and Adaptivity in Space-Time for Poro-mechanics Problems

Kenneth Runesson* **and Fredrik Larsson**
Department of Applied Mechanics
Chalmer University of Technology, Göteborg, Sweden
e–mail: kenneth.runesson@chalmers.se

Summary The paper outlines a novel time-sequential space-time adaptive strategy for the finite element method applied to a class of nonlinear and time-dependent problems. In particular, the non-linear coupled problem of poro-mechanics is studied as a prototype problem.

Introduction

The poromechanics problem, which is of particular relevance in geotechnical engineering, is a coupled problem in displacement and pore pressure (in its simplest form), and it may involve geometrical as well as material nonlinearity. Typically, fine-grained soils are modelled as (visco)plastic media. The natural variational setting allows for space-time FE using dG- or cG-methods in time depending on the expected dominating character (quasistatic or dynamic). Previous work in this area, applied to the mathematically similar problem of thermoelasticity, focuses either on space adaptivity [1] or time adaptivity [2] separately, while restricting to linear elastic response. In this paper, we discuss goal-oriented error computation and the suitable strategy for the combined space-time adaptivity while accounting for non-linearities. In particular, we discuss ways of avoiding complete remeshing in time due to the strong dissipation (damping of error) via a time-sequential space-time adaptation of the mesh. In this manner, neither complete re-computations nor excessive data storage are required.

Numerical results for a geometrically nonlinear hyperelastic porous solid with fluid-filled pores are presented. In particular, we study the accuracy of the presented error estimation and the efficiency of the proposed adaptive strategy for different chosen error measures and different levels of non-linearities.

The abstract problem

We establish the weak form of the space-time problem as follows:

$$\sum_{n=1}^{N} \int_{I_n} \left[(\mathrm{d}_t \Phi[z], \delta z) + a(z; \delta z) \right] \mathrm{d}t + \left(\Phi \left[z(t_0^-) \right], \delta z(t_0^+) \right) + \sum_{n=2}^{N} \left([\![\Phi[z]]\!](t_{n-1}), \delta z(t_{n-1}^+) \right) = \sum_{n=1}^{N} \int_{I_n} l(\delta z) \, \mathrm{d}t + \left(\Phi[z_0], \delta z(t_0^+) \right),$$

where $\Phi[z]$ is the conservation quantity, $a(\bullet;\bullet)$ is a spatially weak form pertinent to the balance relation(s), possibly non-linear, and $l(\bullet)$ represents (spatial) data/loading to the problem. The summation in the weak form is made over each discrete time-step. Moreover, z denotes the unknown solution and Φ_0 is the initial condition on $\Phi[z]$. In the studied case of quasi-static loading of a porous medium, we may set $z = (\boldsymbol{u}, p)$, where $\boldsymbol{u}$ and p are the displacement of the solid skeleton and the pore-pressure, respectively. Given a finite element approximation of z_h, we may compute the space-time residual as $R(z_h; \delta z)$.

Based on duality arguments, we seek the error in a quantity of interest, E, via the solution of the auxiliary dual problem. A hierarchical decomposition of the pertinent dual solution z^* can be expressed as

$$z^* = z_h^* + \Delta^{(\mathrm{s})}z^* + \Delta^{(\mathrm{t})}z^* + \Delta^{(\mathrm{st})}z^*,$$

where z_h^* is the part inside the FE-approximation space, $\Delta^{(\mathrm{s})}z^*$ is the spatial enhancement, $\Delta^{(\mathrm{t})}z^*$ is the temporal enhancement, whereas $\Delta^{(\mathrm{st})}z^*$ is the combined enhancement. Using the hierarchical split of the dual solution, we may express the error in terms of the residual as follows:

$$\underbrace{R(z_h^{\mathrm{SOL}};z^*)}_{\simeq E} = \underbrace{R(z_h^{\mathrm{SOL}};z_h^*)}_{\simeq E_{\mathrm{SOL}}} + \underbrace{R(z_h^{\mathrm{SOL}};\Delta^{(\mathrm{s})}z_h^*)}_{\equiv \overset{(\mathrm{s})}{E}_{\mathrm{FEM}}} + \underbrace{R(z_h^{\mathrm{SOL}};\Delta^{(\mathrm{t})}z_h^*)}_{\equiv \overset{(\mathrm{t})}{E}_{\mathrm{FEM}}} + \underbrace{R(z_h^{\mathrm{SOL}};\Delta^{(\mathrm{st})}z_h^*)}_{\equiv \overset{(\mathrm{st})}{E}_{\mathrm{FEM}}}, \quad (1)$$

where E_{sol} is the error due to incomplete solution of the non-linear set of FE-equations and $\overset{(\mathrm{s})}{E}_{\mathrm{FEM}}$, $\overset{(\mathrm{t})}{E}_{\mathrm{FEM}}$ and $\overset{(\mathrm{st})}{E}_{\mathrm{FEM}}$ are the discretization errors.

Based on a coarse dual solution, i.e. a coarse primal- and dual-solution sweep, the error estimate can be evaluated sequentially, without recursive computations of the entire problem. In this manner, the problem is solved in one single step, aiming for *global* error control in space and time in a quantity of interest.

Numerical example

The proposed strategy is employed for the solution of a non-linear poro-(hyper-)elastic problem. Snap-shots of the resulting spatial meshes for a target accuracy of 0.5% in a time-integrated pressures value is shown in Figure 1.

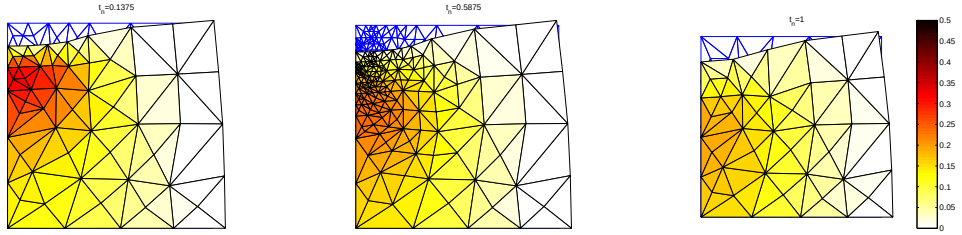

Figure 1: Snapshots of resulting meshes using a time-sequential adaptive strategy. The adaptivity targets the accuracy in a time-integrated (regularized) point-wise pressure.

References

[1] D. Aubry, D. Lucas and B. Tie. Adaptive strategy for transient/coupled problems. Application to thermoelasticity and elastodynamics. *Computer Methods in Applied Mechanics and Engineering* **176**, 41–50, 1999.

[2] F. Larsson, P. Hansbo and K. Runesson. Space-time finite elements and adaptive strategy for the coupled thermoelasticity problem. *International Journal for Numerical Methods in Engineering* **56**, 261–293, 2003.

An integration algorithm for elasto-plastic damage

Mathias Wallin* **and Matti Ristinmaa**

Department of Solid Mechanics
Lund University, Lund, Sweden
e–mail: mathias.wallin@solid.lth.se

Summary In this work the constitutive evolution equations are reformulated using the assumption of constant strain rate which results in a set of ODEs. The set of ODEs is reduced using a compact description of the stress space. To calculate the consistent tangent an extra set of ODEs needs to be solved. This set of additional ODEs is solved simultaneously with the evolution equations, which allows for an efficient numerical treatment. To investigate the solution method an elasto-plastic damage model is considered.

Introduction

To make practical use of constitutive material models some numerical method, e.g. the finite element method, must be employed and the constitutive equations must be solved (integrated) over a finite step in time. Due to the importance and complexity of this problem, several approximative algorithms have been developed with different accuracy and stability properties. However, these algorithms have not only importance for the accuracy of the numerical integration of the constitutive equations, but they also influence the corresponding algorithmic (or consistent) tangent stiffness matrix used in a truly Newton-Raphson scheme when the global equilibrium iterations are performed.

The canonical method, today, for integrating the constitute laws is the closest point projection method. This method is based on an implicit scheme where the yield criterion is enforced at the end of the time step. In the present work the constitutive equations are reformulated using the assumption of constant strain rate within a time step. The assumption allows the evolution equations that govern the response of the material to be rewritten as a set of ordinary differential equations (ODEs). Several methods for solving ODEs exists in the literature and in this work we will make use of a Runge-Kutta scheme.

Assumption of constant strain rate

The finite element solution procedure provides the displacement field at discrete time steps and the task for the constitutive driver is to update the stresses and internal variables accordingly. In order to formulate the constitutive equations as a set of ODEs some assumption of how the strain vary in the time step must be made. For the situation where small strains applies the simplest and most natural assumption is to take the strain rate to be constant during the integration process, i.e.

$$\dot{\boldsymbol{\epsilon}} = \frac{\Delta \boldsymbol{\epsilon}}{\Delta t} \tag{1}$$

where $\Delta\boldsymbol{\epsilon}$ and Δt are the strain increment and time increment between two states in the time discretization, respectively. Using this assumption it will be shown that the evolution laws for the plastic strain and the internal variables can be written as a set of ODEs, i.e.

$$\dot{\boldsymbol{y}} = \boldsymbol{f}(\boldsymbol{y}, \dot{\boldsymbol{\epsilon}}) \tag{2}$$

The size of the system is mainly determined by the number and rank of the internal variables. For complex constitutive models the size of system becomes significant and in the present approach

we will make use of a set of reduced variables to describe the stress space. This approach has been used by Krieg and Krieg [1] and Ristinmaa and Tryding [2] who was able to obtain a closed form solution for some simple constitutive models. It turns out that for the isotropic hardening elasto-plastic damage model that will be considered a system of only three variables must be integrated. However, it turns out that no closed form solution can be obtained, i.e. a numerical integration scheme must be adopted.

Before an integration of (2) can be performed the integration limits must be identified. Using (1) it turns out that one (possible non-linear) scalar function can be used to determine the integration limits, i.e. the time when the response switches from being elastic to elasto-plastic. Having the integration limits a standard ODE solver will provide the solution. A group of solvers that have proved to be reliable for stress updating are the Runge-Family solvers, cf. Wallin and Ristinmaa [3]. One important feature of the Runge-Kutta solvers is that they provide an estimate of the error. This error control can be used to determine an acceptable step-length.

Consistent linearization

The use of the ATS tensor that follows from a consistent linearization of the algorithmic elasto-plastic laws is crucial for the convergence rate in a Newton-Raphson scheme. In the present algorithm it turns out that the set of internal variables $\boldsymbol{y}$ must be differentiated with respect to the new displacement field, i.e.

$$\boldsymbol{X} = \frac{d\boldsymbol{y}}{d\boldsymbol{\epsilon}} \tag{3}$$

must be obtained. Straight forward differentiation of (2) with respect to the strain results in

$$\dot{\boldsymbol{X}} = \frac{\partial \boldsymbol{f}}{\partial \boldsymbol{y}}\boldsymbol{X} + \frac{\partial \boldsymbol{f}}{\partial \boldsymbol{\epsilon}} \tag{4}$$

It should be noted that (4) constitutes a set of ODEs. In the present approach (2) and (4) are solved simultaneously which significantly reduces the computational cost. In conclusion, the set of ODEs that needs to be solved takes the form

$$\dot{\boldsymbol{Z}} = \frac{d}{dt}\begin{bmatrix} \boldsymbol{y} \\ \boldsymbol{X} \end{bmatrix} = \boldsymbol{F}(\boldsymbol{Z}, \dot{\boldsymbol{\epsilon}}) \tag{5}$$

From the updated solution $\boldsymbol{Z}$ it follows that all internal variables as well as the algorithmic tangent stiffness tensor can be calculated.

References

[1] R.D. Krieg and D.B. Krieg. Accuracies of numerical solution methods for elastic-perfectly plastic model. *J. Pressure Vessel Tech*, 99:510–515, 1977.

[2] M. Ristinmaa and J. Tryding. Exact integration of constitutive equations in elasto-plasticity. *Int. J. Numer. Methods. Eng.*, 36:2525–2544, 1993.

[3] M. Wallin and M. Ristinmaa. Accurate stress updating based on constant strain rate assumption *Comp. Methods Appl. Mech, Engrg.*, 190:5583-5601, 2001.

A SPATIAL FORMULATION OF ANISOTROPIC MATERIAL AT LARGE STRAINS WITH APPLICATION TO CUBIC MATERIAL SYMMETRY

Magnus Harrysson*, Anders Harrysson and Matti Ristinmaa
Department of Solid Mechanics
Lund University, Lund, Sweden
e–mail: magnus.harrysson@solid.lth.se

Summary An anisotropic large strain elasto-plastic material model based on a spatial formulation is presented. The anisotropic properties of the material are modeled by structural variables. The evolution of the anisotropy is accounted for by introducing a linear map similar to the deformation gradient, but operating on the substructure instead of the continuum. The performance of the model is investigated for cup drawing of a material with cubic symmetry.

Introduction

The modeling of anisotropic material is often made by introducing additional variables accounting for the directional dependent properties for the material, e.g. [1]. As the material is deformed by external load one would expect that these directional dependent properties would be affected and evolve in some way. When modeling large strains the usual approach is to decompose the deformation gradient into an elastic and a plastic part and by doing so one automatically introduce an intermediate configuration. The orientation of this configuration has to be dealt with by care, especially for anisotropic materials. This was discussed by e.g. [2]. Here the evolution of the substructure was accounted for by a skew symmetric tensor called the plastic spin, describing the spinning of the substructure in reference to the continuum. However, when adopting a spatial formulation it can be shown that no specific choice of the intermediate configuration has to be made. Furthermore, based on [3], the evolution for the substructure is in the presented work described by second order tensors, i.e. a more general format. The development of evolution laws for the continuum and for the directional variables is made in a thermodynamically consistent way. By investigating the dissipation inequality the definitions of the stress, here the Kirchhoff stress, and for the stress driving the evolution of the directional variables can be obtained.

Procedures and results

The modeling of elasto-plastic material at large strains is here accounted for by a multiplicative decomposition of the deformation gradient, $\boldsymbol{F} = \boldsymbol{F}^e\boldsymbol{F}^p$, into an elastic, $\boldsymbol{F}^e$, and a plastic part, $\boldsymbol{F}^p$. To model the anisotropic material behavior unit directional vectors, $\boldsymbol{V}^{(\alpha)}$, are introduced in the reference configuration. These director vectors represent in a phenomenological way the substructure of the material which is assumed to hold the directional dependent properties of the material. As the material is deformed the director vectors are affected and a new set of director vectors in the current configuration is obtained as $\boldsymbol{v}^{(\alpha)} = \boldsymbol{\Delta}^{(\alpha)}\boldsymbol{V}^{(\alpha)}$. $\boldsymbol{\Delta}^{(\alpha)}$ represent linear maps, here called substructural deformation gradients, which operates on respective director vector. It is emphasized that this is a general second order tensor. In a similar fashion as for the deformation gradient these maps are decomposed, $\boldsymbol{\Delta}^{(\alpha)} = \boldsymbol{\alpha}^{(\alpha)}\boldsymbol{\beta}^{(\alpha)}$, into one part associated to the elastic deformation, $\boldsymbol{\alpha}^{(\alpha)}$, and one part associated to the plastic deformation, $\boldsymbol{\beta}^{(\alpha)}$. The kinematics for the continuum and the substructure are summarized in Fig.1 From the multiplicative decomposition of

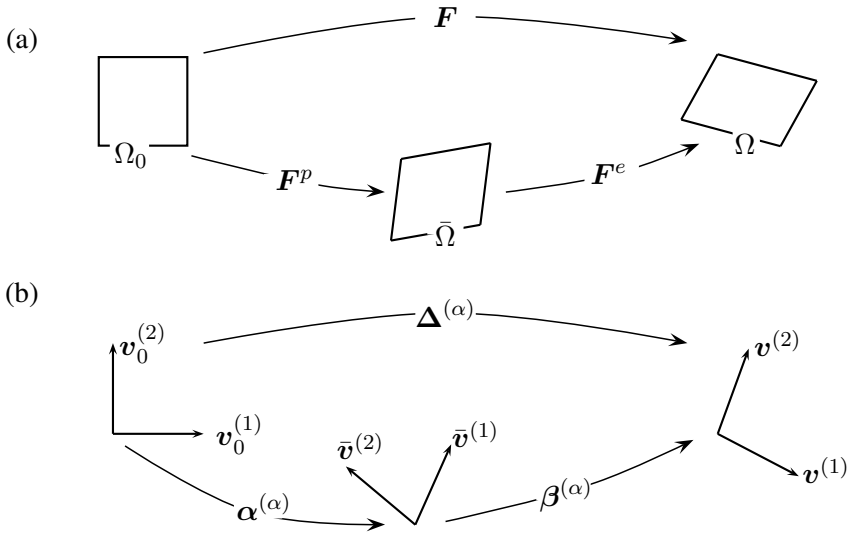

Figure 1: Deformation of the (a) continuum and (b) the substructure.

the deformation gradient and of the substructural deformation gradient one obtains the following relations

$$\begin{aligned} \mathcal{L}_v(\boldsymbol{b}^e) &= -2\text{sym}(\boldsymbol{L}^p\boldsymbol{b}^e) \\ \mathcal{L}_v(\boldsymbol{v}^{(\alpha)}) &= -(\boldsymbol{L}^p - \boldsymbol{\lambda}^{(\alpha)})\boldsymbol{v}^{(\alpha)} \end{aligned} \tag{1}$$

where $\mathcal{L}_v(\boldsymbol{b}^e)$ and $\mathcal{L}_v(\boldsymbol{v}^{(\alpha)})$ denotes the Lie-derivative of the elastic Finger's tensor, $\boldsymbol{b}^e = \boldsymbol{F}^e\boldsymbol{F}^{eT}$, and the Lie-derivative of the spatial director vectors, respectively. $\boldsymbol{L}^p$ represent the spatial plastic velocity gradient for the continuum and $\boldsymbol{\lambda}^{(\alpha)}$ the equivalent quantity for the substructure.

To derive specific evolution laws associative plasticity was assumed where the yield function acts as convex plastic potential function. For the evolution of the substructure the following specific form was adopted

$$\boldsymbol{\lambda}^{(\alpha)} = -\lambda\frac{\eta}{2}\left(\boldsymbol{b}^e\boldsymbol{\tau}\boldsymbol{b}^{e-1} - \boldsymbol{\tau}\right) \tag{2}$$

here λ is the non-negative plastic multilayer, η a material parameter and $\boldsymbol{\tau}$ is the Kirchhoff stress tensor. The result of this specific evolution law will be that the plastic deformation rotates the director vectors in the intermediate configuration to a different orthogonal triad and the unit length will be preserved.

For an anisotropic material the standard exponential integration scheme is not convenient to use, this due to the non-coaxiallity of the stresses and their conjugated flow directions. Here a fairly simple integration routine is used where an extra constrain is introduced to assure plastic incompressibility.

To test the model simulation of a cup drawing process was performed. A typical result from the simulations is viewed in Fig.2. From Fig.2 it is shown that the characteristic "earing" shape of the cup has been successfully simulated.

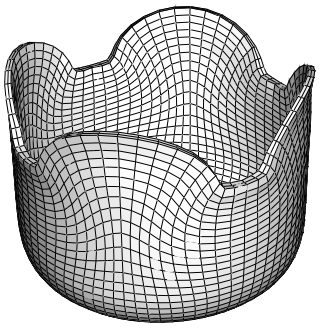

Figure 2: Result from simulation of the cup drawing process.

References

[1] J. Boehler *Applications of tensor functions in solid mechanics*. International Center for Mechanical Sciences, no 292, Udine, Springer Verlag.

[2] Y. Dafalias The plastic spin. *Journal of Applied Mechanics*, **73**, 865–871, (1986).

[3] M. Harrysson, A. Harrysson and M. Ristinmaa Description of evolving anisotropy at large strains. *Mechanics of Materials*, In Press.

Computational Aspects on Multiscale Modeling of Polycrystallines with Gradient Crystal Plasticity

Magnus Ekh*, **Mikkel Grymer and Kenneth Runesson**
Department of Applied Mechanics
Chalmers University of Technology, Gothenburg, Sweden
e–mail: magnus.ekh@chalmers.se

Summary This contribution deals with numerical aspects concerning multiscale modeling of polycrystalline metals. Each grain in the microstructure is modeled by crystal plasticity with gradient hardening in order to capture size-effects in the modeling.

Introduction

This contribution deals with the simulation of the behavior of a grain structure of a polycrystalline metal. If such a grain structure is sufficiently large it can be regarded as a representative volume element (RVE), which plays a key role in multiscale modeling of materials. The behavior of such a grain structure depends on, e.g., grain geometry, volume fraction of different phases, and grain size. A way of including the grain size dependence in the modeling of the grain structure will be presented. Alternative formulations can be found in, e.g., [1], [2].

Within the framework of continuum thermodynamics and finite strains, we formulate a model for crystal (visco)plasticity, crystal and gradient hardening. The gradient hardening gives a contribution for each slip system which is added to the well established local hardening.

In order to solve the arising coupled field equations (for the displacements and the hardening of the slip systems) the dual mixed FE algorithm proposed in [3] is applied. The contribution presents numerical study how model parameters (such as grain size) will influence the homogenized macroscopic stress-strain response of a 2D model of a polycrystal.

Finally, an algorithm that parallelize the total FE problem into an FE problem for each grain is presented.

Crystal plasticity model

In order to include a gradient dependence of the hardening variable k_α associated with the slip direction $\bar{\boldsymbol{s}}_\alpha$, we propose the following free energy (per unit undeformed volume):

$$\Psi(\bar{\boldsymbol{C}}, k_\alpha, \bar{\boldsymbol{s}}_\alpha \cdot \nabla k_\alpha) = \Psi_{\mathrm{e}}(\bar{\boldsymbol{C}}) + \sum_\alpha \left[\frac{1}{2} H_{\mathrm{l}} k_\alpha^2 + \frac{1}{2} H_{\mathrm{g}}\, l_\alpha^2 \left[\bar{\boldsymbol{s}}_\alpha \cdot \nabla k_\alpha \right]^2 \right] \tag{1}$$

where $\bar{\boldsymbol{C}}$ is the elastic Cauchy-Green tensor.

The plastic part of the free energy can now be used to define (by following the arguments put forward by [4] the local hardening stress $\kappa_{\alpha,\mathrm{l}}$ and the gradient hardening stress $\kappa_{\alpha,\mathrm{g}}$:

$$\kappa_{\alpha,\mathrm{l}} = -\frac{\partial \Psi}{\partial k_\alpha} = -H_{\mathrm{l}}\, k_\alpha \tag{2}$$

$$\kappa_{\alpha,\mathrm{g}} = \nabla \cdot \frac{\partial \Psi}{\partial \nabla k_\alpha} = H_{\mathrm{g}}\, l_\alpha^2\, \frac{\partial^2 k_\alpha}{\partial \bar{s}_\alpha^2} \tag{3}$$

Hence, the total hardening κ_α in each slip system consists of a local and a gradient part:

$$\kappa_\alpha = \kappa_{\alpha,\mathrm{l}} + \kappa_{\alpha,\mathrm{g}} = -H_\mathrm{l}\, k_\alpha + H_\mathrm{g}\, l_\alpha^2\, \frac{\partial^2 k_\alpha}{\partial \bar{s}_\alpha^2} \tag{4}$$

In summary, we assume the following evolution equations (of the associative type):

$$\bar{\boldsymbol{l}}_\mathrm{p} = \dot{\boldsymbol{F}}_\mathrm{p} \cdot \boldsymbol{f}_\mathrm{p} = \sum_\alpha \dot{\lambda}_\alpha \frac{\partial \Phi_\alpha}{\partial \bar{\boldsymbol{M}}^t} = \sum_\alpha \dot{\lambda}_\alpha \left[\bar{\boldsymbol{s}}_\alpha \otimes \bar{\boldsymbol{m}}_\alpha\right] \tag{5}$$

$$\dot{k}_\alpha = \dot{\lambda}_\alpha \frac{\partial \Phi}{\partial \kappa_\alpha} = -\dot{\lambda}_\alpha \tag{6}$$

where, in a viscoplastic format, $\dot{\lambda}_\alpha$ can be expressed as

$$\dot{\lambda}_\alpha = \frac{1}{t_*} \left[\frac{\langle \Phi_\alpha \rangle}{C_0}\right]^m$$

A rate-independent solution is obtained if $t_* \to 0$. In the above expression the yield function Φ_α is defined as:

$$\Phi_\alpha = \bar{\boldsymbol{M}}^t : \left[\bar{\boldsymbol{s}}_\alpha \otimes \bar{\boldsymbol{m}}_\alpha\right] - \kappa_\alpha - \sigma_{\mathrm{y},\alpha} \tag{7}$$

where $\bar{\boldsymbol{M}}^t$ is the elastic Mandel stress.

Numerical examples

Henceforth, we consider a square Representative Volume Element (RVE). For simplicity, we assume plane strain for the RVE. All the grains have four slip systems, with directions randomly chosen for all grains. Dirichlet boundary conditions on the boundary $\bar{\Gamma}$ of the RVE are chosen that correspond to a prescribed macro–scale deformation gradient $\bar{\boldsymbol{F}} = \boldsymbol{I} + \bar{\boldsymbol{H}}$. Hence, the boundary conditions are

$$\boldsymbol{u}(\boldsymbol{X}) = \bar{\boldsymbol{H}} \cdot \boldsymbol{X}, \quad \boldsymbol{X} \in \bar{\Gamma} \tag{8}$$

We have assumed the boundary condition $\dot{k}_\alpha = 0$ ($\Rightarrow k_\alpha = 0$) at grain boundaries. Furthermore, the results shown below are for the case of rate-independence (i.e., $t_* \to 0$). The macroscopic shear stress $\bar{P}_{12}$ vs the macroscopic shear strain $\bar{\gamma}$ is shown in Fig. 2 for three values of the square RVE's side–length L.

Fig. 1 shows the size effect due to gradient hardening for fixed material parameters but for increasing grain size. The plot shows a representation of the plastic strain field, in terms of effective hardening strain $k_\mathrm{eff} = \sqrt{k_1^2 + k_2^2 + k_3^2 + k_4^2}$. Since the (absolute) size of the boundary layers with large gradient effects should be approximately the same regardless of the actual size of the grains, the boundary layers will appear thinner when the grain size increases (which is clearly demonstrated in Figure 2).

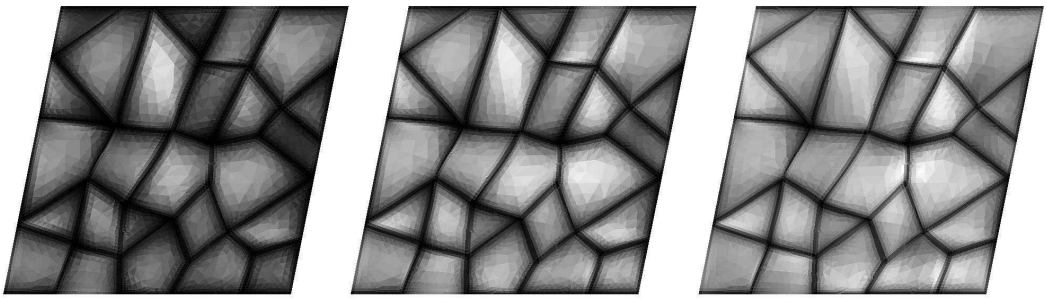

Figure 1: Effective hardening strain k_{eff}. Unconstrained displacement field. Comparison for RVE side lengths 4,8,16 μm (from left to right). The same color scale is used in all plots.

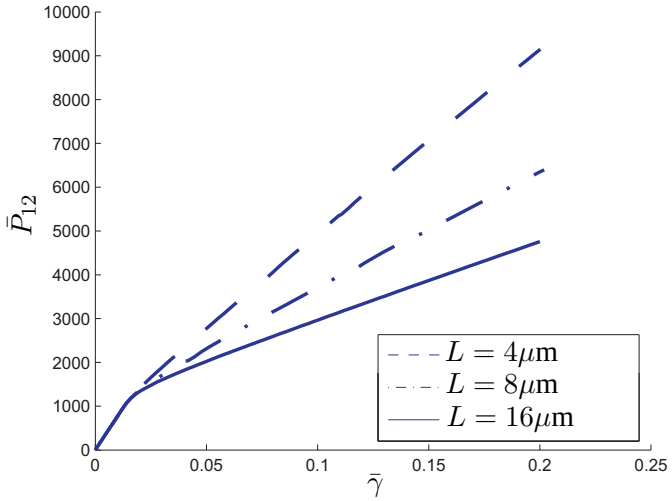

Figure 2: Macroscopic stress–strain response ($\bar{P}_{12}$ vs. $\bar{\gamma}$) showing the size dependence on the amount of hardening.

References

[1] L.P. Evers, D.M. Parks, W.A.M. Brekelmans and M.G.D. Geers. Crystal plasticity model with enhanced hardening by geometrically necessary dislocation accumulation. *Journal of the Mechanics and Physics of Solids*, **50**(11), 2403–2424, 2002.

[2] M.E. Gurtin. Crystal plasticity model with enhanced hardening by geometrically necessary dislocation accumulation. *Journal of the Mechanics and Physics of Solids*, **50**(1), 5–32, 2002.

[3] T. Svedberg and K. Runesson Algorithm for gradient-regularized plasticity coupled to damage based on a dual mixed FE-formulation. *Computer Methods in Applied Mechanics and Engineering*, **161**(1-2), 49–65, 1998.

[4] T. Svedberg and K. Runesson Thermodynamic consistent theory of gradient-regularized plasticity coupled to damage. *International Journal of Plasticity*, **13**(6-7), 669–696, 1997.

On the Implementation of Plane Stress in Computational Multiscale Modeling

Robert Lillbacka[*1,2], **Kenneth Runesson**[1] and **Fredrik Larsson**[1]

1, Department of Applied Mechanics
Chalmer University of Technology, Göteborg, Sweden
e–mail: kenneth.runesson@chalmers.se
2, Swedish National Testing and Research Institute (SP)

Summary Different aspects of the plane stress condition in concurrent two-scale computational (first order) homogenization are discussed. The basic ingredient in computational homogenization is the calculation of the macroscale stress, for given macroscale deformation, via RVE-computations. Two modeling assumptions are compared: The subscale (Hill type) and macroscale type (Taylor type) plane stress conditions. The corresponding iterative strategies and the macroscale algorithmic tangent operators are derived using the primal (conventional) approach. The performance of the various iterative strategies are compared for a single RVE-problem as well as in a fully concurrent analysis of a complex substructure (duplex stainless steel) under realistic subscale modeling based on crystal plasticity with hardening.

Introduction

A general approach to account for the effect of the material substructure in constitutive modeling is to carry out (analytical or) computational homogenization on a Representative Volume Element (RVE) as the key ingredient of Computational Multiscale Modeling (CMM). This presumes complete scale separation such that the subscale solutions interact only via their homogenized results on the macroscale, typically via equilibrium of macroscale stresses. To obtain representative results, the size of the RVE must be sufficiently larger than the characteristic length of the subscale structure, e.g. the particle spacing in a particle-reinforced composite, cf. Zohdi and Wriggers [3].

Fully 3D concurrent multiscale computations for materials with complex substructure are still prohibitidly expensive, which motivates resorting to 2D modeling when possible. Thereby, the plane stress assumption is a classical condition; however, it is possible to impose this conditions in two different ways in the context of homogenization: (i) *Subscale plane stress* means that the plane stress condition is imposed on the subscale everywhere within the RVE (while the corresponding subscale out-of-plane strain componenets are unknowns to be computed), (ii) *Macroscale plane stress* means that the plane stress condition is imposed as the constraint of vanishing macroscale stress (while assuming a Taylor assumption on the corresponding out-of-plane strain components, such that these macroscale components will be computed).

A particular issue is the efficient computation of the macroscale algorithmic tangent stiffness tensor based on the availability of the corresponding subscale tangent (which is obtained upon the appropriate linearization of the time-integrated evolution equations for internal variables pertinent to the subscale constituents).

The presentation is outlined as follows: First, the variational settings for the continuous format of the subscale and macroscale plane stress RVE-problems are established. The FE-formulations and pertinent iterative algorithms are then given, and the pertinent macro-scale algorithmic tangent stiffness (ATS) tensor is computed (using the primal approach). The model problem for the algorithmic evaluation is presented including a short summary of the crystal plasticity model that is used in order to have a realistic subscale modeling of the Duplex Stainless Steel (DSS) material, cf. Ekh et al. [2]. Computational results are given that illustrate the influence of the different

model assumptions as well as the performance of the various iteration strategies both for single RVE computations and for full-fledged concurrent sub-macroscale computation.

Computational results

For all calculations, a cold worked austenitic-ferritic duplex stainless steel (DSS) with a phase fraction of 50% for both phases is considered. The cold working generates the characteristic elongated phase structure that can be seen in Fig. 1. The underlying phase/grain structure is identified in the RVE, which is attached to every Gauss point in the macro-scale grid, cf. Fig. 1. The RVE is generated using a Voronoi polygonization algorithm, cf. Cannmo et al. [1], and it is composed of 64 grains that are discretized using CST elements.

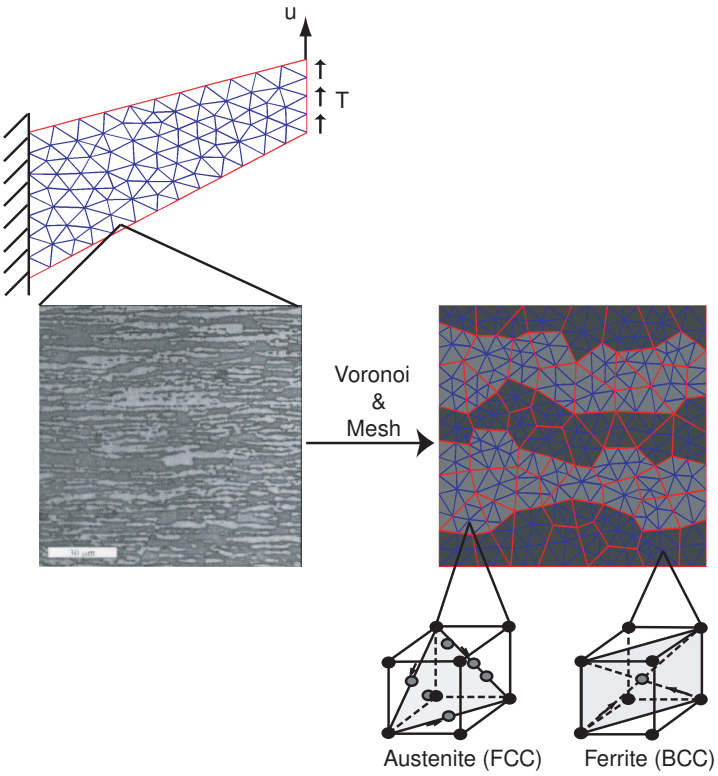

Figure 1: Grain/phase structure of DSS, the 2D RVE and unit cells.

We shall consider the macroscale response of a single RVE for the different plane stress conditions and iteration techniques. The macroscale in-plane deformation mode is simple shear, which is applied to the RVE as a prescribed macro-scale displacement gradient, i.e., $\bar{\boldsymbol{H}}_{\mathrm{I}} = \gamma\, \boldsymbol{e_1} \otimes \boldsymbol{e_2}$. As the macroscale output we compute the Cauchy shear stress $\bar{\sigma}_{12}$.

From the results in Fig. 2 it can be seen that the macroscale plane stress condition gives rise to a stiffer response than does the subscale plane stress condition. This fact can be rationalized by recalling that the macroscale plane stress assumption introduces a state of generalized plane deformation with respect to the out-of-plane direction. Hence, a Taylor type of condition is introduced for the deformations in the out-of-plane direction. Obviously, this condition imposes a kinematic constraint as compared to the subscale plane stress condition, which means that the response will be stiffer (in accordance with numerical observations).

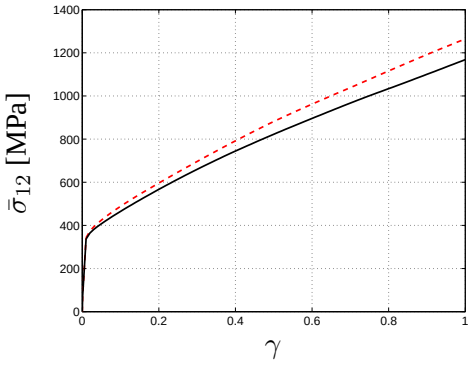

Figure 2: Macroscale Cauchy shear stress vs shear strain. The dashed line corresponds to the macroscale plane stress condition, whereas the solid line corresponds to the subscale plane stress condition.

In order to investigate the difference in the stress and strain distributions on the sub-scale for the two plane stress conditions, the (effective) von Mises stress is shown in Fig. 3. It can be seen that, by-en-large, the macroscale plane stress condition gives a somewhat larger effective stress than the subscale plane stress condition.

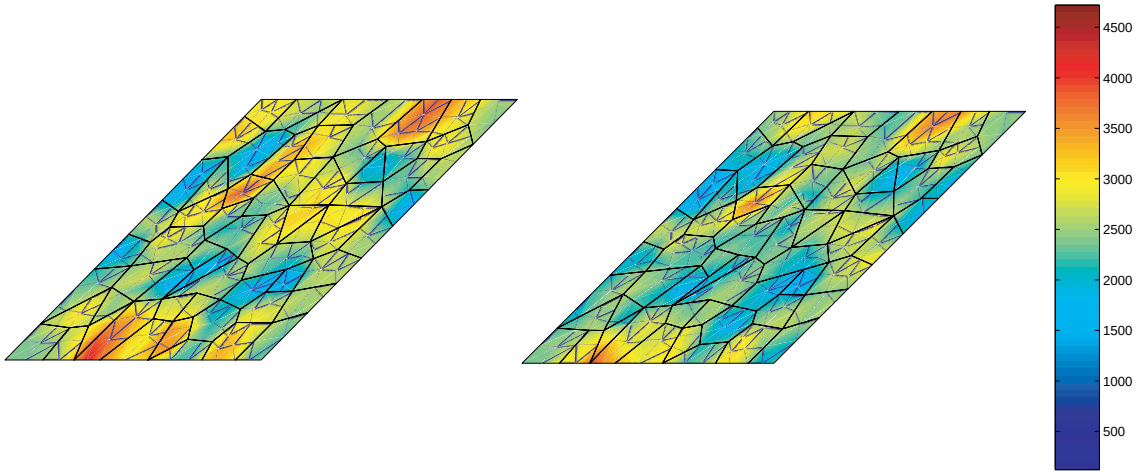

Figure 3: Subscale von Mises effective stress and displacements for γ = 1.0: Macroscale plane stress condition (left) and subscale plane stress condition (right)

Another illustration of the difference between the macro- and subscale plane stress conditions is given in Fig. 4, which shows the distribution of the out-of-plane Cauchy stress, σ_{33}. In particular, for the subscale plane stress condition the Cauchy stress is equal to zero in the whole RVE. However, for the macroscale plane stress condition the stresses vary between large tensile and compressive values, although the volume average is always equal to zero (as imposed).

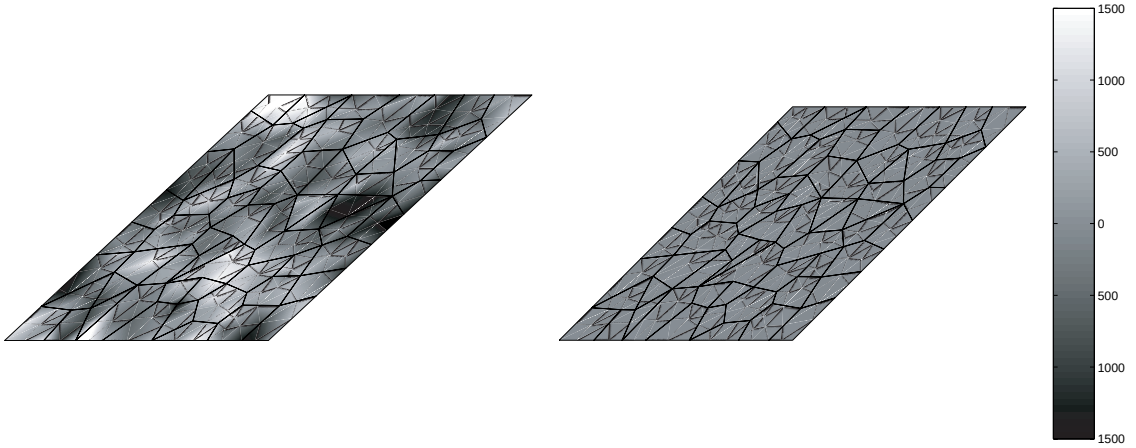

Figure 4: Subscale out-of-plane Cauchy stress σ_{33} for γ = 1.0: Macro-scale plane stress condition (left) and sub-scale plane stress condition (right)

References

[1] Cannmo, P., Runesson, K. and Ristinmaa, M. Modeling of plasticity and damage in a polycrystalline microstructure. *International Journal of Plasticity*, **11**:949–970, 1995.

[2] Ekh, M., Lillbacka, R. and Runesson, K. A model framework for anisotropic damage coupled to crystal (visco)plasticity. *International Journal of Plasticity*, **20**:2143–2159, 2004.

[3] Zohdi, T. I. and Wriggers, P. *Introduction to Computational Micromechanics*. Springer, 2005.

An experimental method to determine compliance curves close to the crack tip and comparison with PD-signal for fatigue cracks exposed to overloads

L. Jacobsson[1], C. Persson[1] and S. Melin[2]

[1] Division of Materials Engineering, [2] Division of Mechanics, Lund University

ABSTRACT. *Fatigue crack propagation rates are affected by the characteristics close to the crack tip. A method is developed to measure the displacements along the crack, close to the crack tip, using high resolution scanning electron microscope images. Images are taken throughout the load cycles to observe the displacements of a crack exposed to one single overload. The potential drop technique is used to measure the electrical contact between the crack surfaces.*
For experiments with R=0.03 and ⊿K in the mid Paris region and higher, a remaining displacement is detected and both the crack opening and closure loads are decreased after the overload. This leads to an increasing effective stress intensity factor range which results in an initially higher crack propagation rate following the overload.

INTRODUCTION

From the work by Elber [1] in the seventies it is well known that the crack closure level has a pronounced influence on the crack propagation rate. The assumption is that the stresses in the crack tip vicinity become positive at the stress level where the crack opens. From this load, measured globally, and maximum load, an effective stress intensity factor range can be calculated. With this entity, the dependence on stress ratio R can be eliminated, so that the crack propagation rates are the same at same effective stress intensity factor range.
When a fatigue crack is exposed to an overload, the crack opening level is changed and the plastic zone size is increased, and this will influence the crack propagation rate da/dN [2], [3], with a the crack length and N the number of cycles. Under small scale yielding conditions the changes in da/dN are related to variations, through the load cycles, in the crack shape close to the crack tip, and the shape may be affected due to residual stresses, crack surface roughness or other features.
To measure the opening and closure stresses levels, different techniques can be used. The compliance method provides the global load versus displacement, measured e.g. at a point far from the crack, at the crack mouth, or along the crack path. For this, different types of extensometers, or clip gages [4] are used, or microscope observations [5] made.
Another method to measure the crack closure and the crack propagation rate is the potential drop technique [6], [7]. This method measures the electrical potential drop over the crack mouth when a direct current passes through the test specimen.
The aim of this study is to investigate the characteristics of the crack tip displacements continuously during the load cycles for the case of a fatigue crack, exposed to one single overload. An in-situ scanning electron microscope (SEM) technique is used to take high

resolution images of the crack tip region, and the images are analyzed with an image analyzing computer program.

EXPERIMENTAL PROCEDURE

In-situ SEM crack propagation experiments were performed on Inconel 718. The experiments were run with load cycles with constant applied minimum and maximum loads, resulting in increasing stress intensity factor with increasing crack length. The crack was grown some distance away from the initial notch where after one single overload cycle was applied. The overload cycle, the cycle before it and the one after were observed. Compliance curves were measured at a small distance behind the crack tip from high resolution SEM images taken during the load cycles.

RESULTS AND DISCUSSION

Compliance curves were produced from displacements close to the crack tip to include effects from the plastic zone. This effect was obvious in the mid and high Paris regions, with stress intensity factor ranges between 40 and 70 MPa√m and including one single overload cycle. During the overload the plastic zone increased, resulting in a remaining deformation of the crack faces, that separates them up to a distance of 10 μm from the crack tip at zero load. This is seen from the compliance curves in fig. 1 for the overload cycle, the cycle before, and the one after the overload. Figure 1 applies to ΔK=65MPa√m, R=0.03, and K_{ol}=82 MPa√m, with K_{ol} denoting the overload stress intensity factor.

The compliance curve after the overload, □ in fig. 1, shows that the opening and closure stresses have lower values as compared to prior to the overload, which gives less crack closure. This results in a higher effective stress intensity factor range, which increases the forces on the material at the crack tip, leading to increasing crack propagation rate directly after the overload.

Observations of the shape of the crack close to the tip during the overload cycle show that at moderate load levels, the crack tip is sharp even during the overload. When the load level is increased, the crack tip starts to blunt due to the large plastic deformations of the grains at the crack tip. These grains are damaged from plastic slip, which results in a crack tip region with numerous sharp micro cracks. The following crack extension starts from one of these micro cracks, and a sharp crack tip is formed through coalescence with the blunted crack tip formed during the overload. There are no remaining displacements in the crack vicinity for the some hundred cycles following the overload.

For every cycle following the overload cycle the opening and closure loads from the compliance curve increase due to increasing length of the sharp crack propagating away from the blunted area. The shape of the compliance curve after the overload gradually approach a shape similar to the one before the overload, but at a higher PD-signal level, i.e. the potential drop is increased due to the increase in crack length.

One characteristic of the potential drop curves is a pronounced knee at high stress intensity factor levels and this provides the level of crack opening and closure loads where the crack surfaces have no electrical contact, cf. fig. 2. This load level is higher

than the opening and closure loads measured from the compliance curves. For loads close to the threshold value there is no knee in the PD curve because the crack tip is sharp and there is still electrical contact between the crack surfaces at maximum load. This is in contrast to cracks in the mid and high Paris regions, where the crack opening displacement is larger, and the crack surfaces are electrically separated at maximum load.

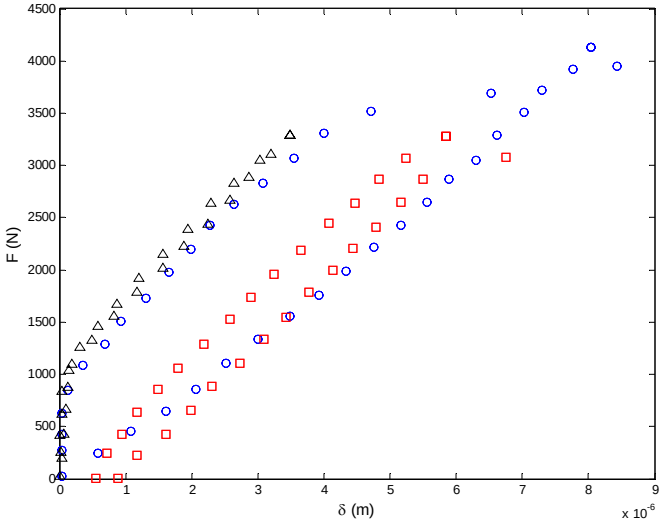

Figure 1. Compliance curves for the cycles before (Δ), during (o) and after (□) the overload cycle. ΔK=65MPa√m, R=0.03, K_{ol}=82 MPa√m. For δ, cf. fig. 1.

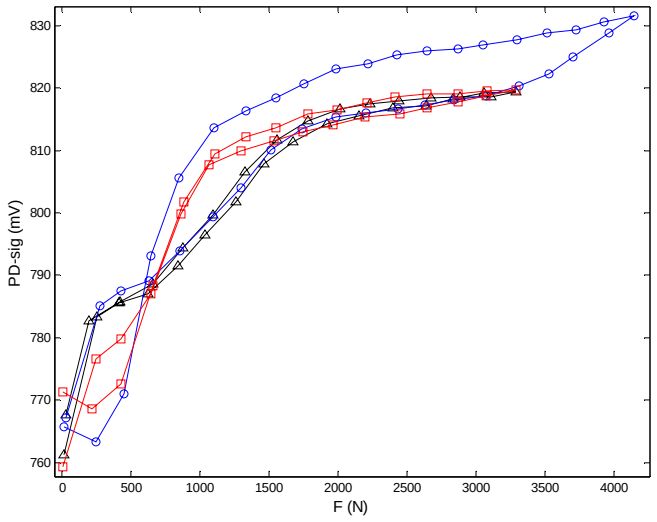

Figure 2. Potential drop signal versus applied load. The curves refer to before (Δ), during (o) and after (□) the overload cycle. ΔK=65MPa√m, R=0.03, K_{ol}=82MPa√m.

CONCLUSIONS

To investigate the mechanisms affecting the crack propagation rate an image analyzing technique was developed to measure the displacements close to the crack tip. Compliance curves were obtained from the measured displacements, and crack opening and closure loads determined for different load sequences.

It was found that the shape of a compliance curve is affected by the plastic zone close to the crack tip, even at small scale yielding.

At potential drop measurements knees during loading as well as during unloading give distinct levels of crack opening and closure. For the mid Paris region, the crack tip was found to be sharp and electrical contact between the crack surfaces, even at maximum load, was observed.

The compliance curves show lower values of crack opening and closure levels than the potential drop measurements. This is because the compliance curve is based on the plasticity influenced displacements close to the crack tip whereas the potential drop technique is based on the electrical contact between the crack surfaces along the full crack length.

ACKNEWLEDGEMENT

To the Swedish Gas Turbine Centre for financial support and to Mr. Z. Zivcovic for valuable assistance during the development of the experimental equipment.

REFERENCES

1. Elber, W., *Eng. Fract. Mech*., 2, 37-45, 1970

2. Shimojo, M., Chujo, M., Higo, Y., Nunomura, S., *Int. J. Fatigue*, vol. 20, no. 5, 365-371,1998

3. Halliday, M.D., Zhang, J.Z., Poole, P., Bowen, P., *Int. J. Fatigue*, vol. 19, no. 4, 273-282, 1997

4. ASTM, E 399-83, Philadelphia, 1983.

5. Halliday, M.D., Poole, P., Bowen, P., *Fatigue and Fracture of Engineering Materials and Structures*, vol. 18, 717-729, 1995

6. Andersson, M., Persson, C., Melin, S., *ICF 9*, 2003

7. Evans, W.J., Spence, S.H., *Int. J. Fatigue*, vol. 19, no. 1, 205-210, 1997

Fracture of Zr-alloy pressure tubes due to hydride blister formation

R. N. Singh[1,2] , P. Ståhle[1,3] and Leslie Banks-Sills[3]

[1] Materials Science, Technology & Society, Malmö Hogskola, Malmö, SE20506Sweden
[2] Materials Science Division, Bhabha Atomic Research Centre, Mumbai-4000085, India.
[3] Department of Mechanical Engineering, TH, Lund University, SE22100 LUND, Sweden
Email: Ram.Singh@ts.mah.se Tel. +46-40-6657704 FAX: +46-40-6657135

1. Introduction

Hydrogen migration under thermal stress gradient in zirconium alloys results in formation of hydride blisters [1]. An array of blisters makes Zirconium alloy components of nuclear reactors susceptible to fracture [2]. The whole process of hydride blister formation and fracture of these components is very complex and involves hydrogen migration under thermal gradient, hydride precipitation, straining of the matrix, setting up of hydrostatic stress gradient, enhanced hydrogen migration under the combined influence of thermal and stress gradient, stress-reorientation of hydrides [3], cracking of hydrides, crack growth by delayed hydride cracking mechanism [4], interlinking of blisters and spontaneous fracture of the component.

In this work we estimate the stress components in hydride blisters and the surrounding matrix for certain assumed blister depths. The estimated stress predicts the hydride orientation in the matrix surrounding the blisters and will be subsequently used to model the hydrogen diffusion under hydrostatic stress and temperature gradients.

2. Computation

The matrix of dimension in the ratio 1:5 was considered. The matrix material was Zr having hexagonal crystal structure with orthotropic elastic constants [5] and zirconium hydride has faced centered cubic with isotropic elastic constants [6]. Computations were made for axisymmetric case with symmetry axis along direction 2 (Fig. 1) and with hydride/matrix yield strength ratio of 0.2 [7] and 1.0. Transformation of zirconium hydrogen solid solution into hydride is associated with about 17 percent positive change in volume [8]. The body was partitioned into several small layers with each layer transformed sequentially (Fig. 1). Phase transformation was achieved by imposing small temperature rise and using thermal expansion command [9].

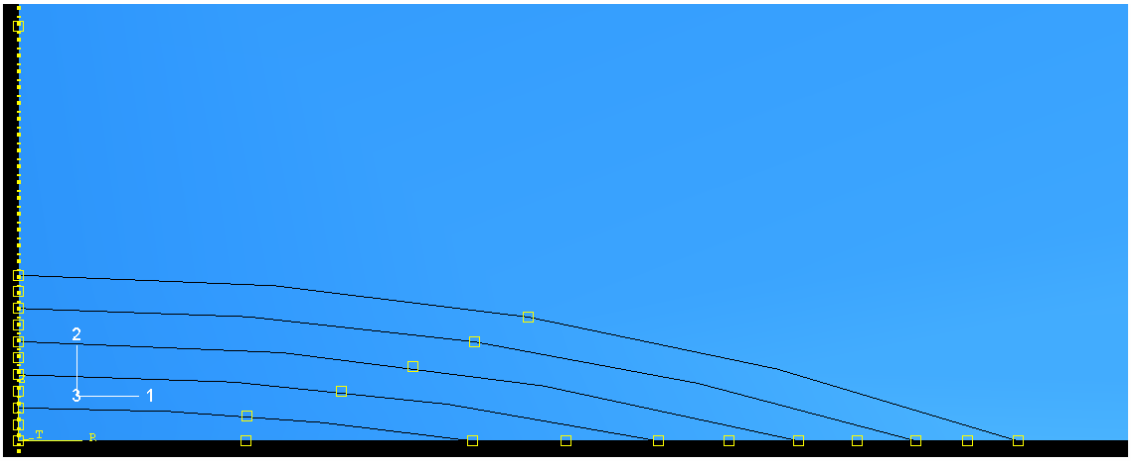

Fig. 1 Part of the body used for computation. Blister aspect ratio of 5 was considered.

3. Results & Discussion

Fig. 2 shows the contour plot of equivalent stress in the blister and matrix around it for the hydride/matrix yield strength ratio of 0.2 [7]. Phase transformation was achieved by raising the temperature. As is evident from this figure most of the regions inside blister and matrix are under negligible stress with a small strip at the boundary between blister and hydride under very high stresses. Since the hydride is having much lower yield strength as compared to matrix, most of the volume change is accommodated inside the blister by hydride plastic flow.

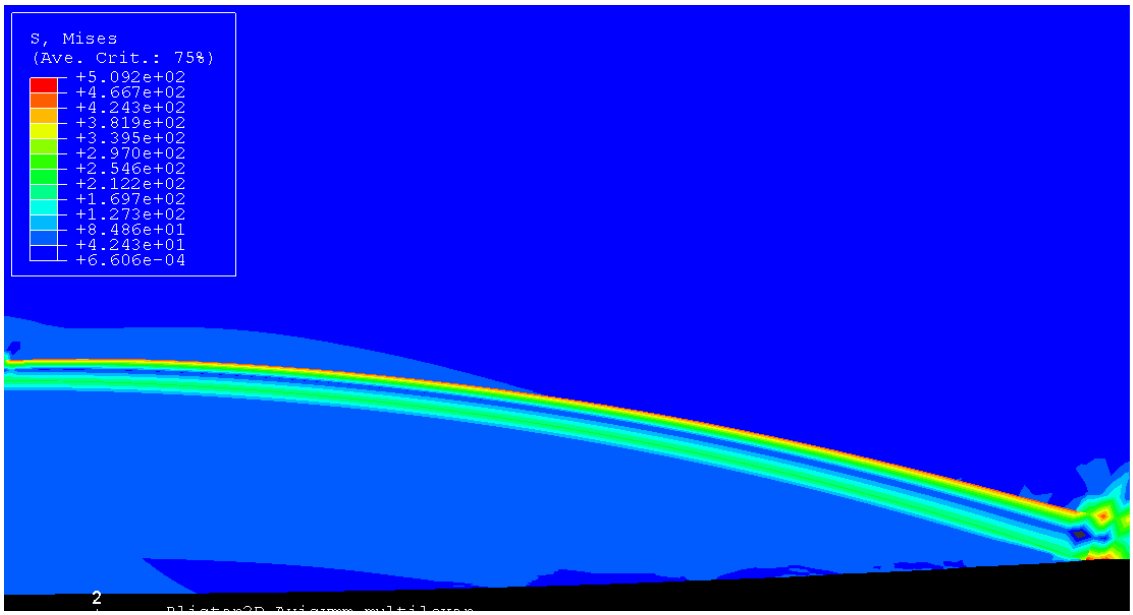

Fig. 2 Contour plot of equivalent stress in the soft blister and matrix around it. Phase transformation achieved in multiple steps.

Fig.3 shows the contour plot of the equivalent stress inside blister and matrix around it with both hydride and matrix having identical yield strength. Phase transformation was achieved by raising the temperature. The maximum value of equivalent stress was observed at the interface between blister and matrix. The stress decays as one move away from the blister matrix interface. All earlier investigations [9-10] on hydride blisters have achieved the phase transformation by raising temperature and allowing the phase transformation of the whole region transforming to hydride in one step. For comparison the contour plot of equivalent stress inside blister and in the matrix around it are shown in Fig. 4. As is evident equivalent stresses in the blister and matrix are higher for single step transformation than that for multistep transformation. Since hydride blister grow sequentially single step phase transformation results in overestimation of stress. For single step transformation elastic, plastic dissipation and total energy are 91, 1369 is 1460 MJ for the whole body (Fig. 1) as compared to 50.9, 1442.6 and 1493.5 MJ, respectively, for multiple step expansion.

Fig.5(a) shows the a section of hydride blister [11]. It is evident from this figure that a section of hydride blister has three regions. Far away from the center of blister lies region I, comprising of matrix and circumferential hydrides (horizontal dark lines). As one approaches the center of blister, region II comprising of matrix, circumferential hydrides and radial hydrides (normal to circumferential ones) can be seen. Region III is the region of single-phase hydride. The texture and microstructure of cold worked and stress relieved Zr-alloy tubes is such that under unstressed condition of hydride precipitation circumferential hydrides form. When hydride precipitation takes place under stress greater than a threshold value, radial hydride may form.

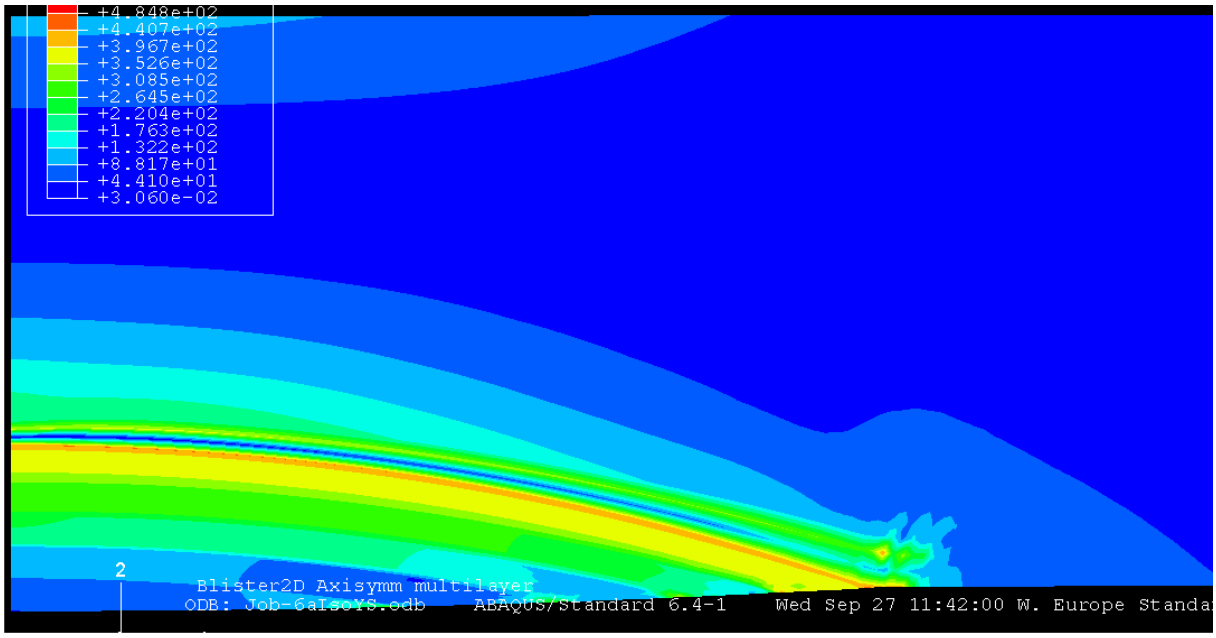

Fig. 3 Contour plot of equivalent stress in the blister and matrix around it for hydride/matrix Yield stress ratio of unity. Phase transformation achieved in multiple steps.

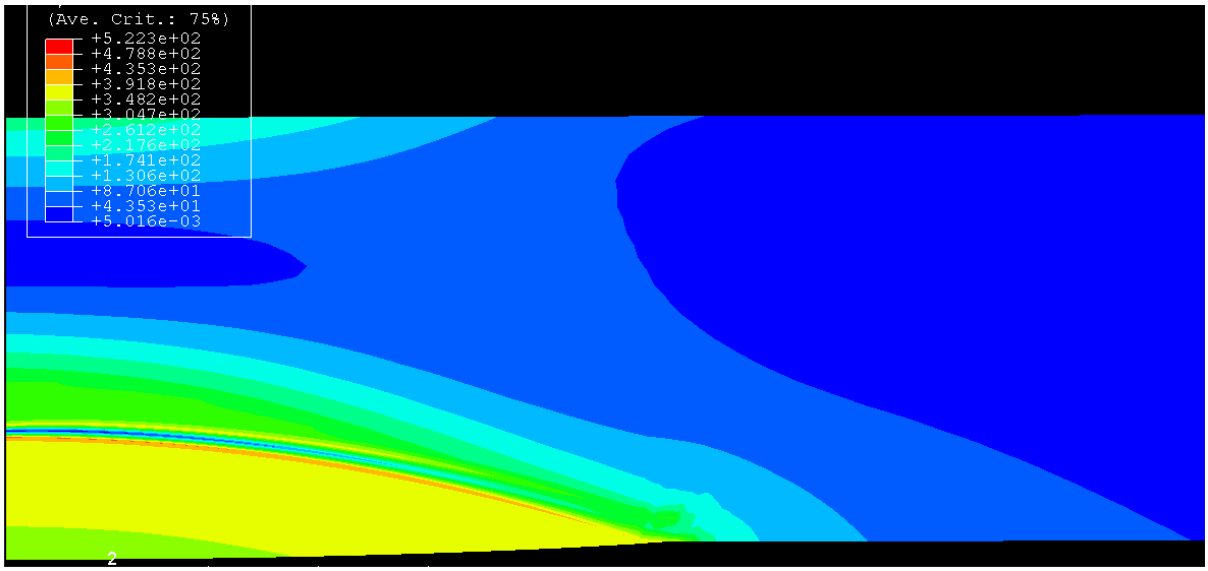

Fig. 4 Contour plot of equivalent stress in the blister and matrix around it for hydride/matrix yield stress ratio of unity. Phase transformation achieved in single step.

In Fig. 5(b), the threshold stress variation across sample thickness is superimposed on the plots of estimated stress for blister depths of 0.2, 0.5 and 1.0 mm. The hydride platelet orientation at any location in the matrix around the blister is governed by the stresses generated due to the hydride blisters. For the regions where tensile stress prevailing at any point in the matrix is greater than the threshold stress for reorientation of hydrides, radial hydride will also precipitate out.

5. Conclusions

Stress field in the hydride blister and Zr-matrix were estimated using finite element method. The estimated stress computed by carrying out the single step transformation of hydride is

higher as compared to that obtained by multi-step transformation. The estimated stress field could explain the formation of radial hydride in the matrix near the interface region.

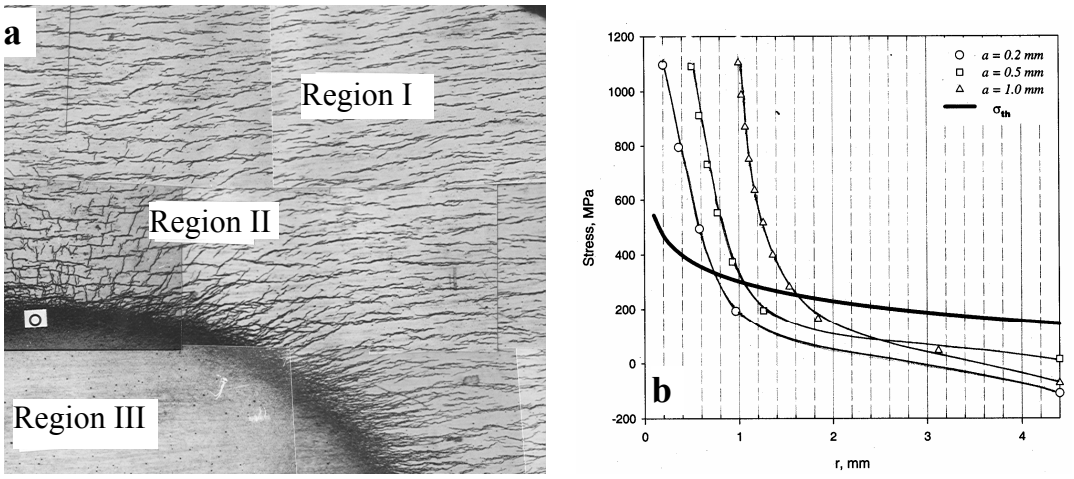

Fig. 5 shows (a) a section of blister in Zr-alloy [11] and (b) Comparison of the estimated stress and threshold stress for reorientation of hydrides across the thickness of the plate used for growing hydride blister.

Acknowledgement

Dr. Singh is on extraordinary leave from Bhabha Atomic Research Centre (BARC), Mumbai, India and is currently working as a Marie Curie Incoming International fellow at Malmo University, which is financially supported by European Commission under its FP6 programme to promote researchers mobility into European Union (Contract No. MIF1-CT-2005-006844**)**.

References

1. Sawatzky, A., *Can. Metall. Q*., **24**(3) (1985) 227.
2. Puls, M. P., *Metall. Trans. A*, **19A** (1988) 2247.
3. R. N. Singh, R. Kishore, S. S. Singh, T. K. Sinha and B. P. Kashyap, *Jl. of Nucl. Mater.* **325** (2004) 26.
4. R. N. Singh, Niraj Kumar, R. Kishore, S. Roychowdhury, T. K. Sinha and B. P. Kashyap, *Jl of Nucl. Mater.* **304**, (2002) 189.
5. E. S. Fisher and C. J. Renken, *Phy. Rev. A* **135** (1964) 482.
6. S. Yamanakaa, K. Yoshiokaa, M. Unoa, M. Katsuraa, H. Anadab, T. Matsudac, S. Kobayashic, *Jl. of Alloys & Comp.* **293-295** (1999) 23.
7. M. P. Puls, S. Q-Shi, J. Rabier, *Jl. of Nucl. Mater.* **336** (2005) 73.
8. D. O. Northwood, and U. Kosasih, *Intl. Metals Rev.s*, **28(2)** (1983) 92.
9. Y. J. Kim and M. L. Vanderglas, *Proc. of ASME-PVP conf*., New Orlearns, USA, June (1985) 161.
10. T. P. Byrne, D. R. Metzger, M. Leger, *Transactions of the 11th international conference on structural mechanics in reactor technology*. Tokyo (Japan). 18-23 Aug 1991. Shibata, Heki (ed.) Atomic Energy Society of Japan. **B** pp. 335-340. (1991).
11. R. N. Singh, R. Kishore, T. K. Sinha, S. Banerjee and B. P. Kashyap, *Mater. Sc. and Engg. A* **339** (2003) 17.

Design of Multiple Tuned Mass Dampers on Flexible Structures

Steen Krenk and Jan Høgsberg
Department of Mechanical Engineering
Technical University of Denmark, Kgs. Lyngby, Denmark
e–mail: sk@mek.dtu.dk , jhg@mek.dtu.dk

Introduction

Tuned mass dampers are increasingly used for structures such as bridges, towers, buildings and structural parts such as e.g. staircases. The classic design basis described e.g. by Den Hartog [1], refers to a single damper mounted on a single structural mass. In the case of flexible structures, such as e.g. the Millennium Bridge in London [2] and the newly completed Langelinie Pedestrian Bridge in Copenhagen [3], several modes must be damped. This may introduce two new effects into the design, namely a change in modal frequencies due to the damper masses associated with the other modes, and a possible change in the mode shapes.

This paper describes a simple procedure for design of a number of tuned mass dampers used to introduce controlled damping in several modes of a flexible structure. The following section gives a brief summary of the design basis for a single damper, and this procedure is then extended to flexible structures via a two-step procedure consisting of an initial estimate and a correction based on modal vibrations including the damper masses, but excluding the damping effect to provide a real-valued vibration problem. The procedure is illustrated by an example concerned with damping of the four lowest modes of a four-span bridge.

Single tuned mass damper

The classic design problem for a single tuned mass damper is illustrated in Fig. 1. The structure is represented by a mass m_0 supported by a spring k_0. The tuned mass damper consists of a damper mass m_d mounted on the structural mass by a spring with stiffness k_d and a viscous damper with damper constant c_d. The motion is described by the motion of the structural mass x_0 and the relative motion x_d of the damper.

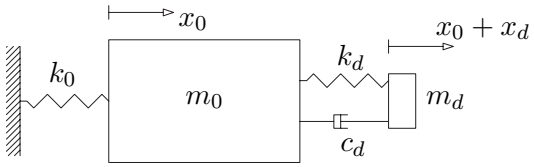

Figure 1: Single degree of freedom with mass damper

The design procedure for a single tuned mass damper mounted on a well defined structural mass makes use of the mass ratio μ, the structural angular frequency ω_0, the angular frequency of the rigidly mounted damper mass ω_d and the damping ratio of the rigidly mounted damper mass ζ_d,

$$\mu = \frac{m_d}{m_0} \quad , \quad \omega_0^2 = \frac{k_0}{m_0} \quad , \quad \omega_d^2 = \frac{k_d}{m_d} \quad , \quad \zeta_d = \frac{c_d}{2\omega_d m_d} \tag{1}$$

The usual design procedure consists in selecting a sufficiently large mass ratio - usually in the order of 3-5%. The optimal frequency tuning and damping ratio are then determined by

$$\omega_d \;=\; \frac{\omega_0}{1+\mu} \qquad , \qquad \zeta_d \;=\; \sqrt{\frac{1}{2}\frac{\mu}{1+\mu}} \tag{2}$$

The classic damping value of Den Hartog [1] has a factor $\frac{3}{8}$, but it has recently been demonstrated that the factor $\frac{1}{2}$ leads to better damping of the structure and minimizes the relative motion of the damper mass, [4]. Use of the optimal tuning parameters in Eq. 2 leads to two coupled structural modes with identical damping ratio $\zeta_s \simeq \frac{1}{2}\zeta_d$, [4]. Thus, a mass ratio of $\mu = 0.05$ leads to a structural damping ratio of $\zeta_s \simeq 0.077$, sufficient to eliminate most vibration problems.

Multiple dampers on flexible structures

Let the flexible structure be represented by a discreized model with the displacement vector $\mathbf{u}$ and equation of motion

$$\mathbf{M}\ddot{\mathbf{u}}(t) \;+\; \mathbf{C}\dot{\mathbf{u}}(t) \;+\; \mathbf{K}\mathbf{u}(t) \;=\; \mathbf{Q}(t) \tag{3}$$

$\mathbf{M}$, $\mathbf{C}$ and $\mathbf{K}$ are the mass, damping and stiffness matrix of the structure, and $\mathbf{Q}(t)$ is the time varying external load vector. Damping is typically introduced into the individual vibration modes $\mathbf{u}_j$, determined from the generalized eigenvalue problem

$$(\,\mathbf{K} \;-\; \omega_j^2\,\mathbf{M}\,)\,\mathbf{u}_j \;=\; \mathbf{0} \quad , \quad j = 1, \cdots, n \tag{4}$$

where ω_j is the natural frequency of mode j. The modal mass is defined as

$$m_j \;=\; \mathbf{u}_j^T\,\mathbf{M}\,\mathbf{u}_j \tag{5}$$

and represents the part of the structural mass that participates for the particular mode. When one or more mass dampers are mounted on the flexible structure to introduce damping into mode j the effective damper mass for this group of dampers is

$$m_j^d \;=\; \mathbf{u}_j^T\,\mathbf{M}_j^d\,\mathbf{u}_j \tag{6}$$

where $\mathbf{M}_j^d$ contains the masses of the dampers in the diagonal at the degrees of freedom corresponding to the locations of the dampers on the structure. Thus, the effective mass ratio of mode j is given as

$$\mu_j \;=\; \frac{m_j^d}{m_j} \tag{7}$$

The optimal parameters for the tuned mass dampers associated with mode j can be found by Eq. 2.

For the flexible structure with dampers the vibration modes and natural frequencies become complex valued due to phase differences. The complex modes and frequencies are found from the expanded symmetric eigenvalue problem

$$\left\{ \begin{bmatrix} \mathbf{K} & \mathbf{0} \\ \mathbf{0} & -\mathbf{M} \end{bmatrix} + i\omega \begin{bmatrix} \mathbf{C} & \mathbf{M} \\ \mathbf{M} & -\mathbf{0} \end{bmatrix} \right\} \begin{bmatrix} \mathbf{u} \\ i\omega\mathbf{u} \end{bmatrix} \;=\; \begin{bmatrix} \mathbf{0} \\ \mathbf{0} \end{bmatrix} \tag{8}$$

where the system matrices $\mathbf{M}$, $\mathbf{C}$, $\mathbf{K}$ and the displacement vector $\mathbf{u}$ include both structure and dampers. The damping ratio is extracted as the relative imaginary part of the natural frequency,

$$\zeta_j \;=\; \frac{\mathrm{Im}[\omega_\mathrm{j}]}{|\omega_j|} \tag{9}$$

Design procedure

The present design procedure for multiple tuned mass dampers relies on the optimal expressions in Eq. 2 for a single tuned mass damper, where the mass ratio is defined in Eq. 7. However, to take the effects from the other dampers into account, the procedure consists of two steps: 1) A preliminary design based on the undamped vibration modes and 2) a correction based on the mode shape for the structure including mass and stiffness (from step 1) of all dampers for *the other modes*. Thus, in step 2 the stiffness k_d and damper parameter c_d from the preliminary design are recalculated based on the modified vibration form due to the tuned mass damper associated with the other modes that are being damped.

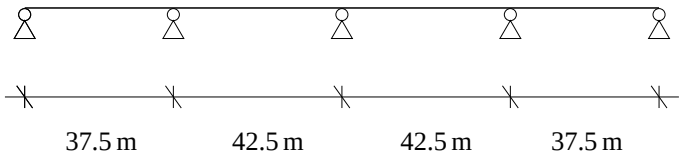

Figure 2: Four-span bridge.

The design procedure is illustrated in terms of the four-span bridge shown in Fig. 2. The elastic modulus E, cross section area A, moment of inertia I, mass per unit length ρ and length L are

$$E = 300\,\mathrm{GPa} \quad , \quad A = 0.5\,\mathrm{m}^2 \quad , \quad I = 0.08\,\mathrm{m}^4 \quad , \quad \rho = 6400\,\mathrm{kg/m} \quad , \quad L = 160\,\mathrm{m}$$

These properties represent typical values for e.g. pedestrian bridges with span lengths as shown in Fig. 2. The aim is to introduce damping into the lowest four vibration modes with mode shapes shown in Fig. 3. Two tuned mass dampers with equal properties are introduced for each mode and placed according to the maximum of the associated vibration modes as indicated in Fig. 3.

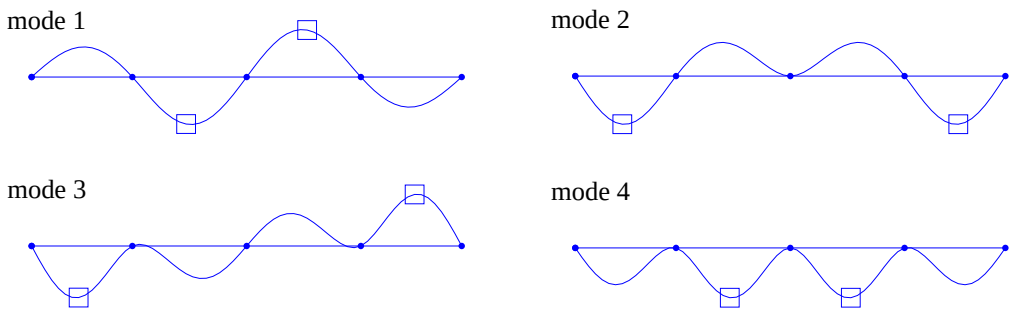

Figure 3: Undamped vibration modes and damper location.

In the idealized form with a single structural mass the use of a single damper splits the original undamped mode into two modes with equal damping ratio $\zeta_s \simeq \frac{1}{2}\zeta_d$. The use of two dampers introduces a third mode in which the dampers act in opposite phase and thereby retain the full damping ratio $\zeta_s \simeq \zeta_d$. For flexible structures the behavior of the dampers may be more complicated as illustrated for mode 1 in Fig. 4 showing the real part of the three vibration forms.

The desirable mass ratio of the design procedure is $\mu = 0.05$ for all four modes. The results of the two-step procedure is summarized in Table 1, where the damper parameters and the damping ratio for the structural modes are given for both the preliminary tuning (step 1) and the correction (step 2). It is seen how the correction step leads to a larger critical damping ratio for each mode.

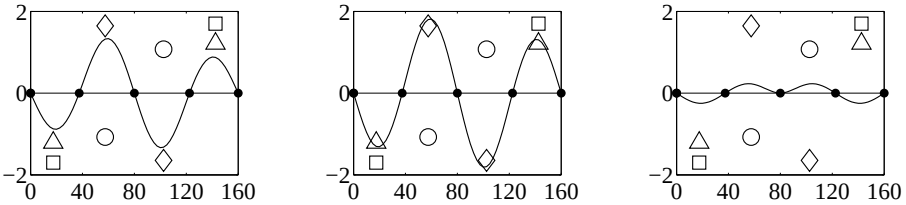

Figure 4: Mode shapes with dampers for mode 1. Dampers tuned to: mode 1 (circle), mode 2 (square), mode 3 (triangle) and mode 4 (diamond).

	mode j	1	2	3	4
	ω_0	16.51	20.97	27.17	32.31
	Damper mass	4700 / 4700	4450 / 4500	3900 / 3900	4150 / 4150
Step 1	ω_d	15.72	19.97	25.87	30.77
	ζ_d	0.155	0.154	0.155	0.154
	ζ_j	0.055 / 0.107	0.069 / 0.110	0.096 / 0.103	0.116 / 0.083
Step 2	ω_d	14.91	17.17	26.26	32.29
	ζ_d	0.163	0.161	0.153	0.147
	ζ_j	0.071 / 0.074	0.075 / 0.081	0.083 / 0.099	0.091 / 0.091

Table 1: Modal properties of bridge with $\mu = 0.05$.

The effect of the correction step is illustrated in Fig. 5, showing the complex natural frequencies for modes 1 and 2. The solid lines represent two half circles, representing the root loci for a single tuned mass damper, see [4]. These loci initiate from the three natural frequencies when $c_d \to 0$. The dashed line represent the expected damping ratio of $\zeta_j = 0.077$, whereby the two intersections (circle) between the dashed line and the small locus represent the expected optimal tuning. The three natural frequencies from step 1 (asterisk) are seen to be relatively far away from the the expected locus. However, following step 2 of the procedure the natural frequencies (crosses) move very close to the expected locus and to the intersections (circle), representing the desired efficiency of 7.77% of critical damping.

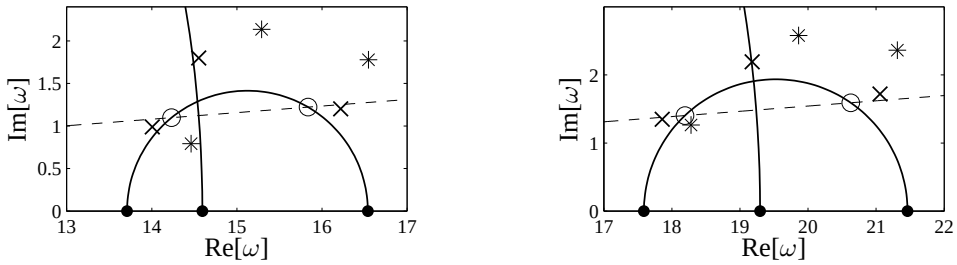

Figure 5: Complex roots for mode 1 (left) and 2 (right).

References

[1] J.P. Den Hartog. *Mechanical Vibrations*. McGraw-Hill, London, Fourth edition, (1956). Reprinted by Dover, New York, (1985).

[2] P. Dallard, A.J. Fitzpatrick, A. Flint, S. Le Bourva, A. Low, R.M. Ridsdill Smith, and M. Willford. The London Millenium footbridge. *The Structural Engineer*, **79** (22), 17–33, (2001).

[3] S. Krenk, A. Brønden and A. Kristensen. Placement and tuning of resonance dampers on footbridges. *Proceedings of Footbridge 2005 – Second International Conference*, Venice, Italy, (2005).

[4] S. Krenk. Frequency analysis of the tuned mass damper. *Journal of Applied Mechanics*, **72**, 936–942, (2005).

On optimal control of hydraulic cranes

Torbjörn Ekevid*
School of Tecnology and Design
Växjö University, Växjö, Sweden
e–mail: torbjorn.ekevid@vxu.se

Summary In the design of control systems, modeling is an important tool when studying how the controlled system responds to a certain input. Often, modeling makes it also possible to identify existing errors, if any, before the algorithms are used in real-world applications. The paper presents ongoing work aiming at improve the maneuverability and facilitate for operator of the hydraulic cranes mounted on forestry. Since the application should be able to run in real-time, the description of the system is based on the rigid body assumption and generalized coordinates using the smallest number of variables possible to describe the state. The paper presents results from numerical simulations of orthogonal crane tip control.

Introduction

In the design process of robot manipulators or other mechanical systems, accurate modeling of the dynamics is vital to access forces applied to the structure. Moreover, modeling is also important when designing fast and robust control systems[1].

Hydraulic cranes may be regarded as robot manipulators where the hydraulic cylinders serves as actuators. Such cranes are very common in the rational and highly mechanized forestry but to operate a crane efficiently is a highly qualified work that requires years of practice. The overall aim of our work is to apply control theory to facilitate for beginners to handle the crane and make it possible to have short breaks during the operation. This has been applied to mobile cranes[2].

Two approaches to model mechanical systems when the bodies are considered as rigid can be distinguish. The first approach, used in most commercial rigid body softwares, uses six degrees of freedom (three translations and three rotations) for each body. The coupling between bodies is managed by constraint equations which are added to the systems of Ordinary Differential Equations (ODE) such that a system of Differential Algebraic Equations (DAE)[3] is formed. The second approach uses a minimum number of parameters termed generalized coordinates[4, 5] (either joint distances or rotational angles) to describe the motion. The resulting system of ODE:s is comparably small, but more complicated to establish and to solve numerically. However, since the models will be used in real-time computations in this application, we have adopted the second approach in this work.

The hydraulic crane of forwarders

The crane (RK62) is mounted at a Rottne forwarder. In principle, it consists of mechanical links (with som flexibility), joints (translational and rotational) and hydraulic actuators, see Fig.1 a. In normal operating conditions, a rotator and a grapple is attached to the crane tip to handle the logs. The maximum length is 6.9 m and the mass is approximately 1100 kg. Fig.1 b shows the idealized crane used in the model. It is composed of rigid body parts, joints (positioned at the origin of the coordinate systems), key points, rigid links (blue), and actuator elements (red). The motivation of introducing rigid links is explained below.

Rigid body dynamics

Let us define a set of joint variables (generalized coordinates) $\boldsymbol{q}$ as either being rotations or translation between two coordinate frames. The state[5] of the rigid body systems could be determined

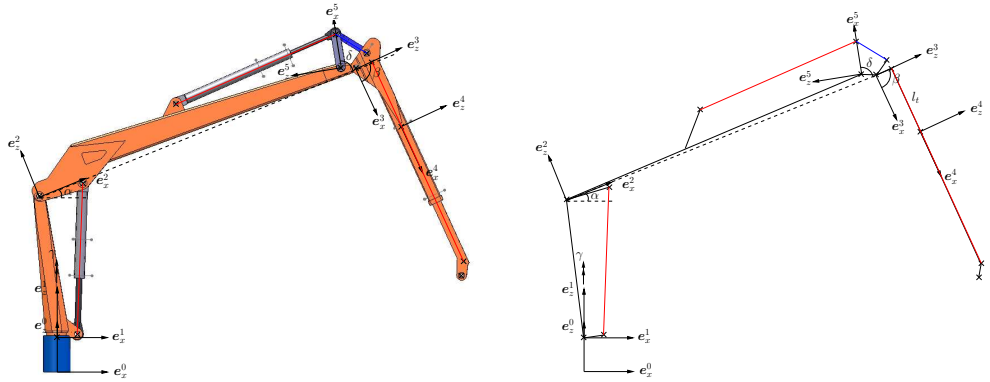

a) b)

Figure 1: a) CAD model of the crane. b) The idealized crane including the actuators and the torque link.

from

$$\boldsymbol{B}(\boldsymbol{q})\ddot{\boldsymbol{q}} + \sum_{k=1}^{n} \frac{\partial \boldsymbol{B}\left(\boldsymbol{q}\right)}{\partial q_k}\dot{q}_k\dot{\boldsymbol{q}} - \frac{1}{2}\dot{\boldsymbol{q}}^T\frac{\partial \boldsymbol{B}\left(\boldsymbol{q}\right)}{\partial \boldsymbol{q}}\dot{\boldsymbol{q}} - \boldsymbol{g}\left(\boldsymbol{q}\right) = \boldsymbol{Q} \tag{1}$$

where $\boldsymbol{Q}$ is the generalized force vector associated to $\boldsymbol{q}$ and $\boldsymbol{g}\left(\boldsymbol{q}\right)$ the gravity force vector. Further, $\boldsymbol{B}(\boldsymbol{q})$ is the mass matrix defined by

$$\boldsymbol{B}(\boldsymbol{q}) = \sum_{i=1}^{n} \left(\boldsymbol{J}_x(\boldsymbol{q})_i\right)^T m_i \boldsymbol{J}_x(\boldsymbol{q})_i + \left(\boldsymbol{J}_\omega(\boldsymbol{q})_i\right)^T \boldsymbol{R}^{0,i}\boldsymbol{I}^i\boldsymbol{R}^{0,i^T}\boldsymbol{J}_\omega(\boldsymbol{q})_i \tag{2}$$

where m_i is the mass, $\boldsymbol{I}^i$ is the inertia tensor and $\boldsymbol{J}_x(\boldsymbol{q})_i$ denotes the velocity Jacobian and $\boldsymbol{J}_\omega(\boldsymbol{q})_i$ the angular velocity Jacobian of the center of gravity of body i, expressed in frame $(\boldsymbol{e}_x^0, \boldsymbol{e}_y^0, \boldsymbol{e}_z^0)$. An actuator force u_{ij} between two points P_i and P_j contributes to $\boldsymbol{Q}$ in (1) by

$$\boldsymbol{Q}_{ij} = u_{ij}\left(\boldsymbol{J}_x(\boldsymbol{q})_{P_j} - \boldsymbol{J}_x(\boldsymbol{q})_{P_i}\right)^T \boldsymbol{e}_{ij}^0 \tag{3}$$

where $\boldsymbol{e}_{ij}^0$ is the unit vector from P_i to P_j and $\boldsymbol{J}_x(\boldsymbol{q})_{P_i}$, $\boldsymbol{J}_x(\boldsymbol{q})_{P_j}$ are the velocity Jacobian of point P_i and P_j, respectively.

Closed chains

To create rigid body models in a systematic manner using the concept of generalized coordinates, adding of a mechanical link implies adding of a new joint variable. However, in certain cases the links of the manipulator form closed chains i.e. the torque link of the crane. To resolve these cases, a set of constraint equations

$$\boldsymbol{\Psi}\left(\boldsymbol{q}(t), t\right) = \boldsymbol{0} \tag{4}$$

are used. Differentiating (4) with respect to time two times yields

$$\frac{\partial \boldsymbol{\Psi}}{\partial \boldsymbol{q}}\ddot{\boldsymbol{q}} = \boldsymbol{Q}^c \tag{5}$$

where

$$\boldsymbol{Q}^c = -\ddot{\boldsymbol{\Psi}} - 2\frac{\partial \dot{\boldsymbol{\Psi}}}{\partial \boldsymbol{q}}\dot{\boldsymbol{q}} - \frac{\partial}{\partial \boldsymbol{q}}\left(\frac{\partial \boldsymbol{\Psi}}{\partial \boldsymbol{q}}\dot{\boldsymbol{q}}\right)\dot{\boldsymbol{q}} \tag{6}$$

and if the Lagrange multiplier approach is adopted, (1) is expanded by the constraint equations according to

$$\begin{bmatrix} \boldsymbol{B}(\boldsymbol{q}) & \boldsymbol{\Psi}_{,\boldsymbol{q}}^{T} \\ \boldsymbol{\Psi}_{,\boldsymbol{q}} & \boldsymbol{0} \end{bmatrix} \begin{bmatrix} \ddot{\boldsymbol{q}} \\ \boldsymbol{\lambda} \end{bmatrix} = \begin{bmatrix} \boldsymbol{Q} + \boldsymbol{g}(\boldsymbol{q}) - \boldsymbol{C}(\boldsymbol{q}, \dot{\boldsymbol{q}})\dot{\boldsymbol{q}} \\ \boldsymbol{Q}^{c} \end{bmatrix} \tag{7}$$

where $\boldsymbol{\lambda}$ is a vector of Lagrange multipliers.

Motion control of the crane

Orthogonal control

The layout of the crane makes it possible to reach most points within the working space by an infinite number of configurations since there is a redundant set of joint variables. One choice among others to eliminate the redundancy and facilitate for the operator is orthogonal control, where the objective is to minimize a certain quantity e.g. fuel consumption given the velocities $\dot{\boldsymbol{x}}_{ct}^{0}$ of crane tip. Let us define the optimization problem

$$\begin{aligned} min \quad & h(\dot{\boldsymbol{q}}_d) = \frac{1}{2}(\dot{\boldsymbol{q}}_d - \dot{\boldsymbol{q}}_0)^T(\dot{\boldsymbol{q}}_d - \dot{\boldsymbol{q}}_0) \\ s.t. \quad & \dot{\boldsymbol{x}}_{ct}^{0} - \boldsymbol{J}_x\dot{\boldsymbol{q}}_d = \boldsymbol{0} \end{aligned} \tag{8}$$

where $\dot{\boldsymbol{q}}_0$ is a vector of joint velocities which reflect the quantity of interest to minimize[5]. The optimal solution $\dot{\boldsymbol{q}}_d^*$ can be computed from

$$\dot{\boldsymbol{q}}_d^* = \boldsymbol{J}^{\dagger}\dot{\boldsymbol{x}}_{tt} + \left(\boldsymbol{I} - \boldsymbol{J}^{\dagger}\boldsymbol{J}\right)\dot{\boldsymbol{q}}_0 \tag{9}$$

where

$$\boldsymbol{J}^{\dagger} \stackrel{\text{def}}{=} \boldsymbol{J}^{T}\left(\boldsymbol{J}\boldsymbol{J}^{T}\right)^{-1} \tag{10}$$

is the *right pseudo inverse* and $\boldsymbol{I}$ is the identity matrix.

Feedback control

Let $\bar{\boldsymbol{q}}_d$ denote the vector describing the desired trajectories expressed either in joint variables or length of the actuator elements and $\bar{\boldsymbol{q}}$ the vector of their actual values. By defining the error

$$\bar{\boldsymbol{e}} = \bar{\boldsymbol{q}}_d - \bar{\boldsymbol{q}}, \tag{11}$$

the PID[4] control law with gravity compensation imposes the control forces

$$\boldsymbol{u} = \boldsymbol{g}(\boldsymbol{q}) + \int_0^t \boldsymbol{K}_i\bar{\boldsymbol{e}}\,dt + \boldsymbol{K}_p\bar{\boldsymbol{e}} - \boldsymbol{K}_d\dot{\bar{\boldsymbol{q}}}, \tag{12}$$

where $\boldsymbol{K}_i$, $\boldsymbol{K}_p$ and $\boldsymbol{K}_d$ are positive definite matrices, to be applied by the actuators to the crane.

Simulation of orthogonal crane control

To give one example of orthogonal control, $\dot{\boldsymbol{q}}_0$ is chosen such that the hydraulic cylinders should remain as far as possible from their minimum and maximum length. At the crane tip a mass of 200 kg is attached. The crane is initially in rest and positioned as Fig.2 a indicates. The trajectory to follow, is a triangle in the plane spanned by $\boldsymbol{e}_x^0$ and $\boldsymbol{e}_y^0$ shown in see Fig.2 a. In the same figure result from the simulation is shown. Fig. 2 b shows the desired and actual length of the actuator elements.

Fig.3 a shows the error $\bar{\boldsymbol{e}}$ between the desired and actual length of the actuators and Fig.3 b shows the actuator forces applied to the structure. However, the gravity forces $\boldsymbol{g}(\boldsymbol{q})$ c.f. (12), is not included in the result shown.

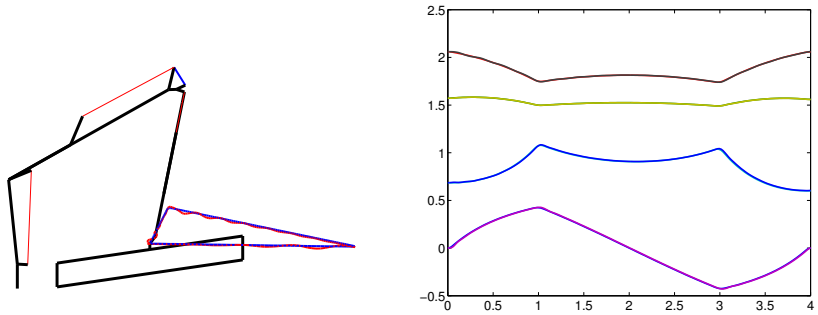

a) b)

Figure 2: a) The initial position of the crane and the trajectory. b) Desired and actual length of the actuators.

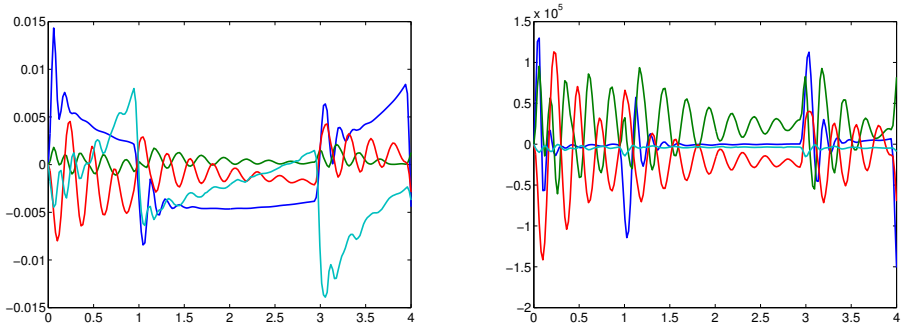

a) b)

Figure 3: a) The error between desired and actual length of the actuators. b) Forces applied by the actuator.

Concluding remarks, further research

The paper has presented an approach to model rigid body dynamics based on generalized coordinates. The approach is systematic and generates systems of ODE with a comparably small number of unknowns. It was used to model orthogonal control of a hydraulic crane and in the near future, the results will be realized and tested in laboratory conditions on a small-sized crane.

Acknowledgements

The financial support from Sparbanksstiftelsen Kronan is gratefully acknowledged. Also the technical support from Rottne Industry AB is very valuable and should be acknowledged.

References

[1] S. Arimoto, Control Theory of Non-linear Mechanical Systems: A Passivitity based and Circuit-theoretic Approach, Oxford University Press, 1996.

[2] M. Ebbesen, M. Hansen, T. Andersen, Optimal tool point control of hydraulically actuated flexible multibody system with an operator-in-the-loop, in: European Congress on Computational Mechanics, ECCM2006, Lisabon, Portugal, 2006.

[3] A. A. Shabana, Computational Dynamics, 2nd Edition, Wiley, New York, 2001.

[4] M. W. Spong, S. Hutchinson, M. Vidyasagar, Robot Modeling and Control, Wiley, 2006.

[5] L. Sciavicco, B. Siciliano, Modelling and Control of Robot Manipulators, 1st Edition, Springer, London, Great Britain, 2000.

Modelling the Dynamic Properties of Rubber in Rolling Contact

A. K. Olsson* **and P-E Austrell**
Division of Structural Mechanics
Lund University, Lund, Sweden
e–mail: bmako@byggmek.lth.se

Summary The dynamic response of rubber is dependent of both amplitude and frequency. This paper studies two different finite element procedures to include amplitude and frequency dependent effects in conjunction with rolling contact. It is shown how the non-linear dynamic characteristics of the rubber material influences the rolling contact. Analyzed examples include rolling on a flat surface and rolling over a groove.

Introduction

The purpose of this paper is twofold. The first is to examine two different methods of incorporating amplitude dependent effects into finite element models of rubber in rolling contact. The second purpose is to highlight some important aspects of non-linear material characteristics in general and amplitude dependence in particular when rolling contact is studied.

For a harmonic load, the amplitude dependence can be seen as a decrease in dynamic modulus for increasing amplitude. For an increasing amplitude the damping will at first increase until a maximum is reached after which further increased amplitude will result in decreased damping. Partly depending on the application and partly on the specific rubber properties, the amplitude dependent effects are in many cases far more pronounced than the rate or frequency dependence (Olsson & Austrell 2001). This is especially obvious for applications with moderate amplitudes and low to moderate frequencies, as well as for rubber with a high proportion of filler particles. For very low or very high strain amplitudes these effects are usually of less interest.

This paper studies two different methods to account for combined amplitude and frequency dependence in a rolling contact finite element analysis. The first method uses an elastoplastic-viscoelastic model previously presented in (Austrell & Olsson 2001) and the second is based on an approximate time-domain viscoelastic model presented in (Olsson et al. 2006). Both methods are based on simple engineering approaches and utilize commercially available finite element codes, keeping the added complexity to a minimum. The material tests have previously been presented in (Olsson & Austrell 2001).

Rubber covered rollers

From an industrial point of view, rubber covered rollers are of great importance in many industrial applications. From a scientific perspective the simple geometry and loading of rubber covered rollers make them ideal to study the dynamic effects of rubber material during rolling.

Depending on what industrial application or process the roller is found in, different contact parameters are important. Contact parameters such as contact width, maximum pressure, pressure gradient and surface strains are all governed by material properties and design variables such as rubber thickness, roller radius, applied load and rolling velocity, as seen in figure 1. In general the design variables are simple to control but are hard to correlate to what is happening in the the contact region. The contact parameters on the other hand are easier to correlate to the process but harder to control. Hence, a good model describing the relationship between contact parameters and design variables is the key to control the process.

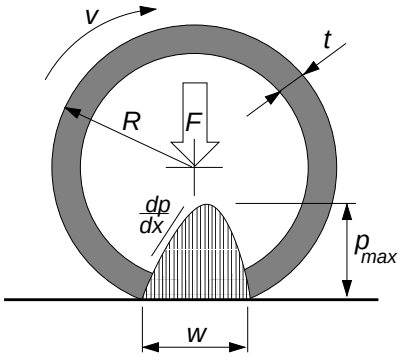

Figure 1: Rubber covered roller, design variables and contact parameters.

Rolling over a smooth surface

In the this section a rubber coated roller is studied when rolling over a flat surface. Using this example, both the equivalent viscoelastic and viscoelastic-elastoplastic models are used to analyze the influence of the dynamic material properties.

The analyzed rubber coated roller has a rubber coat of $28mm$ and an outer radius of $200mm$. The rolling velocity is $10m/s$ and the compressive displacement of the roller is $0.8mm$. The roller is modelled as a long rigid cylinder coated with a thin layer of rubber.

The contact pressures from both the equivalent viscoelastic and the viscoelastic-elastoplastic finite element model are shown in figure 2. Both models show good agreement with each other. Unfortunately it was not possible to obtain any experimental data to compare with, but the agreement between the two separate models suggests that the result is reliable.

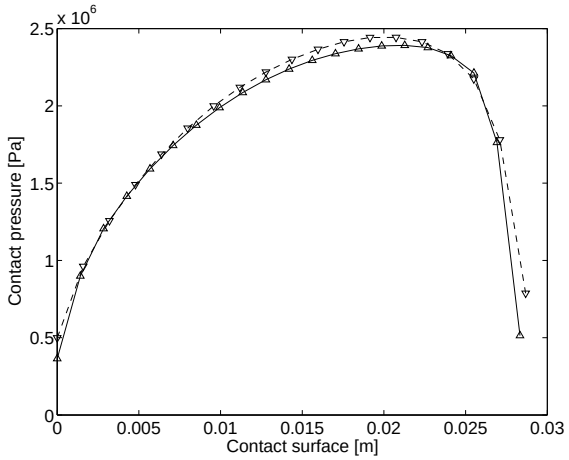

Figure 2: Contact pressure when rolling over a flat surface. Dotted line: Overlay method; Solid line: Equivalent viscoelastic method.

The asymmetric shape of the pressure distribution can be explained by the non-elastic properties of the rubber material. At the first phase of the contact surface the rubber material is loaded until it reaches the maximum contact pressure after which it is unloaded. Similar to a cyclic material test,

the contact pressure response when unloading will deviate from the load curve. This behaviour is caused by damping and will result in a loss of strain energy. Thus, the asymmetric shape of the contact pressure is a result of the material damping. The asymmetric pressure results in an increased initial pressure gradient which can be beneficial for some applications where fluids need to be driven away from the contact area.

Rolling over a non-smooth surface

In this section a rubber covered roller is studied to see how different material properties will influence the contact prpoerties.

As was seen in figure 2 both the equivalent viscoelastic and elastoplastic-viscoelastic model will give the same pressure distribution rolling over a flat surface. Trying different material models indicated that the pressure distribution was not affected by the material characteristics. The pressure distribution over the contact area was the same irrespective if the rubber were modelled as elastoplastic or viscoelastic.

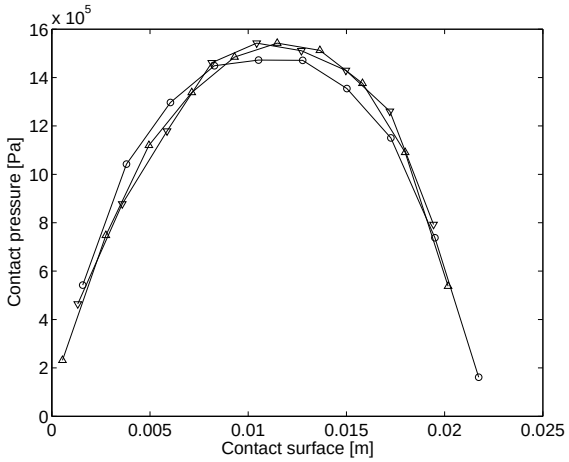

Figure 3: Contact pressure when rolling over a flat surface using fictive material models. ◯: Elastic model; ▽: Elastoplastic model; △: Viscoelastic model.

To further prove this point two fictive materials were derived; one purely viscoelastic and one purely elastoplastic. Both material models were fitted to exhibit a constant damping of $d = 0.35$ for a frequency range of 5 to 180 *Hz* and a shear strain amplitude range of 1 to 12%.

When rolled over a flat surface both models gave the same shape of the contact pressure distribution, only differing in the maximum pressure. Figure 3 show the contact pressure as both models are rolling at a speed of 10*m/s* over the flat surface. A purely hyperelastic model is also shown as a reference.

Using the previously derived fictive material the same roller was studied when rolling over a shallow groove. The groove is 5*mm* wide and 0.8*mm* deep with the same length as the roller and situated in the axial direction of the roller.

As seen from figure 4, the elastoplastic model better adapts to the shape of the groove. The elastoplastic model incorporates amplitude dependence. Although the viscoelastic and elastoplastic models give the same result when rolled over a flat surface, it can be concluded that including

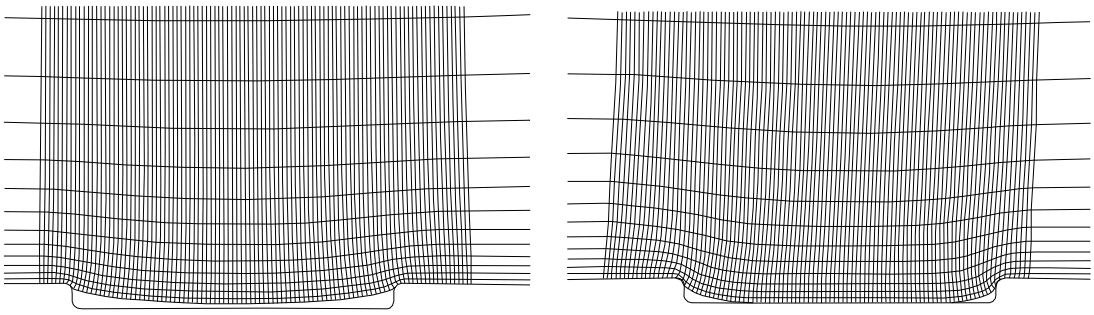

Figure 4: Element deformation when running over a small groove using an viscoelastic (left) and an elasto-plastic (right) finite element model.

the amplitude dependence, as done in the elastoplastic model, will result in a softer and more deformable contact region.

Summary

Two different methods to include frequency and amplitude dependence are studied. Both models gave the same results for a flat surface, suggesting that the contact pressure when rolling over a flat surface is mainly governed by dynamic modulus and damping and is not dependent on how the damping is modelled.

When comparing viscous and plastic damping mechanics, it was seen that amplitude dependent rubber resulted in much softer behaviour of the high strain regions of the rubber surface. This local softening effect will make the rubber deform more easily and better adapt to the geometry of the groove.

References

[1] Abaqus Inc. Abaqus Theory Manual, Version 6.5. , *Providence, RI, USA*

[2] Akutagawa K. et al. An analysis of a new class of integration algorithms for elastoplastic constitutive relations. *Third European Conference on Constitutive Models for Rubber*, UK, (2003).

[3] Austrell P-E., Olsson A.K. *A Method to Analyze the Non-Linear Dynamic Behaviour of Carbon-Black-Filled Rubber Components Using Standard FE-codes.* Second European Conference on Constitutive Models for Rubber, Germany, (2001).

[4] Kaliske M. & Domscheit A. *Modelling of softening effects in elastomeric material and its application in tire computations.* Second European Conference on Constitutive Models for Rubber, Germany, (2001).

[5] Olsson A.K., Austrell P-E. *A fitting procedure for a viscoelastic-elastoplastic material model*. Second European Conference on Constitutive Models for Rubber, Germany, (2001).

[6] Olsson A.K. 2006 *Considering amplitude dependent effects during cyclic loads by an equivalent viscoelastic model.*. PhD thesis, Modelling the dynamic properties of elastomers, Paper IV, Lund University, Sweden, (2006).

Conceptual design of the enclosure of an extremely large telescope

Sandberg G. and Persson K.
Division of Structural Mechanics
Lund University, Lund Sweden
e–mail: goran@byggmek.lth.se

Revstedt J.
Division of Fluid Mechanics
Lund University , Lund, Sweden
e–mail: johan.revstedt@vok.lth.se

Introduction

The present project embraces the overall aim of developing an extremely large telescope capable of performing major astronomic research, as well as its iconic and metaphorical value in transmitting scientific interest and curiosity to a wide variety of persons and to the public generally. Here the enclosure is investigated that introduces a number of special features. The major ones are: the aerodynamic shape of the body of the construction that is planned, its elevated position and the variable size of its opening to the outside, achieved through use of airfoil-like panels. A basic conception involved in the proposal is that of the structure's having a compound asymmetrically curved body or shell. Its overall shape is to be an aerodynamic one.
The enclosure stands at a considerable distance above the ground supported by pylons, raising the entire installation to a level well above the layer of turbulent air located at ground level, generated by wind or produced thermally. The body of the enclosure is bisected by a combined observation and ventilation aperture – the variable opening of which is controlled by adjustments achieved through use of a series of shutters or panels that are aerofoil-like in section and are capable of assuming a wide range of different deployment configurations. The possibilities that are found of producing different configurations of the blades provides a means of actively creating a laminar flow over the surface of the telescope and of achieving increased structural integrity when called for during astronomic observations.

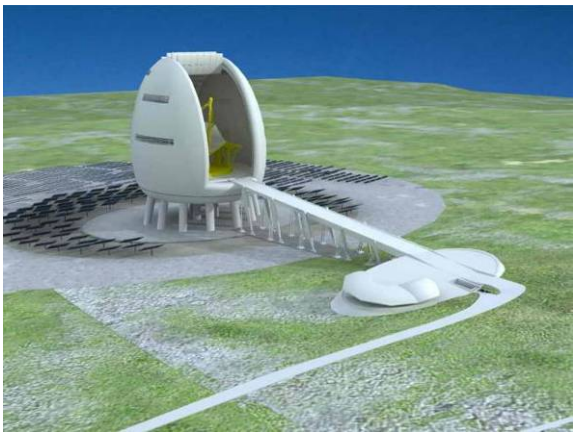

Figure 1: The telescope, the enclosure and the energy plant.

The present report is concerned primarily with CFD analysis of the action of wind, involving computation of the wind action, wind turbulence and vorticity density, structural analysis based on wind loading.

Statistics of the building structure		A single blade	
Total mass	$18{,}000 \cdot 10^3$ kg	Mass	$50 \cdot 10^3$ kg
Total height	166 m	Size	$50 \times 17.2 \times 3$ m^3
Mass of the turnable part	$4000 \cdot 10^3$ kg		

Structural Model and Analysis

Complete three-dimensional models of the structural investigation, based on preliminary analysis of the conceptual model, were generated, see Figure 2. The models are formulated in a manner accommodating each type of structural analysis referred to below.

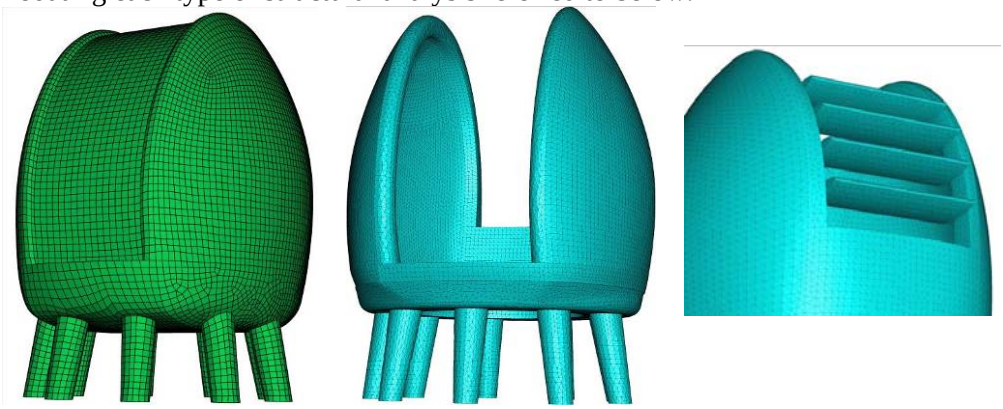

Figure 2: The finite element models used for analyzing the dome in closed, opened and opened with blades configurations.

The structural topology of the shell has not yet been defined in its entirety. The shell is modelled as a sandwich structure, the core of which is defined in terms of its material density percentage. The parametric model is defined in a manner allowing the material content to vary over the height of the structure. This generates a true mass distribution over the structures entire height, also allowing the dynamic behaviour of the structure to be simulated.
The model includes the following parameterized entities: t = overall thickness, t_1 = thickness of the inner layer, t_2 = thickness of the outer layer, t_3 = thickness of the core, E_1 = modulus of elasticity of the inner layer, E_2 = modulus of elasticity of the outer layer, t_3 = modulus of elasticity of the core, see also Figure 3.

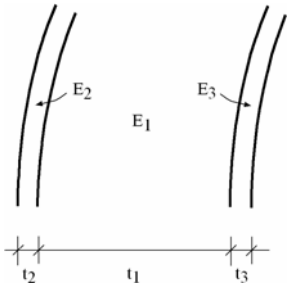

Figure 3: Schematic sketch of the parameters used in the shell calculations.

Load cases

Three different configurations have been analysed for various load cases to determine the deformations and stresses on the enclosure, the base ring and the columns:

Closed dome

- Survival loads
    - Gravitation + Wind speed, 60m/s + Snow, 2000mm + Ice, 230mm

Open enclosure

- Operational loads
    - Gravitation + Wind speed, 27m/s + Snow, 200mm + Ice, 50mm
- Effects of angular acceleration
    - Gravitation + Angular acceleration
- Effects of loads produced by the moving blades

Open enclosure with four blades in an up position

- Operational loads
- Gravitation + Wind speed, 27m/s + Snow, 200mm + Ice, 50mm

Wind loads were applied as pressure on one side of the enclosure according to their distribution as calculated on the basis of CFD-analyses. The snow load was applied to the top part of the enclosure, whereas the ice load was applied to the enclosure in its entirety, except for the bottom part. The pre-processor used in modelling was Abaqus CAE, a general-purpose pre-processor. The various structural analyses conducted were performed using the general finite element program Abaqus Version 6.5. The total number of elements was 370,000 and the total number of unknowns employed was 280,000. The model was exported from Abaqus CAE to a general file format that included the geometrical data for the CFD analyses. Some resulting stress and deformations are shown in Figure 4.

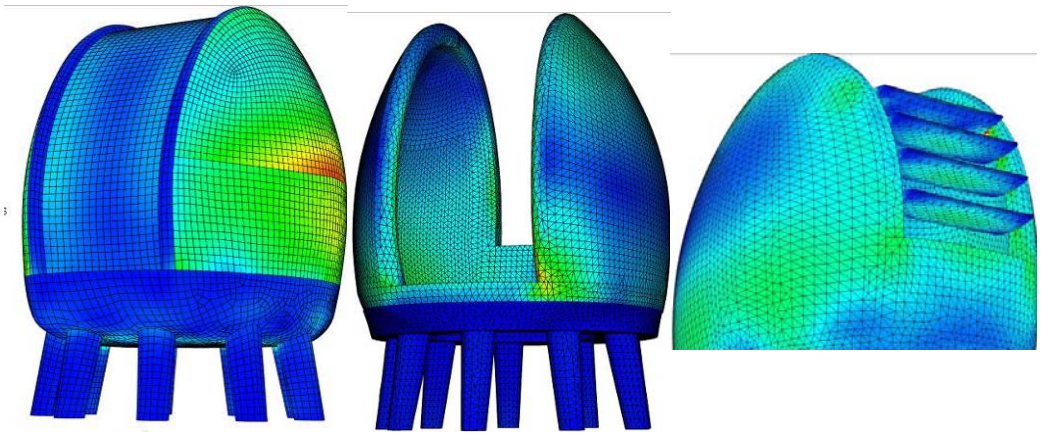

Figure 4: Stresses and deformations for enclosure in closed, opened and opened with blades configurations.

Analysis of the wind and fluid dynamics

The aim of the fluid mechanics study was to investigate the following: the wind load on the building envelope, the airflow inside the building for various blade configurations, and the loading of the blades. It was of interest here to examine how the flow direction is affected by the blades and how the presence of the blades affects the turbulence. In the first part of the study, the closed

building at wind speeds of 27, 40 and 60 m/s was considered and in the second part a configuration in which the building was almost fully open but the wind speed was very moderate, 4 m/s.
The third part of the study involved two-dimensional simulations of a single blade and a set of several blades at a wind speed of 27 m/s. The results of the closed-envelope simulations are used as boundary data for structural analysis of the dome.

Assumptions and limitations

Simulating flow inside and around such a large structure is a formidable task, due to the extremely high Reynolds number that applies, which results in very thin boundary layers along the structure. Since use of time-resolved simulation methods (such as Large Eddy simulation) is not practical here, a Reynolds Averaged Navier-Stokes approach in which statistically stationary wind conditions are assumed was employed instead. The resolution close to the wall is critical to obtaining the correct flow separation for the structure which in turn affects the pressure distribution downwind of the building and thus the force loading as well. The pressure distribution on the upwind side is more accurate since it is less sensitive to the point of separation. The flow is assumed in both cases to be incompressible, density variations thus being neglected.

Analyses, tools and methods

Studies of the following were performed:

- The airflow around the closed building at high wind speeds for certain wind directions
- The airflow in and around the open building at low wind speed.
- The airflow around several of the blades at moderate wind speed.

The first two studies are 3-dimensional, whereas the third one is 2-dimensional in order to enable a higher resolution of the flow to be obtained, particularly in the boundary layers.
For modelling the turbulence, use is made of the RNG k-ε model, which is an improvement over the standard k-ε model through its employing a renormalisation group theory. This allows the eddy viscosity close to the solid surfaces to be damped through the modification of C_μ. The equations and parameters of the model are presented below.
The equations are applied to an unstructured tetrahedral grid, using a first-order upwind finite-volume formulation. The size of the computational domain fro the three-dimensional cases is $1000\times1000\times500$ m^3, in the stream-wise and the cross-stream direction and in the direction normal to the ground, respectively.
In the three-dimensional cases there are about 700,000 node points. Far away from the building, the node distances are of about 25 m, whereas in the region close to the building the grid is refined to the degree that on the building surface itself there are node distances of 1 m each. For the two-dimensional case, the node distances vary from some 25 m in the far field to 1 m close to the blades. Close to solid surfaces, further refinement is added, the first node being located 0.05 m from the walls, resulting in a total of about 75,000 node points. A uniform velocity profile is set at the inlet and the outflow, Neumann conditions being used for all the variables. Slip conditions are set at the upper and the side boundaries. At the walls, no-slip conditions are assumed for the velocities, and standard wall functions are used for the values for k and ε. The air density is set to 0.96 kg/m^3 and the ambient static pressure to 75,000 Pa. At the inlet the turbulence intensity is set to 1%, a dissipation-length scale of 1 m being employed. Figure 6 show some results of the analyses.

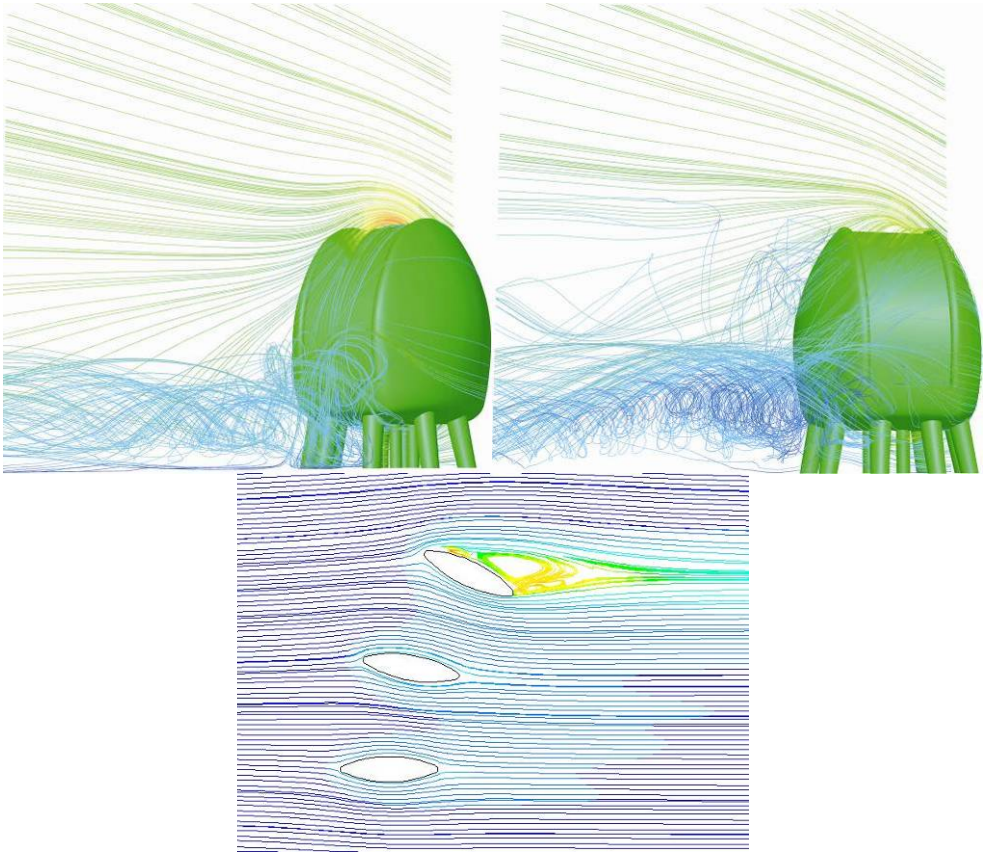

Figure 6: Top: Streamlines for two wind directions, 0 and 45 degrees measured from the rear of the building, below: Streamlines for the 2D flow around a blade configuration, coloured in terms of turbulence intensity.

Crack branching - experiment and simulation of strain assisted corrosion cracking

U. Hejman* **and C. Bjerkén**
Department of Solid Mechanics
MalmœUniversity, Malmœ, Sweden
e–mail: ulf.hejman@ts.mah.se

Summary Crack growth as the result of strain assisted chemically activated material dissolution is numerically and experimentally investigated. The dissolution determines the position of the body surface including the crack tip and crack surfaces, in contrast to conventional models for sharp crack tips using a crack path criteria. A photelastic investigation during the experiment was also performed and indicated that the cracks are prown to follow path dominated by a local Mode I, which also corresponds to the numerical findings.

Introduction

Thin films of metals, ceramics and polymers are used on tools, instruments, mechanical and electronic components to improve corrosive, tribological, electrical, immunological and other properties. Often present in the film is an appreciable residual stress that is a potential driving force for growing cracks. Here interest is focused on strain promomoting material dissolution.

During strain assisted dissolution, loss of atoms to the environment leads to crack growth. The interacting dissolution and mechanical load can, due to surface instabilities, lead to the formation of corrosion pits, cf. Ståhle *et al.* [1]. From such pits or pre-existing notches cracks can develop. Growth rate and growth direction are defined by the dissolution process. The crack path is determined simply as the evolution of the body surface. Thus, crack growth criteria are not needed. Neither are crack path criteria needed, while also the direction of the crack extension is the result of the evolution of the body surface. This means that corrosion cracks are expected to branch repeatedly, in contrast to ordinary cracks [5].

In the present study, crack paths in a bimaterial composite are calculated using an adaptive finite element procedure, cf. [2]. At each time step the strain concentration computed from the load and the geometry predicts the dissolution rate. The geometry is then re-meshed to reflect the updated body geometry. The calculated paths show a large scatter of paths. Experiments are performed to explore the source of this scatter. Here, experiments were performed in polycarbonate that fracture through a dissolution process when it is under mechanical stress and is exposed to acetone. An advantage of this choice is that photoelastic studies could be performed to verify the stress calculations more directly.

Strain Dissolution Crack Growth

A plane surface subjected to strain assisted dissolution is an unstable configuration and perturbation of the surface will develop a waviness with a stress dependent wavelength, cf. Grinfeldt [3] and Asaro and Tiller [4]. The process is driven by the variation of the straining of the surface that accompanies the waviness. Depressions into the body are sites with larger strain, where the material corrodes faster. This leads to pitting and accelerated dissolution. The continuous transition from waviness via pitting to initial cracks makes up the initiatial phase of strain assisted dissolution crack growth.

It is believed that there is a threshold strain, ε_f, under which the mechanical straining does not give any significant material dissolution. For low loads this prohibits all further dissolution. For loads larger than the threshold, the dissolution rate v perpendicular to the surface is assumed to increase as follows:

$$v = C\left(\varepsilon - \varepsilon_f\right) \qquad \text{for} \qquad \varepsilon > \varepsilon_f, \tag{1}$$

where C is a parameter depending only on the materials ability to resist dissolution at the surface and ε is the surface strain. Here the analysis is restricted to crack growth, assuming that a pit or a notch is already present. The growth rate and growth direction of these cracks are results of the dissolution process only. Thus the fracture process is naturally integrated in the model. No other fracture processes are considered. Therefore criteria for crack growth and crack path are not needed. The model brings additional features to the crack tip that solves many of the problems that accompany the assumption that the fracture process region is treated as a point.

Experiments

To study a corrosive process leading to crack growth, polycarbonate exposed to acetone was chosen. The stress field during crack growth was investigated in a standard polariscope.

A specimen was cut from a polycarbonate plate 100 mm wide, 50 mm high and 5 mm thick. A force couple was applied at the mouth of a crack. The polycarbonate plate was glued to a thick beam of aluminium along the side adjacent to the force couple using at two-component epoxy glue. Care was taken to minimise imposed residual stresses from the interface due to the curing of the epoxy. The aluminium bar is regarded as rigid as comparded with the polycarbonate. A 10 mm deep notch was made at the middle of the long free edge of the plate and in between the two loading grips. The experimental configuration is shown in Fig. 1.a.

The load was increased to a level when the dissolution crack started propagating and the acetone was supplied with a rate sufficient to sustain a slow dissolution crack growth. Acetone was gently dropped in the notch and was, by capillary action, sucked to the notch tip. Care was taken to prevent the plate sides outside of the notch from being exposed to the fluid. At regular interval, the current crack and the corresponding fringe pattern was photographed during the crack growth. The crack was allowed to propagate all the way through the specimen. The crack growth rate was estimated to be roughly 20 to 50 mm/s.

The crack width was analysed with an ordinary light microscope to deduce the amount of material dissolved in the process.

The relatively low load at which the cracks grow, made photoelastic observations difficult. Therefore to each experiment a second specimen was used. In this a crack was sawed along the path obtained at the experiment. The crack paths were incrementally sawed with an ordinary contour saw making a 0.5 mm wide notch in the polycarbonate. At each increment the crack length was increased approximately 4 mm and the plate was mounted in the polariscope. Then resulting fringes were photographed using an ordinary digital system camera to identify the local stress state at the crack tip. Even though a much larger load was applied to these stationary cracks not any plastic deformation was observed.

Simulation of the crack propagation

To further explore crack growth based on the dissolution process, a numerical simulation was performed using the finite element procedure developed by Jivkov, cf. [2]. The initial notch needed

to get a reliable result had to be longer than at the experiments and here the initial notch is 0.4L. The development of the crack was followed in small time increments, the material removal is governed by Eq. (1) and the material model asumes a linear elastic material. The resulting evolution of the crack surface demands re-meshing after each time increment. Approximately 2000 elements are used during one time increment, and the ratio of the largest and the smallest element sides is around 4000. The crack growth was followed during 2900 time increments.

Results and Discussion

Figure 1.a shows the resulting crack in its final state from simulation. A curved crack path and branching was obtained in the case of the growth of a surface crack. These features were also found in the experiment. As observed crack branching occurs when the crack has returned to the same depth measured from the free edge, now with a direction heading towards the upper edge. In the experiments however, the crack branched several times and never deviated considerably from the initial direction of growth, towards the rigid interface, see Fig. 1.f. A reason for this could be that in the simulations, plane strain condition and linear elastic prpoerties are assumed, while in the experiment the elastic layer was a thin polycarbonate and polycarbonate does not behave as a intirely linear elastic meterial.

An analysis of the stress field around the crack tip before and after branching is shown in Fig. 1.c and d. This shows that the crack follows a path maintaining a mode I stress state in front of the crack tip. To experimentally confirm this a replica of the crack was made with a saw in the polycarbonate. The plate was stressed and the fringe pattern shown in Fig. 1.e indicate a dominating mode I stress state at the cracktip. This was true for the intire crack path.

For energetic reasons the stress intensity factor of the branches after symmetric branching are around 70 % of the stress intensity factor of the main crack immediately before branching. Thus, the total width of a branched crack should be approximately the same as before branching. This is supported both by the experiment and by the simulation. The average ratio of width after branching versus width before branching is 0.48. The scatter is large and the standard deviation is 0.17. A crack branch is shown in Fig 1.b. This supports the suggested theory that the crack would branch only if it could maintain a constant stress intensity factor after branching. A crack growing in this manner could be caracterised as a fracture toughness controlled crack.

Additionally, at the location where acetone was applied initially there is evidence of a large area of damaged material which may influence the experimental result. However, it is believed that the criterion free method can be a plausible choice for studying situations where criteria for crack growth, crack branching and crack path criteria fail, e.g. interface cracks, crack initiation from notch or surface and meeting cracks.

Concluding remarks

Chemically assisted crack growth can be performed in polycarbonate.

Corrosion crack growth can be computed as a moving boundary problem. Crack growth and path criteria are not needed. The crack follows a pure mode I path.

A threshold strain for acetone affected polycarbonate can be estimated. Finite element calculations are confirmed by photoelastic experiments. This is in the sense that the individual cracks follow near a pure mode I path. The scatter was large both in the experiments and simulations. We draw the conclusion that the source of the scatter is connected to a wobbling crack path.

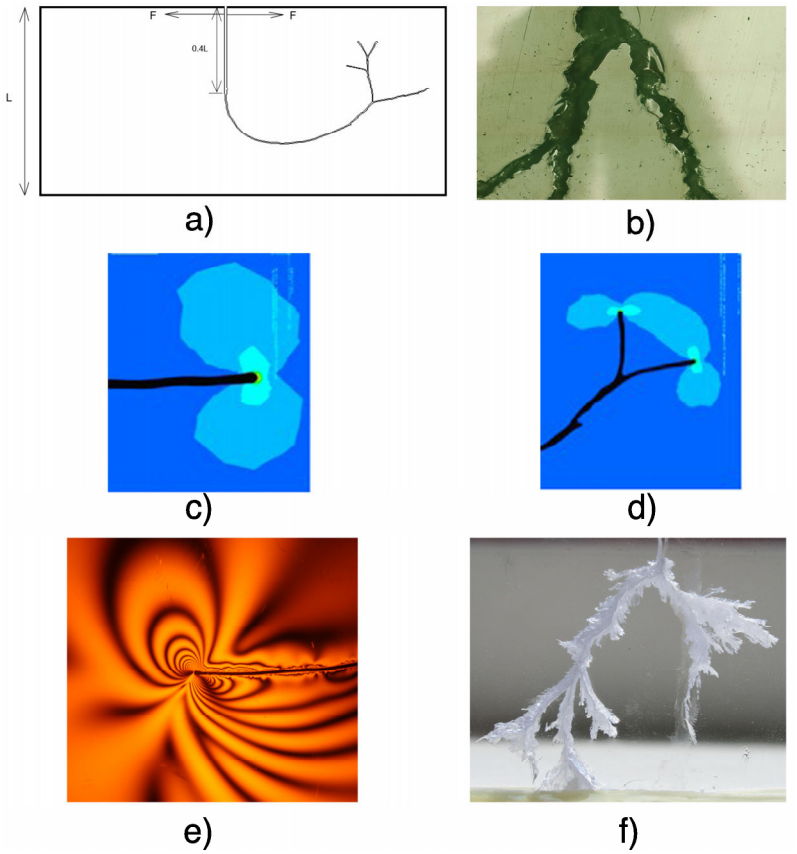

Figure 1: a) Numerical result from a stress corrosion crack gowth simualtion of a surface crack in a polycarbonate layer attached to a steel bar. b) A typical crach branching in polycarbonate from the experiment. c) Stressfield around the cracktip before branching. d) Stressfield around the cracktip after branching. e) Fringepattern at the cracktip. f) The final shape of the corrosion crack in polycarbonate.

Acknowledgement

Support from The Knowledge Foundation for "Biofilms - Research Center for Biointerfaces" under grant no. 2003/0123 is acknowledged.

References

[1] P. Ståle and C. Bjerkén and A. P. Jivkov *On dissolution driven crack growth* Accepted for publication in*Int. J. Solids Struct.*

[2] A. Jivkov PhD thesis, Lund University, Sweden

[3] M.A. Grinfeld *J. Nonlin. Sci.*, **3**, 35–83, (1993).

[4] R.J. Asaro and R.J. Tiller *Met. Trans.*, **3**, 1789–1796, (1972).

[5] R.H. Jones. *Stress- corrosion cracking.* ASM International, Ohio, 0-87170-441-2, (1992).

Dislocation modelling of short fatigue cracks

P. Hansson and S. Melin
Division of Mechanics
Lund Institute of Technology, Box 118, SE-22100 LUND
Per.Hansson@mek.lth.se

ABSTRACT. *The influence of different load cycles on the growth of a short edge crack has been studied using a discrete dislocation technique. The external boundary is modeled with dislocation dipole elements and the plasticity is modeled by discrete dislocations. The crack is located within one grain in a bcc material, and is assumed to grow through a single shear mechanism, due to nucleation and annihilation of discrete dislocations along preferred slip planes.*

INTRODUCTION

It is well known that the behavior of short cracks deviates from that of long cracks. Short cracks can grow at load levels well below the threshold value for long cracks at high rates. Often, a large portion of a components life is spent by propagating of microstructurally short cracks, typically of the size of a few grains. Such small cracks can not be treated by the standard methods for long cracks due to the relative large plastic zone and strong influence from the surrounding microstructure.
Experimental studies has shown that short cracks grow through a single shear mechanism, cf. Surresh [1], creating a zigzag shaped crack. Other studies showing the formation of a zigzag shaped crack were made by Uematsu et al. [2] in the low K region in silicon iron and by Zhang [3] in ultra-fine grain size aluminum.
For very low growth rates, in the order of a few Burgers vectors per cycle only, it is important to account for the discrete dislocations within the material. Riemelmoser et al. [4] and Riemelmoser and Pippan [5] have developed such a discrete dislocation model for a long mode I crack to study the cyclic crack tip plasticity and plastically induced crack closure. A similar model describing a short propagating mode I crack subjected to fatigue loading, was developed by Bjerkén and Melin [6, 7], to study the growth behavior and influence of grain boundaries on the crack growth.
In this study a discrete dislocation model is developed to study a short propagating edge crack, subjected to cyclic loading, located within one grain in a bcc material. Both the geometry and the plasticity are described with discrete dislocations. The crack growth is in this model due to nucleation, movement and annihilation of discrete dislocations along preferred slip planes in the material.

STATEMENT OF THE PROBLEM

The growth of a microstructurally short edge crack located within one grain, subjected to fatigue loading, cf. Fig. 1, have been investigated under plane strain conditions. The crack grows in a single shear mechanism under quasi-static conditions due to nucleation, movement and annihilation of discrete dislocations along preferred slip planes separated an angle β, dashed lines in Fig. 1, within the material. The initial crack, of length a_0 and inclined an angle α to the normal of the free edge, is located

within a semi-infinite body. The load is applied parallel to the free edge and is varied between a maximum value $\sigma^{\infty}_{yy\,max}$, and a minimum value $\sigma^{\infty}_{yy\,min}$. The grain boundary is parallel to the free edge, located a distance of l_{GB} in front of the original crack tip position, and is treated as an impenetrable hinder for the dislocations.

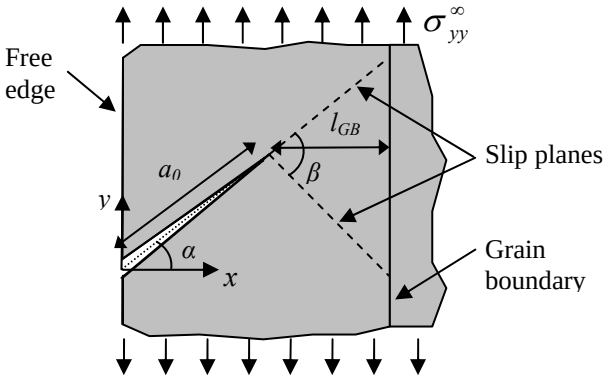

Fig. 1. Initial geometry of the edge crack

DISCRETE DISLOCATION FORMULATION

The model in this study rests solely on a discrete dislocation formulation, describing both the geometry and the plasticity by discrete dislocations. Only plane problems are addressed and therefore only edge dislocations are used in the formulation.

External boundary

The external boundary, defined as the free edge together with the crack itself, is modeled using dislocation dipole elements, cf. Hansson and Melin [8]. A dipole element consists of four dislocations, two glide dislocations and two climb dislocations with equal size of the two dislocations, with same character, but opposite sign. The dislocations are situated at the end points of the element and the stress is calculated at the center of the element. By both including climb and glide dislocations in the formulation, both gliding and opening between the crack surfaces can be modeled.

The dipole elements were placed along the free edge, at distances from the crack mouth far larger than the crack length, to model the semi infinite body. While the crack continued to grow along the upper slip plane only, the element size of the elements closest to the crack mouth was increased, in order to model the growth of the straight crack. When the crack started to grow in a zigzag shape additional elements were added to model the newly formed crack surfaces.

The stress at an arbitrary point within the material is calculated as the sum of the stress contributions from all dislocations, both the physical dislocations along the slip planes and the dislocations in the dipole elements and the applied external load. The magnitudes of the dipole dislocations are determined from an equilibrium consideration, Eq. (1), describing the normal and shear stress along the external boundary. Knowing that the normal and shear stresses must equal zero for the free edge and the parts of the crack that is open, the magnitude of the dipole dislocations can be calculated.

$$\mathbf{G}\mathbf{b}_{\mathbf{boundary}} + b\mathbf{G}_{\mathbf{internal}} + \boldsymbol{\sigma} = 0 \qquad (1)$$

In Eq. (1) **G** is matrix containing the influence functions, cf. Hills et al [9], describing the stress field created by a dislocation along the external boundary. $\mathbf{b}_{\mathbf{boundary}}$ is a vector holding the magnitudes of the dipole dislocations. *b* is the Burgers vector of the material, $\mathbf{G}_{\mathbf{internal}}$ is a vector containing the influence functions for the internal dislocations and $\boldsymbol{\sigma}$ is a vector containing the contribution from the applied external load.

Dislocation nucleation, motion and annihilation

At each load level, the resolved shear stress is calculated a small distance r_{nuc} in front of the stress concentrations, i.e. the crack tip and eventual corner points of the crack. If the resolved shear stress exceeds the nucleation stress, a dislocation pair is assumed to nucleate along the slip plane emanating from this stress concentration. A dislocation pair consists of two dislocations of equal size but opposite sign separated a small distance, r_{nuc}. When nucleated, the dislocation with burgers vector pointing inwards in the material, moves inwards in the material along its slip plane. Such a dislocation is called a positive dislocation. The other dislocation, called a negative dislocation, remains at the crack tip causing either the crack surfaces to open or glide, depending on which slip plane it is situated on. The positive dislocation moves along its slip plane as long as the resolved shear stress at its position exceeds the lattice resistance τ_{crit}, of the material. The equilibrium position for the positive dislocation is found through an iterative process, moving the dislocation a small distance a time until the resolved shear stress at its position falls below τ_{crit}.

Due to the complex geometry of the crack, a new method for determining the nucleation stress was used [8]. The nucleation stress is defined as the lowest stress at the nucleation point for which the positive dislocation in the newly nucleated pair travels inwards in the material when nucleated. This definition of nucleation stress is geometry dependent, meaning that the nucleation stress must be determined for all new crack geometries, at the beginning of each new load cycle.

During the unloading part of the loading cycle, dislocations will move back towards the crack. When a dislocation gets close enough, it annihilates with its negative counterpart. Under the assumption that no healing of the crack surfaces occurs, this results in crack growth a distance of one Burgers vector in the corresponding direction.

Crack growth

It is assumed that no dislocations exist within the material at the beginning of the first load cycle. A description of the first load cycle is seen in Fig. 2. When the applied load is increased, dislocation pairs will nucleate from the crack tip and the positive dislocations will move inwards in the material along its respective slip plane, whereas the negative dislocations will remain at the crack tip. The nucleation of new dislocations continues until the maximum load is reached and pile ups of dislocations have been formed at the grain boundary. When the load is decreased, the dislocations starts to move back towards the crack and some will eventually annihilate with its negative counterpart. Annihilation results in crack growth in the corresponding direction. If annihilation occurs along a new slip plane a kink is formed at the crack tip and a new active slip plane is introduced.

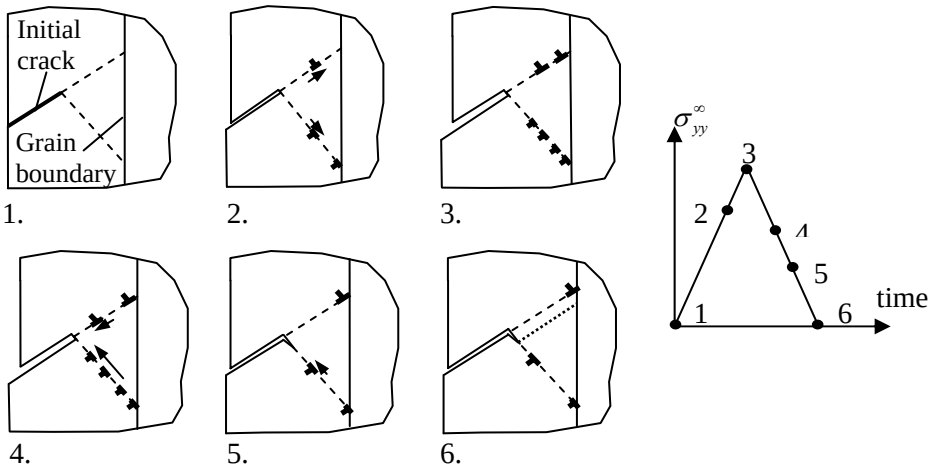

Fig. 2. Schematic description of the first load cycle. Dashed lines are original slip planes, dotted line is the new activated slip plane at the new crack tip position.

Initial conditions

The material in this study is pure iron and is assumed to be linear elastic with a body centred cubic (bcc) crystal structure. The material parameters at room temperature are shown in Table 1, cf. Askeland [10].

Table 1. Material data for bcc-iron

Shear modulus, μ	80GPa
Poisson's ratio, v	0.3
Burgers vector, b	0.25nm
Lattice resistance, τ_{crit}	40MPa
Distance to nucleation point, r_{nuc}	$6b$
Nucleation stress, τ_{nuc}	1.3-2.0GPa

In a bcc material, slip occurs in the close packed {110} planes in <111> directions, cf. Hull and Bacon [11]. In this study slip is assumed to take place in the (110) and ($\bar{1}10$) planes, giving four possible slip directions. When constructing a 2-D model of the slip system by combining two of these slip directions, two different 2-D systems are created, depending on which slip directions that is considered. The difference between the two 2-D models is the angle between the active slip planes, β, cf. Fig. 1, either β = 70.3° or β = 109.4° [8].

RESULTS

The developed dislocation based model can be used for a number of different simulations regarding the growth behavior of short cracks. Some examples are simulations of the development of the plastic zone, the effects of overloads, influence of the applied load range, crack growth per load cycle da/dN, resulting crack shape, crack opening and crack closure.

REFERENCES

[1] SURESH S.: *Fatigue of Materials, second edition*. University Press, Cambridge, 1998.

[2] SUGETA A., UEMATSU Y., HASHIMOTO A., JONO M.: Atomic force microscopy of fatigue crack growth behaviour in the low K region. *Int Jnl of Fatigue,* 26:1159-1168, 2004.

[3] ZHANG J.Z.: A shear band decohesion model for small fatigue crack growth in an ultra-fine grain aluminium alloy. *Engineering Fracture Mechanics,* 65:665-681, 2000.

[4] RIEMELMOSER F.O., PIPPAN R., KOLEDNIK O.: Cyclic crack growth in elastic plastic solids: a description in terms of dislocation theory. Computational Mechanics, 20:139-144, 1997.

[5] RIEMELMOSER F.O., PIPPAN R.: Mechanical reasons for plasticity-induced crack closure under plane strain conditions. *Fatigue & Fracture of Engineering Materials & Structures,* **21**:1425-1433, 1998.

[6] BJERKÉN C., MELIN S.: A tool to model short crack growth using a discrete dislocation formulation. *Int Jnl of Fatigue,* 25(6):559-566, 2003.

[7] BJERKÉN C., MELIN S.: A study of the influence of grain boundaries on short crack growth during varying load using a dislocation technique. *Engineering Fracture Mechanics,* 71(15):2215-2227, 2004.

[8] HANSSON P., MELIN S.: Dislocation-based modeling of the growth of a microstructurally short crack by single shear due to fatigue loading. *Int Jnl of Fatigue,* 27:347-356, 2005.

[9] HILLS D.A., KELLY P.A., DAI D.N.,KORSUNSKY A.M.: Solution of Crack problems: The distributed dislocation technique. Kluwer Academic Publisher, 1996.

[10] ASKELAND D.R.: *The Science and Engineering of Materials*, third edition. Stanley Thornes (Publishers) Ltd, 1998.

[11] HULL D., BACON D.J.: Hull, D. and Bacon, D, J. *Introduction to Dislocations*, fourth edition. Butterworth-Heinemann, 2001.

Dissolution Driven Fracture – Simulation of Crack Growth

C. Bjerkén
Division of Materials Science
Malmö University, Malmö Sweden
e–mail: christina.bjerken@ts.mah.se

Summary The growth of a crack subjected to corrosion fatigue is studied using adaptive finite elements. The crack growth is the result of a repeated cycle of dissolution of the material, formation of a protective oxide film and break-down of the oxide film due to straining at the surface. The dissolution rate is assumed to be proportional to this stretching. The growth of a semi-infinite crack lying in an infinite strip subjected to different degrees of mixed-mode loading is studied.

Introduction

During stress corrosion, loss of atoms to the environment leads to crack growth. This is a dissolution process that starts i.e. if bare metal is exposed to aggressive environments. Fortunately, an impermeable film of mainly metal oxides or hydroxides is formed by dissolved metal on several metals. Even though the thickness of this film is typically not more than 10 nm, it reduces the rate of dissolution by several orders of magnitude, cf. [1]. An intact protective film increases the life of the structure tremendously. However, repeated changes of the electrochemical conditions or cyclic mechanical load damage the film, which leads to additional material loss. Several experimental reports show that active loading in terms of either monotonically increasing or fatigue load is an essential prerequisite for development of corrosion cracks, cf. [2]. The passivating film is, as being an oxide or hydroxide compound, believed to have ceramic material properties. As such it is presumably brittle. Here it is supposed to fracture when stretched more than a threshold strain, ε_f.

If the threshold strain is exceeded, the film breaks and leave gaps where bare metal is exposed to the environment. The area extent of these gaps is assumed to be proportional to the strain exceeding the threshold strain. The broken film leaves gaps that give a discontinuous exposure to environment. In the present study, the dissolution rate is simply assumed to be proportional to the mechanical stretching of the body surface reduced with the threshold strain.

The film is known to be extremely thin as compared with the linear dimensions of the body. Therefore it is not contributing in any significant way to the structural stiffness. In the present analysis, the presence of the film, broken or unbroken, is ignored when the mechanical behaviour of the structure is computed.

The interacting dissolution and mechanical load leads to a roughening of the body surface, and, after localization, to initiation of corrosion pits. For large threshold strains, the pits assume the shape of cracks. These cracks are integral parts of the body surface. Growth rate and growth direction are results of the dissolution process. The model brings additional features to the crack tip in contrast to an assumed sharp crack tip, where the fracture processes are confined to a point and all the details of the crack tip state is given by a single parameter, such as a stress intensity factor or a crack tip driving force. This permits determination of the crack growth simply as the evolution of the body surface. Thus, crack growth criteria are not needed. Neither are crack path criteria needed, while also the direction of the crack extension results from dissolution rate along the body boundaries in the crack tip vicinity.

In the present study, crack paths are calculated using an adaptive finite element procedure. The strain concentration computed from the load and the geometry of the crack tip vicinity

predicts dissolution, i.e. removal of material and crack growth. The geometry is repeatedly re-meshed as the body shape is updated to accommodate the extending crack. The mesh maintains a resolution sufficient for a detailed calculation of the strain distribution in the crack tip region to ensure that the crack growth direction is accurately predicted.

Paths are found for a few cases involving different degrees of mixed mode loading. The results are compared with results for established crack path criteria.

Computational method

In the present study, a computational method that evolves a body surface by an adaptive finite element procedure is used, cf. Jivkov [3]. The finite element code ABAQUS [4] is adopted for computing the strains along the surface. During loading, the oxide film is assumed to crack if the strain along the surface exceeds the threshold strain ε_f. This results in dissolution of material. Thus stretching of the body surface controls the rate of dissolution. A linear relation between the surface strain ε and the dissolution rate v is assumed:

$$v = C\,(\varepsilon - \varepsilon_f) \quad \text{for } \varepsilon > \varepsilon_f \tag{1}$$

where C is a constant depending only on the environment. The rate v is, in the present context, the linear extent per load cycle. The period of the load cycle is assumed to be long enough to allow full recovery of the protective oxide film. The electrochemical potential of the system is contained within C. The surface boundary is moved according to Eq. 1 along the normal direction of the surface. Because of the extremely small thickness of the oxide film, it is not included in the finite element model. Six-node triangular elements are used and re-meshing is done for each load cycle. Further details of the model cf. Jivkov [3]. The material is assumed linear elastic, and is subjected to fatigue loading under plane strain conditions.

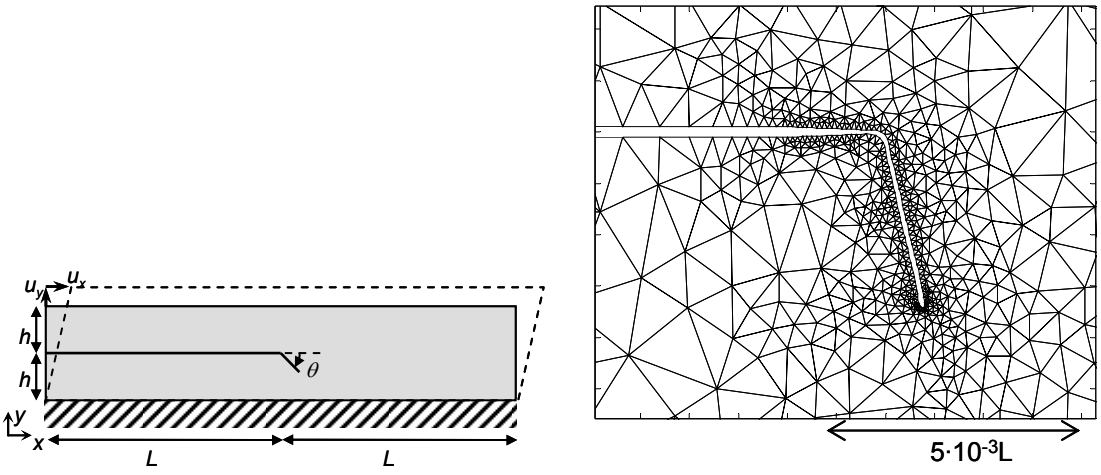

a) b)

Figure 1.a) Geometry of the large strip used for the finite element analysis b) Mesh after 200 load cycles for a strip with global K_{II} load.

Results

The crack propagation during is simulated for a semi-infinite crack in a strip, with the initial crack oriented parallel to the surface of the strip, loaded in different degrees of mixed mode. The

geometry used for the simulations are shown in Fig. 1.a. The length of strip is $2L$ and the thickness $2h$, and the lower edge of the strip is allowed to move in the x-direction but is fixed in the y-direction. The load is applied at the upper edge as prescribed displacements u_x and u_y. The crack has an initial length L and it is located at $y = h$, between $x = 0$ and L, with its tip at $x = L$. Simulations are performed for a few hundred cycles for eight different degrees of mixed mode loading. In Fig. 1.b, a typical finite element mesh is shown. Approximately 2000 elements are used during one load cycle, and the ratio of the largest and the smallest element sides is around 4000. The displacement ratio u_x/u_y equals K_{II}/K_I, and the following ratios are investigated: 0, 0.2, 0.5, 1, 2, 5, 10 and ∞.

In Fig. 2.a, the crack paths after 200 load cycles for the investigated K_{II}/K_I-ratios are shown. The kinked part of a crack is approximately $4 \cdot 10^{-3} L$, the width of the crack is governed by the load and ε_f, cf. [3]. It can be seen that the larger the K_{II}, the more stable the shape of the crack. The crack driven by a global K_I-loading shows a tendency to branch at the crack tip. It can also be noted that for pure K_I global load the present method results in a crack path that is not horizontal initially. Though, after additionally a few hundred cycles this crack will flatten and find a path that is parallel with the initial crack.

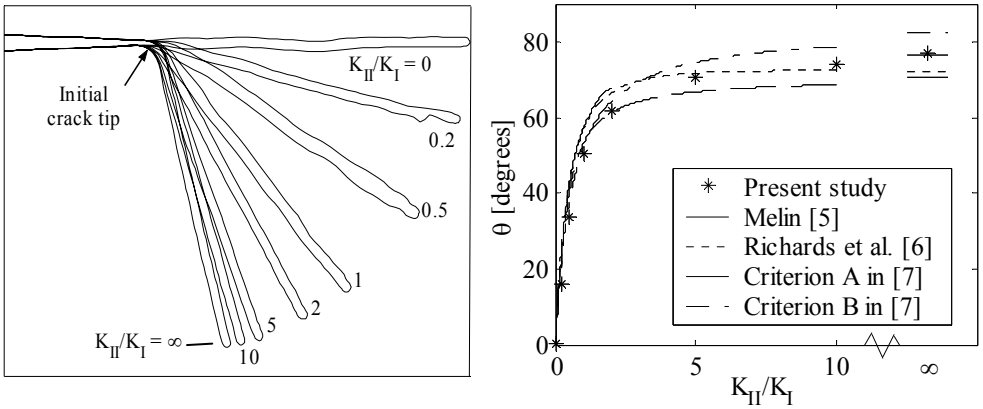

Figure 2.a) Crack paths for different K_{II}/K_I-ratios b) Kink angles versus K_{II}/K_I for different criteria

The kink angle, θ, is measured to the centre line of the crack, and the values are plotted in Fig. 2.b. These results are compared to kink angles obtained by four different crack paths criteria for sharp cracks found in the literature. Melin [5] computed kink angles by maximizing the local mode I stress intensity factor, k_I, at the tip of an infinitesimal kink of a sharp crack. Richard et al. [6] use a criterion based on a numerical adoption to experimental findings. Additionally, two of the criteria studied by Bergqvist and Guex [7] are used for comparison; the criteria of maximum principle stress by Erdogan and Sih [8] (Criterion A) and of the maximum J-integral by Sih [9] (Criterion B). All criteria give similar results as in the present study. For dominating global K_{II} loading, i.e. $K_I=0$, the hypothesis of maximum k_I shows best agreement.

Discussion

The present method is based on the calculations of strains along the parts of a body that are assumed to be in contact with a corrosive media. The tip of the resulting crack has a finite geometry as opposed to conventional methods where it is treated as a single point. The part of the crack tip region that exceeds the threshold strain for oxide film breakage will dissolve and the

crack grows by evolving the surface of the body. During crack growth local broadening of the crack tip region will develop, which in turn can induce crack branching.

Conclusions/Concluding remarks

In the present study, it is shown that crack paths can be followed without criteria for neither crack growth nor crack path. An adaptive finite element procedure was used to simulate the moving boundary of a body subjected to strain driven corrosion fatigue.

Results for kink angles due to mixed mode loading of a crack computed with the presented criteria free method was found to agree well with predictions from criteria for sharp cracks found in the literature. The best agreement was found for dominating global K_{II} loading, while for dominating K_I loading the deviation was larger.

It is believed that the criterion free method can be a plausible choice for studying situations where criteria for crack growth, crack branching and crack path criteria fail, e.g. interface cracks, crack initiation from notch or surface and meeting cracks.

References

[1] Smallman, R.E. and Bishop, R.J. *Modern Physical Metallurgy Materials Engineering*, 6th ed, pp. 376-387, Butterworth-Heinemann, Avon, UK, (1999).

[2] Jones, R.H., and Ricker, R.E., *Stress-Corrosion Cracking*, pp. 1-39, Jones, R.H. (Ed.) ASM International, USA, (1992).

[3] Jivkov, A.*, Strain-assisted corrosion cracking and growth rate inhibitors*, PhD thesis, Lund University, Sweden, (2002).

[4] *ABAQUS User's manual*, Version 6.4, Abaqus Inc. ,(2004).

[5] Melin, S., Fracture from a straight crack subjected to mixed mode loading, *Int. J. Fract. Mech.* **32**, 257-263, (1987).

[6] Richard, H.A., Fulland, M. and Sander, M., Theoretical crack path prediction, *Fatigue Fract. Engng Mater. Struct.* **28**, 3-12, (2005).

[7] Bergkvist, H. and Guex, L., Curved crack propagation, *Int. J. Fract.* **15***,* 429-441, (1979).

[8] Erdogan, F. and Sih, G.C., On the crack extension in plates under plane loading and transverse shear, *J. Basic Engng*, **85**, 519-527, (1963).

[9] Sih, G.C., Strain energy density factor applied to mixed mode crack problems, *Int. J. Fract.*, **10**, 305-321, (1974).

Micromechanical modeling of rupture in combined tension and shear

Imad Barsoum and Jonas Faleskog
Department of Solid Mechanics
Royal Institute of Technology, Stockholm, Sweden
e–mail: imad@hallf.kth.se, jonasf@hallf.kth.se

Summary A micromechanics model based on the theoretical framework of plastic localization into a band introduced by Rice [1] is developed. The model employed consists of a planar band with a square array of equally sized cells, with a spherical void located in the centre of each cell. The micromechanics model is applied to analyze failure by ductile rupture in experiments on double notched tube specimens subjected to combined tension and torsion carried out by the present authors [2]. Two rupture mechanisms can be identified, void coalescence by internal necking at high triaxiality and void coalescence by internal shearing at low triaxiality. The two failure criteria capture the transition between the two rupture mechanisms successfully and are in good agreement with the experimental result.

Introduction

In [3], experiments are carried out on a double notched tube specimen subjected to a combination of tension and torsion. By applying different ratios of torsion and tension, stress triaxiality can be controlled and varied in the tests. At sufficiently high stress triaxiality, the specimens fail by a ductile rupture mechanism characterized by voids that have grown to impingement and coalesce by internal necking, as seen by the fractograph in Figure 1(a). However, at sufficiently low stress triaxiality failure occurs by plastic shear localization in ligaments between voids, see fractograph in Figure 1(b). In the present work a micromechanics model was developed with the purpose to investigate the conditions that govern the transition between the two rupture mechanisms observed in the experiments [3] and shown in Figure 1.

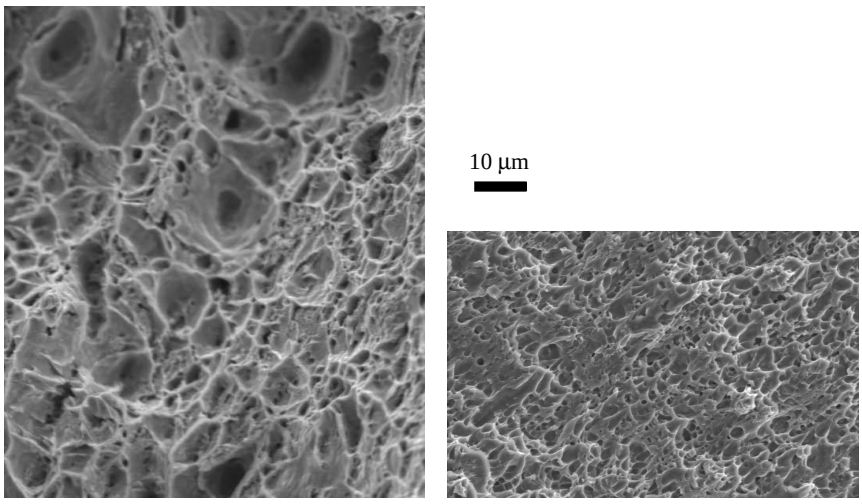

Figure 1: Scanning electron microscope fractographs illustrating two different rupture mechanisms: (a) void coalescence by internal necking and (b) void coalescence by internal shearing.

Micromechanical model

To model the failure in the tube experiment[3], we employ a micromechanical model where the material deforms under the macroscopic stress state of combined generalized tension and generalized shear as shown in Figure 2(a). The material is assumed to contain an initial planar band with a regular square array of pre-existing voids, which can be viewed as initial imperfections that may induce localization into a symmmetric mode, a shear mode or a combination of both [1]. Due to the regular array of voids, attention can be restricted to a three-dimensional unit cell as indicated in Figure 2(b). The initial ratio of void size to void spacing is defined as $\chi_0 = R_0/D_0$, where D_0 is the initial width of the unit cell. The behavior of the matrix material is taken to be homogeneous, elastic-plastic with isotropic hardening and modeled by a finite strain J_2 flow theory. The unit cell is loaded such that the macroscopic stresses acting on the cell follow the proportional history

$$\Sigma_{22}/\Sigma_{11} = \Sigma_{33}/\Sigma_{11} = \rho_n, \qquad \Sigma_{12}/\Sigma_{11} = \rho_s, \tag{1}$$

where ρ_n and ρ_s are prescribed constants. By varying ρ_n and ρ_s a stress state of combined generalized tension and generalized shear can be accomplished. Hence, stress triaxiality T and the Lode parameter μ will remain constant during the load history as

$$T = \frac{\Sigma_{\mathrm{h}}}{\Sigma_{\mathrm{e}}} = \frac{1+2\rho_n}{3\sqrt{(1-\rho_n)^2+3\rho_s^2}}, \tag{2}$$

$$\mu = \frac{2\Sigma_{\mathrm{II}} - \Sigma_{\mathrm{I}} - \Sigma_{\mathrm{III}}}{\Sigma_{\mathrm{I}} - \Sigma_{\mathrm{III}}} = -\frac{(1-\rho_n)}{\sqrt{(1-\rho_n)^2+4\rho_s^2}}, \tag{3}$$

where Σ_{h} and Σ_{h} are the mean and the Mises effective value of the macroscopic stresses respectively and $\Sigma_{\mathrm{I}} \geq \Sigma_{\mathrm{II}} \geq \Sigma_{\mathrm{III}}$ are the principal stresses.

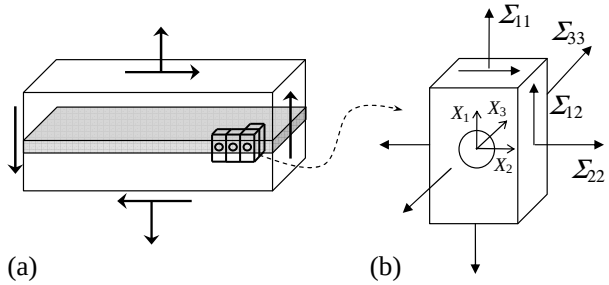

Figure 2: Micromechanics model: (a) homogeneous material with a band containing pre-existing voids and (b) macroscopic stresses acting on the unit cell referring to a Cartesian coordinate system with origin at the centre of the void.

The deformation of the unit will consist of an uniform part outside the band of localized deformation and a non-uniform part pertaining to the band of localized deformation. The volume average of the deformation gradient for the 3D unit cell can be expressed as

$$\bar{\mathbf{F}} = \mathbf{F}^0 + \bar{\mathbf{F}}^q \tag{4}$$

Here, $\mathbf{F}^0$ denotes the uniform part the deformation gradient outside the band of localized deformation whereas $\bar{\mathbf{F}}^q$ is the non-uniform part. Hence localization of deformation into a narrow planar band can be defined as [4]

$$\left\|\dot{\bar{\mathbf{F}}}\right\| / \left\|\dot{\mathbf{F}}^0\right\| \to \infty. \tag{5}$$

For further details regarding the micromechanical model and the numerical implementation c.f. [2, 5].

Results

Two materials with different stress-strain behavior were considered, Weldox 420 and Weldox 960. The loading conditions of the unit cell, Eqn. (2, 3), were chosen such that it resembles the stress state at failure in the centre of the notch of the double notched tube specimen. The stress state, T vs. μ, at failure for the two materials is depicted in Figure 3, which were obtained from the experimental work in [3].

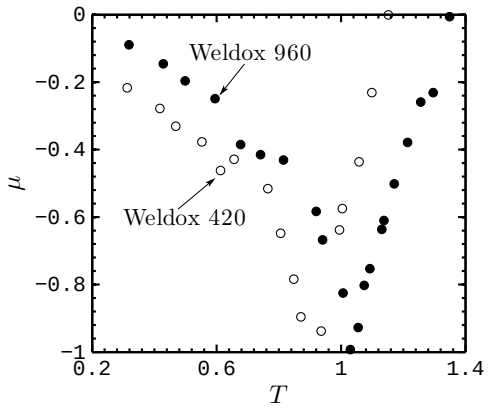

Figure 3: The Lode parameter μ vs. stress triaxiality T in the centre of the notch at failure (c.f. [3]). Open circles pertain to Weldox 420 and solid circles pertain to Weldox 960.

The outcome of the micromechanics analysis are summarized and compared with the experimental results in Figure 4(a) for Weldox 420 and in Figure 4(b) for Weldox 960, where critical values of strain E_e are plotted vs. triaxiality T. The solid circles represent the effective plastic strain in the centre of the notch at failure in the experiments. The thin solid lines, corresponding to the three different χ_0 values, are theoretical curves from the micromechanics model that indicate failure by localization according to Eq. (5), which marks the onset of void coalescence by internal necking between voids and subsequent fracture by ductile rupture. Note that the theoretical curves captures the experimental results well for triaxiality values larger than about 0.8 and 1.0 for Weldox 420 and Weldox 960, respectively. In the low triaxiality regime the solid lines representing the localization criterion do not at all capture the experimental outcome. In fact the pre-existing layer of voids does not seem to play a role for the onset of fracture. Instead a simple criterion based on the attainment of a critical shear deformation was employed. For this purpose it was assumed that failure occurs when the shear component $\bar{F}_{21}$ of the volume average

of the deformation gradient, Eq. (4), reaches a critical value. The thick lines in Figures 4 signifies this failure criterion. It can be observed that the agreement with the experimental results are good.

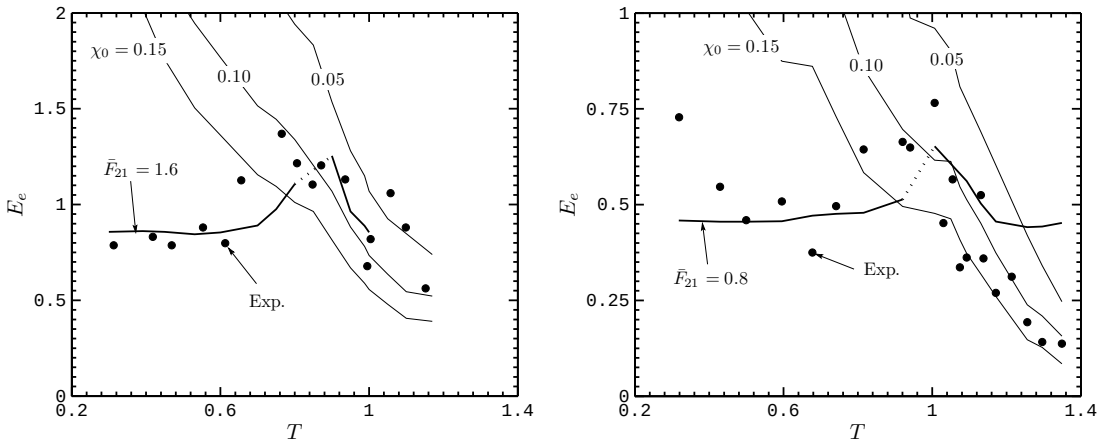

Figure 4: Failure locus for (a) Weldox 420 and (b) Weldox 960, where the macroscopic effective strain E_e at failure is plotted vs. stress triaxiality T. The solid circles represents experimental results. The three thin lines indicate failure by localization according to Eq. (5) and the thick line indicates failure when $\bar{F}_{21} = 1.6$ and 0.8 is attained for Weldox 420 and Weldox 960, respectively.

Concluding remarks

In this study a micromechanical model to investigate the rupture mechanisms in combined tension and shear is performed. The model which enables the examination of two rupture mechanisms leading to ductile rupture, void coalescence by internal necking and void coalescence by internal shearing, captures the experimental trend and the transition between the two rupture mechanisms well. The void coalescence by internal necking is predicted by the onset of localization of deformation, whereas shear failure is predicted by a critical shear deformation criterion.

References

[1] J R Rice. The localization of plastic deformation. In W T Koiter, editor, *Theoretical and applied mechanics*, pages 207–220. North-Holland, 1977.

[2] I Barsoum and J Faleskog. Rupture mechanisms in combined tension and shear—micromechanics. *Submitted for publication*, 2006.

[3] I Barsoum and J Faleskog. Rupture mechanisms in combined tension and shear—experiments. *Submitted for publication*, 2006.

[4] A Needleman and V Tvergaard. Analysis of plastic flow localization in metals. *Applied Mechanics Reviews*, 45:S3–S18, 1992.

[5] I Barsoum. *Ductile failure and rupture mechanisms in combined tension and shear.* Licentiate thesis in Solid Mechanics, Royal Institute of Technology, Stockholm, Sweden., 2006.

MIXED MODE ENERGY RELEASE RATE ANALYSIS BY A BEAM THEORY APPLIED TO TIMBER BEAMS WITH A HOLE

P. J. GUSTAFSSON
Division of Structural Mechanics, Lund University, SE-221 00 Lund, Sweden

ABSTRACT before NSCM October, 2006, in Lund

Wood is very weak perpendicular to its grain and the strength of timber structural elements and joints is therefore often governed by tensile and shear fracture perpendicular to the grain. Strength design relating to such fracture is in timber engineering codes of practice commonly dealt with by empirical strength equations or by some simple maximum stress criterion. More rational strength analysis is feasible by use of various material models and fracture criteria: deterministic/stochastic linear/nonlinear material models with finite/infinite strength and zero/finite fracture energy of the material, Table 1. The conventional deterministic linear elastic stress criterion assuming finite strength and zero fracture energy is predominant in general timber engineering strength design. The possibility of engineering applications of linear elastic fracture mechanics is however gaining increasing attention. This is mostly by two reasons: a) element and joints with some kind of stress singularity can not be analysed by conventional stress criteria and, b), the insight that timber engineering application of fracture mechanics is often possible and simple by use of beam theory. The study discussed in this presentation relates to further development of beam theory linear elastic fracture mechanics. The material is assumed to be linear elastic with strongly anisotropic properties giving crack growth according to the orientation of the material. The specific engineering application considered is strength analysis of a glulam timber beam with rectangular hole, Figure 1 b). For this case is comparison made with experimental data. Evaluation of beam theory results is also made means of plane stress finite element analysis.

Table 1. Methods of strength analysis. G_f denotes fracture energy and f_t material strength.

	Deterministic		Stochastic	
	f_t finite	$f_t \to \infty$	f_t finite	$f_t \to \infty$
$G_f = 0$	Conventional stress criteria	--	Weibull weakest link model	--
$G_f \neq 0$	Non-linear fracture mechanics	Linear elastic fracture mechanics	Probabilistic non-linear fract. mech	Probabilistic linear fract.mech.

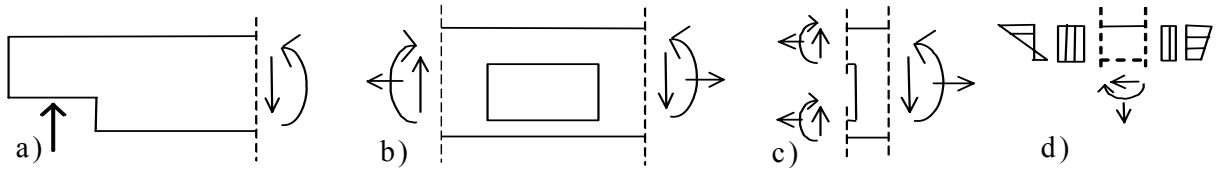

Figure 1. An end-notched beam (a), a beam with a hole (b), a part of infinitesimal length (c) and its upper part (d).

An equation for the energy release rate during crack extension and the corresponding strength of end-notched beams (Figure 1 a)) derived by compliance analysis using conventional beam theory was presented and applied to timber beams about 20 years ago. This strength equation is now used in timber engineering codes of practice. Use of the same kind of approach to beams with a hole may seem close at hand but has proved to be more difficult both in relation to engineering analogies with end-notched beams and more basic beam theory studies. This is due to: (1) significant influence of

shear makes division of the total energy release rate into modes 1 and 2 necessary, (2) normal force acting on the cross section must be considered and (3) the cross sectional forces and moments acting on the parts above and below the hole are statically indeterminate. Issue (1) is of a basic nature and issues (2) and (3) makes the calculations more comprehensive.

An infinitesimally short part of the beam at the end of the hole is considered (Figure 1c)). The horizontal and vertical forces and the bending moment acting across an infinitesimal horizontal section (Figure 1d)) along the beam part can be calculated by the equations of equilibrium. The energy release rates for modes 1 and 2 can then be obtained by using the method of work of crack closure calculation with consideration to the deformations of the infinitesimal parts below and above the horizontal section. The vertical force contributes to mode 1, the horizontal force to mode 2 and the moment influences both modes. The strength of the beam is then found by using a mixed mode fracture criterion, e.g. the Wu criterion. The general case gives an extensive strength equation, but for various special cases of engineering interest can more user-friendly equations be found. Figure 2 shows an example of theoretically predicted and experimentally determined strength. The example relates to centrically located square holes with side length S, and with and without rounded corners. b is the width of the beam, h is the height and V_c is the shear force at failure.

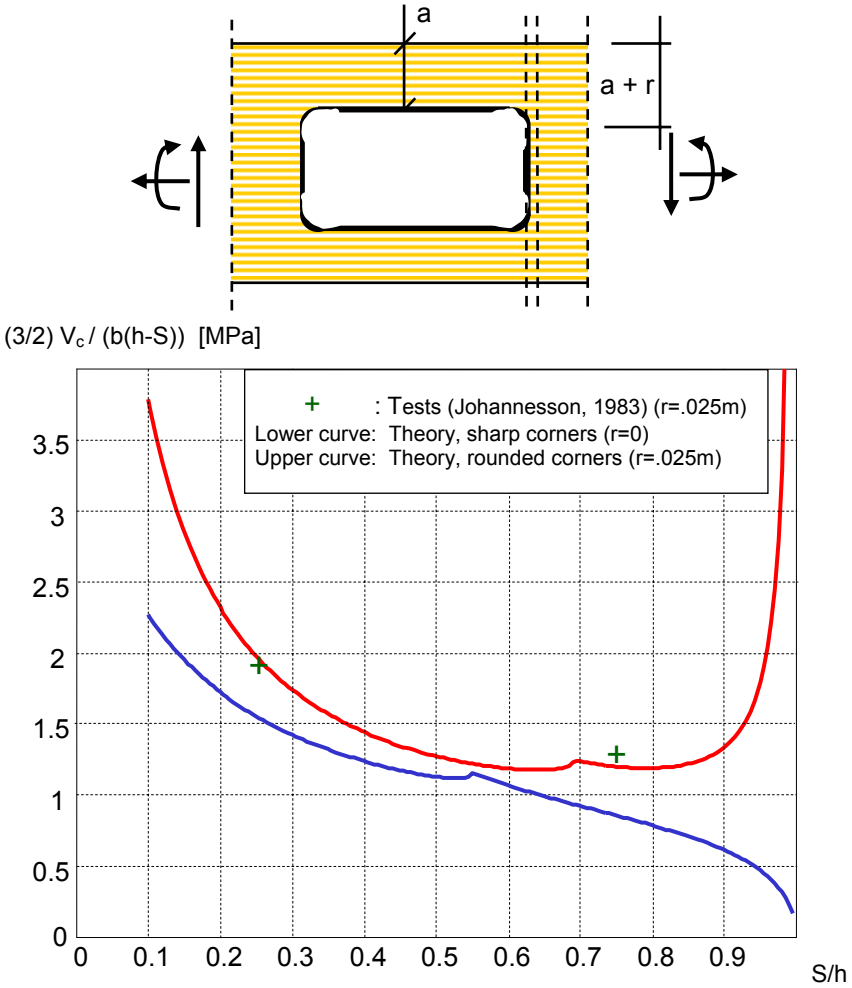

Figure 2. Shear strength of a glulam beam with a square hole with and without rounded corners.

A new collocation method for solving the nonstationary Navier-Stokes equations based on application of Bézier surfaces and curvilinear coordinates

Jaroslav Zapoměl
Department of Mechanics
VSB - Technical University of Ostrava, Ostrava, Czech Republic
e–mail: jaroslav.zapomel@vsb.cz

Summary The flow of Newtonian liquids is governed by the Navier Stokes equations and the equation of continuity. A new collocation method based on application of Bézier surfaces and curvilinear coordinates has been developed for their solution. In the plane case there are three unknown functions, pressure and two velocity components, that depend on time and on two space coordinates. The procedure starts from division of the plane domain into a certain number of quadrilateral subdomains, whose geometry is described by control points of Bernstein polynomials. Then the pressure and the velocity functions in each subdomain are approximated by Bézier surfaces and these approximations are substituted into the Navier-Stokes equations and the equation of continuity. The unknowns are the control points and their calculation starts from satisfying the Navier-Stokes equations and the equation of continuity at a specified number of collocation points, whose positions in the domains are defined by the curvilinear coordinates. This procedure results into a set of overestimated linear algebraic equations. Magnitudes of the control points of the approximated functions must satisfy some additional conditions that describe their continuity and continuity of their derivatives at borders of the adjacent subdomains. Advantage of this approach is that it does not require space discretization of the domains. This can be utilized especially in the case when the shape of the investigated region is changed significantly (large boundary displacements).

Introduction

The isothermal 2D flow of incompressible Newtonian liquids is governed by a set of Navier-Stokes equations (1) - (2), the equation of continuity (3), and by the relationships for the boundary conditions

$$\frac{\partial p}{\partial x_1}+\rho\left(\frac{\partial v_1}{\partial t}+v_1\frac{\partial v_1}{\partial x_1}+v_2\frac{\partial v_1}{\partial x_2}\right)-\eta\left(\frac{\partial^2 v_1}{\partial x_1^2}+\frac{\partial^2 v_1}{\partial x_2^2}\right)=\rho g_1 \tag{1}$$

$$\frac{\partial p}{\partial x_2}+\rho\left(\frac{\partial v_2}{\partial t}+v_1\frac{\partial v_2}{\partial x_1}+v_2\frac{\partial v_2}{\partial x_2}\right)-\eta\left(\frac{\partial^2 v_2}{\partial x_1^2}+\frac{\partial^2 v_2}{\partial x_2^2}\right)=\rho g_2 \tag{2}$$

$$\frac{\partial v_1}{\partial x_1}+\frac{\partial v_2}{\partial x_2}=0 \tag{3}$$

x_1, x_2 - x, y cartesian coordinates,
v_1, v_2 - velocity components in a cartesian frame of reference in x, y directions respectively,
p, t - pressure, time,
ρ, η - density, dynamical viscosity of the liquid,
g_1, g_2 - components of the gravity accelerations in x, y directions.

Equations (1) - (3) represent a set of nonlinear partial differential equations where the unknown functions, pressure p and velocity components v_1 and v_2, depend on the space coordinates and on

time. To solve them some numerical method must be used because their solution in a closed form cannot be obtained. Application of a finite difference method requires to perform both the space and time discritization and to replace the derivatives by corresponding differencies. A similar approach is needed if a finite element or a finite volume methods are used.

Applicability of these methods depends on the shape of the domains and their usage is siutable especially if it does not change. If it changes, the space discretization must be repeatedly modified and the solution continues with newly created finite differencies, elements or volumes. To avoid this problem a new collocation approach based on application of Bézier surfaces and curvilinear coordinates has been developed.

Bézier surfaces

In general a Bézier surface is a function that assignes a value of some quantity to the points situated in a quadrilateral domain and whose positions are defined by curvilinear coordinates. The borders of this domain do not need to be straight lines but they can have a curvilinear form.

A Bézier surface is defined by a Bernstein polynomial

$$s = \sum_{i=0}^{M} \sum_{j=0}^{N} s_{ij} \binom{M}{i} u_1^i (1-u_1)^{M-i} \binom{N}{j} u_2^j (1-u_2)^{N-j} \tag{4}$$

where

s - quantity,
M, N - nonnegative integer numbers defining the number of the control points,
s_{ij} - control points (i = 0, 1, 2 ... M, j = 0, 1, 2, ... N),
u_1, u_2 - curvilinear coordinates describing position of points in the domain,
($0 \le u_1 \le 1, 0 \le u_2 \le 1$).

To achieve the required boundary conditions of the Bézier surfaces control points of the Bernstein polynomials must satisfy some additional conditions.

If the Bézier surface should have a certain value at its domain border, then it must hold for the control points

if $u_1 = 0$ then $s_{0j} = s_0$ for j = 0, 1, 2, ... N (5)

if $u_1 = 1$ then $s_{Mj} = s_0$ for j = 0, 1, 2, ... N (6)

if $u_2 = 0$ then $s_{i0} = s_0$ for i = 0, 1, 2, ... M (7)

if $u_2 = 1$ then $s_{iN} = s_0$ for i = 0, 1, 2, ... M (8)

If two Bézier surfaces should be continuous at the common side of two adjacent domains, then their control points must satisfy the conditions

if $u_1 = 1$ (domain 1), $u_1 = 0$ (domain 2) then $s_{Mj} = q_{0j}$ for j = 0, 1, 2, ... N (9)

if $u_2 = 1$ (domain 1), $u_2 = 0$ (domain 2) then $s_{iM} = q_{i0}$ for i = 0, 1, 2, ... M (10)

If two Bézier surfaces should be smooth on their common border (their first partial derivatives with respect to the variable curvilinear coordinate on their common border are equal), then it is valid for their control points

if $u_1 = 1$ (domain 1), $u_1 = 0$ (domain 2) then $q_{1j} = 2s_{Mj} - s_{M-1j}$ for j = 0, 1, 2, ... N (11)

if $u_2 = 1$ (domain 1), $u_2 = 0$ (domain 2) then $q_{i1} = 2s_{iN} - s_{iN-1}$ for i = 0, 1, 2, ... M (12)

s_0, s_{ij}, q_{ij} - required value, control point of domain 1, control point of domain 2.

Solving a 2D flow by means of application of Bézier surfaces

The set of equations (1) - (3) must be solved numerically. For the time discretization a finite difference scheme has been adopted. The Navier-Stokes equations are related to time t, the equation of continuity to time t+Δt, and the derivatives of the velocity components with respect to time are replaced by their forward differencies (Δt - time increment)

$$\frac{v_{1,t+\Delta t}}{\Delta t} = -\frac{1}{\rho}\left[\frac{\partial p}{\partial x_1}\right]_t - \left(v_{1,t}\left[\frac{\partial v_1}{\partial x_1}\right]_t + v_{2,t}\left[\frac{\partial v_1}{\partial x_2}\right]_t\right) + \frac{\eta}{\rho}\left(\left[\frac{\partial^2 v_1}{\partial x_1^2}\right]_t + \left[\frac{\partial^2 v_1}{\partial x_2^2}\right]_t\right) + g_1 + \frac{v_{1,t}}{\Delta t} \quad (13)$$

$$\frac{v_{2,t+\Delta t}}{\Delta t} = -\frac{1}{\rho}\left[\frac{\partial p}{\partial x_2}\right]_t - \left(v_{1,t}\left[\frac{\partial v_2}{\partial x_1}\right]_t + v_{2,t}\left[\frac{\partial v_2}{\partial x_2}\right]_t\right) + \frac{\eta}{\rho}\left(\left[\frac{\partial^2 v_2}{\partial x_1^2}\right]_t + \left[\frac{\partial^2 v_2}{\partial x_2^2}\right]_t\right) + g_2 + \frac{v_{2,t}}{\Delta t} \quad (14)$$

$$\left[\frac{\partial v_1}{\partial x_1}\right]_{t+\Delta t} + \left[\frac{\partial v_2}{\partial x_2}\right]_{t+\Delta t} = 0 \quad (15)$$

x_1, x_2 - cartesian coordinates,
v_1, v_2 - velocity components in x_1, x_2 directions.

The developed collocation approach for solving the Navier Stokes equations and the equation of continuity [2], [3], [4] consists in dividing the region, in which the flow is investigated, into one or more quadrilateral domains and in approximation of the cartesian coordinates, of the pressure, and of the velocity components by Bézier surfaces in each domain. The required boundary conditions are achieved by adding the appropriate relations (5) - (8), (9) - (10) and (11) - (12).

Magnitudes of the unknown control points are calculated utilizing the assumption that the resulting equations are satisfied at a specified number of collocation points, which are defined by chosen values of the curvilinear coordinates u_1 and u_2. This manipulation arrives at a set of overestimated linear algebraic equations. Its solution is performed by means of a matrix pseudoinversion.

Example

The investigated 2D region (Fig.1) is a channel through which the Newtonian liquid (density 1000 kg/m^3, dynamical viscosity - 0.002 Pas) flows. The flow is induced by a pressure difference between the inlet and outlet sides (pressure at the inlet side - 150 kPa, pressure at the outlet side - 100 kPa) and it is assumed that the liquid perfectly adheres to the channel surfaces. The task was to analyze the pressure and the velocity fields.

The region was divided into 12 subdomains (Fig.1). The geometry of each of them was described by 49 control points. In each subdomain the unknown pressure and velocity functions were approximated by Bernstein polynomials and each of them was defined by 132 control points. The calculation arrived at an overestimated set of 3960 linear algebraic equations having 3428 unknown parameters.

At the beginning the liquid was in rest. Fig.2 shows the pressure distribution in the channel at time 1.35 ms. The profiles of the total velocity of the flow in sections of the channel having the x coordinates 300 mm and 700 mm related to the same point of time are drawn in Fig.3.

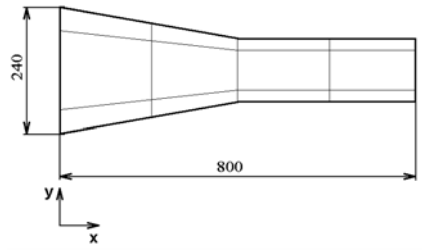

Figure 1: Investigated channel

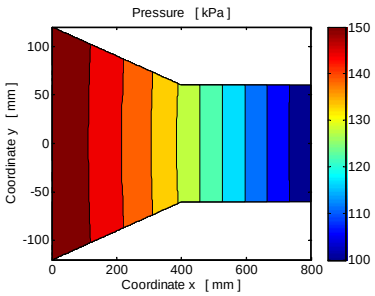

Figure 2: Pressure distribution

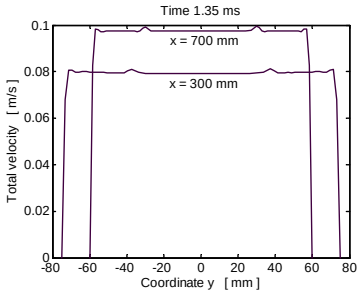

Figure 3: Velocity profiles

Conclusion

The flow of Newtonian liquids is governed by the Navier-Stokes equations, by the equation of continuity, and by relationships for the boundary conditions. The first step of application of a finite difference, a finite element or a finite volume methods for their solution is a time and space discretization of the region through which the liquid flows. If the region changes its shape, the discretization must be done repeatedly. This disadvantage can be removed by application of a new collocation method based on introduction of a curvilinear coordinates and approximation of the geometry and distribution of the pressure and velocity fields by Bezier surfaces (2D flow) or bodies (3D flow). Change of the shape of the investigated region has no influence on specification of the position of collocation points because they are defined by curvilinear coordinates. The procedure avoids solving a set of nonlinear algebraic equations at each integration step. Instead of this manipulation it arrives at calculation of an overestimated set of linear algebraic ones. Magnitudes of the control points from which the pressure distribution and the velocity field in the investigated region is calculated are the results.

Acknowledgement

This research work has been supported by the grant projects GA 101/06/0152. The support is gratefully acknowledged.

References

[1] J. Crank. *Free and mooving boundary problems*. Oxford Science Publications, (1996)

[2] F. Pochylý, S. Fialová and V. Habán.Flow with large deformation of boundaries. *Strojnícky časopis*, **56**, 211-220, (2005)

[3] F. Pochylý and J. Koutník. The appriximate solution of partial differential equations by means of Bézier surfaces, *Engineering Mechanics*, **1**, 165-176, (1994)

[4] E. Malenovský. *Příspěvek k dynamice rotorových soustav (A contribution to the dynamics of rotor systems)*, DrSc. thesis, Brno, 2000

[5] J. Zapoměl. A collocation method utilizing curvilinear coordinates and Bézier surfaces for analysis of a flow of Newtonian liquids, *Zeszyty Naukove Katedry Mechaniky Stosowanej*, no.31, 161-164, (2006)

Use of Richardson Extrapolation in Error Estimation of LES

Tellervo T. Brandt
Laboratory of Aerodynamics
Helsinki University of Technology, Finland
e–mail: tellervo.brandt@tkk.fi

Summary The justification of estimating the numerical and modelling error of large eddy simulation using the Richardson extrapolation is studied in a turbulent channel flow between two parallel walls. In the present test case, the Richardson extrapolation is found to describe the effect of the subgrid-scale model on the mean-velocity profile but not the effect of the numerical error.

Introduction

In large eddy simulation (LES), the so-called large scales of fluid motion are solved from the filtered Navier–Stokes equations, and a subgrid-scale (SGS) model is applied to describe the effect of the small scales on the resolved ones. Often, the grid resolution defines the separation between the resolved and SGS scales, and the smallest resolved flow scales are of the same size as the grid resolution. When, in addition, low-order finite-difference-type methods are applied to discretization, the numerical error may be large in comparison to the effect of the SGS model [1, 2]. Many of the error estimation methods applied in LES require data from direct numerical simulation (DNS) or measurements (see e.g. [1, 2]) which are not usually available for complex LES applications. For this purpose, use of the Richardson extrapolation has been suggested [3]. In this paper, this method is applied in a similar test case as in [3] but with a different grid resolution. The assumptions made in [3] about the actual order of the numerical method and the effect of SGS modelling are studied, and the obtained error components are compared to results obtained with an approach based on the so-called grid-independent LES (see [4]).

Test Case

Here, the Richardson extrapolation is applied in a fully-developed turbulent channel flow between two infinite parallel walls at Reynolds number $\mathrm{Re}_\tau = 395$ based on the friction velocity and channel half-height, or $\mathrm{Re} \approx 6800$ based on the mean bulk velocity. For this flow case, accurate DNS exists [5], and it is thus possible to compare the total error obtained by the Richardson extrapolation to the true total error. The LES equations are written here in the non-dimensional form as:

$$\frac{\partial \tilde{u}_i}{\partial t} = -\frac{\partial \tilde{p}}{\partial x_i} + \frac{\partial}{\partial x_j}\left(-\tilde{u}_i\tilde{u}_j - \tau_{ij} + \frac{1}{\mathrm{Re}_\tau}\left(\frac{\partial \tilde{u}_i}{\partial x_j} + \frac{\partial \tilde{u}_j}{\partial x_i}\right)\right), \tag{1}$$

where $(x_1, x_2, x_3) = (x, y, z)$ refer to non-dimensional streamwise, wall-normal and spanwise spatial coordinates, respectively, t to time, $(\tilde{u}_1, \tilde{u}_2, \tilde{u}_3) = (u, v, w)$ to resolved velocity vector and $\tilde{p}$ to resolved pressure. Here, an eddy-viscosity-type model, the standard Smagorinsky, is applied to model the SGS stress tensor $\widetilde{u_i u_j} - \tilde{u}_i\tilde{u}_j$:

$$-\tau_{ij} = \mu_T 2S_{ij} = \underbrace{(C_S\Delta_S)^2\sqrt{2S_{ij}S_{ij}}}_{=\mu_T}\left(\frac{\partial \tilde{u}_i}{\partial x_j} + \frac{\partial \tilde{u}_j}{\partial x_i}\right) \tag{2}$$

In the above, $C_S = 0.085$ is the model coefficient and Δ_S the model length scale, which controls the size of the smallest resolved flow scales. In the base test case, Δ_S is equal to grid spacing

$\Delta_S = \Delta = (\Delta x\, \Delta y\, \Delta z)^{1/3}$. In the near-wall regions, the van Driest damping is applied to reduce the model length scale. The resolution of the LES grid for which the error analysis is performed is given in Table 1. The second-order central-difference scheme is applied to space discretization and an explicit, third-order Runge–Kutta method to time integration.

Table 1: Domain size and resolution of the applied LES grid in the base test case.

	streamwise (x)	spanwise (z)	wall-normal (y)
extent of the domain / channel height	3.0	1.6	1.0
number of grid points	54	54	60
size of the grid cell in wall units (Δ^+)	44	23	2,...,27

wall units: $x^+ = \mathrm{Re}_\tau x$, where x is scaled by the channel half-height.

Numerical and Modelling Error using Richardson Extrapolation

In the approach to error estimation proposed in [3], the difference between the exact solution, u, and a numerical LES solution, $\tilde{u}_\Delta$, obtained on a grid with resolution Δ, is approximated as

$$\tilde{u}_\Delta - u = c_n \Delta^n + c_m \Delta_S^m + \mathcal{O}\left(\Delta^{n+1}, \Delta_S^{m+1}\right) \tag{3}$$

where n is the order of the numerical method, m the order of modelling error, Δ is the grid spacing, Δ_S the model length scale and $c_n\Delta^n$ represents the numerical error and $c_m\Delta_S^m$ the effect of the SGS model. If values for n and m are known, three simulations are required to evaluate the error components. As suggested in [3], by repeating the simulation first with a reduced resolution (reducing Δ) and then with a reduced effect of the SGS model (here Δ_S is reduced), one can form two additional equations like (3). If the higher-order terms are assumed to be negligible, i.e. the resolution and the effect of the SGS model are in the so-called asymptotic range where the methods obtain their formal accuracy, $c_n\Delta^n$ and $c_m\Delta_S^m$, can be solved.

Obtained Error Components

To apply the approach presented in [3], the LES of the channel flow described above is repeated with a grid resolution reduced from Table 1 by the factor of 1.5 (case "coarse"), and then with the same resolution as given in Table 1 but with a model length scale, Δ_S, reduced by the factor of 2 (case "light"). As in [3], it is assumed that $n = 2$ and $m = 2$. The mean-velocity profiles from the present simulations are given on the left-hand side of Figure 1 as function of a non-dimensional wall distance, and the obtained error components on the right-hand side. In addition, the true total error obtained as a difference from the DNS of [5] is included. We notice that the sum of the modelling and numerical error is not even close to the true total error. This suggests that either one or both of the error components cannot be approximated with the first term of the Taylor series like in Eq. (3). The study was also repeated with a grid resolution twice the one used here and with larger model length scales, but the results did not improve. In addition, as the grid resolution was varied, the estimate for the total error did not behave in the same way as the true total error.

Order of Numerical and Modelling Error in Present LES

In the previous section, it was assumed that the numerical error and the effect of SGS modelling are both of the second order, i.e. $n = m = 2$. In this section, we test the assumption.

To evaluate the order of the modelling error, m, the simulations are repeated keeping the grid resolution Δ fixed to the one given in Table 1 and varying the model length scale Δ_S. The values

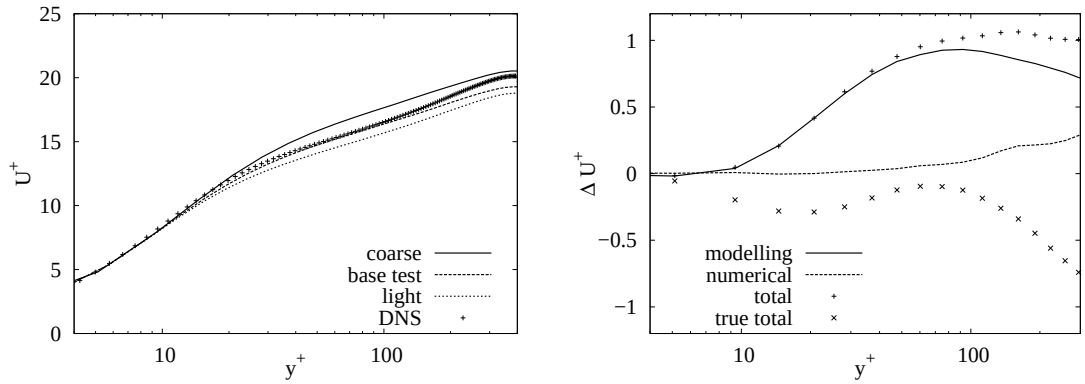

Figure 1: **Left:** Mean-velocity profiles. **Right:** Obtained error components for the base test case.

0.5Δ, Δ and 1.5Δ are applied to Δ_S, and thus three equations like (3) can be written, $c_n\Delta^n$ eliminated and c_m and m solved. The obtained order of the modelling error for the mean velocity is given on the left-hand side of Figure 2. In the logarithmic region, the order of the error is close to the value $m = 2$ which was applied in the previous section. However, in the viscous sublayer, where the total error is almost zero, the modelling error is not in the asymptotic range, and m obtains even negative values. When the study was repeated with a fi ner grid, the area where $m \approx 2$ was somewhat thicker. Since the order for the modelling error is quite close to the theoretical one in the logarithmic layer, the reason for the bad results for the total error obtained in the previous section has to be the numerical error.

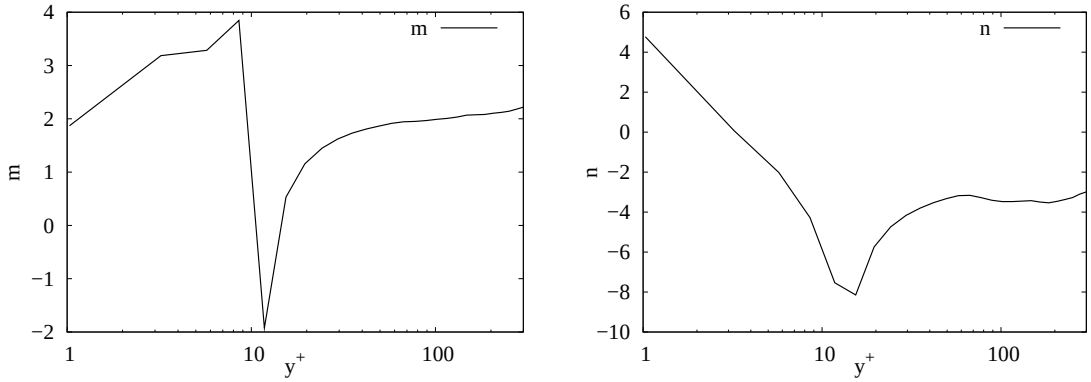

Figure 2: **Left:** Obtained order of SGS modelling error. **Right:** Obtained order of numerical error.

The order of the numerical error, n, can be evaluated in the same way as the one of the modelling error. The simulation was repeated keeping the model length scale Δ_S equal to the grid spacing given in Table 1, and using grid resolutions 1.5 and 1.5^2 times that of Table 1. The obtained order of the numerical error is given on the right-hand side of Figure 2. n has only negative values which indicates that the applied resolutions are not in the asymptotic range and thus the numerical error cannot be described by the fi rst term of the Taylor series, $c_n\Delta^n$.

The study on the error components was also repeated for the diagonal Reynolds stress components, and there the Richardson extrapolation was not able to predict either the numerical or the modelling error, which is a drawback for the usability of the approach. Another possibility could

be to consider an extension of the Richardson extrapolation to cases where the convergence is not monotonic, which is presented in [6].

Comparison with another Approach to Error Estimation

The modelling and numerical error of this same test case with the same numerical methods and SGS model were previously studied using an approach based on the so-called grid-independent LES [7]. The concept of grid-independent LES with the standard Smagorinsky model, which was proposed in [4], has received some criticism, and the Richardson extrapolation was proposed as an alternative approach [3]. Besides the different theoretical basis, the main difference between these approaches is the dependency of the numerical error on modelling. If the error components are defined using the grid-independent LES, smoothing of the resolved flow field provided by SGS modelling is allowed to affect the numerical error. In the definition using the Richardson extrapolation (3), the numerical error is independent of modelling. However, when the modelling errors obtained with the two approaches were compared, the results were quite close to each other. The comparison was repeated for cases with smaller and larger model length scales, and the similarity remained. This reinforces the conclusion on the suitability of the Richardson extrapolation to the estimation of the modelling error.

Conclusions

In this paper, the use of the Richardson extrapolation to evaluation of the numerical and modelling error in LES was studied in the turbulent channel flow. There was a clear difference between the obtained estimation for the total simulation error and the true total error. This difference was explained by the numerical error for which the Richardson extrapolation was not valid at the applied grid resolutions. However, the use of Richardson extrapolation for the effect of the SGS model on the mean-velocity profile was justified in the logarithmic region. As a conclusion we can say that despite the promising results of [3], the use of the Richardson extrapolation in LES is not straightforward, and the justification of its use is highly dependent on the applied grid resolution.

References

[1] S. Ghosal. An analysis of numerical errors in large-eddy simulations of turbulence. *Journal of Computational Physics*, 125:187–206, 1996.

[2] B. Vreman, B. Geurts, and H. Kuerten. Comparison of numerical schemes in large-eddy simulation of the temporal mixing layer. *International Journal for Numerical Methods in Fluids*, 22:297, 1996.

[3] M. Klein. An attempt to assess the quality of large eddy simulations in contex of implicit filtering. *Flow, Turbulence and Combustion*, 75:131–147, 2005.

[4] B. J. Geurts and J. Fröhlich. A framework for predicting accuracy limitations in large-eddy simulation. *Physics of Fluids*, 14(6):L41–L44, June 2002.

[5] R. D. Moser, J. Kim, and N. N. Mansour. Direct numerical simulation of turbulent channel flow up to $\mathrm{Re}_\tau = 590$. *Physics of Fluids*, 11(4):943–945, April 1999.

[6] I. Celik, J. Li, G. Hu, and G Shaffer. Limitations of Richardson extrapolation and some possible remedies. *Journal of Fluids Engineering*, 127:795–805, July 2005.

[7] T. Brandt. *A posteriori* study on modelling and numerical error in LES applying the Smagorinsky model. In S. Kassinos, C. Langer, G. Iaccarino, and P. Moin, editors, *Complex Effects in Large Eddy Simulations*, volume 56 of *Lecture Notes in Computational Science and Engineering*, pages 185–202. Springer, 2007. ISBN: 3-540-34233-8, To appear.

Teaching Principal Stresses by Truss Analogies

Gunnar Tibert* **and Magnus Krantz**
Department of Mechanics
KTH Engineering Sciences, Stockholm, Sweden
e–mail: tibert@kth.se

Summary An approach to increase students' understanding of principal stresses and the flow of stresses in complex structures is proposed. The strut-and-tie models for structural concrete provide a clear picture of the stress flow in complex structures. In order to provide students with more time for critical thinking and reflection, the equivalent trusses are generated by the user-friendly and web-based topology optimisation software TopOpt, developed at DTU.

Introduction

In the civil engineering courses on elasticity theory at KTH in Stockholm, principal stresses and strains have been taught only by showing how they are calculated: by formulas, Mohr's circle or as an eigenvalue problem. The distribution of principal stresses in a complex structure and their importance in practical design have not been discussed in the lectures. As a result, many students graduate without knowing how to use principal stresses in practical design; *the vital connection between theory and practice is missing.*

The self-taught software ForcePAD, developed at LTH in Lund, can derive the flow of stresses in a complex two-dimensional continuum with minimum effort by the students. Although ForcePAD illustrates the stress flow well, it provides only limited information useful for design purposes, especially for complex geometries, Figure 1.

Methods to illustrate the stress flow in a continuum as a truss have been available since the early 1900s [1]. The truss-analogy for structural concrete, *the strut-and-tie method*, has led to a safe and unified design approach where the overall flow of forces in critical regions are not overlooked as they would be in a sectional design approach, [2], cf. the sinking of the Sleipner-A offshore platform in 1991. Truss analogies are also used to determine the post-buckling load capacity of thin sheets; the *tension field theory* by Wagner [3] assumes that the wrinkled web of a steel beam behaves like a truss by replacing the wrinkles with bars in tension.

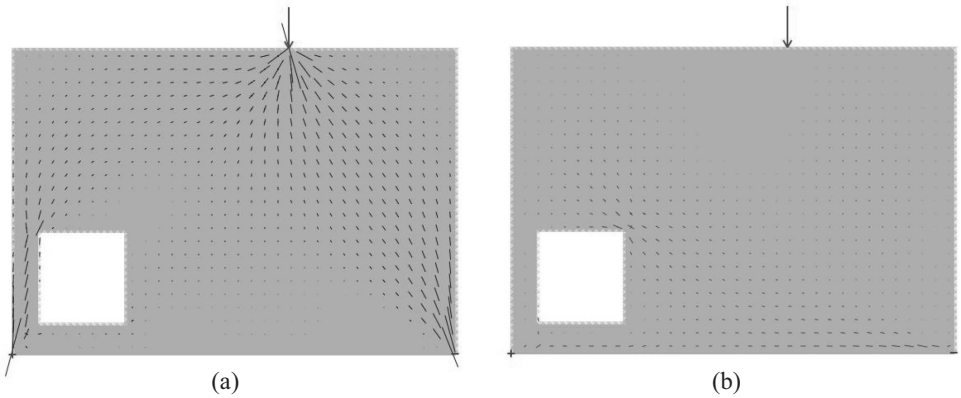

Figure 1: ForcePAD-computed principal stresses for a deep beam with a hole: (a) compressive and (b) tensile stresses.

The transformation of a complex continuum into a less complex truss makes it possible for both designers and students to use simple truss calculations methods. Nevertheless, the difficulty of the truss analogies lies in finding the geometry and topology of the truss that best represents the force flow in the actual structure. The strut-and-tie method requires considerable experience before suitable truss topologies can be obtained for more than the most simple structures, [4]. To use the tension field theory, the post-buckling shape of the thin-sheet must be found, which usually requires time-consuming non-linear finite element computations.

This study investigates the use of topology optimisation algorithms for the automatic generation of the equivalent truss for the strut-and-tie method, [5], and how it can be implemented into a course on elasticity theory for civil engineers.

Computer aided learning and critical thinking

A computer software can enhance students' learning, but it needs to be tailored for educational purposes and implemented with care to avoid opposite learning effects. The idea in this study is to use a software to help students understand and interpret the flow of forces in a complex continuum. However, if the software performs all the calculations for the students, the students do not necessarily learn or understand. Jennings [6] warned already a decade ago about the risks of replacing traditional education in structural analysis by software: *A computer package for structural analysis is a lethal tool if put in the hands of a structural engineer with poor training but, if the training is appropriate, the capabilities of the structural engineer will be very much enhanced.*

Personal experience and a recent study at KTH [7] suggest that computer software require careful implementation in structural mechanics education. General mathematics programs, such as MATLAB and MathCAD, certainly help the students perform more calculations in less time. However, if the students are unfamiliar with the use of the programs, their attention is shifted from the structural analysis to the handling of the program. General finite element programs produce impressive plots, but they require understanding of the underlying principles in order to produce reliable results and experience to be used effectively. Thus, the generality of these programs make them less user-friendly and more time is spent on learning the program than solving the problem. As a result, the students often have no time left to reflect on their obtained solutions. Hence, the challenge here is to increase, or at least preserve, the level of critical thinking and reflection among students while using computer software to aid learning. In this respect, educational structural analysis software has been developed at LTH, i.e. ForcePAD, and at CTH in Gothenburg, i.e. pointSketch2D [8]. These programs are limited in capacity and generality, but very user-friendly thanks to their tab-based user interface.

Truss models by topology optimisation

As described in the introduction, the strut-and-tie method provides a clear and simple explanation of the stress flow in a structure, but the design of the equivalent truss is very difficult for an unexperienced person. Since the strut-and-tie method can significantly increase the understanding of complex concrete structures it can be considered an important element of the civil engineering curriculum. Therefore, the following simplification can be made to allow more time for learning: the strut-and-tie model is automatically generated by a topology optimisation software so that the students can concentrate on evaluating various designs in terms of stresses, reactions, amount of reinforcement, etc.

Topology optimisation software

Topology optimisation capability is included in some general finite software, e.g. ANSYS and MSC.Nastran, but, as explained above, these are not suitable for computer aided learning. At DTU in Lyngby, the web-based topology optimisation software TopOpt has been developed (`www.topopt.dtu.dk`), [9]. This software is as easy to use as ForcePAD and therefore suitable for educational purposes.

Example

Constructing a complete truss model for the deep beam with a hole, Figure 2(a), based on the stress trajectories is difficult and requires experience. Schlaich *et al.* [2] derive a complex model, Figure 2(b), which actually is a combination of two different truss models. The optimal models by Liang *et al.* [5] and the present by the TopOpt software are similar and not unlike the model by Schlaich *et al.*. The important stress flows are well captured by the optimal models.

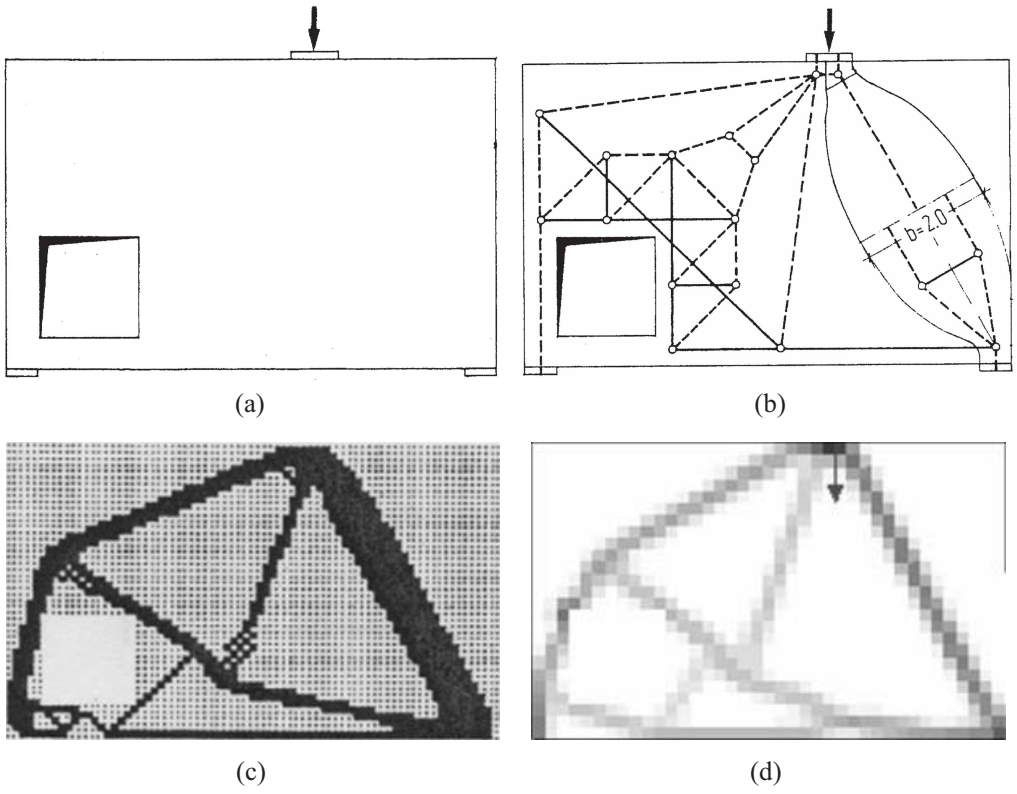

Figure 2: Comparison of strut-and-tie models for a deep beam with an opening: (b) Complex model by Schlaich *et al.* [2], (c) optimal model by Liang *et al.* [5] and (d) present optimal model by TopOpt.

The TopOpt program enables quick changes of geometry and load conditions, so the students can see how the internal stresses take different paths as a result of those changes. In Figure 3(a), a change in load position leads to a totally different truss model. In Figure 3(b), the hole is substituted by a cut-out on the left side, with the loads concentrated on the left side of the beam, clearly illustrated by the blackness of the structure.

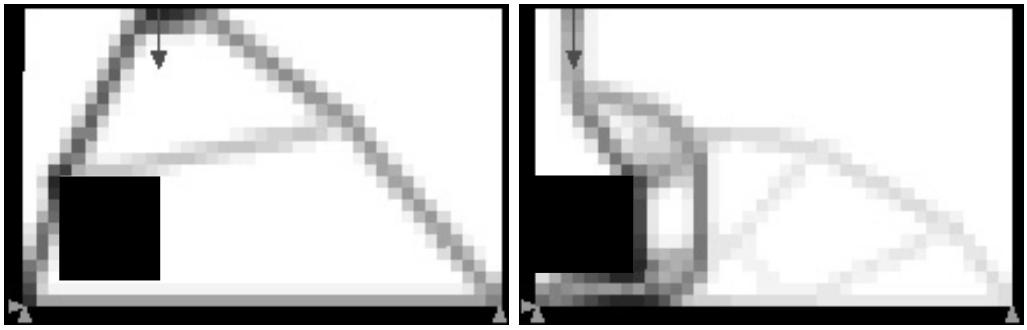

(a) (b)

Figure 3: Change of strut-and-tie model as the load and hole positions vary: (a) load position changes and (b) hole and load position changes.

Concluding remarks

The proposed implementation of the programs ForcePAD and TopOpt in education will take place in Spring 2007 in a 4th-year course on the civil engineering programme at KTH. The aim is to provide the students with a tool that shows how the stress flow in a continuum can be illustrated by a truss. The students can thus relate the analysis of continuum structures to their prior knowledge of analysis of trusses. Hopefully, their understanding of the relationships between forces and stresses will increase. A valuable bonus that surely will be appreciated by the students is the direct connection between the truss analogy and practical design routines.

References

[1] W. Ritter. Die Bauweise Hennebique (*The Hennebique System*). *Schweizerische Bauzeitung*, **33**(7), 59–61, (1899).

[2] J. Schlaich, K. Schäfer and M. Jennewein. Towards a consistent design of reinforced concrete structures *PCI Journal*, **32**(3), 74–150, (1987).

[3] H. Wagner Ebene Blechwandträger mit sehr dünnem Stegblech (*Flat sheet metal girder with very thin metal web*). *Zeitschrift für Flugtechnik und Luftschiffart*, **20**(8–12), 200–207, 227–233, 256–262, 279–284, (1929).

[4] K.-H. Reineck (Ed.). *Examples for the Design of Structural Concrete with Strut-and-Tie Models*. ACI SP-208, American Concrete Institure, Michigan, USA (2002).

[5] Q.Q. Liang, Y.M. Xie and G.P. Steven. Topology optimization of strut-and-tie models in reinforced concrete structures using an evolutionary procedure. *ACI Structural Journal*, **97**(2), 322-330, (2000).

[6] A. Jennings. Dilemmas in structural engineering education. *Advances in finite element technology*, CIMNE, Barcelona, Spain, N.E. Wiberg (ed.), 114–134, (1995).

[7] A. Ansell. Datorstöd i byggkonstruktionsundervisningen. *Pedagogiskt projekt i kursen Lärande och undervisning 2, KTH Learning Lab*, 24 pages, February 17 (2006).

[8] P. Olsson. *Conceptual Studies in Structural Design*. PhD Thesis, Chalmers University of Technology, Gothenburg, Sweden, (2006).

[9] D. Tcherniak and O. Sigmund. A web-based topology optimization program. *Structural and Multidisciplinary Optimization*, **22**(3), 179–187, (2001).

A Lightweight Application Portal for the Grid

Jonas Lindemann* **and Göran Sandberg**
Lunarc
Lund University, Lund, Sweden
e–mail: jonas.lindemann@lunarc.lu.se

Summary Taking advantage of grid resources often requires an understanding of the underlying concepts of grid computing. The Lunarc Application Portal is an effort to provide an application oriented grid portal, providing targeted user interfaces for commonly found applications used at Lunarc. The developed portal also provides a plugin based architecture that can be used as a framework for developing web based user interfaces for other grid-based applications. The portal is also implemented using lightweight tools making it easy deploy and maintain.

Introduction

To take advantage of grid resources today often requires an understanding of the underlying concepts of grid computing and related middleware tools. To make the grid an attractive alternative for more users, grid user interfaces must be provided on several levels. Currently most grid client tools are command line based. This excludes a large user population from easily taking advantage of grid resources. There are also traditional HPC-users, that just want to get the work done, without creating scripts and typing commands.

The client tools provided by many grid middlewares [1, 2] are often command line based and have a quite advanced job description languages such as RSL [3], xRSL [4] or jdsl [5]. Adding to this complexity is also a security model based on public key encryption that many users are unfamiliar with. Even users experienced with high performance computing (HPC) have difficulties using grid client tools. Providing web based user interfaces is an effective way of providing platform independent access to grid resources, only requiring a recent web browser. There exists today a number of projects for implementing web based interfaces for grid resources, such as gridsphere[6], CrossGrids[7], GridBlocks[8] and many more. Most of these are still geared towards providing a lot of advanced functionality not needed for many users.

The Lunarc Application Portal is an effort to provide an application oriented web based environment for users not experienced in a HPC or grid environment, providing targeted user interfaces for commonly available applications. The portal can also be used as a framework for easily implementing web interfaces to user applications, without much development effort. The Lunarc Application Portal has also been used by NTNU for developing their portal solution, GRIDportal [9].

Lunarc Application Portal

To provide users easy access to grid resources as well as resources provided locally, Lunarc has initiated the development of a web based application oriented portal (LAP) that provides an easy to use environment for submitting, monitoring and retrieving results from grid jobs. The portal web interface provide specific user interfaces for a number commonly used applications at Lunarc, such as MATLAB [10], OCTAVE [11], ABAQUS [12] and MOLCAS [13]. The portal is also used to provide wider access to research applications in the field of astronomy and fire safety.

User interface

The fundamental design goal of the portal user interface is to provide a complete easy to use environment for the user to get access to grid resources. More specific, to provide:

- Certificate management on all platforms.
- User virtual organisation (VO) registration.
- Specific user interfaces for commonly used applications.
- A general user interface for job submit, management and monitoring.
- A user interface for job result retrieval and downloading output from jobs on storage elements.
- A user interface for managing users for a ”Portal VO”, that can be easily added to grid sites controlling access to resources.

The overall user interface is designed in such way that user interface elements are ordered in the same way as the portal workflow.

Logging into the portal

When the user opens the portal url, a simple user interface is shown with a limited set of menu choices. The first menu, Information, contains portal documentation, such as a **Getting started** guide, **A User’s guide** and a **Programming guide**. The **Getting started** guide provides a systematic guide on how to download the Grid Certificate Manager, getting a signed certificate and how to log into the portal. The second menu, Session, at this point only provides 2 menu choices, Log in ... (proxy) and Log in .. (MyProxy). By choosing the first menu item, a simple login window is shown. From this window, the user selects the previously generated proxy-certificate and selects Login. If a correct proxy-certificate was submitted, the portal now shows a complete set of menus for all functionality.

Main portal user interface

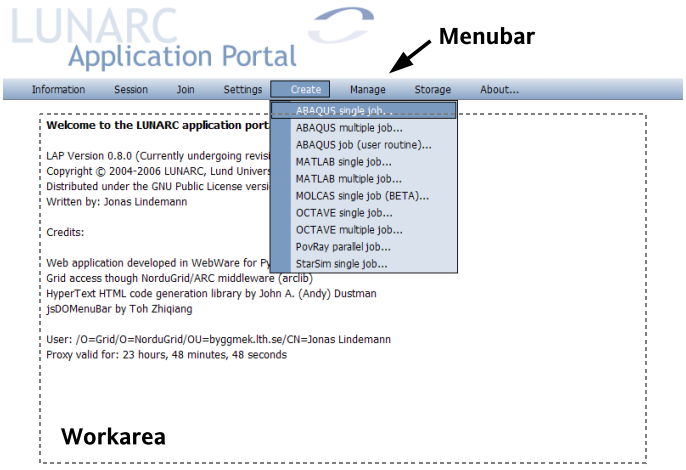

Figure 1: Main portal user interface

The main portal user interface designed as a normal desktop application with a menu bar and a work area. From the menu bar, all functionality of the portal can be accessed. In the workarea below the menubar all forms, windows and message boxes are displayed. Figure 1

Job creation and job definitions

The Lunarc Application Portal uses the concept of job definitions. A job definition contains a job description (xrsl), associated job files and any needed scripts for running the jobs on the grid. The user provides any settings and input files using the web interface provided by the portal.

The portal comes with a number of job definition plugins for commonly found applications at Lunarc. A job definition is created from the **Create** menu. When a job definition template is selected from the menu a input box appears asking for a job name. This name is used later on for identifying the job in the management and monitoring menus. When This menu is completed the main job definition window appears displaying more job options, see figure 2.

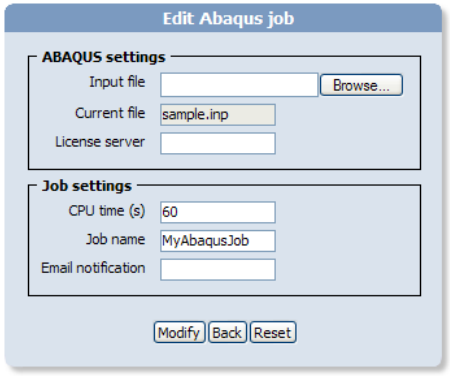

Figure 2: Editing the job definition

In figure 2 the settings for an ABAQUS job is shown, with a browse button for selecting an input file and an input box for providing a hostname to a license server. All job definition user interfaces also contain common settings such as requested CPU-time, Job name and an email address for job state notification.

Managing existing job definitions

All job definitions created can be managed from the **Manage/Job definitions** menu. Selecting this menu displays window with a list of all created job definitions. In the lower half of this window, there are a set of buttons for managing the job definitions:

- **Edit** – Brings up the job definition user interface for the selected job definition.
- **Submit** – Submits the selected job definition for execution on grid resources.
- **View results** – Displays a list of downloaded result files for the selected job definition.
- **Delete** – Deletes the job definition including any associated results from the portal.

Managing running grid jobs

When a job has been submitted to a grid resource it is managed using the **Manage Grid Jobs** window accessible from the **Manage/Running jobs... menu**. This window displays the status of all the job submitted by the user, see figure 3.

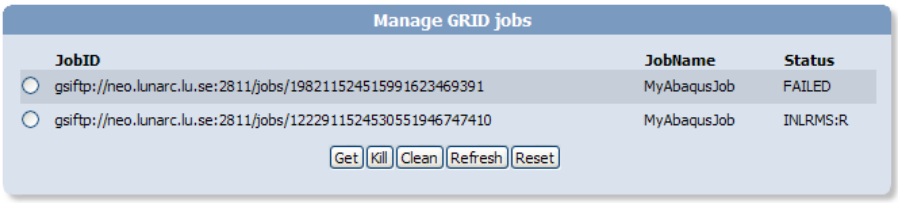

Figure 3: Manage Grid Jobs window. From this window all running or finished grid jobs can be managed.

There are three buttons in the lower part of this window:

- **Get** – Download the job into the job definition result folder. This requires that the job has finished (FINISHED) is in a failed state (FAILED).
- **Kill** – Kills a running job. Requires the job to be in a executing state (INLRMS, EXECUTED).
- **Clean** – Removes a finished job from a grid resource without downloading any results. This requires that the job has finished (FINISHED) is in a failed state (FAILED)

When a job is downloaded using the **Get** button, the output files are placed together with the associated job definition. When a job definition has been submitted several times, each result is stored in separate folders marked with the download time and date.

Viewing job output files

To view the downloaded output files, the **View results** button is clicked with a job definition selected. This shows a window with a list of all output files downloaded for this job definition. To view a specific output file folder, the **View directory** button is clicked. This brings up a list of all the downloaded files for the specific grid job, see figure 4.

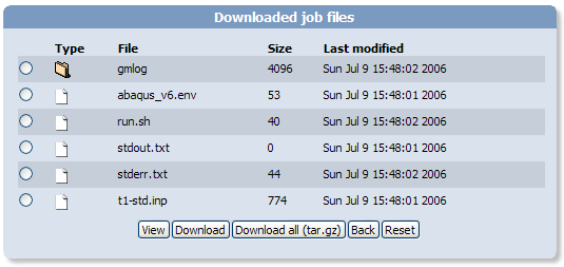

Figure 4: Output files generated by a grid job.

In the window shown below, there are several buttons:

- **View** – View a file as text. Brings up a simple window with scrollbars displaying the contents of the file.
- **Download** – Downloads the selected file to the users browser, displaying a download dialog.
- **Download all (.tar.gz)** – Compresses the entire directory and downloads it to the users browser, displaying a download dialog.

By providing the user with tools for examining the output from a job, the user can save bandwidth by not downloading failed or unsuccessful jobs.

Ongoing application projects

The following sections describe ongoing projects based on the Lunarc Application Portal framework. The goals of these projects are to further the use of applications currently only available locally on the Lunarc clusters. By providing a easy to use interface these applications can be easily used by researcher world-wide, without having to recompile and configure them for a specific cluster.

StarSim – Astronomy

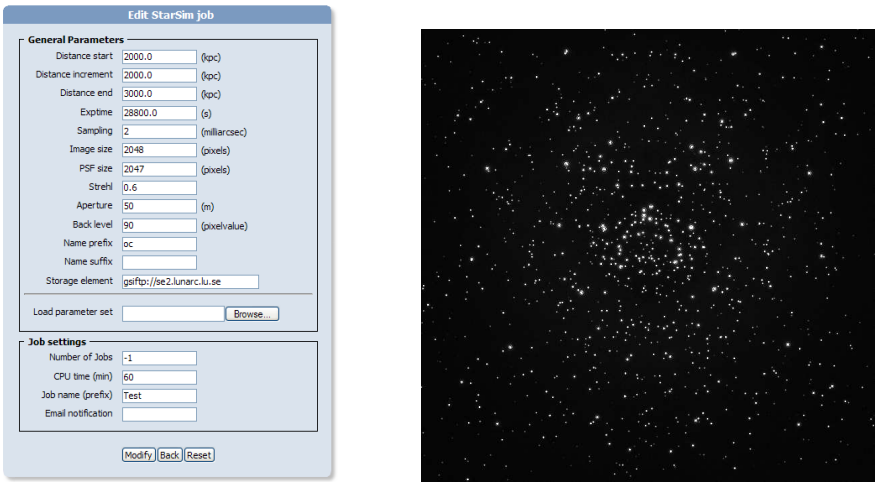

Figure 5: User interface and typical results from the StarSim application

One of the applications that have been using the resources at Lunarc, is the simulation the adaptive optics [16, 15] of a coming extremely large telescope ELT in the EURO50 project. To make these simulations available for more researchers a project at Lunarc is implementing a special plugin for the Lunarc Application Portal, providing a easy to use web interface for the simulation code. Typical results from the simulation code and the initial user interface is shown in figure 5.

SMAFS – Fire safety design

An ongoing project is to integrate the SMAFS CFD application used for fire safety simulations [17, 18, 19]. The goal here is to create an easy to use interface for the user to submit generated input files to the Lunarc resources. The target users are from the industry and a licensing model is under development.

Implementation

The main implementation goals of the Lunarc Application Portal (LAP) framework are:

- **Lightweight** – Easy to understand without large dependencies on other libraries. Easy to deploy and maintain.
- **Extendible** – It should be easy to extend the portal using a built in plugin-architecture.

- **Customizable** – The graphical design should be customizable to adapt to existing web designs.
- **Available** – The next release will be available under an open source license (GPL).

The portal framework is designed around the python web application toolkit Webware [20]. This is a lightweight toolkit for developing object-oriented web applications. The toolkit contains design patterns for applications servers, server pages, servlets, session management and many other features. The toolkit is modular and easily extendable.

The portal uses Webware as an application server integrated in the Apache webserver [21] using a special Apache module provided with Webware called mod_webkit. For security reasons the Apache webserver serves the web pages using the HTTPS protocol.

To access the grid the portal uses the ARC [1] middleware. This middleware has special bindings for Python, arclib [22]. The present version of the portal uses arclib for certificate handling and querying for resources, but a transition is underway to make the portal use arclib exclusively as this eliminates the need for problematic parsing of output from the ARC command line interface.

Plugin architecture

The portal framework also implements a plugin-architecture for easily extending the portal without modifying the existing portal source code. The portal supports the following types of plugins:

- **Job definition plugins** – These plugins enable support for different type of applications on the grid. Implemented by 2 classes, one for the user interface and a second for describing the job.
- **Documentation plugins** – Implements HTML based documentation with the portal. Implemented by 2 python classes (Secure and Non secure) and a HTML document.
- **VO plugins** – Implements registration processes for different kinds of virtual organisations.

The plugins are located in a special directory in the portal main directory and is parsed by the portal application to generate the menu structure. Each directory contains the needed python files and a special information file containing the text that is to appear in the portal menu.

Conclusions

Most users are application expert and know how to generate input for his or her application. By using an application oriented web based grid portal, like the Lunarc Application Portal, a new group of user can benefit from the advantages of grid resources. By providing explicit user interfaces for user applications, eliminates the need for users to learn details of the underlying grid infrastructure.

The Lunarc Application Portal provides a lightweight and extendable implementation of a web based grid portal. Using lightweight tools in the implementation, such as Python [14] and WebWare [14], enable easy deployment and maintenance of the portal. The arclib [22] library provided an effective tool for interfacing the ARC grid middleware [1] with the portal.

Extending the portal with additional application types can be done without a large development effort, using the plugin architecture of the portal framework. The portal framework has also been used successfully by other grid portal projects [23].

References

[1] Advanced Resource Connector ARC, http://www.nordugrid.org, (2006)

[2] gLite – Lightweight Middleware for Grid Computing, http://glite.web.cern.ch/glite/ (2006)

[3] The Globus Resource Specification Language RSL v1.0, http://www-fp.globus.org/gram/rsl_spec1.html

[4] O. Smirnova, XRSL (Extended Resource Specification Language), http://www.nordugrid.org/documents/xrsl.pdf, (2006)

[5] The JSDL Specification (version 1.0, draft 28) – GFD-R-P.056, https://forge.gridforum.org/projects/jsdl-wg/document/draft-ggf-jsdl-spec/en/18, (2006)

[6] gridphere portal framework, http://www.gridsphere.org/gridsphere/gridsphere, (2005)

[7] Developing new Grid components, http://www.crossgrid.org/main.html, (2005)

[8] GridBlocks, http://gridblocks.sourceforge.net, (2005)

[9] The NTNU Application Portal, https://norgrid.ntnu.no/gridportal/default/WelcomePage, (2006)

[10] The MathWorks, http://www.mathworks.com, (2006)

[11] GNU Octave, http://www.octave.org, (2006)

[12] ABAQUS, http://www.abaqus.com, (2006)

[13] MOLCAS 6, http://www.teokem.lu.se/molcas, (2006)

[14] Python, http://www.python.org, (2006)

[15] A. Ardeberg & P. Linde, Clusters as probes of Distance, Evolution and Chemistry of Galaxies. 2nd Bckaskog Workshop on Extremely Large Telescopes, Proc. SPIE 5382, Bckaskog (2003)

[16] P. Linde, Peeking into Eternity - Extremely Large Telescope Observations Modelling, http://www.astro.lu.se/ torben/euro50/publications/lindePaper1.pdf, (2006)

[17] Yan, Z., CFD Modeling of A Large Complex Fire, Report 3120, http://www.brand.lth.se/bibl/3120.pdf, (2000).

[18] Yan, Z., Numerical Modeling of Turbulent Combustion and Flame Spread, Report 1018, http://www.brand.lth.se/public/bibl1018.htm, (1999)

[19] Yan, Z., Holmstedt, G., Numerical Prediciton of Heat Flux from Flame in Room Fire, Report 3090, http://www.brand.lth.se/public/bibl3090.htm, (1997)

[20] Python Web Application Toolkit, http://www.webwareforpython.org, (2004)

[21] The Apache HTTP Server Project, http://httpd.apache.org, (2006)

[22] J Nielsen, ARClib, a client library for ARC, http://www.nordugrid.org/documents/arclib.pdf, (2006)

[23] M. Matusiak, Grid Application Portal, http://www.fys.uio.no/epf/nordic-network/xi/talks/gridportal_ngn05.pdf, (2005)

Direct numerical simulation of non-isothermal turbulent wall-jets

Daniel Ahlman*, Geert Brethouwer and Arne V. Johansson
Department of Mechanics
Royal Institute of Technology, Sweden
*e–mail: ahlman@mech.kth.se

Summary
Direct numerical simulation is used to study the development and statistics of turbulent non-isothermal wall-jets. The simulation code developed employs compact finite differences to solve the fully compressible Navier-Stokes equations. Simulations are performed with substantial density differences, including the use of a temperature depending viscosity. Parallelization of the solution procedure is achieved by using Message-passing-interface (MPI) routines.

Background

A plane wall-jet is obtained by injecting fluid along a solid wall in such a way that the velocity of the jet supersedes that of the ambient flow. The structure of a developed turbulent wall-jet can formally be described as two adjacent shear layers of different character. The inner layer, reaching from the wall up to the maximum mean streamwise velocity, resembles a thin boundary layer, while the outer part, positioned above the inner layer and reaching out to the ambient flow, can be characterized as a free shear flow. As a consequence of this twofold nature, properties such as mixing and momentum transfer exhibit distinctively different character throughout the wall-jet.

Walls-jets are in practice often used for mixing and transport of scalars like heat and fuels. Examples of applications are for instance in thin film cooling, ventilation and in separation control. Wall-jets are also of interest in connection to combustion, since all combustion applications contain regions where mixing and reaction takes place close to and are affected by a wall.

In the present study, we perform three-dimensional direct numerical simulations in order to analyze the development and properties of plane turbulent non-isothermal wall-jets. The jets are non-isothermal in the sense that varying temperature and density profiles are specified at the inlet. The current work is a continuation of and builds on previous simulation efforts[1], where the development and mixing in an isothermal wall-jet was investigated.

Simulation technique

The simulations are performed by employing a sixth order compact finite difference scheme[3] for the spatial discretization, and a third order low-storage Runge-Kutta scheme for the temporal integration. The governing flow equations solved for are the fully compressible Navier-Stokes equations

$$\frac{\partial \rho}{\partial t} + \frac{\partial \rho u_j}{\partial x_j} = 0 \tag{1}$$

$$\frac{\partial \rho u_i}{\partial t} + \frac{\partial \rho u_i u_j}{\partial x_j} = -\frac{\partial p}{\partial x_i} + \frac{\partial \tau_{ij}}{\partial x_j} \tag{2}$$

$$\frac{\partial \rho E}{\partial t} + \frac{\partial \rho E u_j}{\partial x_j} = -\frac{\partial q_j}{\partial x_j} + \frac{\partial (u_i(\tau_{ij} - p\delta_{ij})}{\partial x_j} \tag{3}$$

where ρ denotes the mass density, u_j the three velocity components, p the pressure, τ_{ij} the viscous stress tensor, E the total energy and q_i the heat diffusion.

In the simulations the viscosity varies with temperature according to Sutherland's law

$$\mu = C\frac{T^{3/2}}{T+S_0} \tag{4}$$

where T is the fluid temperature and C and S_0 constants.

The simulation code is written in Fortran and uses MPI routines to enable parallel simulations on distributed memory computers. The parallelization is achieved by domain decomposition and distribution over the participating CPUs.

The domain used is a rectangular box with a no-slip wall positioned at the bottom. The inlet Reynolds number employed is $Re_h = U_J h/\nu = 2000$, where U_J is the the inlet jet center velocity and h is the inlet jet height. The corresponding inlet Mach number used in the simulations is $M = U_J/c = 0.5$. Above the jet a constant coflow of $U_c = 0.10U_J$ is applied. The density and temperature is varied over the jet profile to achieve either a cold jet propagating in a warm surrounding or a heated jet in a cold surrounding. The wall temperature is kept constant and equal to the ambient flow temperature.

Results

The simulation code developed has been found capable of handling wall-jets with significant density variations. Presently a smaller test simulation of a cold jet in a warm surrounding has been performed. The cold jet is defined by a density difference of $\Delta\rho = (\rho_J - \rho_a)/\rho_J = 0.4$, where ρ_J is the inlet jet density and ρ_a the density of the ambient fluid. The inlet jet center temperature in the simulation is set to $293\ K$. The domain size used is $20h \times 12h \times 2.4h$ in the streamwise, wall normal and spanwise directions respectively, and the number of nodes used is $128 \times 128 \times 32$. Examples of results from the simulation are presented in figure 1-3. Figure 1 shows a snapshot of the wall-jet streamwise velocity. The jet is injected along the wall in the lower left corner. The jet propagation is initially laminar, before transition to turbulence is initiated. Downstream of the transition the jet propagates fully turbulent. The wall-jet temperature is shown in figure 2. As the cold jet propagates downstream it is heated by its warmer surroundings. Figure 3 shows the growth rate and streamwise velocity fluctuation intensity, at a downstream position of $x/h = 15$, and compares it to results from the previously simulated isothermal wall-jet. The same inlet Reynolds and Mach numbers, as well as inlet disturbances are used in both simulations. The growth rate is evaluated using the velocity half-width, $y_{1/2}$, defined as the distance from the wall to the outer shear layer position where the mean streamwise velocity is $U = (U_m - U_c)/2$. Observing the half-width, the transition to turbulence is found to be slightly faster in the cold jet. The developed growth rate, downstream of the transition, is also found to be higher. However only the last 10 inlet heights contain fully developed flow, and hence a simulation using a larger box is needed to confirm the validity of these observations. The mass-weighted velocity fluctuation, $u'' = u - \widetilde{U} = u - \overline{\rho u}/\bar{\rho}$, is found to agree well for the two cases, apart from in the inner region, where the fluctuation intensity is higher in the cold case. This in turn confirms the observation of a faster transition.

Further work

As noted above further work include a larger, better resolved, simulation of the present cold jet case. Also the opposite situation, a warm jet propagating in a cold surrounding will be simulated. The statistics from the non-isothermal jet will be investigated in order to draw conclusions on how a varying density affects the wall-jet development and dynamics. Comparisons will be made with present simulation[1] and experimental data[2] of isothermal wall-jets.

References

[1] Ahlman D., Brethouwer, G., Johansson A. V., Direct numerical simulation of a plane turbulent wall-jet including scalar mixing *Submitted to Phys. Fluids*.

[2] Eriksson J.G., Karlsson R.I., Persson J., 1998, An experimental study of a two-dimensional plane turbulent wall jet *Experiments in Fluids* **25**, 50-60.

[3] Lele S. K., 1992, Compact finite difference schemes with spectral-like resolution *J. Comp. Phys.* **103**, 16-42.

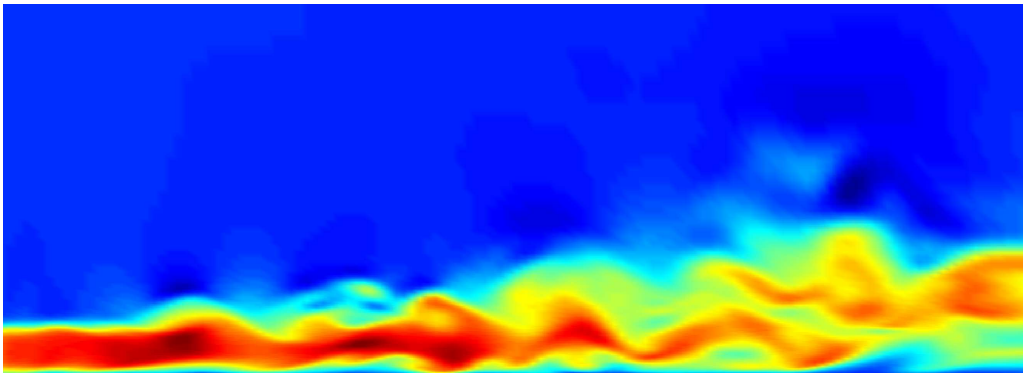

Figure 1: Snapshot of the cold wall-jet ($\Delta\rho = 0.4$) streamwise velocity

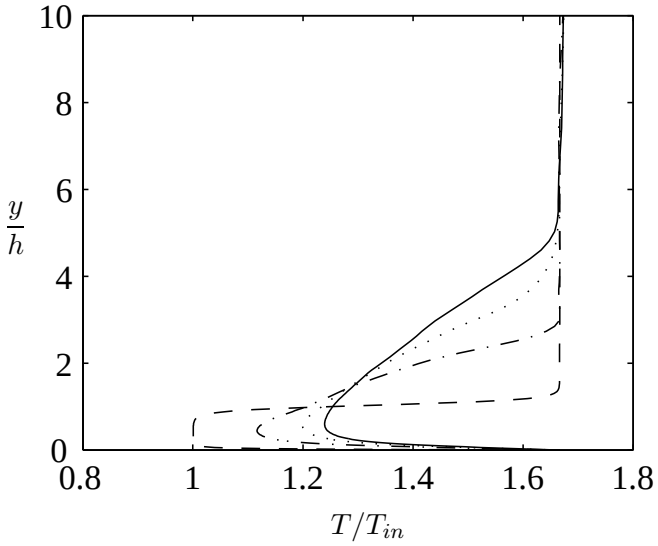

Figure 2: Cold wall-jet temperature (inlet normalized). Profiles at $x/h = 0$ (dashed), $x/h = 10$ (dash-dotted), $x/h = 15$ (dotted) and $x/h = 18$ (solid)

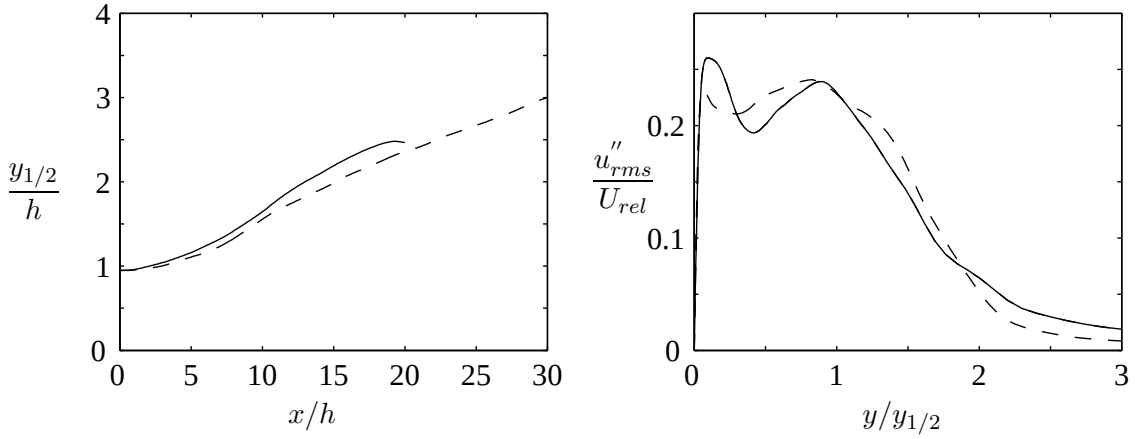

Figure 3: Wall-jet growth in terms of the velocity half-width (left) and streamwise velocity fluctuation intensity at $x/h = 15$ using outer scaling, where $U_{rel} = U_m - U_c$ (right). Solid lines represent the cold jet results and dashed lines isothermal results.

POD analysis of the acoustic field in a gas turbine combustion chamber

Robert Z. Szasz* **and Laszlo Fuchs**
Department of Energy Sciences
Lund University, Lund, Sweden
e–mail: robert-zoltan.szasz@vok.lth.se

Summary The acoustic field in an annular gas turbine combustion chamber is determined using a hybrid approach. The flow solver is based on Large Eddy Simulations to account for turbulence and on a flamelet-based method to model combustion. The acoustic part solves an inhomogeneous wave equation. POD is used to identify the resulting acoustic modes.

Introduction

Thermo-acoustic instabilities are a major concern in the development of gas turbine combustion chambers. The amplification of pressure oscillations may lead to the malfunctioning of the device, or, in the worst case, to its failure [2], thus it is needed that the combustion instabilities are predicted as early as possible.

Here we focus on the acoustic field generated by a reacting flow field in an annular gas turbine combustion chamber. The acoustic field can be determined by solving the compressible Navier-Stokes equations using Direct Numerical Simulations (DNS) or Large Eddy Simulations (LES) [3]. This direct method being highly inefficient for low-Mach number flows a hybrid method is used in the present paper. The compressible Navier Stokes equations are split in a set of incompressible Navier Stokes equations and a set of acoustic equations. Using first-order approximations, the acoustic equations may be reorganized into an inhomogeneous wave equation. The method was implemented by Mihaescu et al. [4] and further developed further by Duwig et al. [1] to predict thermo-acoustic instabilities in a model gas turbine combustion chamber. Szasz et al. [5] applied this hybrid approach to determine how the perturbations of the acoustic sources are influencing the generated acoustic field.

The present work is a continuation of [5]. Proper Orthogonal Decomposition (POD) is used to identify the dominant acoustic modes. The results show that except the case with perturbations in time, an axial mode dominates the acoustic field.

Numerical methods

The acoustic field in an annular gas turbine combustion chamber is determined. The combustion is equiped with thirty burners arranged equidistantly in azimuthal direction (see Fig. 1(a)). In the followings all lengths are expressed in terms of the premixing tube diameter. The computations are carried out in two steps. First, the flow field is computed and the acoustic sources are stored. In the second step the acoustic sources are read in into the acoustic solver and eventually altered.

Since the flow computations are numerically expensive, the flow field is determined in a region of the combustion chamber corresponding to a single burner (Fig. 1(b)). The flow computations are based on LES to account for turbulence and on a flamelet-based approach to model combustion.

In the acoustic solver a non-homogeneous wave equation is solved on a cartesian grid. The whole geometry is taken into account. In the base case the sources are copied identically in thirty instances to account for the presence of thirty burners. To emulate counter-rotating motion, in the

second case, the acoustic sources are imposed in a mirrored way for every second burner. In the third case the acoustic sources are rotated around the symmetry axis of the burner with six degrees. The last case accounts for time shifts between consecutive burners by reading in the sources saved at different time instances.

For each case, the acoustic density fluctuation in a longitudinal cross section (through the symmetry axis of the combustion chamber) and two transversal cross sections (at axial distances of 4 and 8 diameters) have been saved every fiftieth timestep for postprocessing. The data was postprocessed using POD to identify the dominant modes. Fur further details about the numerical methods the reader is referred to [5].

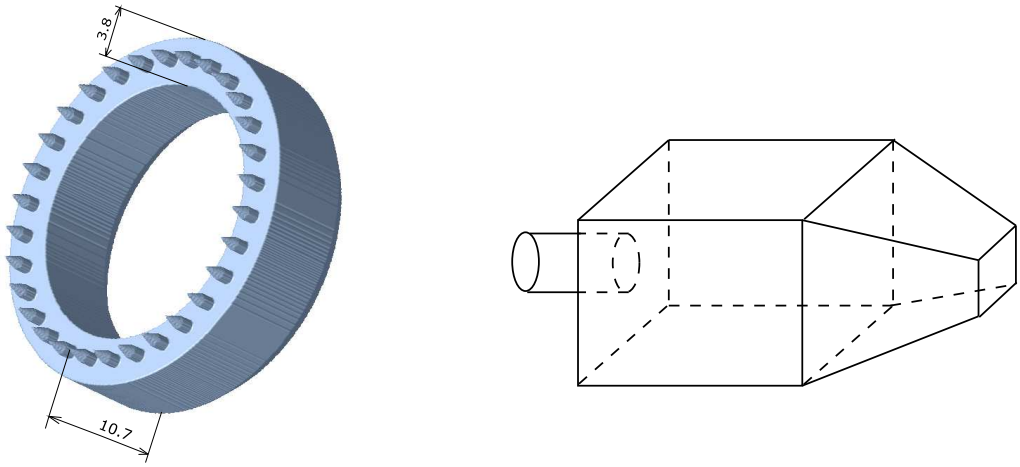

(a) (b)

Figure 1: The geometry of the combustion chamber (a) and sketch of the region considered in the flow computations (b)

Results

Previous computations [5] revealed that counter-rotation or phase shift in space of the acoustic sources have relatively small influence on the resulting acoustic density field which is restricted to the higher frequencies of the spectra. Significant influence on the low frequencies was observed only for the case when a time shift was imposed for the sources imposed at consecutive burners.

Figure 2 shows the isocontours of the first most dominant mode in a transversal cross section located at an axial position of eight diameters. One can observe that in all cases except the case with time shift (Fig. 2(d)) the dominant mode is an axial one. This is not surprising, since the flow computations revealed also the presence of a dominant axial mode. Reconstruction of the first dominant mode has shown that the observed axial mode has a Strouhal number of 0.6. This agrees well with the observed dominant frequency in the acoustic density fluctuation spectra [5]. For the last case, the time shift imposed between consecutive burners results in the excitation of an azimuthal mode. This azimuthal mode becomes the most dominant one.

The second most dominant mode for the considered cases is plotted at the same axial position in Figure 3. One can observe that the imposed perturbations have significant influence on the second

mode. In the base case and spatial phase-shift case a radial-azimuthal mode can be seen. The counter-rotating case is characterized by a clear azimuthal mode while in the case with time shift the axial mode became the second most dominant.

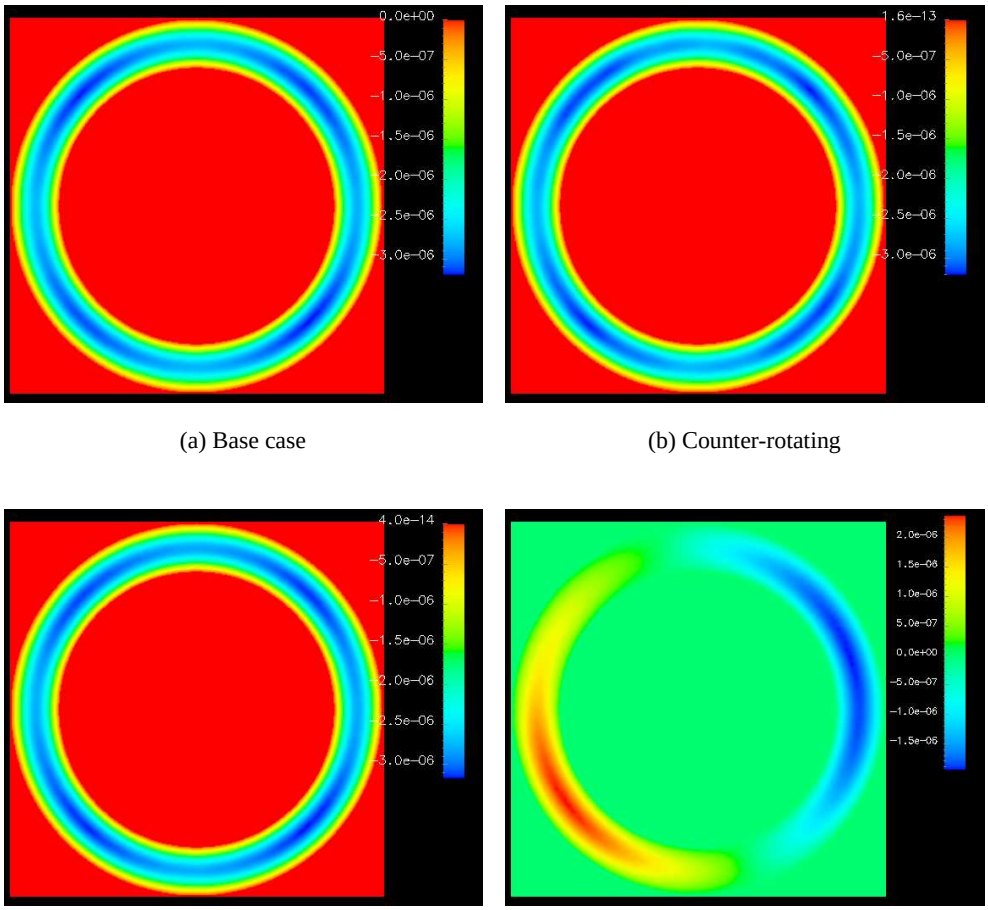

(a) Base case (b) Counter-rotating

(c) Space shift (d) Time shift

Figure 2: The first most dominant acoustic mode

Concluding remarks

POD has been used to identify the acoustic modes computed using a hybrid method in an annular gas turbine combustion chamber. The results show that an axial mode dominates all cases, except when the acoustic perturbations were perturbed in time. The second most dominant mode was different in each case.

References

[1] C. Duwig, B. Gherman, M. Mihaescu, M. Salewski, and L. Fuchs. Numerical study of thermo-acoustic waves generation ny a swirling flame using a new approach based on large eddy simulation. *ASME paper*, (GT2005-68136), 2005.

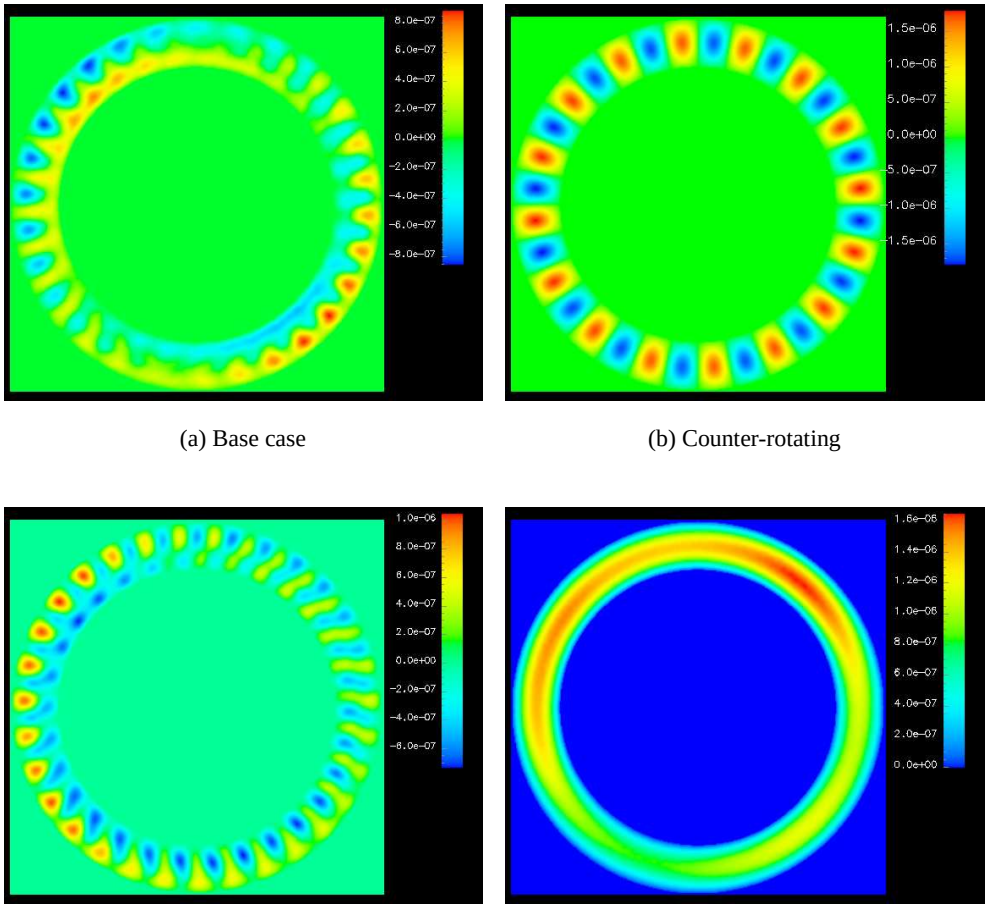

(a) Base case

(b) Counter-rotating

(c) Space shift

(d) Time shift

Figure 3: The second most dominant acoustic mode

[2] T. Lieuwen and V. Yang. *Combustion Instabilities in Gas Turbine Engines: Operational Experience, Fundamental Mechanisms and Modeling*. Number 210 in Progress in Astronautics and Aeronautics. AIAA, 2006. ISBN 156347669X.

[3] S. Menon, C. Stone, V. Sankaran, and B. Sekar. Large-eddy simulation of combustion in gas turbine combustors. *AIAA paper*, AIAA 2000-0960, 2000.

[4] M. Mihaescu, R.Z. Szasz, L. Fuchs, and E. Gutmark. Numerical investigations of the acoustics of a coaxial nozzle. *AIAA paper*, 2005-0420, 2005.

[5] R.Z. Szasz, C. Duwig, and L. Fuchs. Computation of the acoustic field in an annular gas turbine combustion chamber. In T. Lajos and J. Vad, editors, *Proceedings of the Conference on Modelling Fluid Flow*, volume I, pages 363–370, H-1111 Budapest, Bertalan L.U. 4-6, Hungary, 2006. Budapest University of Technology and Economics, Department of Fluid Mechanics, Budapest University of Technology and Economics. ISBN 963 06 0361 6.

Simulation of the Acoustics Behind a Barrier Generated by Periodically Passing Vehicles

Magnus Åberg* **and Robert-Zoltan Szasz**
Department of Energy Sciences
Lund University, Lund, Sweden
e–mail: magnus.aberg@vok.lth.se

Laszlo Fuchs
Department of Energy Sciences
Lund University, Lund, Sweden

Summary Noise generated by vehicles is a major environmental problem at inhabited areas along highways. A way of reducing such noise is by introducing a sound barrier (wall) on the sides of the road.
In this work we consider a line of moving objects, representing a vehicles, which are subject to a low Mach number air stream and passing parallel to a wall. A hybrid approach is used in order to investigate the influence of periodicity on acoustic field. Increasing the frequency of the vehicle passing rate leads to increase in the intensity of the main acoustic modes. The effect on the frequency content itself is less pronounced.

Introduction

Due to the development and increase of road traffic, noise pollution is an important factor for the nearby community. Federal restrictions and public interest have led to the development of several noise control devices, acoustic barriers being a common solution. Traffic noise and attenuating effects of barriers have been modelled using empirical expressions for acoustic power emission and then analytical or empirical formula for expressing the diffraction [1]-[2] over a screen or barrier. In the current work, a more systematic approach is proposed. This approach is based on computing the flow induced acoustical sources and than computing the acoustic wave propagation. The time-dependent flow field is handled by Large Eddy Simulations (LES) to account for the turbulence of the flow. As compared to a Reynold Average Navier-Stokes (RANS) closure, all of the energy bearing eddies are resolved in space and time. Since the acoustic sources are due to the spatial fluctuations of the flow field, this implies that the acoustic source spectrum is also well resolved. Once the acoustical sources are found, the wave propagation can be handled on a different, less resolved grid, since the wave numbers associated with the acoustics are much smaller than those associated with the turbulent flow. The present hybrid approach which takes advantage of the separation of turbulent and acoustic scales is characterized by its numerical efficiency while maintaining good accuracy. The approach has been used by Mihaescu and Moroianu [3] to evaluate the acoustic emission and propagation around a wind turbine and for assessing the acoustics due to running jet engines [4].

Method

In the hybrid approach used, the flow and acoustics are decoupled by assuming that the acoustic pressure fluctuations are much smaller than the pressure fluctuations in the flow field. Thus, the flow field generates the noise sources and the wave-equation is used to propagate the acoustic waves.

Governing equations

The flow solver is based on equations 1-2 which describe the isothermal and incompressible conditions in non-dimensional form.

$$\frac{\partial u_i}{\partial x_i} = 0 \tag{1}$$

$$\frac{\partial u_i}{\partial t} + \frac{\partial u_i u_j}{\partial x_i} = -\frac{\partial p}{\partial x_i} + \frac{1}{Re}\frac{\partial u_i}{\partial x_i x_j} \tag{2}$$

In the momentum equation, Eq.2, Re is the Reynolds number based on the object frontal characteristic width, D, and free-stream velocity.

In order to obtain an acoustic analogy in form of a wave equation, a decomposition of variables is introduced in the full Navier-Stokes equations and the viscous terms are neglected. The different terms are then recast into a form of an inhomogeneous wave equation in terms of ρ'.

$$\frac{\partial^2 \rho'}{\partial t^2} - \frac{1}{Ma^2}\frac{\partial^2 \rho'}{\partial x_i \partial x_i} = \frac{\partial^2 (u_i u_j)}{\partial x_i \partial x_j} \tag{3}$$

The primed variabl ρ' is referring to a perturbation around the incompressible state. Higher order terms of of the perturbation have been neglected by assuming that they are small.

Numerical method

The system of governing equations is discretized on Cartesian grids using finite differences.

The flow equations are discretized on a staggered grid with third and fourth order spatial schemes for the convective and viscous terms, respectively. For time marching, a first order implicit scheme is used. In order to achieve high resolution without refining the whole grid, local refinements are used in areas where high gradients are expected.

The wave equation, Eq.3, is discretized using a Lax-Wendroff like method that is second order in both time and space and solved using the Thomas algorithm line wise.

The solver algorithm consists of two major steps. In the first step, the flow solution equations 1-2 is integrated one time step. The source-term field in Eq.3 is then evaluated and interpolated to the acoustic grid using first order linear interpolation. In the second step, the wave equation is integrated while the flow field is advanced to next time step.

Problem setup

The computational domains for the flow and acoustics are schematicly shown in Fig.1 The vehicle comprises of two bricks of width D. The distance from the ground (xz-plane) is 0.25D. The bulk of the vehicle (the bottom brick) has a height of 0.5D and the total vehicle height from the ground is D. The length, in z-direction, is 2D for the bulk and 1D for the top brick. The height of the barrier is 1D and the vehicle is located at 0.5D from the barrier. In order to simulate a row of vehicles periodic conditions are set between the inlet and outlet boundaries. A no-slip condition is imposed on the vehicle surface, on the ground and on the barrier. Slip condition is used on the remaining walls.

In the acoustic solver, the barrier, ground and vehicle surface have reflecting boundary conditions. All other boundaries are assumed to be non-reflecting. The flow and acoustics are resolved using approximately 10 and 8 million cells, respecively. The acoustic solver has a spatial size of

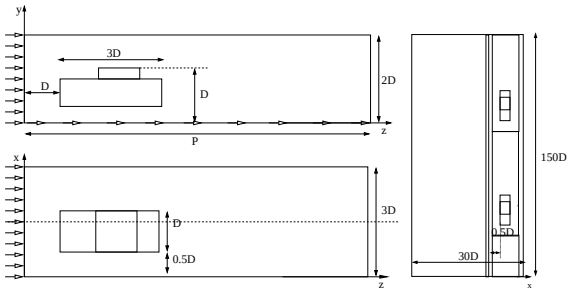

Figure 1: The computational domain for the flow and acoustic solvers. To the left, the flow field where the acoustic sources are calculated can be seen. The right figure shows the acoustic domain including the flow field from where the sources are interpolated

0.1D. Four periodic distances are considered 20D, 30D, 40D and 50D corresponding to the traffic Strouhal numbers, Stt, 0.025, 0.0167, 0.0125 and 0.01 The ReD in Eq. (2) is 60000 for all the cases and the Ma in Eq. (5) is 0.1.

Results

The source calculated from the flowfield is shown in Fig.2 A high magnitude of the source is, not surprisingly, located in the vicinity of the wake where velocity gradients are largest.

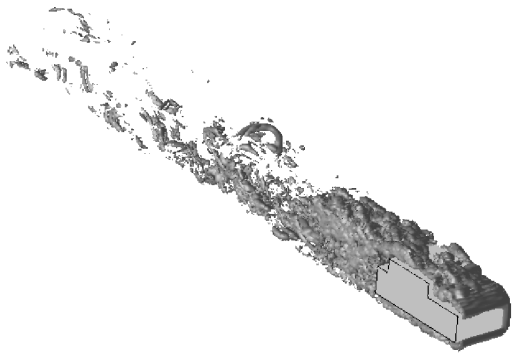

Figure 2: Visualisation of instantaneous iso-contours of the non-dimensional acoustic source.

The acoustic spectral content of the four traffic frequencies is plotted in Fig. 3. The frequency distribution does not have significant differences which indicates that the large wave-numbers induced by traffic load does not influence the small ones. It can also be seen that the acoustic signal for all of the St contains harmonics of St 0.2. These signals are harmonics of the periodic shear instability around each vehicle. The increase of amplitude with the trafic frequency is due to an inrease of source region rather then a change of the acoustic sources as such.

Concluding remarks

A hybrid approach is used in order to investigate the influence of periodicity on the flow and acoustic field. In this method the problem is solved in two steps firstly, the flow field around a line of moving vehicles parallel to a barrier is modelled with LES and the induced acoustic sources

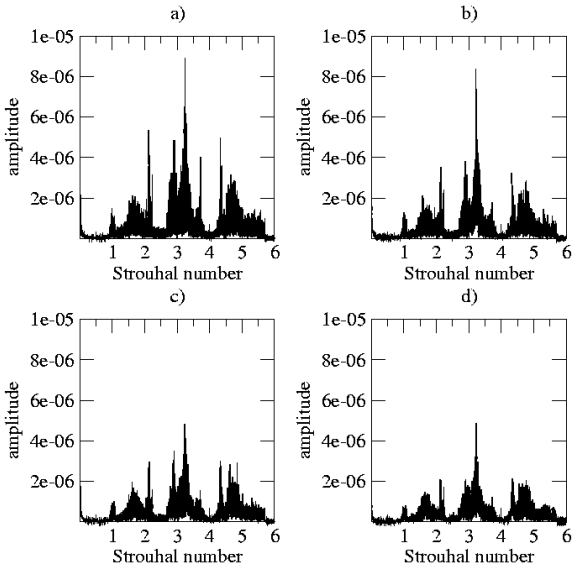

Figure 3: The acoustic spectra is plotted for the four traffic frequencies at one point located in (x,z)=(3D,75D) in the acoustic domain. St numbers are a) 0.025, b) 0.0167, c) 0.0125 and d) 0.01

are evaluated. Secondly, the acoustics is evaluated by using an acoustic analogy in form of an inhomogeneous wave equation. Most of the energy carrying frequencies are resolved and it is seen that periodicity is not influencing the spectral content of the signal which is dominated by harmonics of the dimensionless frequency of about 0.2. This frequency is related to the instability of the shear-layer close to and in the wake of the vehicles.

References

[1] Maekawa, Z. Noise reduction by screens. *Applied Acoustics*, (1968).

[2] Dae S. Cho, Jin H. Kim, Tae M. Choi, Byung H. Kim. Highway traffic noise prediction using method fully compliant with ISO 9613: comparison with measurement. *Applied Acoustics 65*, (2004).

[3] Moroianu, D. Mihaescu, M. Fuchs, L. Numerical computation of the acoustical field around wind-turbines. *tenth international congress on sound and vibration.*, (2003).

[4] Mihaescu, M., Gutmark, E., Szasz, R., Fuchs, L. Flow and Acoustics of a Coaxial Nozzle: a Sensitivity Study to the Inlet Boundary Conditions. *AIAA paper, AIAA-2006-619*, (2006).

Large Eddy Simulation and Proper Orthogonal Decomposition of a swirling turbulent flow.

Christophe Duwig* and Laszlo Fuchs
Department of Energy Sciences – Divison of Fluid Mechanics
Lund University, Lund Sweden
*e–mail: Christophe.Duwig@vok.lth.se

Summary Modelling turbulent flow is a vital issue in numerous engineering fields ranging from aerospace to biomechanics. An example of very complex four-dimensional turbulent flow relates to the vortex-breakdown. In the present paper, we consider a swirling flow undergoing an axis-symmetric sudden expansion. The low pressure region along the combustor axis induces a backflow creating a forward stagnation point. The dynamics of the stagnation point is studied using Large Eddy Simulation. The data are further analyzed using Proper Orthogonal Decomposition.

Introduction

Modelling and understanding of swirling flow is a key issue in many industrial applications e.g. flame stabilization. A swirling motion is given to a jet. The swirling jet is subject to centrifugal forces leading to a radial expansion of the jet. A low-pressure region appears around the axis region, close to the expansion. If the swirling motion is strong enough, the longitudinal pressure gradient induces an axial back flow and leads to vortex breakdown. However, despite of more than 40 years of research, the mechanisms of vortex breakdown are only partially understood [1]. The main difficulty of the problem is the non-linear and unsteady behaviour of this type of flow: large structures resulting from vortex breakdown and the swirling shear-layers, affect strongly the flow field. An example of the large scale unsteady motions arising during vortex breakdown is the precessing vortex core (PVC) [1-3]. Experimental and numerical works [2, 3] have reported that vortex breakdown might result in an off-axis precession of the central recirculation zone. The recirculation zone undergoes a periodic rotation around the axis and the instantaneous flow field is far from being axis-symmetric. However, time averaging over several cycles restores the axis-symmetry.
The present work focuses on simulation and study of PVC arising during the vortex-break down. The unsteady and multidimensional nature of the problem makes that one need to resolve both in time and space the PVC and leads to use of Large Eddy Simulation (LES) based techniques. However, capturing the PVC leads to an accumulation of a large amount of data and we use the Proper Orthogonal Decomposition (POD) [4] to extract relevant information (i.e. related to the PVC) from the collected data.

Numerical techniques

LES modelling

The basic equations describing the motion of an isothermal incompressible fluid are the conservation of momentum, mass. In the case of LES the averaging operation corresponds to spatial filtering (i.e. applying a “low-pass” filter which removes all the Fourier components that have shorter length scale than the filter size). The filtering operator is linear and is assumed commutative with time- and space-derivatives but is not commutative with non-linear terms. Thus,

non-linear terms lead to expressions that cannot be expressed in terms of the filtered quantities requiring subgrid scale (SGS) modelling. In the momentum equations, the SGS terms should account for the dissipative character of turbulence on the small (unresolved) scales as well as for the transfer of energy among the resolved and unresolved scales. A computational grid can support only Fourier components that have longer wavelengths than the grid size. Thus, a dependent variable that is represented on a grid that is used together with a discrete approximation for the derivatives leads to an implicit filtering. If no explicit SGS terms are added, then the numerical scheme should account at least for the small scale dissipation. This is attained by using a dissipative discretization scheme and is referred as implicit LES [5].
A Cartesian grid based finite difference LES code was used [5]. The spatial discretization is done using a fourth order centered scheme except for the convective term in the momentum equations that are treated using a third order upwind scheme. A second order finite difference scheme is used for time discretization, the time integration is done implicitly [5].

Proper Orthogonal Decomposition

In order to extract only relevant information from the large amount of LES data, we perform a proper orthogonal decomposition (POD) of the resolved turbulent flow. Within the POD, one seeks to project the turbulent flow field on a vector base that maximizes the turbulent kinetic energy content for any subset of the base. It allows an accurate description of the turbulent data using only few modes [4]. Given a vector Q containing the field variables and a vector base Φ, the POD gives:

$$Q(\mathbf{x},t) \approx Q^N(\mathbf{x},t) = \sum_{i=0}^{N} a_i(t)\Phi_i(\mathbf{x}) \qquad (1)$$

Note that the approximation Q^N of the turbulent data set Q converges to Q when N goes to infinity and that $i=0$ corresponds to the averaged field. The base vectors are computed so that they satisfy the eigenvalue problem [4]:

$$< Q(\mathbf{x},t) \cdot Q^T(\mathbf{x},t) > \Phi(\mathbf{x}) = \lambda\Phi(\mathbf{x}) \qquad (2)$$

where the superscript T denotes the transposed of the vector and <.> is the time averaging operator. It is worth noticing that the vectors Φ are the eigenvectors of the temporal auto-correlation tensor. The eigenvalue λ_i characterizes the turbulent kinetic energy content of the mode i. For practical reasons, it is seldom possible to solve Equation (2) if the turbulent data set is large. Instead, one may reduce the computational costs by using Sirovich's *method of snap-shots* e.g. [6].

Presentation of *Dellenback*'s swirling flow

LES together with POD was used for simulating and studying vortex breakdown in a model combustor corresponding to the experiments conducted by Dellenback et al. [3]. The setup consists of a swirling jet flowing into a pipe of diameter D that issues into a coaxial pipe of diameter $2D$. Figure 1 (left) shows a sketch of the geometry of the case.
Here we restrict our study to a Reynolds number of 30000 and a jet swirl number of 0.6 [3]. The computational domain is a $12D*2D*2D$ box starting at the $2D$ upstream of the expansion as presented on figure 1. The inflow conditions are enforced at $X=-2D$ and were taken from measured velocity profiles [3]. Non-slip walls and zero-gradient mass conservative boundaries where used for the wall and outlet modelling. The computational grids contain $\sim 1 \cdot 10^6$ mesh-points with about 50 cells across the diameter D.

The data are normalized with the pipe diameter D and the bulk velocity U_0 in the pipe (i.e. the total volume flow / πD^2).

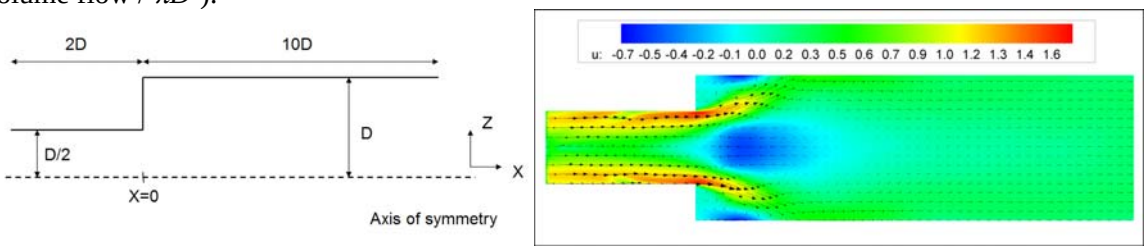

Figure 1: Left: Computational geometry corresponding to Dellenback's experiment. Right: Time averaged normalized axial velocity and velocity vectors obtained from LES.

Results

Time averaged results

Figure 1 (right) shows the time averaged normalized axial velocity. The flow field is axis-symmetric. The flow is distributed over the pipe cross section and evolves toward an annular jet as getting closer to the expansion. Consequenlty, a forward stagnation point appears on the axis close to the expansion. Downstream of the expansion, two negative axial velocity regions are seen, one central recirculation zone (CRZ) close to the axis and one toroidal external recirculation zone (ERZ) close to the expansion. The CRZ results from vortex breakdown. Between the two recirculation zones, the positive axial velocity is concentrated into an annular jet.

Figure 2 (a) shows the averaged profiles obtained by LES together with some experimental data [3]. The agreement is good indicating that the averaged flow field is well captured by the LES. In particular, the size and strength of the two recirculation zones are simulated accurately. Figure 2 (b) compares the root-mean-squared (RMS) of the axial velocity fluctuations obtained by measurements and simulation. The data shows that high levels of fluctuation are seen in the shear-layer between the annular jet and the recirculation zones. The overall agreement is reasonable but the numerical results over-estimate the fluctuation intensity. However, the present results reproduce well the vortex-breakdown and can be used for investigating the nature of the velocity fluctuations.

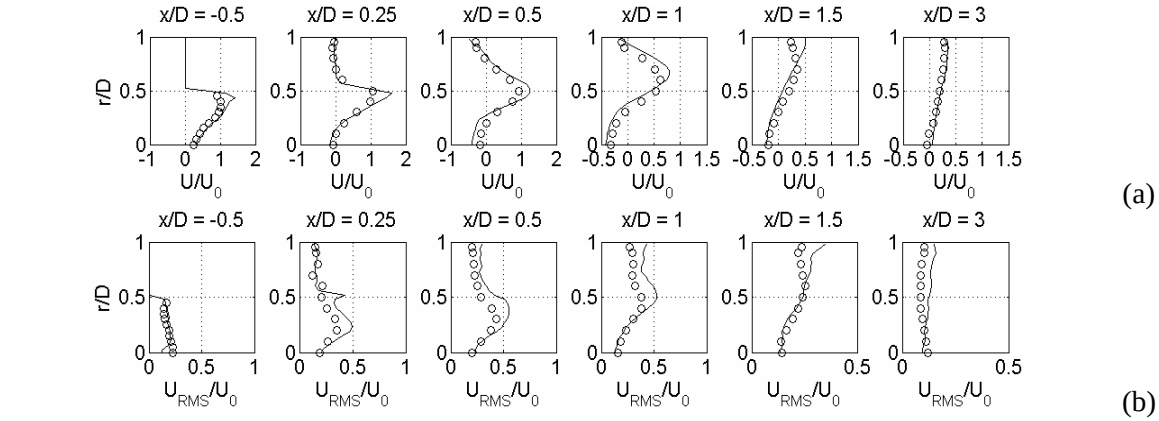

Figure 2: Statistical data plotted along radial lines at different locations in the combustor (a) Time averaged axial velocity. (b) Root Mean Squared of the axial velocity fluctuation. The solid line represents the LES predictions and the symbols are Dellenback's measurements [3].

Analysis of the large turbulent structures

POD Modes 1 and 2 dominate clearly the other modes representing together ~20% of the total turbulent kinetic energy. Figure 3 (a) shows a vortex-core visualization of mode 1. The mode consists of a double helix that originates ~1D upstream of the expansion. The double helix covers the region of vortex-breakdown. Note that mode 2 (not shown here) is almost identical to mode 1 rotated around the axis by $\pi/2$ so that the combination of the two modes results in a rotation at the PVC frequency. Figure 3 (b) shows the axial velocity fluctuation associated with mode 1. The fluctuation is organized with a spiral shape and is anti-symmetric. The effect of mode 1 and 2 on the averaged flow results in off-axis rotation of the central recirculation zone referred as PVC.

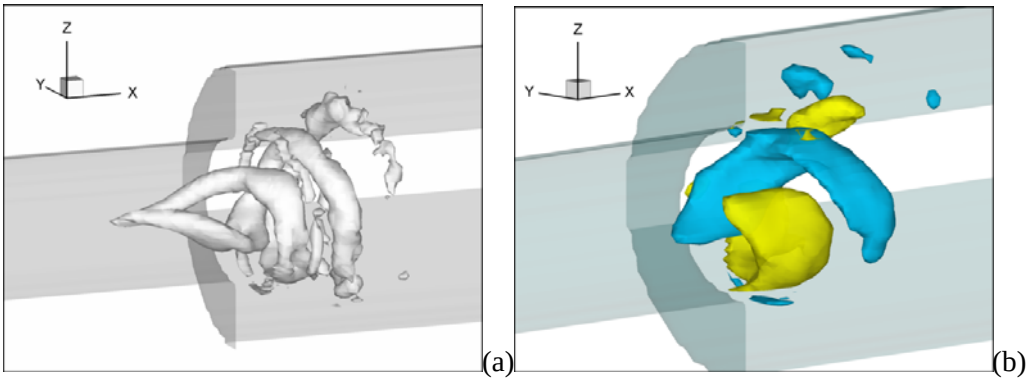

(a) (b)

Figure 3: Visualization of the POD modes (a) λ_2-visualization [7] of POD-mode 1. (b) Axial velocity iso-surfaces (negative in yellow; positive in blue).

Concluding remarks

Large Eddy Simulation together with Proper Orthogonal Decomposition was used to study a turbulent swirling flow. The results indicated that LES captures accurately the flow and the POD enables to isolate large scale coherent structures. This methodology is suitable for studying and understanding turbulent swirling flows.

References

[1] Lucca-Negro O., O'Doherty T., "Vortex breakdown: a review", *Prog. in Energy and Comb. Sci.*, 27, pp. 431-481, (2001)

[2] Syred N., "A review of oscillation mechanisms and the role of the precessing vortex core (PVC) in swirl combustion systems", *Prog in Energy and Comb. Sci.*, 32, pp. 93-161, (2006)

[3] Dellenback P.A., Metzger D.E., Neitzel G.P., "Measurements in turbulent swirling flow through an abrupt axisymmetric expansion", *AIAA J.*, 26(6), pp. 669-681, (1988)

[4] Berkooz G., Holmes P., Lumley J. L. (1993), "The Proper Orthogonal Decomposition in the Analysis of Turbulent Flows", *Annu. Rev. Fluid Mech.*, 25, p 539. (1993)

[5] Gullbrand J., Bai X.S., Fuchs L. (2001), "High-order Cartesian Grid Method for Calculation of Incompressible Turbulent Flows", *Int. J. Num. Meth. Fluids*, **36**, p 687.

[6] Smith T., Moehlis J, Holmes P. (2005), "Low-dimensional Modelling of Turbulence Using the Proper Orthogonal Decomposition: A Tutorial", *Nonlinear Dyn.*, 41, pp. 275.

[7] Jeong J., Hussain F. (1995), "On the Identification of a Vortex", *J. Fluid Mech.*, 285, p 69-94.

Application of an adaptive response surface approach for efficient structural reliability analysis

Thomas Most* **and Christian Bucher**
Institute of Structural Mechanics
Bauhaus-University, Weimar, Germany
e–mail: thomas.most@uni-weimar.de

Summary In this paper an adaptive response surface approach for reliability analysis is presented. The obtained numerical results are compared to these of directional sampling and the fekete point method.

Introduction

In engineering science the modeling and numerical analysis of complex systems and relations plays an important role. In order to realize such an investigation, for example a stochastic analysis, in a reasonable computational time, approximation procedure have been developed. A very popular approach is the response surface method, where the relation between input and output quantities is represented for example by global polynomials or local interpolation schemes as Moving Least Squares introduced by [1]. In recent years artificial neural networks (ANN) have been applied as well for such purposes in several studies for stochastic analyses, e.g. in [2].

Recently an adaptive response surface approach for reliability analyses was proposed in [3]. This method is very efficient concerning the number of expensive limit state function evaluations, but due to the applied simplex interpolation the procedure is limited to small dimensions. In [4] the original approach in [3] was extended for larger dimensions using combined ANN and MLS response surfaces for evaluating the adaptation criterion. In this paper this approach is compared to the standard directional sampling method [5] and the fekete point method [6].

Reliability analysis, response surface method and adaptivity

By assuming a random vector

$$\mathbf{X} = [X_1, X_2, \ldots, X_n] \tag{1}$$

of n mutually independent, standard normal random variables X_i and a limit state function $g(\mathbf{x})$ the probability of failure $P(F)$ reads

$$P(F) = \int_{g(\mathbf{x})\leq 0} \varphi_n(\mathbf{x}) d\mathbf{x} \tag{2}$$

where $\varphi_n(.)$ denotes the n-dimensional normal probability density. The limit state function divides the random variable space into a safe domain $S = \{\mathbf{x} : g(\mathbf{x}) > 0\}$ and a failure domain $F = \{\mathbf{x} : g(\mathbf{x}) \leq 0\}$.

The computational challenge in determining the integral of Eq. 2 lies in evaluating the limit state function $g(\mathbf{x})$, which for non-linear systems usually requires an incremental/iterative numerical approach. For reliability analysis it is most important to obtain support points for the response surface very close to or exactly at the limit state $g(\mathbf{x}) = 0$. For this purpose the random vector $\mathbf{X}$ in Eq. 2 is replaced by a random direction unit vector

$$\mathbf{A} = [A_1, A_2, \ldots, A_n] \tag{3}$$

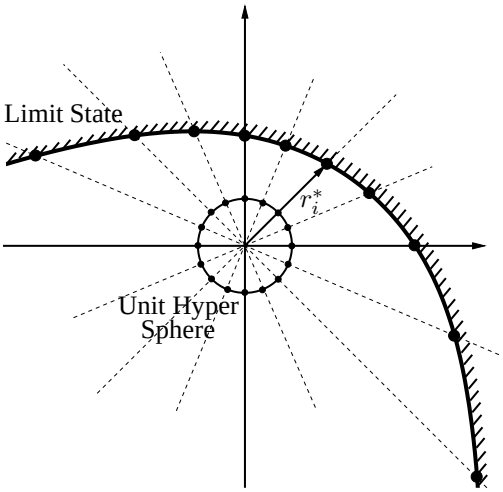

Figure 1: Limit state with discrete points

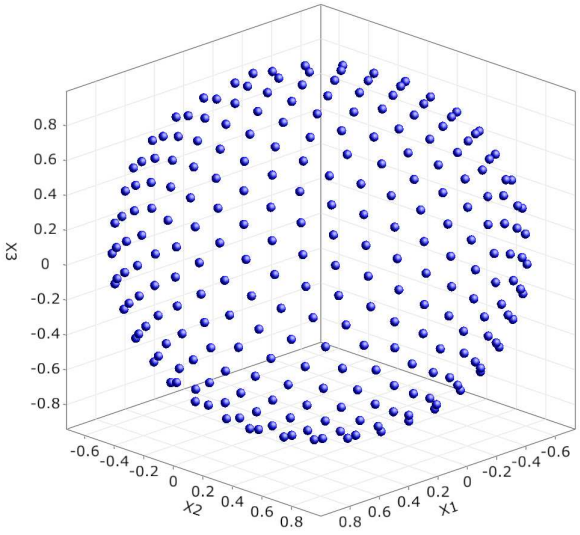

Figure 2: 3D Fekete point set with 500 points

and a random radius R which leads to

$$\mathbf{X} = \mathbf{A}R. \tag{4}$$

Then the integral from Eq. 2 reads

$$P(F) = \int_{r(\mathbf{a})=1} [1 - \chi_n^2(r^{*2}(\mathbf{a}))] f_{\mathbf{A}}(\mathbf{a}) ds(\mathbf{a}) \tag{5}$$

with

$$g(\mathbf{a}r^*(\mathbf{a})) = 0 \tag{6}$$

whereby $f_{\mathbf{A}}(.)$ is the probability density of the random directional unit vector $\mathbf{A}$, $\chi_n^2(.)$ is the χ^2 distribution function with n degrees of freedom and $ds(\mathbf{a})$ denotes integration over the unit hyper-sphere $r(\mathbf{a}) = 1$. For evaluating Eq. 5 only the distances $r^*(\mathbf{a})$ of the limit state surface from the origin in the direction of $\mathbf{a}$ have to be known.

The points required for the response surface approximation of the limit state $g(\mathbf{x}) = 0$ can be determined using Monte Carlo simulation based on directional sampling [5]. In Fig. 1 the limit state with discrete points is shown in principle.

Better approximations can be achieved if the support points are generated in order to cover the unit hyper-sphere almost uniformly. A very efficient method for this purpose are Fekete point sets [6] which can be generated very simply even in high dimensions. In Fig. 2 such a point set is shown for three random variables.

In this paper an adaptive response surface approach is applied which was presented by the authors in [4] and is based on the method proposed by [3]. In [3] two independent response surfaces each having a separate set of supports are used, whereby each response surface interpolates the conditional probabilities of failure using simplices. As error estimate used for the adaptation the maximum difference between both response surfaces concerning the conditional probabilities of failure was applied. Due to the limitation of the simplex interpolation for small dimensional problems, in [4] the adaptive approach was extended for the application of neural networks and Moving Least Squares. There only one set of points with the two different approximation methods was used.

The adaptation criterion is carried out by using the maximum difference of the conditional probabilities of failure of both response surfaces

$$e_p = max|(p_i^*)_2 - (p_i^*)_1|; \quad i = 1 \dots N_{DS}, \tag{7}$$

where i is the evaluated directional sample out of a set of N_{DS} realizations. The conditional probabilities of failure are computed as follows

$$p_i^* = [1 - \chi_n^2(r^{*2}(\mathbf{a}_i))]. \tag{8}$$

Numerical examples

In this section three numerical examples are investigated: limit state functions consisting of one and two hyperplanes. In Fig. 3 the limit state functions are given with the corresponding probability of failure. Whereby LSF 1 and 3 contain only one efficient region, LSF 2 contains two regions with equal contribution to the failure probability. LSF 1 and 2 can be reproduced much better by directional sampling and the fekete point method as LSF 3, since in LSF 1 and 2 a larger area on the unit hyper-sphere is covered by the effective regions. The adaptive response surface approach leads for LSF 1 and 3 to better results with a smaller number of samples as the already efficient fekete point method. For LSF2 similar results as in the fekete point method could be obtained.

Concluding remarks

The presented adaptive response surface approach can be applied very efficiently for structural reliability analysis. For problems with effective regions covering a medium or small area on the unit hyper-sphere, which can be found mainly in practical problems, this method is very attractive compared to the fekete point method concerning the number of required samples to obtain a certain accuracy. If the effective regions cover a relatively large area on the hyper-sphere similar results could be obtained as with fekete points. In comparison to directional sampling the proposed method is always significantly more efficient.

References

[1] P. Lancaster and K. Salkauskas. Surface generated by moving least squares methods. *Mathematics of Computation*, 37:141–158, 1981.

[2] M. Papadrakakis, V. Papadopoulos, and N. D. Lagaros. Structural reliability analysis of elastic-plastic structures using neural networks and Monte Carlo Simulation. *Computer Methods in Applied Mechanics and Engineering*, 136:145–163, 1996.

[3] M. Macke and J. Riedel. Adaptive response surface method for structural reliability calculation. In R.B. Corotis et al., editors, *Proc. 8th Int. Conf. Structural Safety and Reliability (ICOSSAR), Newport Beach, USA, June 17-22, 2001*. Swets & Zeitlinger, Lisse, 2001.

[4] T. Most and C. Bucher. Adaptive response surface approach using artificial neural networks and moving least squares. In K. Gürlebeck and C. Könke, editors, *Proc. 17th Int. Conf. Applications of Computer Science and Mathematics in Architecture and Civil Engineering (IKM), Weimar, Germany, July 12-14, 2006*. Bauhaus-University Weimar, 2006.

[5] P. Bjerager. Probability integration by directional simulation. *Journal of Engineering Mechanics*, 114:1288–1302, 1988.

[6] J. Nie and B. R. Ellingwood. Directional methods for structural reliability analysis. *Structural Safety*, 22:233–249, 2000.

Limit state function 1: $g(\mathbf{x}) = -x_1 + 4 \qquad \hat{P}(F) = 3.1686 \cdot 10^{-5}$

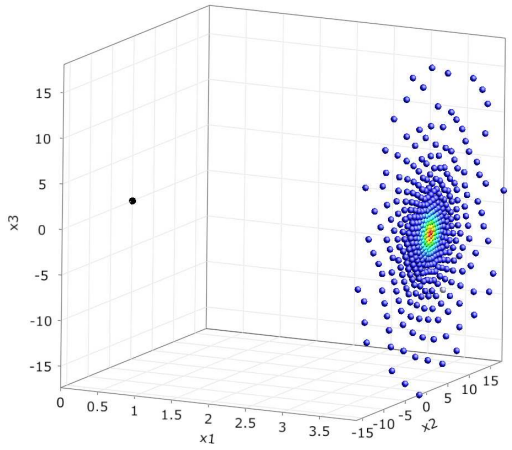

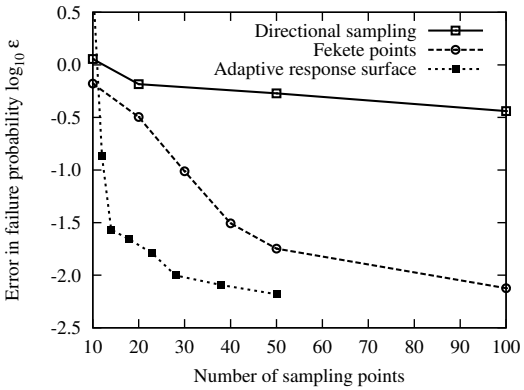

Limit state function 2: $g_1(\mathbf{x}) = -x_1 + 4$ OR $g_2(\mathbf{x}) = -\sum x_i + 4\sqrt{n} \qquad \hat{P}(F) = 6.2408 \cdot 10^{-5}$

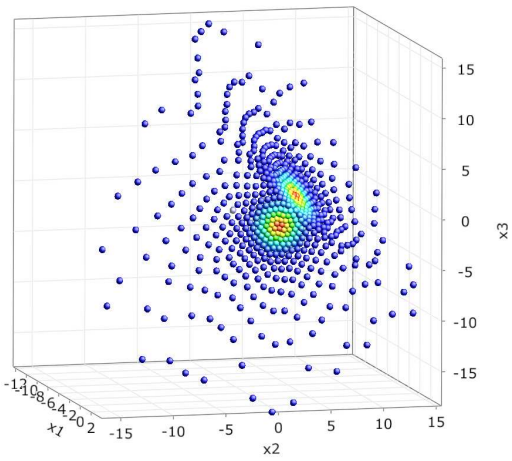

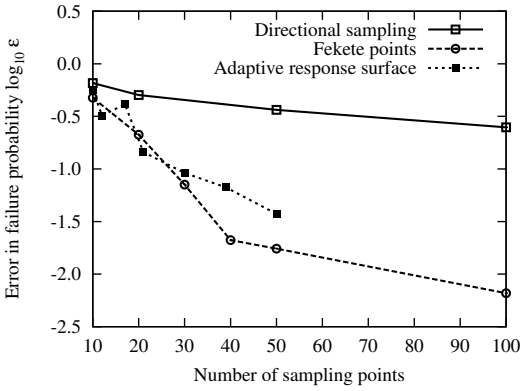

Limit state function 3: $g_1(\mathbf{x}) = -x_1 + 3$ AND $g_2(\mathbf{x}) = -\sum x_i + 3\sqrt{n} \qquad \hat{P}(F) = 1.2415 \cdot 10^{-4}$

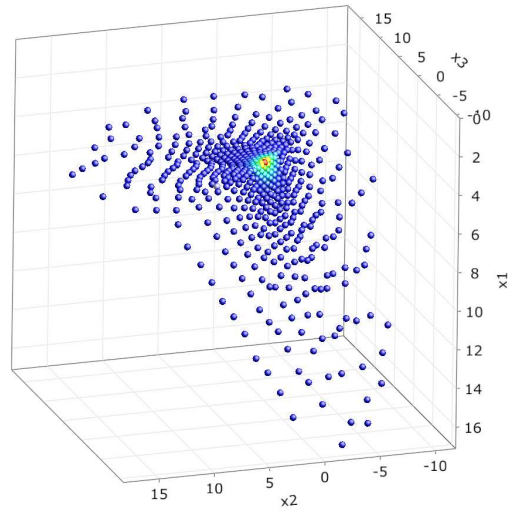

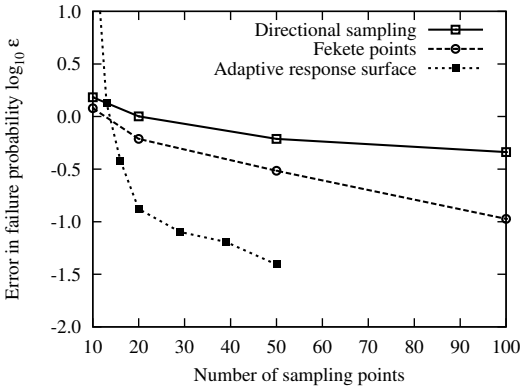

Figure 3: Limit state functions consisting of one or two hyperplanes with corresponding mean errors for 50 runs by using direction sampling, fekete points and adaptive response surface approach

A parallel method for solving discrete topology design problems

M.H. Rasmussen* **and M. Stolpe**
Department of Mathematics
Technical University of Denmark, Kgs. Lyngby, Denmark
e–mail: M.L.H.Rasmussen@mat.dtu.dk

Summary This work achieves global solutions to several truss topology optimization problems by solving a mixed-integer convex problem based on the Simultaneous ANalysis and Design (SAND) formulation. Furthermore, we present additional valid inequalities and cuts (Combinatorial Benders' and projected Chvátal-Gomory) that strengthen the formulation and, hence, improve the efficiency, measured in solution time and speed-up, of a parallel Branch-and-Bound method.

Introduction

The subject of this work is solving discrete truss topology optimization problems with local stress- and displacement constraints to global optimum. We consider a formulation based on the Simultaneous ANalysis and Design (SAND) [5] for the ground structure approach to topology optimization of trusses [4]. The intrinsically non-convex SAND problem is reformulated as a Mixed-Integer Linear Program (MILP) by use of the mathematical structure of the problem as described in [1, 7]. This MILP is solved with a parallel implementation of the deterministic and convergent algorithm Branch-and-Bound. For the parallel implementation, we use the master-worker paradigm implemented in the open-source software SYMPHONY 5.0 [6].

Additional valid inequalities and cuts are introduced to give a stronger representation of the problem. The valid inequalities represent the physics, and the cuts (projected Chvátal-Gomory [2] and Combinatorial Benders' [3]) come from an understanding of the particular mathematical structure of the reformulation. This work shows that adding the valid inequalities and projected Chvátal-Gomory- and Combinatorial Benders' cuts to the problem formulation significantly improves the speed-up and decreases the solution time.

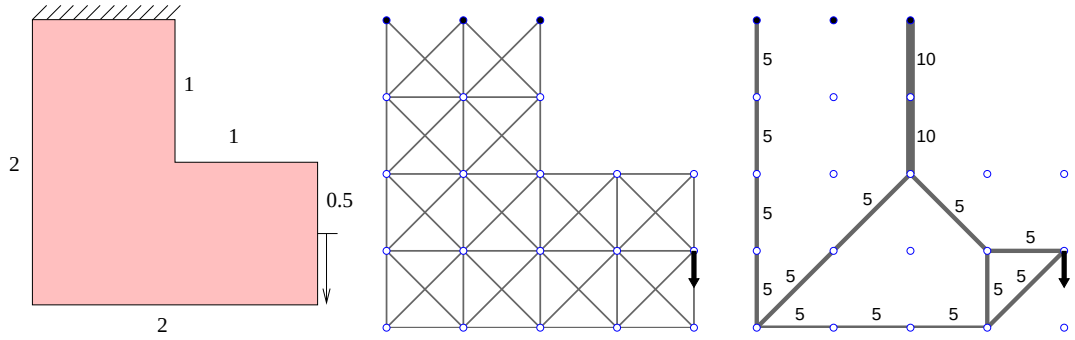

(a) The design-domain, with lengths given in meters and the load component $f = 450$ kN.

(b) The ground structure with $J = 54$ bars and $d = 36$ degrees of freedom.

(c) The optimal cross section areas are given in 10^{-3} m^2. The volume is $V^* = 0.0466$ m^3.

Figure 1: The design-domain (a), the ground structure (b), and an optimal structure (c) for the L-shape truss.

Problem formulation

The problem, that we consider, is to minimize the volume of a truss structure subject to force equilibrium-, displacement-, and stress constraints. A given design-domain with defined supports and an external load vector (see Figure 1 (a) for an example) is discretized into a ground structure, i.e., a set of potential straight bars connecting a set of frictionless nodes, see e.g. Figure 1 (b). A bar can take an area a_i from a given set $a_i \in \{a_1, \ldots, a_I\}$, or else the bar is not present in the design. The actual number of possible cross-section areas is $I + 1$, since 0 is not represented in the set $\{a_1, \ldots, a_I\}$. We denote x_{ij} the binary design-variable, where

$$x_{ij} = \begin{cases} 1 & \text{if the } j\text{th bar is present in the design with area } a_i, \text{ and} \\ 0 & \text{if the } j\text{th bar with area } a_i \text{ is not present in the design.} \end{cases}$$

The truss structure is represented by the vector of design variables $\mathbf{x} \in \mathbb{B}^{IJ}$, where J is the number of potential bars in the ground structure.

For the jth bar, the length is denoted l_j and Young's modulus is E_j. We denote by $\mathbf{b}_j \in \mathbb{R}^d$ the direction cosine vector in global coordinates for the jth bar, where d is the number of degrees of freedom. The stiffness matrix $\mathbf{K}(\mathbf{x}) \in \mathbb{R}^{d\times d}$ in global coordinates is then

$$\mathbf{K}(\mathbf{x}) = \sum_{j=1}^{J}\sum_{i=1}^{I} x_{ij}(E_j a_i/l_j)\mathbf{b}_j\mathbf{b}_j^T\,, \quad \text{and} \quad \mathbf{K}(\mathbf{x})\mathbf{u} = \mathbf{f}$$

expresses the force equilibrium constraints with the displacement- and external force vectors denoted by $\mathbf{u} \in \mathbb{R}^d$ and $\mathbf{f} \in \mathbb{R}^d$, respectively.

The representation of the force equilibrium constraints is nonlinear. We reformulate these into sets of linear inequality constraints. In the reformulation, continuous variables s_{ij} are introduced, and the direction cosine-relationships are represented in the matrix $\mathbf{B} \in \mathbb{R}^{d\times IJ}$. The continuous variables s_{ij} represent the internal normal forces. Furthermore, the constants $c_{ij}^{\min}$ and $c_{ij}^{\max}$ are introduced. These constants ($c_{ij}^{\min}$ and $c_{ij}^{\max}$) are determined from the limits $\mathbf{u}^{\min}$ and $\mathbf{u}^{\max}$ on the displacements, which denote, respectively, the minimal and the maximal allowed displacements.

The problem of minimizing the volume subject to force equilibrium-, displacement-, and stress constraints formulated as a MILP is

$$\begin{aligned}
\min_{\mathbf{x}\in\mathbb{B}^{IJ},\mathbf{u}\in\mathbb{R}^d,\mathbf{s}\in\mathbb{R}^{IJ}} & \sum_{j=1}^{J} l_j \sum_{i=1}^{I} a_i x_{ij} && && \text{(volume)} \\
\text{s.t.} \quad & \mathbf{B}\mathbf{s} = \mathbf{f}\,, && && \text{(force equilibrium)} \\
& x_{ij}a_i\sigma^{\min} \le s_{ij} \le x_{ij}a_i\sigma^{\max}, && \forall(i,j) && \text{(stress constraints)} \\
& \frac{E_j a_i}{l_j}\mathbf{b}_j^T\mathbf{u} - s_{ij} \ge (1 - x_{ij})c_{ij}^{\min}, && \forall(i,j) && \text{(compatibility)} \\
& \frac{E_j a_i}{l_j}\mathbf{b}_j^T\mathbf{u} - s_{ij} \le (1 - x_{ij})c_{ij}^{\max}, && \forall(i,j) && \text{(compatibility)} \\
& \sum_{i=1}^{I} x_{ij} \le 1\,, && \forall j && \text{(at most one area per bar)} \\
& \mathbf{u}^{\min} \le \mathbf{u} \le \mathbf{u}^{\max}, && && \text{(displacement constraints)} \\
& x_{ij} \in \{0,1\}\,, && \forall(i,j)\,. && (j\text{th bar with } i\text{th area})
\end{aligned} \tag{1}$$

Note that representing the SAND formulation as a MILP is made possible from the fact that the design variables are binary ($x_{ij} \in \{0,1\}$) and the displacement variables $\mathbf{u}$ are bounded.

	Without *valid inequalities and cuts*					***With*** *valid inequalities and cuts*				
P.	T_1	*Speed-up*				T_1	*Speed-up*			
	[s]	2	4	8	16	*[s]*	2	4	8	16
L_{σ_1}	33612	1.99	2.83	3.04	3.24	508	1.98	3.94	7.53	15.10
L_{σ_2}	200117	1.52	1.58	1.70	1.69	8585	2.02	4.10	8.21	16.80
L_{σ_3}	549	2.01	4.07	8.12	16.11	337	1.94	3.82	7.95	14.62
C_{σ_1}	56610	1.85	2.82	2.86	2.88	2359	2.06	1.83	3.74	8.73
C_{σ_2}	19375	2.10	4.07	6.42	7.02	13553	2.17	4.47	9.91	19.90
C_{σ_3}	73839	1.87	2.65	2.76	2.78	213091	1.83	2.45	2.75	2.77

Table 1: Solution statistics comparing Branch-and-Bound with and without added valid inequalities and cuts. Notice the improved speed-up and the faster optimization time after adding valid inequalities and cuts.

Figure 1 illustrates a truss structure from design-domain (a), to ground structure (b), to the optimal structure (c) found by solving the problem (1). The material data used in this example represents aluminum (with Young's Modulus $E = 70$ GPa), and the external load vector has the single load component $f = 450$ kN. The stress limits are $\sigma^{\max} = -\sigma^{\min} = 170$ MPa, and the displacement constraints are ± 2 m. The area set consists of 3 areas, $a_i \in \{5, 10\}10^{-3}$ m^2 and the area 0 m^2 is also possible. This structure has the optimal volume $V^* = 0.0466$ m^3.

Numerical Experience

The parallelized Branch-and-Bound method implemented in SYMPHONY 5.0 [6] is based on a master-worker paradigm. The master manages information which it sends to and receives from the workers. The workers solve subproblems of the original problem, in our case, continuous relaxations of the optimization problem (1).

For the master-worker paradigm, to show good performance, the workers should be constantly busy solving subproblems. This is measured by the speed-up, where we compare the time for 'one master – one worker' to 'one master – several workers'. Denoting the computational time for 'one master – x workers' by T_x [s], the speed-up is

$$\text{Speed-up} = \frac{T_1}{T_x} .$$

The ideal is to have the same speed-up as the number of workers. Note, however, a speed-up of 19.90 in Table 1 when using 16 workers. These even larger speed-up values are because the number of solved subproblems may differ.

The performance of this parallelized Branch-and-Bound method is presented in Table 1. We see for each problem (*P.*) the time for solving the problem using 'one master – one worker' (T_1) and the speed-up when using several (2, 4, 8, and 16) workers. The problems we solve are the L-shape truss problem from Figure 1 and a Cantilever 3D truss, see Figure 2. Figure 2 (c) illustrates the optimal structure when using Young's Modulus $E = 70$ GPa, the load vector with four load components of $f = \sqrt{2} \cdot 100$ kN, the stress limits $\sigma^{\max} = -\sigma^{\min} = 170$ MPa, and the displacement constraints ± 2 m. The area set consists of 5 areas, $a_i \in \{2.5, 5, 7.5, 10\}10^{-3}$ m^2 and the area 0 m^2 is also possible. This structure has the optimal volume $V^* = 0.438$ m^3.

Both the L-shape truss and the Cantilever 3D truss are solved with the three different stress limits

$$\sigma_1^{\max} = -\sigma_1^{\min} = 170 \text{ MPa}, \quad \sigma_2^{\max} = -\sigma_2^{\min} = 120 \text{ MPa}, \quad \text{and} \quad \sigma_3^{\max} = -\sigma_3^{\min} = 90 \text{ MPa}.$$

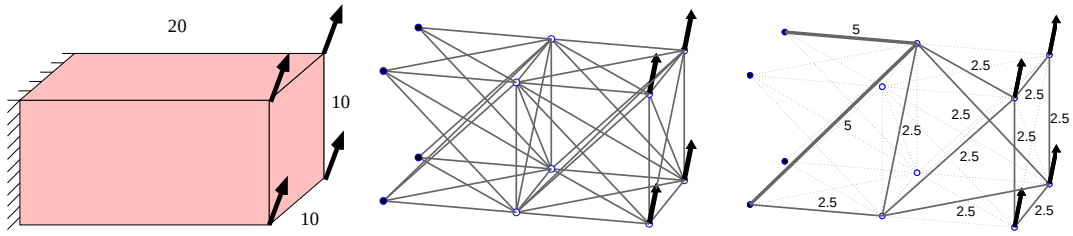

(a) The design-domain, with lengths given in meters and the four load components of $f = \sqrt{2} \cdot 100$ kN.

(b) The ground structure with $J = 40$ bars and $d = 24$ degrees of freedom.

(c) The optimal cross section areas are in 10^{-3} m^2. The volume is $V^* = 0.438$ m^3. The dotted lines represent areas of 0 m^3.

Figure 2: The design-domain (a), the ground structure (b), and an optimal structure (c) for the Cantilever 3D truss.

The L-shape truss problem with stress constraint σ_1 is denoted L_{σ_1}, and similarly, C_{σ_1} denotes the Cantilever 3D truss problem with stress constraint σ_1.

Notice the improved speed-up and the faster optimization time after having added valid inequalities and cuts in all problems but the C_{σ_3} problem, i.e., the Cantilever 3D truss problem with stress constraint σ_3. We believe that with more cuts, the speed-up will be better also for the C_{σ_3} problem.

The reason we see such improved speed-up is because the workers are inactive for long time for the problems without added valid inequalities and cuts, and the workers are almost constantly busy in the problems with added valid inequalities and cuts. Furthermore, the added valid inequalities and cuts give a stronger representation of the problem such that the Branch-and-Bound algorithm shows better convergence in the sense of faster solution time.

Acknowledgements

We wish to thank Martin Bendsøe and Ole Sigmund for their comments and advice. We acknowledge Bernd Damman for his technical help and support. This research is funded by the Danish Research Council for Technology and Production Sciences, and supported by the Danish Center for Scientific Computing (grant CPU-1104-11 *Global Optimization of Topology Design Problems*).

References

[1] S. Bollapragada, O. Ghattas, and J.N. Hooker. Optimal design of truss structures by logical-based branch and cut. *Oper. Res.*, 49(1):42–51, 2001.

[2] P. Bonami, G. Cornuéjols, S. Dash, M. Fischetti, and A. Lodi. Projected Chvátal-Gomory cuts for mixed integer linear programs. Technical report, Department of Information Engineering, University of Padova, Italy, 2005.

[3] F. Codato and M. Fischetti. Combinatorial Benders' cuts. In *Integer programming and combinatorial optimization*, volume 3064 of *Lecture Notes in Comput. Sci.*, pages 178–195. Springer, Berlin, 2004.

[4] W. Dorn, R. Gomory, and M. Greenberg. Automatic design of optimal structures. *J. Méc.*, 3:25–52, 1964.

[5] R.T. Haftka. Simultaneous analysis and design. *AIAA Journal*, 23(7):1099–1103, 1985.

[6] T.K. Ralphs. *SYMPHONY 5.0 User's Manual*. COIN-OR, 2004. (http://www.coin-or.org/).

[7] M. Stolpe and K. Svanberg. Modelling topology optimization problems as linear mixed 0-1 programs. *Internat. J. Numer. Methods Engrg.*, 57(5):723–739, 2003.

Topology optimization - Improved checker-board filtering with sharp contours

Christian Gejl Pedersen, Jeppe Jessen Lund,
Lars Damkilde* and Anders Schmidt Kristensen

Esbjerg Institute of Technology
Aalborg University, Esbjerg, Denmark
*e–mail: ld@aaue.dk

Summary In topology optimization it is mandatory to use a filtering technique in order to prevent checker-boarder solutions. The paper examines a new filtering principle and demonstrates an improved sharpness in the contours. This was not realized in the original proposal of the filter. Furthermore the paper offers an explanation of the advantage of the filtering technique.

Introduction

Topology optimization is an important field in mechanics, and the book of Bendsøe and Sigmund [1] gives an excellent overview of the field. In this paper we concentrate on a small subject namely the problem of distributing a given volume of material in order to reach the maximum stiffness. Only a single loadcase is considered, and the problem is plane and linear. The problem is discretized by the finite element method.

The basic idea is to introduce a so-called relative material density $\rho \in [0;1]$ for each element. In order to penalize intermediate densities which from a construction point of view is not suitable the finite element solution is made by a reduced stiffness proportional to ρ^p, where p typically is 3. In this way intermediate densities are not very effective. The method is denoted SIMP (Solid Isotropic Material with Penalization), and detailed explanations can be found in [1]. The analysis continues through a number of iterations leading finally to an optimal design. In this paper we use the Optimal Criteria Method which is very easy to implement and suitable see [1]. An alternative optimization method can be based on the Method of Moving Asymptotes (MMA), and in this way optimization problems with several loadcases and nonlinear mechanical behaviour can be treated, see [1].

In the optimal solution all elements have the same strain density, and the solution is also a 0-1 density distribution i.e. elements are either with no (small) density or full density. If no special precautions are made the solutions may have so-called checker-boarder patterns i.e. areas where the density jumps from 0 to 1 between neighboring elements. In this way an intermediate material density can be created without penalization. In order to avoid this non-physical phenomenon a filtering technique can be implemented, see the pioneering work of Sigmund [2].

Checker-boarder filter

In the optimization algorithm the derivative of the strain density w with respect to density variations are needed. The basic idea of Sigmund [2] was to filter these sensitivities as shown in (1)

$$\widehat{\frac{\partial w_i}{\partial \rho_i}} = \sum_{j=1}^{N} \frac{\partial w_j}{\partial \rho_j} \rho_j (R - r_j) / (\rho_i \sum_{j=1}^{N} (R - r_j) \tag{1}$$

where the summation from 1 to N involves the neighboring elements as shown in Figure 1. The sensitivities are weighted according to the difference between a chosen averaging radius R and the

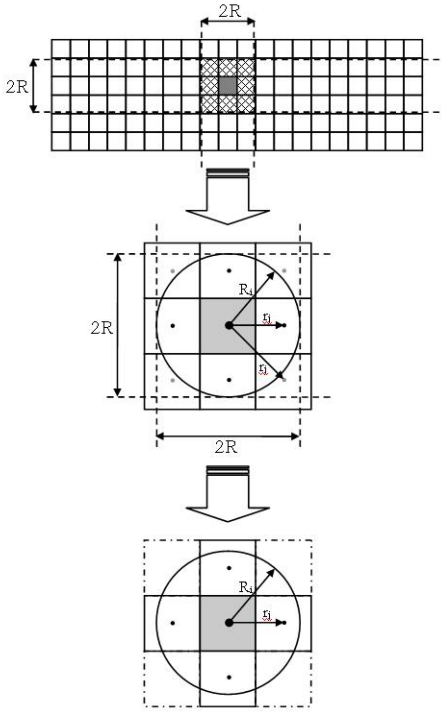

Figure 1: Elements participating in filtering for element i

distance r_j from the center of element i to the center of element j times the density of the element ρ_j. In this filtering method variations in densities will have a large influence leading to less sharp contours between voids and solid material. The filter technique has proven effective, but in the literature different improvements are discussed, see e.g. [4] and [5].

Improved filter

The filter technique used in this paper was original proposed by Back-Pedersen see [3], but the paper did not fully recognized all the positive consequences. This might be due to the fact that a more complicated problem was investigated involving several loadcases.

The basic idea is to remove the influence of density on the results. The sensitivities in the optimal solutions will be equal both in elements with large and small densities. However, the density weighting will change a smooth pattern along boundaries between dense parts and voids. The proposed filtering process only secures continuous sensitivity solutions, and the checker-boarder pattern is solemnly due to the finite element discretization. In (2) the filtering formula is given:

$$\widehat{\frac{\partial w_i}{\partial \rho_i}} = \sum_{j=1}^{N} \frac{\partial w_j}{\partial \rho_j} v_j (R - r_j) / (\sum_{j=1}^{N} v_j (R - r_j) \tag{2}$$

where the notation is similar to the notation used in (1). In the filter we have included the influence of different element volumes to have consistency for different element sizes.

Example

The example is solved with an algorithm similar to the 99-line program in [1] where more details can be found. In Figure 2 an example with a cantilever beam is given. The design depends on

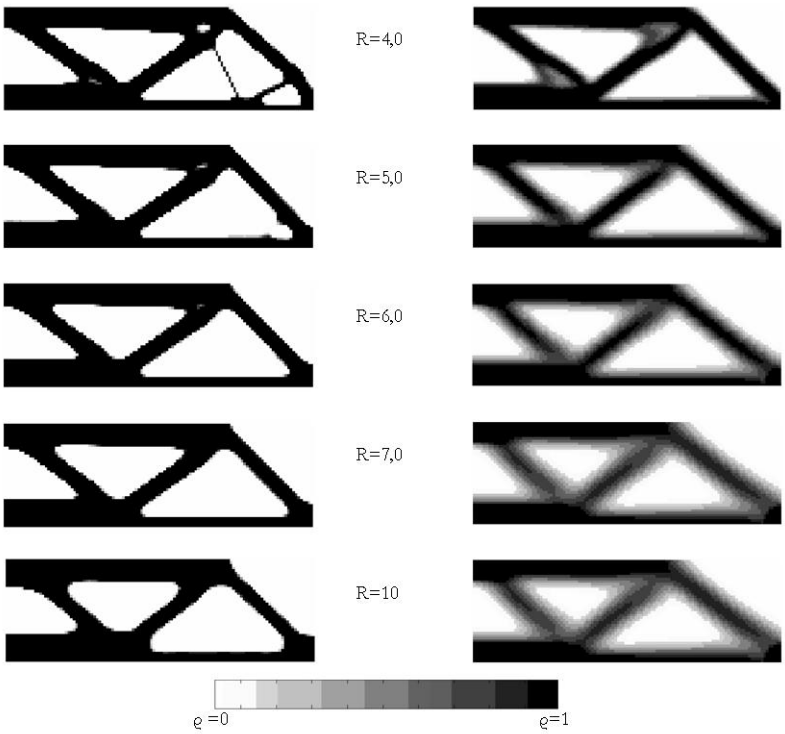

Figure 2: Different designs depending on R. To the left the improved filter and to the right Sigmund's filter.

the chosen material volume and the filtering radius R. A large value of R will give a more simple design on the cost of more material. The advantage of the improved filter is that the material distribution becomes closer to the 0-1 design. The number of elements with intermediate densities is very small with the new filter. This can improve the transfer of design data from the optimization program to the CAD environment.

A big difference between the original filter and the improved is the ability of the filter to operate with sharp transitions from 0 to 1 density. This is illustrated in Figure 3 and Figure 4. In Sigmund's filter the transition will normally involve an element with intermediate density, and this can be seen in the gray parts of the design. Further it may be noticed that the R-value has a very reduced influence on the cost of the design in the new filter compared to Sigmund's filter.

Conclusion

The paper discusses a new filtering technique in topology optimization. The idea is to filter the derivative of the strain densities with respect to density solely as a geometric filtering not including the material density. In this way the checker-boarder pattern is avoided, and it is regarded solemnly as a finite element discretization problem. The new filter results in a design with very limited intermediate densities, and the contours are sharper. This will ease the transfer of data from the

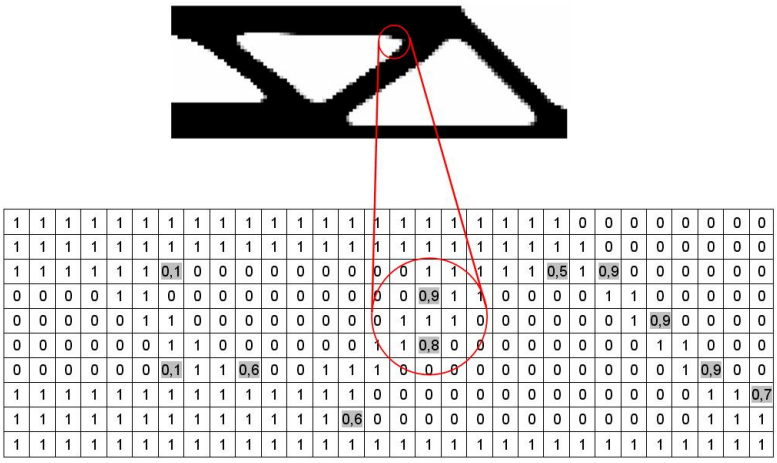

Figure 3: Density variation with the improved filter.

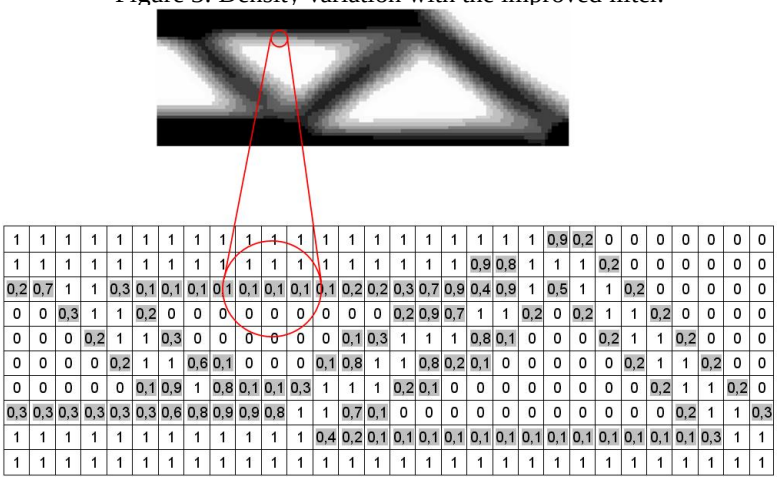

Figure 4: Density variation with Sigmund's filter.

optimization analysis to the CAD-programs. The conclusion is based on a simple linear problem where the optimization is easy, and work on more complicated problems is in progress.

References

[1] M. Bendsøe and O. Sigmund. Topology Optimization - Theory, Methods and Applications. Springer Verlag, Berlin Heidelberg New York , (2002).

[2] O. Sigmund. Design of Material Structures using Topology Optimization. Ph.D. Thesis, Technical University of Denmark, (1994).

[3] A. Back-Pedersen. Designing an impeller hub using topology optimization. In Proceedings of Ansys Conference on simulating real life, 2.81–2.90 , (1998).

[4] T. E. Bruns A reevaluation of the SIMP method with filtering and an alternative formulation for solid-void topology optimization. *Struct. Multidisc. Optim.*, **30**, 428–436, (2005).

[5] M. Y. Wang and S. Wang. Bilateral filtering for structural topology optimization. *Int. J. Num. Meth. Eng.*, **63**, 1911–1938, (2005).

Vibration reduction of structures using global and local optimization techniques

Hamid Movaffaghi
Department of Applied Mechanics, Division of Material and Computational Mechanics,
Chalmers University of Technology**,** Sweden
e−mail: hamid.movaffaghi@chalmers.se

Summary In order to solve vibration problem in large-scale structures a global optimization program based on genetic algorithms has been integrated into an existing local optimization tool consisting of a commercial finite element program and a local optimization program based on gradient methods. The developed optimization tool has been tested on a 3D structure for vibration reduction purposes using seismic load as excitation forces.

Introduction

The structural vibration optimization problem involves finding optimal parameters, called design variables, in order to minimise or maximise an objective function with or without constraints. Turner [1] and Tong and Jiang and Liu [2] considered the natural frequencies of the structure as constraints in order to reduce the vibration level by avoiding structural resonance. Vibration reduction may also be achieved by maximising the natural frequencies of the structure as done by Negm and Maalawi [3]. Cheng, Kang, and Wang [4] have studied multiple-objective vibration optimization of a turbine foundation using both weighs and vibration amplitude to consider safety and costs simultaneously. Memari and Madhkan [5] studied 2D analyses of steel frames subjected to seismic load considering the weight of the structure as the objective function.

In this work, the objective is set to minimise the maximum translational acceleration obtained over all times t and over all finite element nodes in the structure when it is excited by ground motions from earthquake.

Global and local optimization techniques

Global optimisation technique based on genetic algorithms, PIKAIA

The genetic algorithm (GA) is a global optimization technique based on evolution, where the user provides the objective function and an environment. The environment consists of a population of individuals represented by chromosomes with binary or decimal alphabet strings, which have encoded the design variables. GA performs iteratively operations on individuals of each generation to produce new generations of individuals until some termination criterion, which in many cases is the number of generations, is satisfied. The best solution that appeared in any generation is designated as the result of the GA for the run. The major disadvantages of GA are that they can not take advantages of gradients during the search process resulting in generally slower convergence than the local techniques. Moreover, GA does not guarantee the true global optimal solution.

PIKAIA is a GA-based function optimizer written in FORTRAN77 that seeks to maximize a user supplied objective function. The program provides an input file, where the user can define 12 control-parameters to control the behaviour of the GA.

Local optimization technique based on gradient, IDESIGN

Most of the local techniques use direct search methods based on a chosen initial design and an iteration process to find a better design. The algorithm finds first the best direction to move in and then the best size of the step in that direction. The convergence criterion is based on the norm of the design change and the violation of the constraints. The major disadvantages of gradient-based algorithms are that the results of these algorithms depend on the choice of the starting point. The optimums these algorithms find are usually in the neighbourhood of starting point. It means that in the process of finding a global optimum one needs to run the algorithm several times with different starting points. Moreover, computations of gradients are often time-consuming.

IDESIGN has several facilities that permit the user to interact with and control the optimization process. The program is written in FORTRAN77 and a number of optimization algorithms are available. The user must prepare the input data, such as the initial design, lower and upper limits on design variables, problem parameters, convergence criteria, output-levels and write some additional FORTRAN subroutines for the problem at hand.

Optimization design tool

In order to solve the vibration reduction problem, PIKAIA has been integrated with an existing local optimization tool consisting of the finite element program ABAQUS and IDESIGN to create a combined global and local optimization design tool.

3D building structure

As an application of the developed optimization tool, a large 3D four-story three span steel structure subjected to the ground motion excited from earthquake has been analysed. The forcing functions due to excitation from the El Centro N-S earthquake have been applied in the 1-direction of the structure at the support points. The building structure, with the overall dimensions LxWxH=13x13x14 m includes beams and columns with rigid connections and quadratic cross-sections. A 3-D view of the structure is shown in Figure 1.

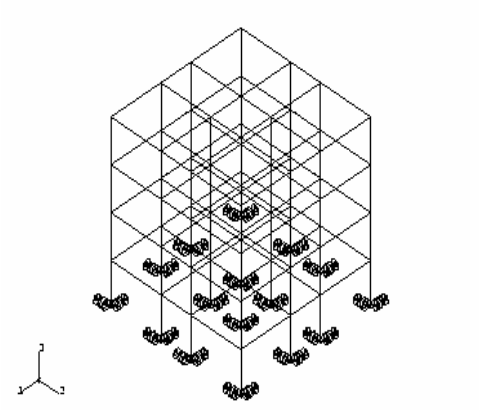

Figure 1: 3D view of the building structure.

The dynamic response of the structure calculated in the time domain by using parameterized ABAQUS finite element models within the developed design optimisation tool. The problem is

formulated as: optimize cross-section dimensions for beams (A_b)and columns (A_c)as well as rotational stiffness (k_q) and rotational damping (C_q) coefficients at the support points of the structure by minimizing the objective function

$$f(t)_{peak} = \sqrt{\sum_{i=1}^{3} a_i^{\,2}(t)} \qquad (1)$$

which is the peak, during the simulation time interval, of a vectorial sum of all three translational accelerations over the whole structure and over all time increments

Results

Table 1 gives the results of the vibration reduction problem using PIKAIA. Figure 2 shows the history of the objective function as a function of the generation number. Table 2 gives the results of the vibration reduction problem by IDESIGN using PIKAIA's optimum results as initial design.

Design variable	Lower	Upper	Optimum design	Obj. fun.
k_q [Nm]	0·5*4·6E8	2·0*4·6E8	0·5756*4·6E8	
C_q [Nms]	0·5*1·0E6	2·0*1·0E6	1·4932*1·0E6	0·7309
A_c [m]	0·5*0·2	2·0*0·2	1·2951*0·2	[m/s^2]
A_b [m]	0·5*0·2	2·0*0·2	1·5071*0·2	

Table 1: Vibration reduction results by PIKAIA.

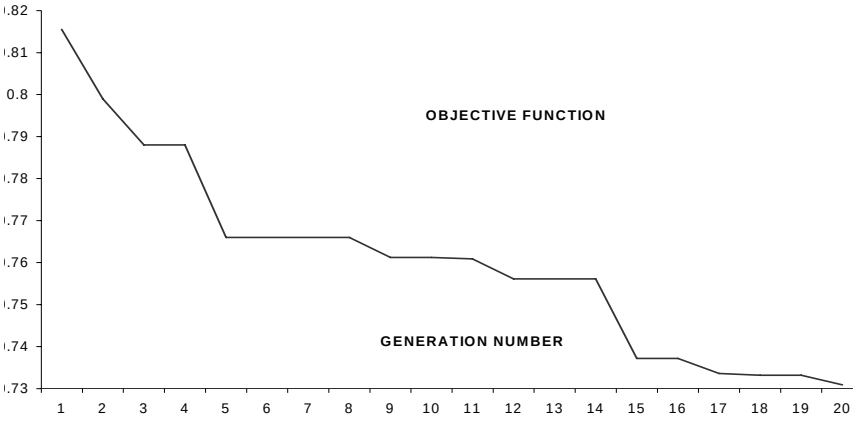

Figure 2: History of objective function against the generation number.

Design variable	Lower	Upper	Initial design	Final design	Obj. fun.
k_q [Nm]	0·5*4·6E8	2·0*4·6E8	0·5756*4·6E8	0·5756*4·6E8	
C_q [Nms]	0·5*1·0E6	2·0*1·0E6	1·4932*1·0E6	1·4932*1·0E6	0·7309
A_c [m]	0·5*0·2	2·0*0·2	1·2951*0·2	1·2951*0·2	[m/s^2]
A_b [m]	0·5*0·2	2·0*0·2	1·5071*0·2	1·5071*0·2	

Table 2: Vibration reduction results by IDESIGN.

Discussions

The GA optimisation took almost 12 days of computer time. It shall be noted that with an increased number of generations, it is possible for PIKAIA to reduce the vibration level even

more. Clearly, the optimisation process should in itself be further optimized by switching automatically from PIKAIA to IDESIGN at some best points during the optimization.

Concluding remarks

Genetic algorithms in conjunction with gradient-based optimization combine searching capabilities of the global and excellent convergence behaviour of the local techniques in the neighbourhood of an optimum. Vibration reduction of a structure subjected to ground motions has been presented by means of integrating available programs in order to develop a combined global and local optimisation design tool. The work can be improved by the considering of the following 1) multiple-objective optimisation in order to consider both costs and safety simultaneously, 2) vibration reduction only in some part of the structure, 3) using more powerful computers and parallel processing in order to reduce computational time to make the tool more practically applicable and efficient to use for vibration reduction tasks.

References

[1] M. J. Turner. Design of minimum mass structures with specified natural frequencies. AIAA Journal, **5**, 406-412, (1968).

[2] W. H. Tong and J. S. Jiang and G. R. Liu. Dynamic design of structures under random excitation. Computational Mechanics, **22**, 388-394, (1998).

[3] H. M. Negm and K. Y. Maalawi. Structural design optimization of wind turbine towers. Computers and Structures, **74** (2000), 649-666, (1998).

[4] G. Cheng and Z. Kang and G. Wang. Dynamic optimization of a turbine foundation. Journal of Structural Optimization, **13**, 244-249, (1997).

[5] A. M. Memari and M. Madhkhan. Optimal design of steel frames subject to gravity and seismic codes prescribed lateral forces. Journal of Structural Optimization, **18**, 56-66, (1999).

Optimal design of inelastic spherical caps with cracks

J. Lellep and E. Tungel
Institute of Applied Mathematics,
University of Tartu 2 Liivi str., Tartu, Estonia
e–mail: jaan.lellep@ut.ee, ernst.tungel@ut.ee.

Summary

Problems of analysis and optimization of inelastic stepped spherical caps are studied. The problem of maximization of limit load under given weight is discussed in a greater detail. Necessary optimality conditions are derived with the aid of variational methods of the theory of optimal control. Numerical results are presented for a simply supported spherical cap with single step of thickness.

Keywords: optimization, spherical shell, crack.

Introduction

Optimization of thin-walled plates and shells have both, theoretical and practical significance. Various approaches to and results of load carrying capacity of spherical caps can be find in books by Hodge (1981); Save, Massonnet, Saxce (1997); Chakrabarty (2000).
Optimal designs of spherical caps with a central hole were established by Lellep and Tungel (2002) assuming that the thickness was piece wise constant and the material obeyed generalised square yield condition. Spherical shells of Mises material were studied by Lellep and Tungel (2005).
In the present paper stepped spherical caps with cracks at re-entrant corners of steps are considered making use of approximations of the Tresca and Mises yield conditions. The aim of the paper is to establish minimum weight designs of the shell under fixed limit load.

Formulation of the problem and basic equations

Consider a spherical cap of radius A simply supported or clamped at the edge with central angle $\varphi = \beta$ (Fig. 1). The shell is subjected to the uniform external pressure of intensity P. The pressure loading is quasi-static, inertial effects will be neglected in this paper. It is assumed that the thickness of the shell is piece wise constant, e.g. $h = h_j$, for $\varphi \in (\alpha_j ; \alpha_{j+1})$ where $j = 0,...,n$ and $\alpha_{n+1} = \beta$. Thicknesses $h_j (j = 0,...,n)$ and angles $\alpha_j (j = 1,...,n)$ will be treated as design parameters to be defined so that a cost function attains its minimal value. In the fracture mechanics it is wellknown that sharp corners in structures generate stress concentration which entails cracks. It is assumed herein that at $\varphi = \alpha_j, (j = 1,...,n)$ circular cracks are located. We treat the cracks as stable part through surface cracks of length c_j at $\varphi = \alpha_j$. Note that the deepness of the crack is not necessarily constant. In this case the length c_j stands for the maximum of the deepness of the crack at $\varphi = \alpha_j$ over the corresponding circle.
We are looking for the minimum weight design of the spherical cap for the fixed limit load. The other problem we are dealing with consists in the maximization of the limit load for given material consumption.

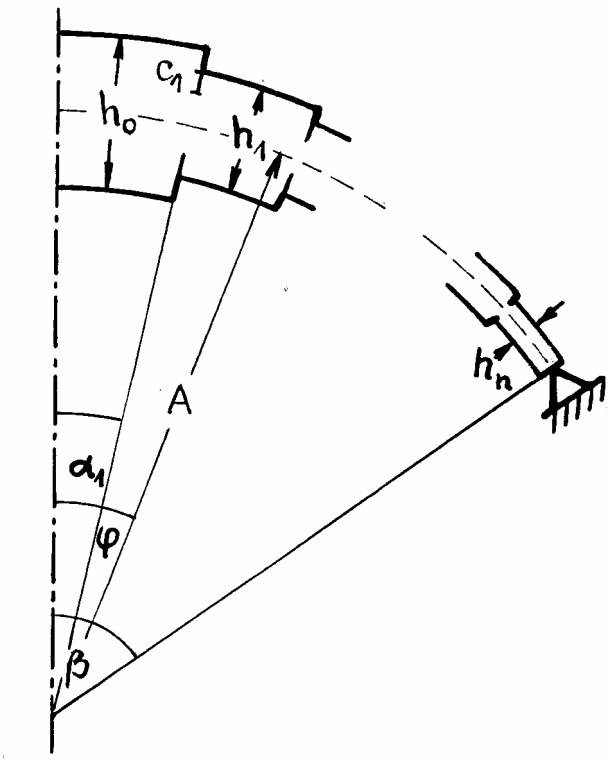

Figure 1: Geometry of the shell.

There are different approaches to the evaluation of the material volume of a spherical cap. In the present paper we assume that the material volume of the cap can be assessed as

$$V = 2\pi A^2 \sum_{j=0}^{n} h_j (\cos\alpha_j - \cos\alpha_{j+1}) .$$

In the case of the problem which consists in the maximization the of ultimate load to be sustained by the cap the volume V is considered as a given constant.
Due to the rotational symmetry the equilibrum equations of a shell element can be presented as (see Chakrabarty, 2000)

$$(N_\varphi \sin\varphi)' - N_\theta \cos\varphi = S\sin\varphi,$$
$$(N_\varphi + N_\theta + PA)\sin\varphi = -(S\sin\varphi)',$$
$$(M_\varphi \sin\varphi)' - M_\theta \cos\varphi = AS\sin\varphi$$

In (2) N_φ, N_θ stand for membrane forces and M_φ, M_θ for bending moments in the two principal directions, respectively, and S is the shear force. Here and henceforth prims denote the differentiation with respect to φ.
Shells made of Tresca and Mises materials are considered. In the case of Tresca condition the portion of the surface corresponding the ridge

$$\frac{M_\theta}{M_{0j}} = \pm(1-(\frac{N}{N_{0j}})^2)$$

is used. Here $M_{0j} = \sigma_0 h_j^2/4$, $N_{0j} = \sigma_0 h_j$, σ_0 being the yield stress of the material.

In the case of a von Mises material the exact yield surface in the space of generalized stresses is approximated as

$$\frac{1}{M_{0j}}(M_\varphi^2 + M_\theta^2 - M_\varphi M_\theta) + \frac{1}{N_{0j}}(N_\varphi^2 + N_\theta^2 - N_\varphi N_\theta) = 1$$

for $\varphi \in (\alpha_j, \alpha_{j+1})$; $j = 0,...,n$.

Numerical results

In order to derive necessary optimality conditions for minimum of the functional V under the condition that governing equations of the problem are satisfied we introduce Lagrange'an multipliers and compile and extended functional. Calculating the total variation of the extended functional yield necessary conditions of optimality. The obtained set of equations is solved numerically.

The distributions of the bending moment M_φ / M_0 are presented in Fig 2 for a shell simply supported at the edge of the cap and made of Tresca material. Fig 2 corresponds to the case of the shell with a single step and $\beta = 0.4$. Here the solid line is obtained for the optimal solution whereas the dotted line is associated with the reference shell of constant thickness. Optimal values of parameters α_1 and h_1/h_0 are presented in Table 1 for cap with $\beta = 1.0$.

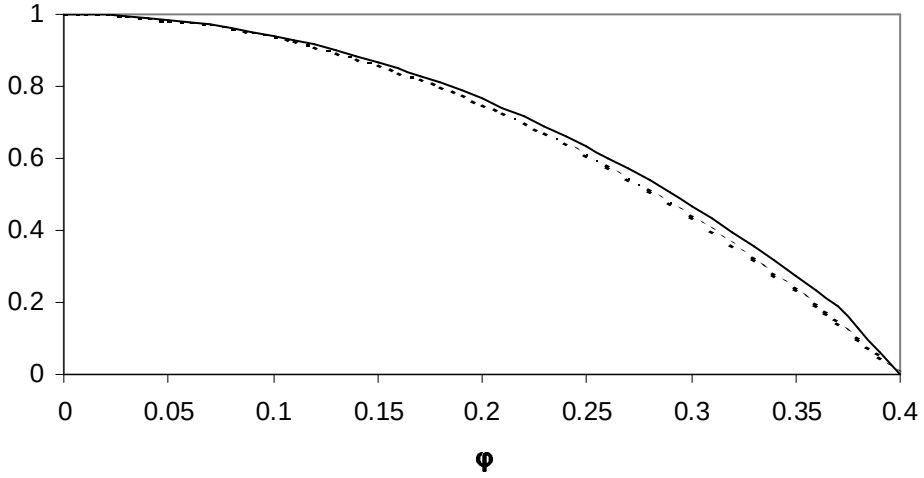

Figure 2: Bending moment M_φ / M_0.

Concluding remarks

Methods of optimization of inelastic spherical caps subjected to external pressure loading are accommodated for shells having part-through surface cracks at the re-entrant corners of steps. It has been established that the deepness of the crack has quite weak influence on the design parameters of the optimized shell.

Table 3: Optimal design for $\beta = 1.0$.

p	α	γ_1	$e = V / V_0$
$0.99P_0$	0.9837	0.2338	0.9773
$0.98P_0$	0.9658	0.3342	0.9588
$0.97P_0$	0.9458	0.4144	0.9430
$0.96P_0$	0.9230	0.4859	0.9234
$0.95P_0$	0.8959	0.5542	0.9180
$0.93P_0$	0.8071	0.7111	0.9049

Acknowledgement. The support from Estonian Science Foundation through the grant N° 5693 is acknowledged.

References

J. Chakrabarty: Applied Plasticity. Springer, Berlin, New York, (2000).

P.G. Hodge: Plastic Analysis of Structures. Krieger, New York, (1981).

J. Lellep and E. Tungel: Optimization of plastic spherical shells with a central hole. Struct Multidisc Optim, 23, 3, 233-240, (2002).

J. Lellep and E. Tungel: Optimization of plastic spherical shells of von Mises material. Struct Multidisc Optim, 30, 5, 381-387, (2005).

M. Save, C. Massonnet and G. Saxce: Plastic Limit Analysis of Plates, Shells and Discs. Elsevier, Amsterdam, (1997).

Equivalent Diagonal Strut Width Computation for Infill Frame with Central Window Opening

Assoc. Prof. Prajwal Lal Pradhan, *Civil Engineering Department, IOE Pulchowk Campus Lalitpur Nepal*
Prof. Karl Vincent Hoiseth, Department of Science and Technology, NTNU Norway
Prof. Dr. C.V.R. Murty, *Civil Engineering Department, IIT Kanpur, India*
Prof. Mohan Prasad Aryal, *Civil Engineering Department, IOE Pulchowk Campus Lalitpur Nepal*

ABSTRACT: The paper presents experimental and analytical micro model analyses on one bay and one storey brick masonry infill frame with different sizes of central window opening with varying opening lengths and heights, subjected to in plane lateral load. Based on the parametric studies obtained from diagonal strut model analyses results, in plane lateral stiffness of the infill frames have been computed. Further, this lateral stiffness versus strut width reduction factors have been computed. Nomographs have been made for different combinations of opening height and opening length ratios.

1. INTRODUCTION

Application of Infill frames are in common practice these days. They are often constructed as composite reinforced concrete skeleton frames with infill masonry walls, with or without openings. The infill frame structures are assumed to carry the transverse load separately, resisting the entire load primarily in flexure. It is well understood that infill actions of brick masonry with different wall openings inhibit lateral displacement compatible with the composite frame action. There is no doubt that a frame with infill wall, with or without opening, is considerably stiffer than the bare frame. However, the stiffness and strength contribution of the infill can be difficult to assess.

Since the brick masonry wall possesses heterogeneous characteristics, a microscopic approach could be an adequate tool for analysis. The model should account for nonlinear behavior due to separation of bricks, cracking, bond slip in mortar joints and dowel actions. Such an approach is much more complicated than earlier practice, but not necessarily more accurate, due to the uncertainties involved.

2. RESEARCH OBJECTIVES

Consultants need efficient calculation tools in their daily business. The brick infill is there for usually neglected in design of lateral load carrying capacity. An improvement would be to include the stiffness and capacity by a strut and tie model, however a representative strut width can be a tedious matter to estimate. The main objective of the study was to develop a procedure for determination of equivalent strut width for infill with various openings, by experiments as well as nonlinear analysis. Further on, the purpose was to present the results by means of nomographs, for use in design.

3. PREVIOUS RESEARCH

For half a decade, almost, researchers have been investigating the mechanical behavior of infill frames, by analytical as well as experimental works. Several studies were related to the estimation of lateral stiffness and strength. Polyakov (1948) studied a hinged steel frame with infill under monotonic incremental loading, and found that infill without openings lost their load carrying capacity by cracking of the mortar joints along the compressive diagonal (strut). Holmes (1961) proposed semi-empirical methods showing the relation between lateral load carrying capacity of the geometry and the compressive strength of the masonry. He used steel and RCC frames with masonry infill. Smith (1968) concluded that when the gravity load reaches half of the load carrying capacity, the maximum lateral failure load is achieved. Smith and Carter (1969) have predicted the lateral stiffness of the infill frame using equivalent strut models. R.Jagadish et. al. (1992) studied the effect of different types of stiffeners around the opening on the behavior of infill frames subjected to lateral load. Finite element analysis showed that when perfect bond was assumed at the interface of the infill and the frame, stiffeners do not have any considerable effect on the lateral stiffness. However, when separation at the interface occurred, stiffeners played an active part in improving the lateral stiffness. Syed Shakeeb-ur Rahman et. al. (1992) studied the effect of the size of infill panels on the behavior of infill frames subjected to lateral loads.

4. EXPERIMENTAL WORK

The experimental work was performed in the heavy lab of the Civil Engineering department, Institute of Engineering, Pulchowk Campus. The model specimens were made in one third reduced scale. The column and beam sizes used in the prototype test specimens were 7.5 x 7.5 cm^2 and 7.5 x 10.0 cm^2 respectively. A concrete mix design, which produced a concrete grade of 7 MPa was used. The model bricks, of size 7.5x3.5x2.5 cm^3 (Table 4.1) obtained from Harisiddhi Brick and Tile Industry, were cut from eight inches square shaped tiles with a 1 inch thickness. The production of the specimens, the form work and the infill masonry, is illustrated in Fig 4.1- 4.2.

Figure. 4.1 Form work and laying reinforcements for beam and column elements

Figure. 4.2 Infill masonry wall

Figure. 4.3 Infill wall with 60% central opening before loading

Figure. 4.4 Infill wall with 60% central opening after loading

The horizontal in plane lateral loading was applied at the left top corner of the infill frame using a hydraulic ram of 25 mm diameter, see Fig. 4.3. The loading device was set as a force control device. Horizontal deformations were measured with a dial gauge, see Fig. 4.4. Ten samples were tested, with and without central opening in the wall. Openings were considered as 0% (No opening), 30%, 60%, 90% and 100% (Bare frame).

Table 4.1 Material properties adopted for laboratory experiment as well as BINAP simulation

Material Properties	Model Brick(75x35x25 mm^3)	Mortar 1:3 (50x50x50 mm^3)	Model Concrete (M7)
Ultimate Strength (MPa)	16.8	11.3	9.8
Crushing Strength (MPa)	7.8	9.6	8.3
Yielding Strength (MPa)	3.7	1.7	3.9
Modulus of Elasticity (MPa)	5388	9696	13290
Yield Strain	0.00138	0.000331	0.000311
Ultimate Strain	0.00585	0.004386	0.001434

5. NUMERICAL SIMULATION & BINAP APPLICATION

Simulation of the experimental tests were performed using the BINAP program, which receives the input and output database, as generated by SAP2000 v8.0. BINAP performs the geometric as well as material non-linear computations, considering loss of contact between bricks and mortar by interface elements with no tensile capacity. The BINAP program updates the database and exports it as a subsequent input for SAP2000, which consequently accounts also for the deformed shape. The structure is subjected to strength degradation at load steps exceeding the elastic limit. This is accounted for by a stepwise reduction of Young´s modulus of elasticity of the materials for each and every element in the structure.

6. FINITE ELEMENT MODEL

In order to meet the objectives of the study, experimental and analytical small-scale model analyses on brick masonry infill frame with central window opening subjected to in plane lateral load have been performed. A single bay and one storey portal frame with various sizes of openings have been carried out experimentally. The size of the portal frame was reduced to 1:3 scaled. Several analyses have performed, by using micro models, with the same configurations as in the experimental testing. In the analyses, the brick elements were represented by plane stress elements, whereas the mortar joints were modeled by link elements in the vertical as well as the horizontal bed joints, separately. The elements are illustrated in Fig. 6.1. Frame analyses have been performed for a number of opening lengths, opening heights and span lengths.

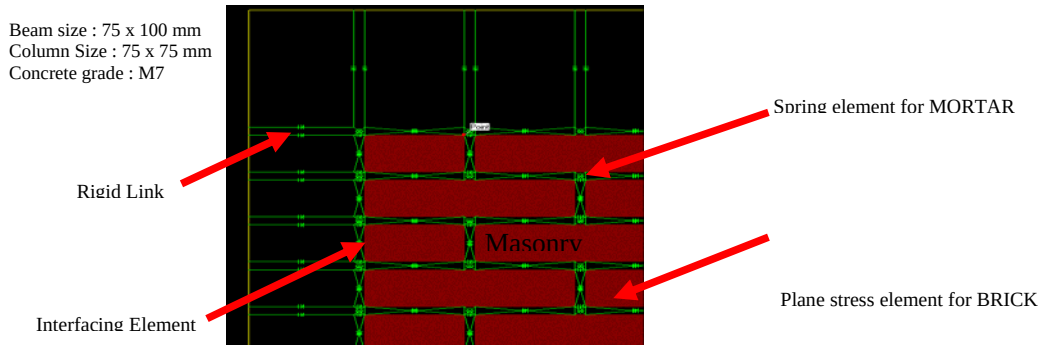

Fig. 6.1 Plane stress model for brick infill wall

7. RESULTS

For the numerical verification of BINAP, micro model for infill frames with the same configurations from the laboratory experiments have been constructed and a series of infill frame analyses were performed using SAP2000 and BINAP in a successive iteration. Load deformation curves were plotted and found more closeness, when there is lesser opening size (Fig. 7.1 a-e).

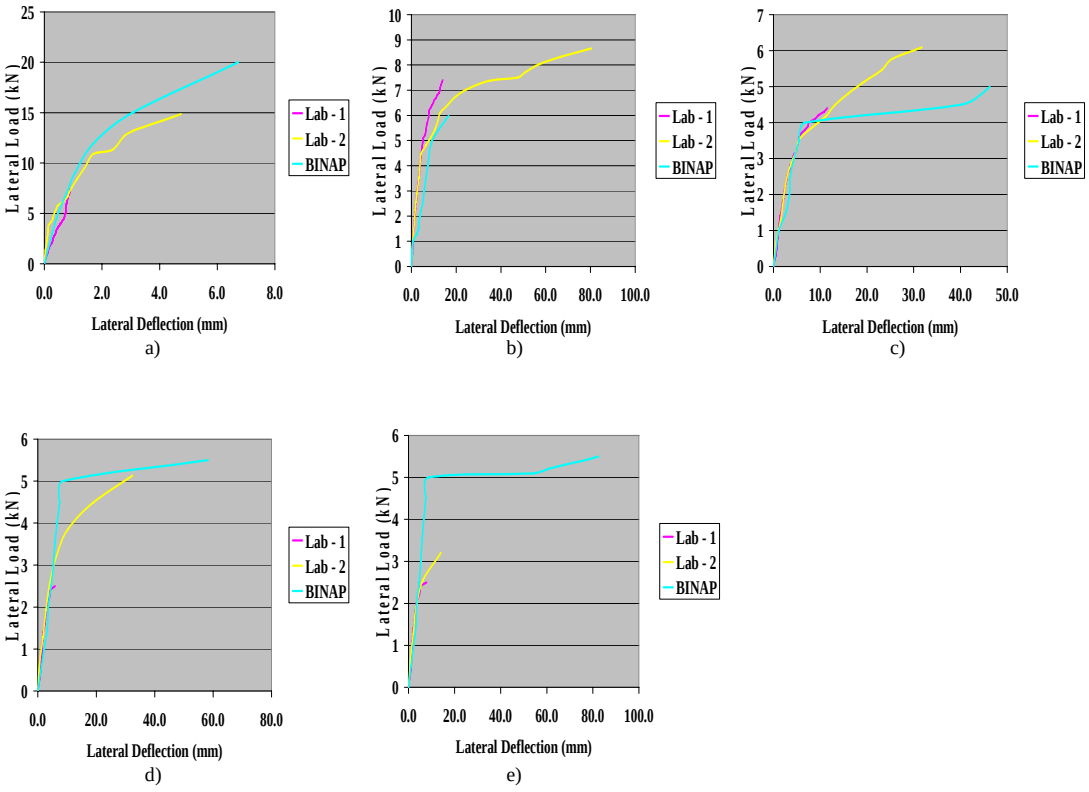

Fig. 7.1 Load/deformation curve for experimental infill frame and BINAP simulation for the same.
a) Full infill b) 30% opening c) 60% opening d) 90% opening e) No opening (Bare frame)

The failure mechanisms were also simulated using BINAP application as shown below in fig. 7.2 and fig. 7.3. The simulations were done for all the laboratory models with successive increments of in plane horizontal loads.

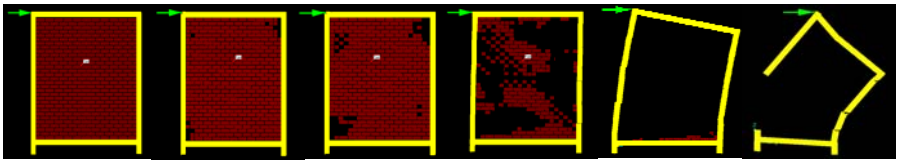

Fig. 7.2 BINAP simulation of infill frame with no opening

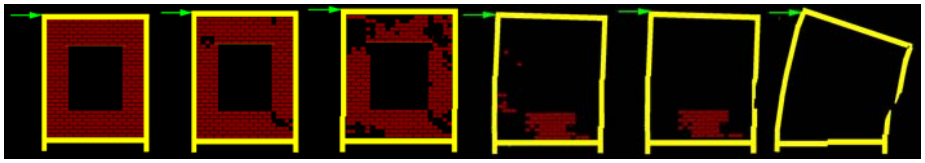

Fig. 7.3 BINAP simulation of infill frame with 60% opening

8. CONCLUSIONS

Based on the numerical and experimental results, equivalent diagonal strut widths have been estimated. Nomographs, showing the relation between strut width reduction and opening dimensions, are given in Fig. 8.1. The figure illustrate the dependency of opening length versus length of span (*l/L*), as well as of the ratio between opening- and storey height (*h/H*). K_0/K_f represents the stiffness relation, that is stiffness with opening/stiffness with complete infill.

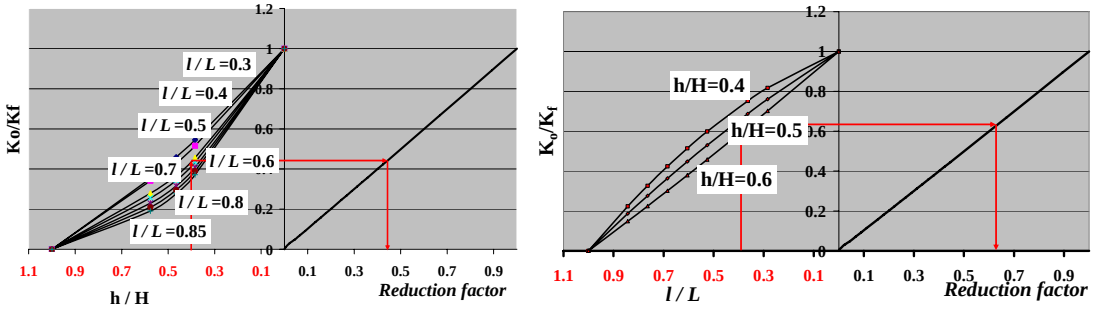

Fig. 8.1 Nomograph for determination of Strut width reduction factor

9. REFERENCES

1. **A.Madan, A.M. Reinhorn, Fellow, ASCE, J.B. Mander, Member ASCE, and R.E. Valles,** *Modeling of Masonry In-fill Panels for Structural Analysis,* Journal of Structural Engineering, Vol. 123, No. 10, October, 1997, Paper No. 13418.
2. **Armin B. Mehrabi, Associate Member ASCE, and P. Benson Shing, Member ASCE,** *Finite Element Modeling of Masonry In-filled RC Frames,* Journal of Structural Engineering, Vol. 123, No. 5, May 1997, Paper No. 12131.
3. **Goutam Mondal,** *Laetral Stiffness of Unreinforced Brick Infill RC Frame with Central Opening,* Thesis Masters of Technology, IIT Kanpur, Department of Civil Engineering, Indian Institute of Technology Kanpur, July 2003
4. **J.W. Bull,** *Computational Modeling of Masonry, Brickwork and Block-work structures,* Civil-Comp Ltd. Stirling, Saxe-Coburg Publications, 2001.
5. **James O Smith, Omur M Sidebottom,** *Inelastic Behavior of Load Carrying Members,* John Willey & Sons New York, NY USA, 1965, pp. 447 ISBN 1124117679
6. **Mallick, D.V. and Garg, R. P.,** *Effect of Openings on the Lateral Stiffness of In-filled Frames,* Proceedings of the Institution of Civil Engineering, Vol. 49, 1971, pp.193-209
7. **Popovics, S.,** *A Numerical Approach to the Complete Stress-Strain Curve of Concrete,* Mag. Concrete Research, Cement & Concrete Association, V3, 1973, pp. 583-599
8. **T.C. Liauw and C.Q. Lo,** *Masonry In-filled Frames Without Shear Connectors,* ACI Structural Engg. Journal, pp. 423-428, July-August 1988

Numerical simulations of RC beams with corroded rebars

I. Sæther* and G. Horrigmoe
Norut Technology Ltd.,
Narvik, Norway
e–mail: irina@tek.norut.no

B. Sand
Norut Technology Ltd.,
Narvik, Norway
e–mail: bjoernar@tek.norut.no

Summary Corrosion of steel reinforcement continues to pose problems with regard to maintenance, performance and service life of reinforced concrete structures. The present work has been devoted to the use of nonlinear finite element analysis to simulate the mechanical response of reinforced concrete structures with corroding steel reinforcement. The finite element simulations of medium scale beams were shown to be in good agreement with the experimental results for different corrosion levels.

Introduction

The deterioration and ageing of the concrete structures and the increased traffic intensities and loads are some of the major problems facing civil engineers, industry and researchers. Deterioration of reinforced concrete may lead to a number of undesirable consequences such as loss of serviceability, loss of load carrying capacity and reduction in safety of structures and traffics [2]. Corrosion of steel reinforcement continues to be the principal cause of deterioration of reinforced concrete structures. Reduction in bar cross sectional area, cracking and spalling of concrete cover, reduction in bond strength and changes in bond stress-slip behaviour may severely impair structural integrity.

Review of available results test data of experimental and numerical studies obtained in international projects are presented in reports and other publications by several authors [1], but no general approach or recommendations have been developed to predict the behaviour of corroded concrete structures. Design Codes and Standards are intended primarily for new construction, and may not contain the information required for an assessment of deteriorated structures. The continued degradation of concrete infrastructure has thus exposed the need for reliable methods to predict residual service life of deteriorated structures. The main objective of this work is to get an opportunity to assess available test data for nonlinear element analysis to obtain realistic prediction of behaviour of corroded concrete structures using commercial finite element programs.

Finite element simulations

The experimental study carried out by Mangat and Elgarf [6] was chosen to be analysed in the present study. Under-reinforced beams were subjected to accelerated corrosion. Different degrees of corrosion were induced, ranging from 1.25 to 10 percent reduction in bar diameter. Details of the beam section are presented in Fig.1. After casting, the beams were tested under four-points bending to determine their load-deflection curves and the ultimate flexural strength. The beams were prevented from shear failure by externally reinforcing the shear zones by means of tubular

steel collars. The middle-third span which undergoes pure bending was free from external shear reinforcement. The beams exhibited a bending failure of an under-reinforced beam.

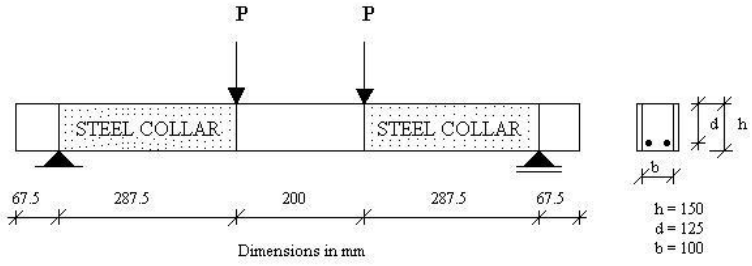

Figure 1: Beam specimens tested by Mangat and Elgarf [6].

The numerical simulations carried out in the present study are based on the commercial finite element code DIANA 9 [4]. Since the beam and loading scheme are symmetrical, it is sufficient to model only the left half of the beam. In this model it was used eight-node quadrilateral CQ16M plane stress elements for concrete and for the collar steel collars. It was assumed that the collar extended over the entire length of the shear span and that the plate thickness was 5 mm. The steel reinforcement was represented by discrete truss CL6TR elements located along the mesh of the concrete elements. Bond stress-slip relations are implemented for intact as well as corroded bars using interface elements IP33.

Basic material parameters for concrete and reinforcing steel were determined experimentally by Mangat and Elgarf [6]. Some of the materials parameters used for finite element simulations were calculated by CEB-FIP Model Code 1990 [3] and the Norwegian Code for Design of Concrete Structures, NS 3473 [5].

In the analyses a fixed crack model based on total strain was used. The compressive stress-strain curve for concrete was approximated by that of an elastic-ideally plastic material. The tensile behaviour of concrete was represented by a bilinear approximation. Reinforcing steel is presented as elastic-perfectly plastic material. The constitutive behaviour of the reinforcement steel and steel collars was modelled by the Von Mises yield criterion. The bond stress-slip relationship for uncorroded steel bars proposed in the CEB-FIP Model Code 1990 [3] for unconfined concrete with good bond conditions was chosen to use in the present numerical simulation.

As the first, the numerical simulations by non-linear finite element method were performed for the reference beam (no corrosion) with the slip values and the bond strength for uncorroded bars given in the Model Code 1990. These values resulted in a structural response which was too stiff compared with the experimental load-deflection diagram. It was found that the best fit to the load-deflection behaviour of the reference beam was obtained with other set of parameters presented in Fig.2.

As the second step, the numerical simulations of corroded bars were carried out. No data is given by Mangat and Elgarf concerning bond strengths of corroded bars. In view of this and the fact that failure of the corroded beams was governed by bond failure, it was decided to scale the bond stress-slip curves for corroded bars the same proportion for both axes. The resulting bond stress-slip curves for the following testes of no corrosion and of corrosion 1.25 %, 2.5 %, 3.75 %, 5.0 %, 7.5 %, 10.0 % are shown in Fig.2.

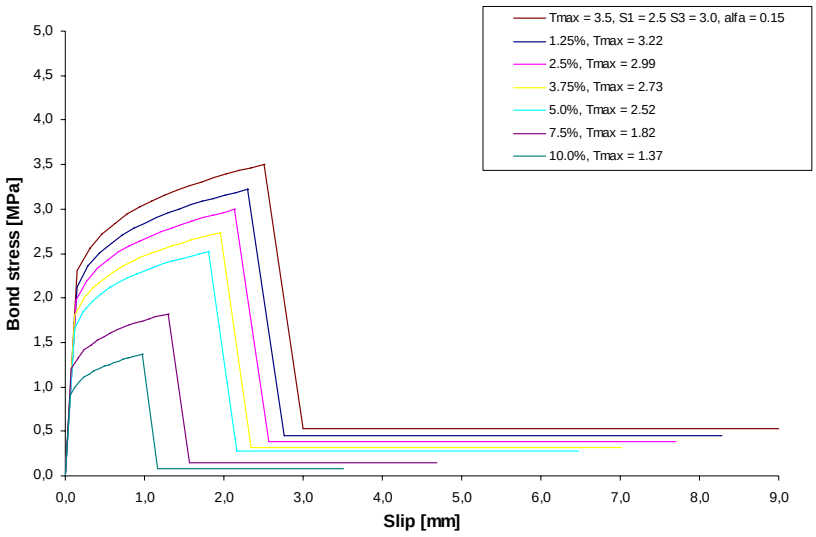

Figure 2: Bond stress-slip curves for noncorroded and corroded bars.

Numerical results

The load-deflection diagram for the reference beam determined in the laboratory test is compared with the behaviour obtained from the finite element simulations (Fig.3). The numerical solution is in very good agreement with the experimental tests. Load-deflection diagrams for beams with increasing levels of corrosion (from 1.25 % to 10.0 % diameter loss) are also shown in Fig.3. In all cases the results from finite element simulations agree well with the experimental data. It is also seen that the calculated mode of failure is bond failure resulting from the fact that the bond stress along tensile reinforcement reaches the bond strength. For the two levels of corrosion (7.5 % and 10.0 %) the finite element analyses predict higher failure loads than the experimental values.

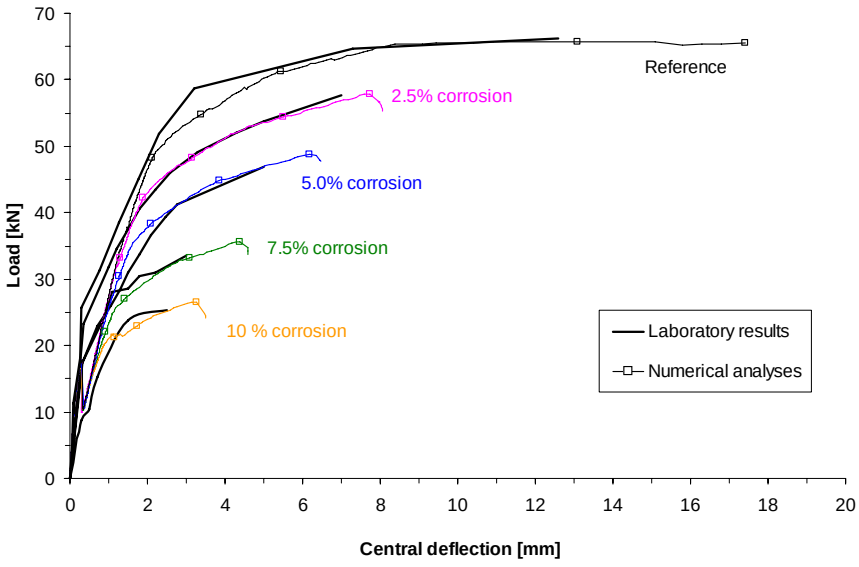

Figure 3: Load-deflection diagrams. 0-10% reduction in diameter.

Conclusions remarks

The present work has been devoted to the use of nonlinear finite element analysis to simulate the mechanical response of reinforced concrete structures with corroding steel reinforcement. The validation of the finite element simulations was limited to the study of medium scale beams tested in the laboratory. The beams tested by Mangat and Elgarf had only tensile reinforcement and exhibited bond failure. The finite element simulations of these beams were shown to be in good agreement with the experimental results for different corrosion levels. The present study has attempted to address this problem by demonstration the potential and capabilities of the finite element method in the analysis of reinforced concrete structures damaged by corrosion using the commercial programs.

Acknowledgements

The research work has been carried out in Norut Technology Ltd. through the "Sustainable bridges" project. A part of the presented work was financed by the Norwegian Research Council through the strategic institute program RECON at Norut Technology Ltd, Norway.

References

[1] *Bond of Reinforcement in Concrete*, State-of-the art report, fib Bulletin No. 10, (2000).

[2] J. Cairns. Consequences of reinforcement corrosion for residual strength of deteriorating concrete structures, *Proceedings of the First International Conference on Behaviour of Damaged Structures*, Rio de Janeiro, (1998).

[3] Comite Euro-International du Beton. *CEB-FIP Model Code 1990*, Design Code, Thomas Telford, London, (1993)

[4] DIANA- *User's Manual*, Release 9, TNO DIANA BV, Delft, The Netherlands, (2005).

[5] *Norwegian Code NS 3473: Design of Concrete Structures* (in Norwegian), Fifth edition, Norges Byggstandardiseringsråd (NBR), Oslo, (1998).

[6] P.S. Mangat and M.S. Elgarf. Flexural strength of concrete beams with corroding reinforcement, *ACI Structural Journal*, Vol. 96, No. 1, 149-158, (1999).

Parameterization and Contact analysis of an Offshore Saddle Tapping Tee System

A. Kristensen*, T. Larsen, and M. O. Bay
Esbjerg Institute of Technology
Aalborg University, Esbjerg, Denmark
e–mail: ask@aaue.dk

K. L. Jepsen
Piping and Mechanical
Rambøll Denmark A/S, Esbjerg, Denmark
e–mail: kuj@ramboll.dk

Summary

A full 3D parametric CAD model of a Saddle Tapping Tee system for offshore maintenance operations has been developed. For the verification of the structural behavior of the system, critical conditions are identified and a parametric FEA model is established, which is automatically updated from user-defined parameters set for the CAD-model. FEA employing contact is performed on a 4"x 4" Saddle Tapping Tee. An increased level of detail has been achieved for verification and documentation in relation to offshore maintenance operations.

Introduction

Often it is necessary to branch off a pipe section on an oilrig. This operation is often performed by introducing a so-called "Hot Tapping" procedure, which involves welding a pipe and a flange onto the pipe section undergoing maintenance. A spherical valve and a gate are mounted onto the flange, i.e. weld-o-let. In order to perform the welding operations a so-called habitat must be constructed. This habitat encapsulates the "Hot Tapping" spot and is relative costly. Thus, to avoid welding operations onto the pipeline, a solution with clamps has been developed, i.e. a Saddle Tapping Tee as shown in figure 1a and 1b as devised by Rambøll.

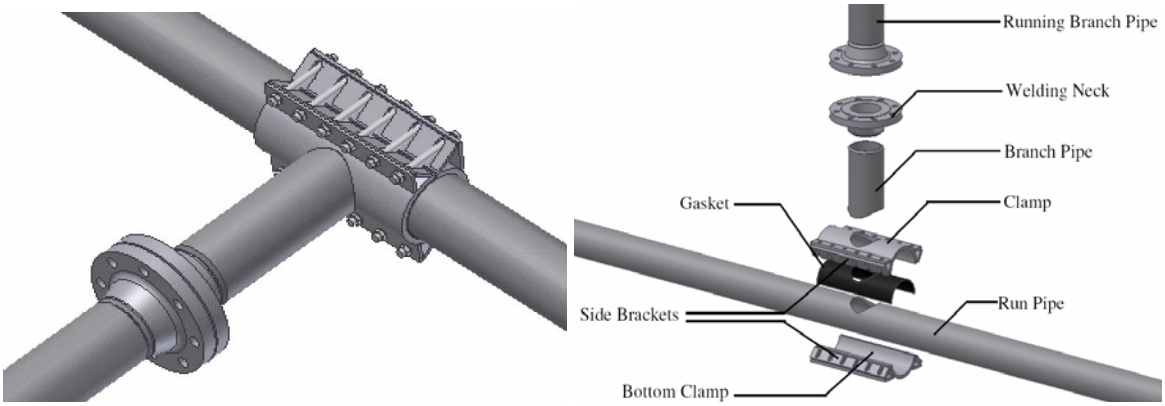

Figure 1: a) The Saddle Tapping Tee in a pipe section. b) The components in a Saddle Tapping Tee.

The Saddle Tapping Tee is clamped on the pipe section applying a gasket, see figure 1b. The system is designed for an allowable pressure of 150[lbs], and the service temperature varies

between -40-38[C], i.e. an allowable pressure of 19.7[bar]. However, the system must be able to withstand a test-pressure of 150% of the allowable non-shock pressure, i.e. the design pressure 30[bar] according to [1].

Parameterization of the structure

A parametric verification model is established based on considerations regarding the compaction of the gasket and the stress level in the brackets of the clamp as illustrated in figure 2a and 2b.

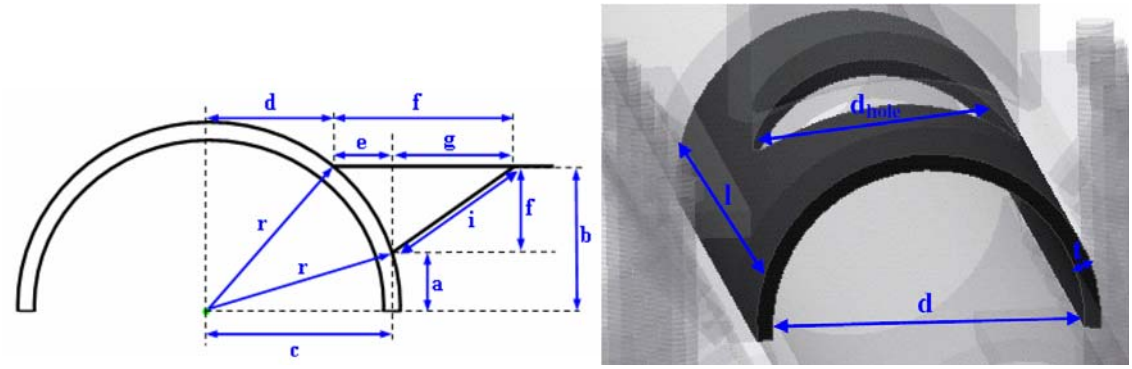

Figure 2: Left) The parameters controlling the clamp geometry. Right) The parameters controlling the gasket geometry.

The required minimum compaction pressure in the gasket is 1.4[N/mm] according to the European Norm for pressure vessels EN13445 [2]. The pressure acting on the gasket is governed by the pretension of the clamp, the position of the gasket, and the deformation of the clamp. The steel applied is of the type ASTM A-420 GR 6, and welding is performed using longitudinal seamless groove welds. The allowable stress in the weld is determined from paragraph K302.3.2 in ASME B31.3 [1]. The material of the gasket is a Polymer Nitrile Rubber (NBR) with E = 3.7[MPa] and Poisson's ratio 0.48.

On the basis of the above considerations a full parametric 3D CAD model of the Saddle Tapping Tee is developed. A number of user-defined parameters are controlled from an Excel spreadsheet for example the parameters are shown in figure 2a defined by:

$$
\begin{aligned}
&c = \sqrt{r^2 - a^2} \\
&d = \sqrt{r^2 - b^2} \\
&e = c - d \Rightarrow \\
&e = \sqrt{r^2 - a^2} - \sqrt{r^2 - b^2} \\
&g = f - e, \text{where f is } w_{plate} - welddisplacement \\
&h = b - a \\
&i = \sqrt{g^2 + h^2} = length \\
&length = \sqrt{\left(w_{plate} - welddisp. - \left(\sqrt{r^2 - a^2} - \sqrt{r^2 - b^2}\right)\right)^2 + (b - a)^2}
\end{aligned}
\tag{1}
$$

The same Excel spread-sheet control a full 3D parametric FEA model which is automatically up-dated from the user-defined parameters set for the CAD-model allowing parameter studies and documentation to be generated effectively.

Analysis and results

As the gasket is subjected to a contact pressure arising from the clamping force acting on the pipe section, a FE contact analysis is carried out. Two situations are examined, i.e. a load equivalent to 50% and 80% of the yield stress acting in the clamp bolts.

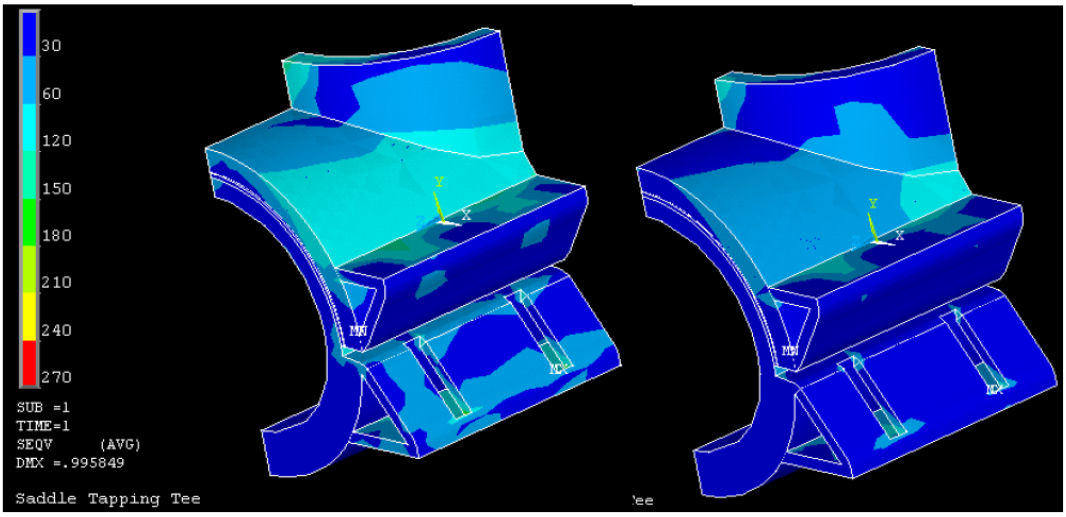

Figure 3: Stresses in the Saddle Tapping Tee type 4”x4”, i.e. stress von Mise stress distribution.

The contact analysis has been performed by applying the nonlinear element types CONTA175/TARGE170 on a Saddle Tapping Tee type 4”x4” as depicted in figure 3. Friction is set to 0.2, and initial penetration has been excluded.

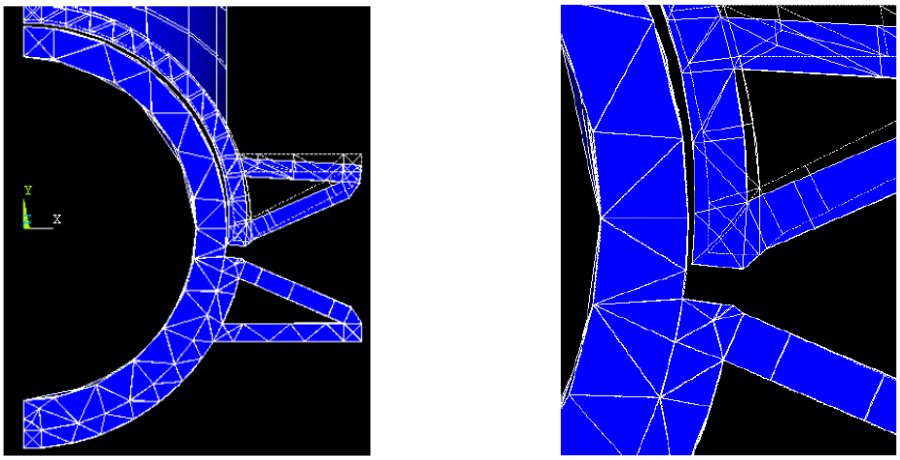

Figure 4: Deformation of the Saddle Tapping Tee clamp and gasket.

The performed FE contact analysis has enabled inspection of deformations of the components in physical contact, of stress levels in critical areas, of perpendicular stresses in the gasket, and friction as shown in figure 4.

Due to the parameterization of the CAD model and the FEA model it is now possible for the engineer to verify deformations of the gasket and stresses in the clamp. Parameter studies are performed effectively for several models with a minimum user-interaction compared to present verification methods. In addition to this, “Det Norske Veritas (DNV)” requires increased amounts of documentation for these Saddle Tapping Tee systems for maintenance operations offshore.

Concluding remarks

The developed procedure allows the engineer to modify any required and relevant user-defined parameter on the Saddle Tapping Tee from a single Excel spreadsheet in both the CAD model and the FE model. A full 3D CAD model is effectively generated for dimensions in the range from NPS ½ to NPS 24, and FEA can be performed to provide documentation of the behavior of a given Saddle Tapping Tee. This documentation must be provided for verification by the “Det Norske Veritas (DNV)”.

References

[1] ASME B31.3. Process Piping. *ASME*, Revision **23**, (2005).

[2] EN13445-1:2002. *Unfired pressure vessels. General*. (2002).

[3] ANSYS. *ANSYS Release 10 Documentation*. (2006).

Optimal Modules in Conceptual Design of Car Product Families

B. Torstenfelt* **and A. Klarbring**
Department of Mechanical Engineering
Linköping University, Linköping, Sweden
e–mail: botor@ikp.liu.se

Summary This paper extends structural optimization from single components, to families of products built from shared partly shared or unique modules. The design variables are local cross sectional properties as well as geometrical positions of important structural joints. The structures are exposed to a variety of different load conditions. The technique is applied to three cars constituting a family, the S40, V50 and the C70 manufactured by Volvo Car Corporation in Gothenburg, Sweden.

Introduction

In an effort to stay competitive and not to loose market shares, many car manufactures offer the customers a variety of new, sometimes closely related, products. The key issue is how to develop various new products, most likely manufactured in shorter series, and still earn money. A basic idea for achieving this goal, is to share as many components as possible, in a family of closely related products.

Another severe restriction is that the time-to-market must not be too long. It is also a well-known fact, that correct decisions as early as possible are of a great importance, both for success from a cost-effective and economical point of view, and from the important perspective of how well the product will fulfill its overall basic technical requirements [1].

Very early in a project, perhaps only the shape of the outer surface is defined, and no geometrical information for how to design typical load-carrying structural components is available. Most of todays available standard CAE-tools for making structural solid mechanics analyses are tailored around geometry modeling tools and require 3D solid geometry definitions for mesh generation. Several authors have identified this as a problem because these tools are too time-consuming to use in very early stages of a project when the lifespan of design ideas is short, see [2] and [3].

The demand for fast, accurate and robust easy-to-use tools for conceptual design is significant.

The objective of this work is to perform simultaneous structural optimization of several products, exposed to a number of load cases, where these products have partly shared identical modules.

The product family optimization problem

We consider a series of more or less similar products composed by a finite number of modules, where each module consists of a number of components. The products define a product family and the modules define a product platform, see [4]. A typical product family is visualized in Figure 1. The number of products or modules can be arbitrary. The major problem, and the extension in this work compared to classical structural optimization, is the sharing of modules and design variables among the products in the family.

We establish a performance measure representing stiffness. This measure is based on solving the state equation

$$\boldsymbol{K}_{\alpha}^{\ell}(\boldsymbol{x}(\alpha))\boldsymbol{u}_{\alpha}^{\ell} = \boldsymbol{F}_{\alpha}^{\ell}(\boldsymbol{x}(\alpha)), \tag{1}$$

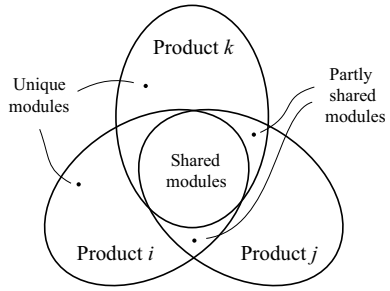

Figure 1: A typical product family made up from shared, partly shared or unique modules.

representing equilibrium for a discretized FE-structure for load case ℓ of product α. $\boldsymbol{K}_\alpha^\ell$ is the global stiffness matrix and $\boldsymbol{F}_\alpha^\ell$ the global load vector. The current state is described by the global degrees-of-freedom vector $\boldsymbol{u}_\alpha^\ell$ obtained by solving equation (1). If $\boldsymbol{K}_\alpha^\ell$ is non-singular we can regard $\boldsymbol{u}_\alpha^\ell$ as a function of the design variables $\boldsymbol{x}(\alpha)$, i.e.,

$$\boldsymbol{u}_\alpha^\ell = \boldsymbol{u}_\alpha^\ell(\boldsymbol{x}(\alpha)) = \boldsymbol{K}_\alpha^\ell(\boldsymbol{x}(\alpha))^{-1}\boldsymbol{F}_\alpha^\ell(\boldsymbol{x}(\alpha)). \tag{2}$$

The performance measure used in this work is the *Compliance* C_α^ℓ, which is a global flexibility measure here defined for every product α and load case ℓ:

$$C_\alpha^\ell(\boldsymbol{x}(\alpha)) = \boldsymbol{F}_\alpha^\ell(\boldsymbol{x}(\alpha))^T\boldsymbol{u}_\alpha^\ell(\boldsymbol{x}(\alpha)). \tag{3}$$

Minimizing this measure means maximizing the stiffness. It is obvious, that in a simplified case with a design independent global load vector $\boldsymbol{F}_\alpha^\ell$ containing only one non-zero component, this expression just means maximizing the stiffness in one direction at one position of the structure.

Design variables

One group of design variables, here called sizing variables, used in this work, comes from the parameterization of the cross section geometry of beams. That is, heights, widths and thicknesses, and also the orientation of the cross section, can be used as design variables, see [5]. A second group of design variables are altering the position of connection points between different beam members. That is, both the length and the orientation of the local beam direction will change during the optimization process, see [6]. Concerning the topology of the structure, sizing variables can take values close to zero, which will remove beam members. One can thus start from a non-manufacturable ground structure and the optimization process will show the optimal load transfer path.

Let us define a global vector $\boldsymbol{x}$ containing all unique design variables involved in a product family represented by n_p products. Note that this is the vector which will be used in the final structural optimization problem defined below. The relation between the design variable vector $\boldsymbol{x}(\alpha)$ for product α and this global vector $\boldsymbol{x}$ is defined by Boolean matrices $\boldsymbol{B}_\alpha$ as follows: $\boldsymbol{B}_\alpha\boldsymbol{x} = \boldsymbol{x}(\alpha),\ \alpha = 1, \ldots, n_p$, where $\boldsymbol{B}_\alpha$ reflects how modules are shared between products.

Objective function

A total performance measure $C(\boldsymbol{x})$ is defined as a weighted sum of compliances, where each product α is exposed to $n_l(\alpha)$ load cases. The scalars w_α^ℓ are weighting factors that reflect the

relative importance of different products and load cases. The following minimizing problem is solved

$$(\mathbb{P}) \quad \begin{cases} \min\limits_{\boldsymbol{x}} \; C(\boldsymbol{x}) = \sum\limits_{\alpha=1}^{n_p} \sum\limits_{\ell=1}^{n_l(\alpha)} w_\alpha^\ell C_\alpha^\ell(\boldsymbol{x}(\alpha)) \\ \text{subject to} \begin{cases} M_\alpha(\boldsymbol{x}(\alpha)) \leq \hat{M}_\alpha, \;\; \alpha = 1, \ldots, n_p, \\ \boldsymbol{x} \in \mathcal{X}, \end{cases} \end{cases}$$

and the stiffest product family is found subjected to constraints where the mass M_α must not be larger than an upper mass limit $\hat{M}_\alpha$ available for product α and $\mathcal{X}$ is a set of admissible designs.

The product family

To explore the power of this technique, an example from the car manufacturer Volvo has been used. Three existing products, the former sedan S40, the estate wagon V50 and the C70 Convertible from 1997 have been at focus. The split of these car body structures into globally shared, partly shared and unique modules is governed by the manufacturing of these existing products. In Figure 2, globally shared modules are shown in red and yellow, partly shared modules in green and unique modules in grey colors. The yellow parts are in the real cars non-existing components. Boundary conditions are illustrated in violet.

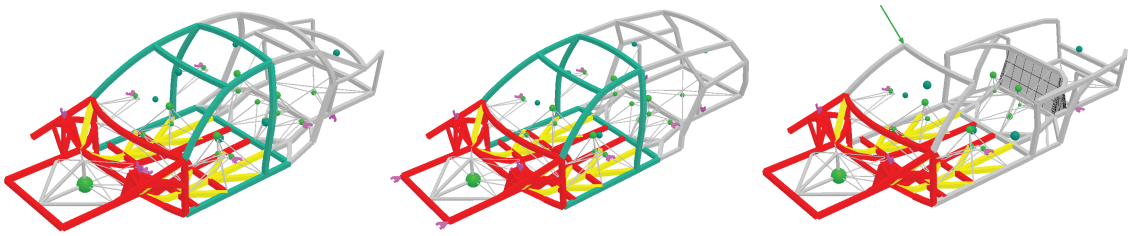

Figure 2: Ground structures and modular decomposition of the involved products

Loading conditions

Attention has been given to modeling the mass distribution as realistically as possible. Mass coming both from load-carrying structural components and from non-structural components are taken into account. That is, the mass distribution is design dependent and design derivatives of the load vectors $\boldsymbol{F}_\alpha^\ell$ are required. The mass from an extensive number of non-structural components is applied as point and line masses and they are treated as design independent. The point masses are attached to the structure by simple weightless bar elements tuned not to add any stiffness but to distribute the forces emanating from the point mass as accurately as possible.

The applied load cases are bending, twisting, front crash and rear crash, all achieved by applying an assumed acceleration vector acting on the current mass distribution. Finally, also a statical roll-over load case is applied, defined by legal provisions.

Optimization algorithm

The optimization algorithm utilized is the well-known and often used Method of Moving Asymptotes (MMA) [7] which has been implemented into the general in-house finite element program TRINITAS [8].

Results

The data output from this type of analysis is enormous and can be examined and evaluated in many different ways. Most obviously, the objective function value, summed up of compliance values from each product and loading case, may serve as a base for comparison. Secondly, the obtained designs from different, closely related, optimization problems can be compared. In this document only a very limited taste of the results can be given. In the left of Figure 3 the optimal design of only the S40 optimized for all load cases and in the right of the figure the optimal design of the S40 exposed to all load cases but here effected by the other two members of the family.

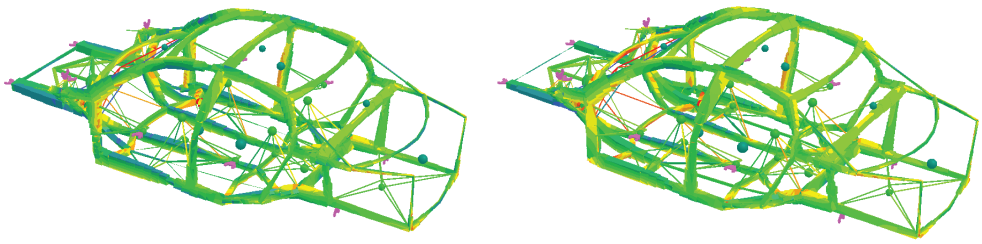

Figure 3: The S40 optimized as one product, or as one product in a family of products

Concluding remarks

This paper presents a technique, that can serve as an efficient tool, for investigations of what will be the loss of performance and/or change in geometry, if one product is forced to share components with other products, in a specific product family.

By use of this technique one can also conclude that sharing or not sharing modules triggers different design solutions, all having closely the same compliance value.

Acknowledgements

The authors are grateful to Kaj Fredin and Harald Hasselblad at Volvo Car Corporation in Gothenburg, Sweden, for providing necessary information for all three involved cars.

References

[1] Gupta, S., Das D., Regli, W. C. and Nau, D. S. Automated manufacturability: A survey. *Research in Engineering Design*, **9**, 168–190, (1997).

[2] Raasch, I. Sizing in conceptual design at BMW. *2004 SAE World Congress*, Detroit, USA, March 8-11

[3] Kikuchi N., *et al.* Modular structural component design using the First Order Analysis and decomposition-based assembly synthesis. *2001 ASME International Mechanical Engineering Congress and Exposition*, New York, USA, November 11-16

[4] Meyer M. H. and Lehnerd A. P. *The Power of Product Platforms*. The Free Press, New York, (1989).

[5] Torstenfelt, B., Klarbring, A. Structural Optimization of Modular Product Families with application to Car Space Frame Structures. *Structural and Multidiciplinary Optimization*, **32**, 133–140 (2006).

[6] Torstenfelt, B., Klarbring, A. Simulataneous Size, Shape and Topology Optimization of Modular Product Families. Submitted

[7] Svanberg, K. The method of moving asymptotes - a new method for structural optimization. *International Journal for Numerical Methods in Engineering*, **24**, 359–373 (1987).

[8] Torstenfelt, B. *TRINITAS' Finite Element Learning Studio, 1995*
`http://www.solid.ikp.liu.se/~botor/Prog/Executables.html`

Crack-growth in a strain gradient dependent plasticity model

Lars P. Mikkelsen
Material Research Department.
Risø National Laboratory, Roskilde, Denmark
e–mail: lars.pilgaard.mikkelsen@risoe.dk

Summary A gradient dependent plasticity model is used modeling crack-growth in an elastic-plastic material. The numerical simulation is based on an implementation of the Fleck-Hutchinson strain gradient plasticity model from 2001. A user-element implementation in the commercial finite element program ABAQUS is used. The crack-growth is modeled using a cohesive finite element. Simulation gives more realistic predictions for crack-growth at strong bonded interfaces compared to a conventional elastic-plastic model.

Introduction

Based on conventional plasticity models, crack growth can only be predicted for weak to moderate strong interfaces. Despite experimental observations, crack growth is prevented by crack tip blunting for interface bond strength above 4-5 times the yield stress of the material even though typical separation stresses for cleavage or decohesion at the atomic level in metals is of the order of 10 times or more the yield stress. In contradiction to experimental observations, such numerical predictions result in cracks unable to grow. Similar separation stresses are observed for polymer-glass interfaces [1].

On the other hand, for enhanced plasticity model such as e.g. the Fleck-Hutchinson [2] gradient dependent plasticity model, more realistic crack growth predicted can be performed [3]. This is do to the fact, that enhanced plasticity models through the incorporated length scales take the microstructure of the material into account in an averaging. This is done without actually modelling the underlying microstructure. In a number of cases, an accurate simulation of highly localized deformation fields is crucial even for realistic predictions on the macroscopic level. An example is the necessarily of an accurate prediction of the stress and strain field around a crack tip in order to make realistic prediction of the overall failure of the overall structure [3].

In the present work, crack growth for a K_I-field dominated crack tip in a homogeneous elastic-plastic material is modelled using the commercial finite element code ABAQUS [4]. The Fleck-Hutchinson [2] strain gradient dependent plasticity model is implemented in the code using a user subroutine interface. The numerical implementation is quite similar to the implementation scheme outlined by Niordson and Hutchinson [5] and Niordson and Redanz [6]. The crack growth is simulated using the cohesive element already available in the code. In the traction versus separation law used in the cohesive elements, the work of separation and the peak separation stress are considered as the two most important parameters [3]. Only for stress levels exceeding the peak separation stress (interfacial bond strength), the crack will actually grow.

The strain gradient plasticity theory and its implementation

The Fleck and Hutchinson (2001) J_2-flow version of the strain gradient dependent plasticity model is implemented in the commercial finite element code ABAQUS using the user subroutine interface (Uel). The implementation is quite similar to the implementation performed by Niordson and Hutchinson [5] and only a brief description is given below.

A power-law hardening material law is used where the tangent modulus depends on a gradient dependent effective plastic strain

$$\dot{E}^{P^2} = \dot{\varepsilon}^{P^2} + A_{ij}\dot{\varepsilon}^P_{,i}\dot{\varepsilon}^P_{,j} + B_{,i}\dot{\varepsilon}^P_{,i}\dot{\varepsilon}^P + C\dot{\varepsilon}^{P^2} \tag{1}$$

The coefficients A_{ij}, B_i and C, see [2] depends on three material length scales, ℓ_1, ℓ_2, ℓ_3, the outward normal the plastic yield, $m_{ij} = (3/2)\, s_{ij}/\sigma_e$, and the gradient thereof, $m_{ij,k}$. A one length scale parameter, ℓ_*, special case of (1) has been formulated as

$$\dot{E}^{P^2} = \dot{\varepsilon}^{P^2} + \ell_*\dot{\varepsilon}^P_{,i}\dot{\varepsilon}^P_{,i} \tag{2}$$

Later, only results for the one parameter version are shown. The equilibrium equation for the strain gradient plasticity model can be formulated trough the virtual work on incremental form

$$\int_V \left[\dot{\sigma}_{ij}\delta\dot{\varepsilon}^e_{ij} + \dot{Q}\delta\dot{\varepsilon}^P + \dot{\tau}_i\delta\dot{\varepsilon}^P_{,i}\right]dV = \int_S \left[\dot{T}_i\delta u_i + \dot{t}\delta\dot{\varepsilon}^P\right]dV + \left[\text{equilibrium correction}\right] \tag{3}$$

where higher order stresses, τ_i, and higher order tractions, t, are introduced.

A plane strain finite element model is formulated where both the nodal displacements and the effective plastic strain is taken as fundamental unknowns. Following the scheme outlined of Niordson and Hutchinson [5,6] the element matrix for the elements in the plastic range is given on the following form

$$\begin{bmatrix} K_e & K_{ep} \\ K_{ep}{}^T & K_p \end{bmatrix}\begin{bmatrix} \dot{U} \\ \dot{\varepsilon}^P \end{bmatrix} = \begin{bmatrix} \dot{F}_1 \\ \dot{F}_2 \end{bmatrix} + \begin{bmatrix} C_1 \\ 0 \end{bmatrix} \tag{4}$$

where $\dot{U}$ and $\dot{\varepsilon}^P$ are the fundamental unknowns and the last term with, C_1, represent the equilibrium correction term. The displacement degree of freedoms $\dot{U}$ are approximated be a 8-noded isoparametric element, while the effective plastic strain $\dot{\varepsilon}^P$ are approximated using the shape function from a 4-node isoparametric element. The element is integrated using 2x2 Gauss-points. This combination is used in order to avoid locking in the shear-dominated part near the crack-tip and spurious zero energy-modes in the degree of freedoms representing the effective plastic strain. In the elastic part, sufficiently large numbers are introduced in K_p in order to avoid spurious plastic strain increments.

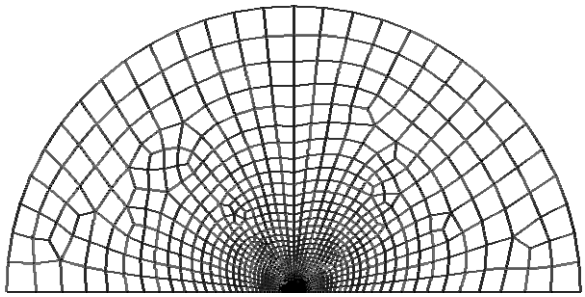

Figure 1: Mesh used in the simulation.

Numerical Results

Crack-tip and growth simulation is performed in a homogenous elastic-plastic material. The mesh used is shown in Fig. 1. The crack is loaded in pure mode I by prescribing a K_I displacement field on the outer boundary. Symmetric boundary condition is prescribed on the lower left boundary while the lower right boundary is free to move representing the crack. For the crack growth simulation, cohesive elements are used in the center of the lower boundary. The cohesive law used has the trapeze form used by a number of authors, see e.g. [3, 7]. Fig. 2 shows the stress and plastic strain distribution near the crack-tip. In Fig. 3, the corresponding variation is shown for a number of cases along the further crack path. Fig. 4. show the result from a few crack growth simulations.

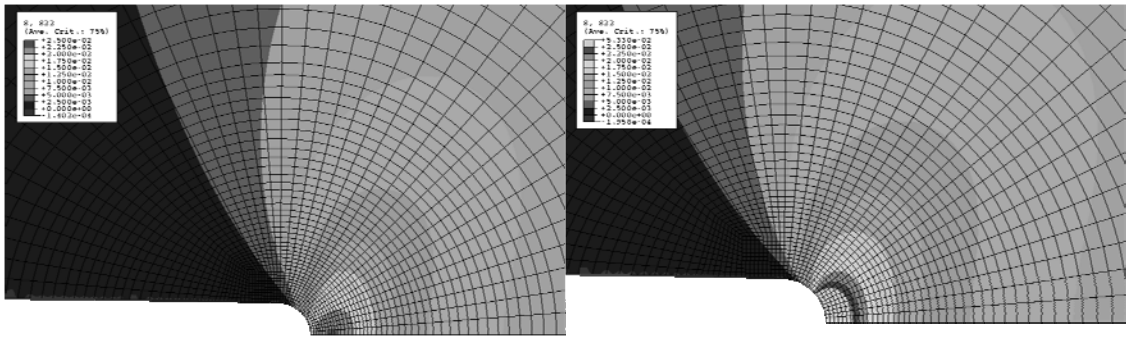

Figure 2: Comparison of the stress levels found at a similar load level for simulation based on a conventional and a strain gradient plasticity theory with a large incorporated length scale, respectively.

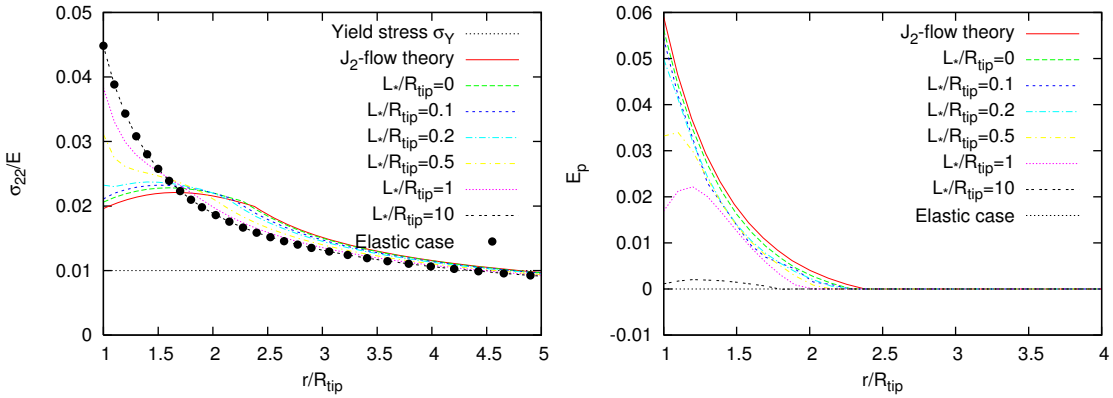

Figure 3: Comparison of the stress level and gradient dependent plastic strain level along the symmetry line found for a number of cases at similar load level.

Conclusion

From the crack tip results, it can be seen that the stress distribution transform smoothly from the stress distribution found for a conventional plasticity solution for small length scale [8] to an elastic kind of singularity for large incorporated length scale. This is supported by the

degreasing level of plastic deformation for increasing length scales as seen in Fig. 3b. As a consequence, the crack-growth is observed to grow at lower steady state values for increasing length scales.

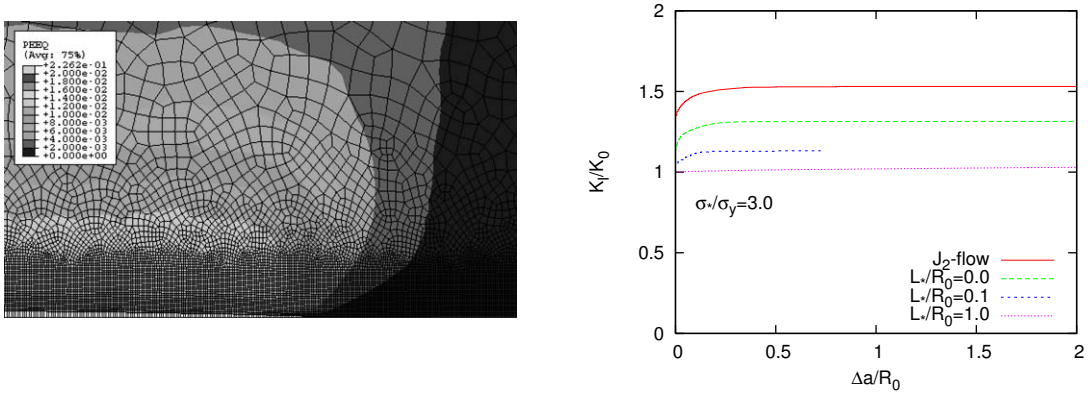

Figure 4: Crack-growth simulation showing the effective plastic strain variation at the instantanous crack-tip and the dependency of the crack-growth resistance curve on the incorporated length scale. The crack length Δa is normalized with a reference plastic zone size.

Acknowledgement: The author wishes to thank Professor John W. Hutchinson, Harvard University and post-doctoral researcher Stergios Goutianos, Risø National Laboratory for many valuable discussions during the course of this work. The work has been financial supported by the Danish Technical Research Council partly in a project entitled "Modeling Plasticity at the Micron Scale" and partly in a project entitled "Interface design of composite materials".

References

[1] Goutianos, S., Drews, J., Nielsen, S.F., Kingshott, P., Hvilsted, S. and Sørensen, B.F., Controlling interface adhesion and fracture properties in composite materials by plasma polymerisation. *Polymer Composite Materials for Wind Power Turbines – Proceedings of the 27th Risø International Symposium on Materials Science*, Risø National Laboratory, Roskilde Denmark, 173-180, (2006).

[2] Fleck, N.A. and Hutchinson, J.W. A reformulation of strain gradient plasticity theory. *J. Mech. Phys. Solids* **49**, 2245-71 (2001)

[3] Wei, Y. and Hutchinson, J.W. (1999) Models of interface separation accompanied by plastic dissipation at multiple scale, *Int. J. of Fracture* **95**, 1-17, (1999).

[4] Hibbitt, Karlsson and Sorensen Inc. ABAQUS/Standard User's Manual, Version 6.6 (2006).

[5] Niordson, C.F. and Hutchinson, J.W. Non-uniform plastic deformation of micron scale objects. *Int. J. Numer. Methods Eng.* **56**, 961–975, (2003).

[6] Niordson, C.F and Redanz, P. Size-effects in plane strain sheet-necking, *J. Mech. Phys.Solids* **52**, 2431–2454, (2004).

[7] Tvergaard, V. and Hutchinson, J.W. The relation between crack growth resistance and fracture process parameters in elastic-plastic solids. *J. Mech. Phys. Solids* **40**, 1377-1397, (1992)

[8] McMeeking, R.M. Finite deformation analysis of crack-tip opening in elastic-plastic materials and implications for fracture. *J. Mech. Phys. Solids* **25**, 357-381, (1977)

A simple and efficient FEM-implementation of the Modified Mohr-Coulomb criterion

Johan Clausen and Lars Damkilde
Esbjerg Institute of Technology
Aalborg University Esbjerg, Esbjerg, Denmark
e–mail: jc@aaue.dk and ld@aaue.dk

Summary This paper presents a conceptually simple finite element implementation of the combined elasto-plastic Mohr-Coulomb and Rankine material models, also known as Modified Mohr-Coulomb plasticity. The stress update is based on a return mapping scheme where all manipulations are carried out in principal stress space which simplifies the calculations. The model supports both associated and non-associated perfect plasticity.

Introduction

Materials such as sand and concrete show pressure dependent strength properties. The simplest material model which incorporates this pressure dependency is the Mohr-Coulomb material model. The yield criterion uses the well known parameters friction angle, φ, and cohesion, c

$$f_{\mathrm{MC}} = k\sigma_1 - \sigma_3 - \sigma_c = 0, \qquad \text{with} \quad k = \frac{1+\sin\varphi}{1-\sin\varphi} \quad \text{and} \quad \sigma_c = 2c\sqrt{k} \tag{1}$$

where σ_1, σ_2 and σ_3 are the principal stresses. In this paper tension is taken as positive.

When $c > 0$ the Mohr-Coulomb model predicts a tensile strength which is larger than the tensile strength observed experimentally, see e.g. references [1], [2] and [3]. This discrepancy can be mended by the introduction of the Rankine or ”tension cut-off” criterion

$$f_{\mathrm{R}} = \sigma_1 - \sigma_t = 0 \tag{2}$$

where σ_t is the ”tension cut-off” value, which is the highest tensile stress allowed in the material. The combination of these criteria is usually referred to as the Modified Mohr-Coulomb Criterion, cf. [2]. On Fig. 1 this criterion can be seen in the principal stress space and in the $\sigma_1 - \sigma_3$ plane. The Rankine part of the criterion, Eq. (2), is taken to be associated whereas the Mohr-Coulomb part is non-associated.

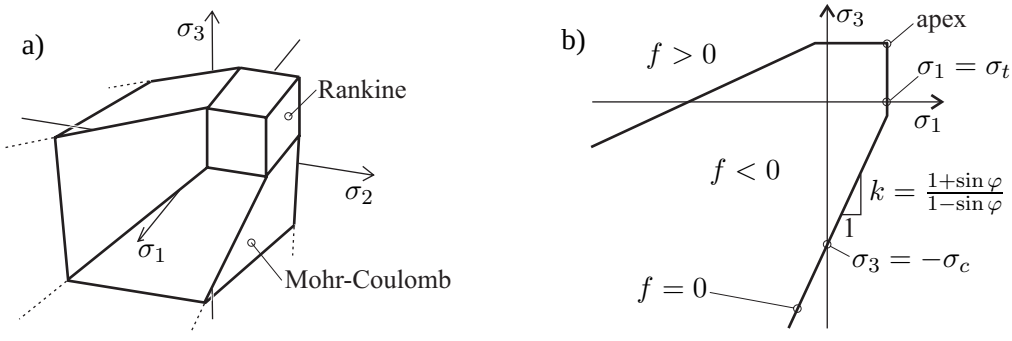

Figure 1: The Modified Mohr-Coulomb Criterion in a) principal stress space and b) the section through the $\sigma_1 - \sigma_3$ plane.

Plastic stress update for yield planes in principal stress space

From Eqs. (1), (2) and Fig. 1 it can be seen that the criterion consists of intersecting planes in the principal stress space. As will be shown later the Modified Mohr-Coulomb criterion leads to nine different types of stress return, which must be properly identified. This can be a cumbersome task in general stress space. Therefore the method of [4] and [5] is very well suited for carrying out the plastic integration and formation of the constitutive matrix. In the following a short summary of the method will be given.

The stress update and formation of the consistent constitutive matrix require the derivative of the yield function and the first and second derivatives of the plastic potential. As only isotropic material models are considered the manipulations can be carried out with respect to any set of coordinate axes. Therefore the predictor stress is transformed into principal stress space and returned to the yield surface. Considering the fact that the stress return preserves the principal directions, the updated stress can then be transformed back into the original coordinate system. This simplifies the manipulations of the return mapping scheme considerably compared to the standard formulation, see, e.g. [6]. There are two reasons for this. Firstly the dimension of the problem reduces from six to three, and secondly, in the three-dimensional stress space the stress states can be visualized graphically, making it possible to apply geometric arguments.

Linear yield criteria in the principal stresses are visualized as planes in principal stress space. These planes intersect in lines and points, making three types of stress returns and constitutive matrices necessary: Return to a yield plane, return to a line, e.g. intersection of two yield planes and finally return to a point, e.g. intersection of three or more yield planes. The three types of return are visualized on Fig. 2.

The formulae for the different returns will be established in the following. The conditions for determining which return is needed will also be established by dividing the stress space into different stress regions.

Vectors and matrices are expressed with respect to the principal axes. This means that the last three components of vectors are always zero and are not be shown as a matter of convenience. Even so all matrices and vectors are six-dimensional.

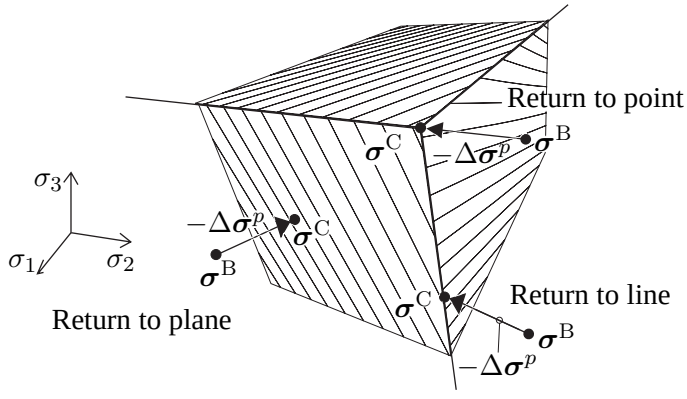

Figure 2: Three intersecting yield planes in principal stress space with three types of return shown.

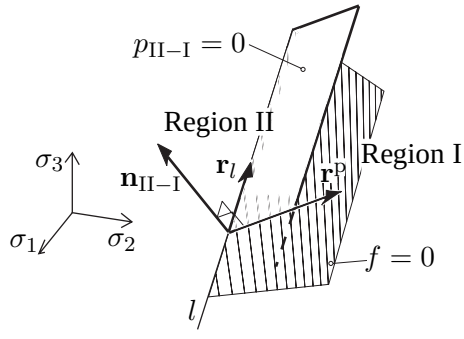

Figure 3: Boundary plane $p_{\mathrm{II-I}} = 0$ with normal $\mathbf{n}_{\mathrm{II-I}}$, which separates the stress regions I and II.

The task is to determine the updated stress, $\boldsymbol{\sigma}^{\mathrm{C}}$, in the equation

$$\boldsymbol{\sigma}^{\mathrm{C}} = \boldsymbol{\sigma}^{\mathrm{B}} - \Delta\boldsymbol{\sigma}^{\mathrm{p}} = \boldsymbol{\sigma}^{\mathrm{B}} - \Delta\lambda \mathbf{D}\frac{\partial g}{\partial \boldsymbol{\sigma}} \tag{3}$$

where $\boldsymbol{\sigma}^{\mathrm{B}}$ is the predictor stress state found by the solution of the global system of FEM equations, $\Delta\boldsymbol{\sigma}^{\mathrm{p}}$ is the plastic corrector stress, $\Delta\lambda$ is a plastic multiplier, $\mathbf{D}$ is the elastic constitutive matrix and g is the plastic potential.

Stress return to a plane

The equation of a yield plane and a plastic potential in the principal stress space can be written as

$$f(\boldsymbol{\sigma}) = \mathbf{a}^{\mathrm{T}}\,(\boldsymbol{\sigma} - \boldsymbol{\sigma}_f) = 0 \qquad \text{and} \qquad g(\boldsymbol{\sigma}) = \mathbf{b}^{\mathrm{T}}\boldsymbol{\sigma} \tag{4}$$

where $\boldsymbol{\sigma}^f$ is a point on the plane and $\mathbf{a}$ and $\mathbf{b}$ are the gradients,

$$\mathbf{a} = \frac{\partial f}{\partial \boldsymbol{\sigma}} \qquad \text{and} \qquad \mathbf{b} = \frac{\partial g}{\partial \boldsymbol{\sigma}} \tag{5}$$

Both $\mathbf{a}$ and $\mathbf{b}$ are constant. The plastic corrector stress can be computed as

$$\Delta\boldsymbol{\sigma}^{\mathrm{p}} = \frac{f(\boldsymbol{\sigma}^{\mathrm{B}})}{\mathbf{b}^{\mathrm{T}}\,\mathbf{D}\,\mathbf{a}}\,\mathbf{D}\,\mathbf{b} = f(\boldsymbol{\sigma}^{\mathrm{B}})\,\mathbf{r}^{\mathrm{p}} \qquad \text{with} \qquad \mathbf{r}^{\mathrm{p}} = \frac{\mathbf{D}\mathbf{b}}{\mathbf{b}^{\mathrm{T}}\,\mathbf{D}\,\mathbf{a}} \tag{6}$$

where $\mathbf{r}^{\mathrm{p}}$ is the scaled direction of the plastic corrector in principal stress space, i.e. $\mathbf{r}^{\mathrm{p}}$ is at an angle with the plastic strain direction, $\mathbf{b}$.

Stress return to a line

A line, l, in principal stress space has the equation

$$l: \quad \boldsymbol{\sigma} = t\,\mathbf{r}^{\ell} + \boldsymbol{\sigma}_l \tag{7}$$

where t is a parameter with the unit of stress, $\boldsymbol{\sigma}_l$ is a point on the line and $\mathbf{r}_l$ is the direction vector. The parameter t can be found as

$$t = \frac{(\mathbf{r}_1^{\mathrm{p}} \times \mathbf{r}_2^{\mathrm{p}})^{\mathrm{T}}(\boldsymbol{\sigma}^{\mathrm{B}} - \boldsymbol{\sigma}_l)}{(\mathbf{r}_1^{\mathrm{p}} \times \mathbf{r}_2^{\mathrm{p}})^{\mathrm{T}}\,\mathbf{r}_l} \tag{8}$$

where $\mathbf{r}_1^{\mathrm{p}}$ and $\mathbf{r}_2^{\mathrm{p}}$ are the plastic corrector vectors from Eq. (6) for the two yield planes intersecting at the line.

Stress return to a point

If the stress is to be returned to a singularity point, $\boldsymbol{\sigma}^{\mathrm{a}}$, e.g. an apex point, see Figure 2, there is no need for calculations, as the returned stress is simply

$$\boldsymbol{\sigma}^{\mathrm{C}} = \boldsymbol{\sigma}^{\mathrm{a}} \tag{9}$$

Stress regions

In this section it will be outlined how to determine to which plane, line or point the stress should be returned. In order to do this the concept of stress regions is introduced, and the boundary planes that separate them are defined. Each yield plane, line and point is associated with a particular stress region. When the predictor stress is located in a given region it must be returned to the corresponding plane, line or point. Two stress regions, I and II, separated by a boundary plane, $p_{\mathrm{II-I}} = 0$ are illustrated on Figure 3.

When the yield functions and plastic potentials are linear in the principal stresses, the boundary planes are also linear. The direction of the plastic corrector, $\mathbf{r}^{\mathrm{p}}$, c.f. (6), and the direction vector of the line, $\mathbf{r}_l$, define the orientation of the plane, and so the equation of a boundary plane can be found as:

$$p_{\mathrm{II-I}}(\boldsymbol{\sigma}) = (\mathbf{r}^{\mathrm{p}} \times \mathbf{r}_l)^{\mathrm{T}}(\boldsymbol{\sigma} - \boldsymbol{\sigma}_l) = \mathbf{n}_{\mathrm{II-I}}^{\mathrm{T}}(\boldsymbol{\sigma} - \boldsymbol{\sigma}_l) = 0 \tag{10}$$

where $\mathbf{n}_{\mathrm{II-I}}$ is the normal of the plane. The indices indicate that the normal points *into* region II *from* region I. The point on the plane is $\boldsymbol{\sigma}_l$, which can be taken as a point that also belongs to l, see Fig. 3 and Eq. (7). If two stress regions are located as seen on Fig. 3, the following is valid for a given predictor stress, $\boldsymbol{\sigma}^{\mathrm{B}}$ located outside the yield locus, i.e. $f(\boldsymbol{\sigma}^{\mathrm{B}}) > 0$:

$$\begin{aligned} p_{\mathrm{II-I}}(\boldsymbol{\sigma}^{\mathrm{B}}) \leqq 0 \quad &\Leftrightarrow \quad \text{Region I} \quad \Leftrightarrow \quad \text{Return to } f = 0 \\ p_{\mathrm{II-I}}(\boldsymbol{\sigma}^{\mathrm{B}}) > 0 \quad &\Leftrightarrow \quad \text{Region II} \quad \Leftrightarrow \quad \text{Return to } l \end{aligned} \tag{11}$$

Constitutive matrix

The consistent constitutive matrix is also formed in principal stress space. Details are given in refs. [4] and [5].

Modified Mohr-Coulomb plasticity

The principal stresses are ordered in descending order, i.e. $\sigma_1 \geqq \sigma_2 \geqq \sigma_3$. This means that the Modified Mohr-Coulomb criterion consists of only two planes in the principal stress space, see Fig. 4. As can be seen on the figure the geometry of the yield planes is bounded by five lines which

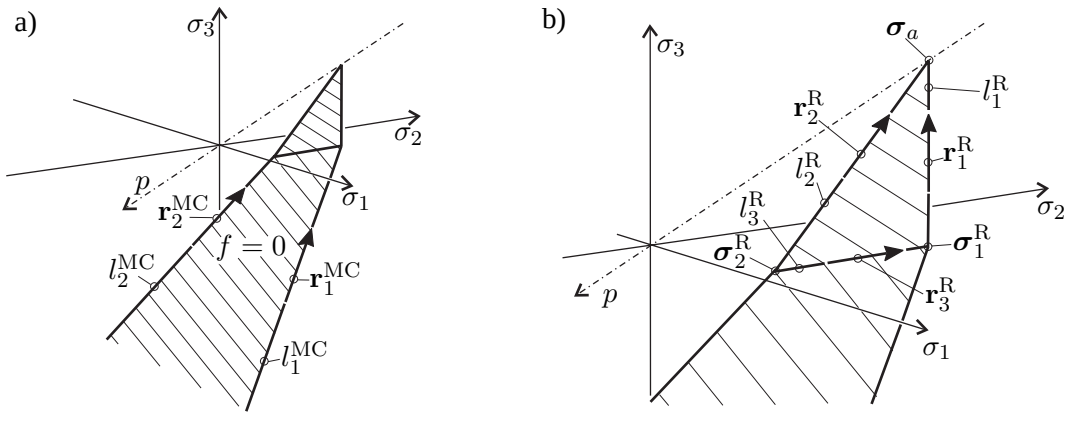

Figure 4: a) The Modified Mohr-Coulomb criterion in principal stress space. b) Detail of the tension cut-off plane, f_{R}. The line, p, is the hydrostatic axis.

intersect at three points. With reference to Fig. 4 the equations for the lines and their direction vectors are

$$l_1^{\mathrm{MC}}: \quad \boldsymbol{\sigma} = t\mathbf{r}_1^{\mathrm{MC}} + \boldsymbol{\sigma}_a^{\mathrm{MC}}, \qquad \mathbf{r}_1^{\mathrm{MC}} = [1 \;\; 1 \;\; k]^{\mathrm{T}} \tag{12}$$

$$l_2^{\mathrm{MC}}: \quad \boldsymbol{\sigma} = t\mathbf{r}_2^{\mathrm{MC}} + \boldsymbol{\sigma}_a^{\mathrm{MC}}, \qquad \mathbf{r}_2^{\mathrm{MC}} = [1 \;\; k \;\; k]^{\mathrm{T}} \tag{13}$$

$$l_1^{\mathrm{R}}: \quad \boldsymbol{\sigma} = t\mathbf{r}_1^{\mathrm{R}} + \boldsymbol{\sigma}_a, \qquad \mathbf{r}_1^{\mathrm{R}} = [0 \;\; 0 \;\; 1]^{\mathrm{T}} \tag{14}$$

$$l_3^{\mathrm{R}}: \quad \boldsymbol{\sigma} = t\mathbf{r}_3^{\mathrm{R}} + \boldsymbol{\sigma}_1^{\mathrm{R}}, \qquad \mathbf{r}_3^{\mathrm{R}} = [0 \;\; 1 \;\; 0]^{\mathrm{T}} \tag{15}$$

where t is a parameter with the dimension of stress, and $\boldsymbol{\sigma}_a^{\mathrm{MC}}$, $\boldsymbol{\sigma}_a$ and $\boldsymbol{\sigma}_1^{\mathrm{R}}$ are the Mohr-Coulomb apex (not shown on Fig. 4), the Modified Mohr-Coulomb apex and the intersection between lines l_1^{MC} and l_3^{R}, respectively. A fourth point, denoted $\boldsymbol{\sigma}_1^{\mathrm{R}}$, is the intersection between lines l_2^{MC} and l_3^{R}. These points have the coordinates

$$\boldsymbol{\sigma}_a^{\mathrm{MC}} = \frac{\sigma_c}{k-1}\begin{Bmatrix}1\\1\\1\end{Bmatrix}, \quad \boldsymbol{\sigma}_a = \begin{Bmatrix}\sigma_t\\\sigma_t\\\sigma_t\end{Bmatrix}, \quad \boldsymbol{\sigma}_1^{\mathrm{R}} = \begin{Bmatrix}\sigma_t\\\sigma_t\\k\sigma_t-\sigma_c\end{Bmatrix}, \quad \boldsymbol{\sigma}_2^{\mathrm{R}} = \begin{Bmatrix}\sigma_t\\k\sigma_t-\sigma_c\\k\sigma_t-\sigma_c\end{Bmatrix} \tag{16}$$

The boundary planes that separate the nine stress regions can be seen on Fig. 5. The equations of the 11 boundary planes will not be given here but can be found from the Eqs. (10) and (12-16).

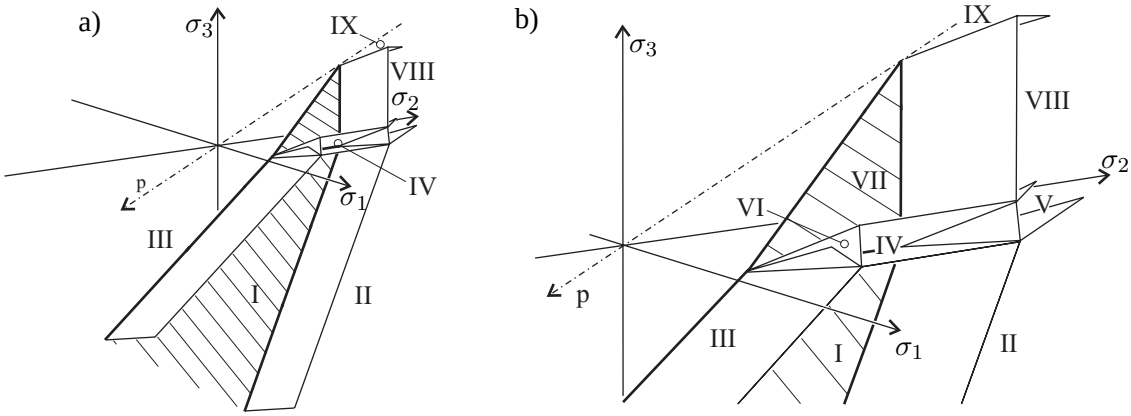

Figure 5: a) Stress regions, denoted by roman numerals. b) Detail.

Numerical example

A finite element calculation is carried out on a rigid smooth footing resting on a frictional cohesive soil. Two material models are employed. The first is a perfectly plastic Mohr-Coulomb model with $\varphi = 20°$, $\psi = 5°$ and $c = 20$ kPa. The second is the Modified Mohr-Coulomb material model with the same parameters and also a tension cut-off, $\sigma_t = 0$. A mesh of six-noded triangular linear strain elements is created, and can be seen on Fig. 6. This element mesh has a total of 347 elements with 1500 degrees of freedom. The radius/halfwidth of the footing is r and the domain has a width of $12r$ and a height of $10r$. A forced displacement is applied to the footing in steps, and the footing pressure q is found from the reaction forces. The soil has a selfweight of $\gamma = 20$ kN/m^3, a modulus of elasticity of $E = 20$ MPa and a Poisson's ratio of $\nu = 0.26$. An initial earth pressure coefficient of $k_0 = 1$ is used.

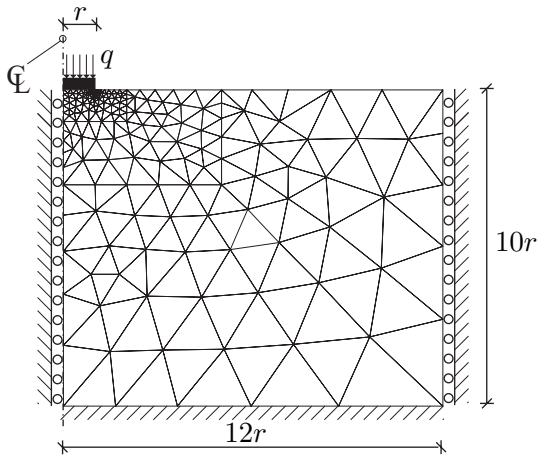

Figure 6: Geometry, boundary conditions and element mesh for the computational example.

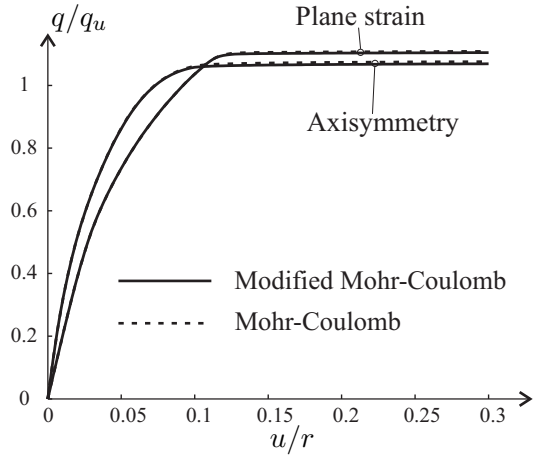

Figure 7: Normalized load-displacement curves.

On Fig. 7 the load-displacement curves can be seen. The displacement has been normalized with respect to the footing radius and the load has been normalized according to Terzaghi's superposition equation for the bearing capacity of surface footings

$$q_u = cN_c + \gamma r N_\gamma \tag{17}$$

Fig. 7 shows that the Mohr-Coulomb and the Modified Mohr-Coulomb model predict almost the same bearing capacity with the Mohr-Coulomb bearing capacity being slightly larger. In a problem with an eccentric load the difference would be more pronounced, as positive normal strains could develop between the soil and a part of the footing without the development of tensile stresses.

Conclusion

A simple and efficient method of performing the plastic stress update for a Modified Mohr-Coulomb material is presented. In the method all manipulations are carried out in the principal stress space which simplifies these considerably compared to the equivalent manipulations in general six-dimensional stress space. A numerical example shows the performance of the method.

References

[1] Mogens Peter Nielsen. *Limit analysis and concrete plasticity*. CRC press, 1999.

[2] Niels Saabye Ottosen and Matti Ristinmaa. *The Mechanics of Constitutive Modelling*. Elsevier, 2005.

[3] R.B.J. Brinkgreve and P.A. Vermeer. *Plaxis, Finite Element Code for Soil and Rock Analyses, Version 7*. A.A. Balkema, Rotterdam, 1998.

[4] Johan Clausen, Lars Damkilde, and Lars Andersen. Efficient return algorithms for associated plasticity with multiple yield planes. *International Journal for Numerical Methods in Engineering*, 66(6):1036–1059, 2006.

[5] J. Clausen, L. Damkilde, and L. Andersen. An efficient return algorithm for non-associated mohr-coulomb plasticity. In B. H. V. Topping, editor, *Proceedings of the Tenth International Conference on Civil, Structural and Environmental Engineering Computing*, Stirling, United Kingdom, 2005. Civil-Comp Press. paper 144.

[6] M.A. Crisfield. *Non-Linear Finite Element Analysis of Solids and Structures*, volume 2: Advanced Topics. John Wiley & Sons, 1997.

Simulation of martensitic phase transformation in austenitic steel

Håkan Hallberg*, Paul Håkansson and Matti Ristinmaa
Department of Solid Mechanics
Lund University, Lund, Sweden
e–mail: hakan.hallberg@solid.lth.se, paul.hakansson@solid.lth.se, matti.ristinmaa@solid.lth.se

Summary A thermodynamically consistent constitutive model for diffusionless phase transformation in austenitic steel is presented. An elasto-plastic model based on a multiplicative split of the deformation gradient is used for the evolving plasticity while a transformation condition governs the evolution of martensitic transformation and transformation strain.

Introduction

Increasing attention is being directed at austenitic steel undergoing martensitic transformation. This is due in no small part to the fact that use of shape-memory alloys and so-called TRIP steels are becoming increasingly common. The transformation from austenite to martensite has appealing traits, such as the high rate at which the transformation occur and the possibility to obtain a material with inhomogeneous ductility, making these steels interesting in practical applications.

Phase transformations in steel occur either through slow diffusional processes or by very rapid microstructural rearrangements, not depending on diffusion. The formation of martensite that takes place when deforming an austenitic steel is of the latter, diffusionless, kind. Martensitic phase transformation also exhibit a strong temperature dependency since elevated temperatures restrain transformation while lower temperatures promote it. The presence of an evolving martensitic phase has substantial influence on the behavior of the material. Since the martensite phase has considerably higher yield stress than the austenite, the martensite will enhance the hardening of the material undergoing deformation. The difference in yield stress between the phases will also induce a localization of the plastic deformation to the weaker austenite phase, inducing additional plastic straining. These phenomena makes effective constitutive models that include phase transformation desirable in many practical applications. One example is the simulation of high-velocity metal forming operations which are too rapid for diffusion-based transformations to occur, but rely on control of the amount and distribution of martensite, e.g. by controlling the temperature of the tooling.

An elasto-plastic model based on a spatial formulation, and suitable for finite-strain simulations, is developed, cf. [2]. The total deformation gradient is multiplicatively decomposed according to $\boldsymbol{F} = \boldsymbol{F}^{r}\boldsymbol{F}^{ir}$ into one reversible part describing the elastic deformation, and one irreversible part which includes both slip deformation and deformation due to phase transformation. The evolution of the transformation strain is assumed to be proportional to both the applied stress and the rate of the transformation. This approach has previously been adopted in e.g. [3] and [4].

The volume fraction of martensite is included into the model as an additional internal variable in the Helmholz free energy function. The evolution of this internal variable is derived from a potential function which also constitute the transformation condition. Following e.g. [1], a conjugated thermodynamic force, driving the transformation, is identified from the transformation potential. The shape of the transformation surface and the direction of the transformation strain are estimated by considering the lattice rearrangement involved in the phase transformation, i.e. the microstructural change between the austenitic fcc lattice and the martensitic bcc lattice.

Discussion

The constitutive model incorporates the irreversible deformation both due to plastic slip and that due to phase transformation. The plastic slip is included through the use of a standard J_2-plasticity model with non-linear isotropic hardening. To determine the evolution of transformation strain, a transformation potential $h(F, z, \theta) \leq 0$ can be formulated, where F is the thermodynamic force conjugated to the volume fraction of martensite. Much like the yield condition indicates if plastic loading has occured or not, this transformation condition determines if phase transformation has taken place. Also the evolution of z is determined from the potential h. The modified Koistinen-Marburger relation – where the evolution of z is driven by both stress and temperature – can be retrieved.

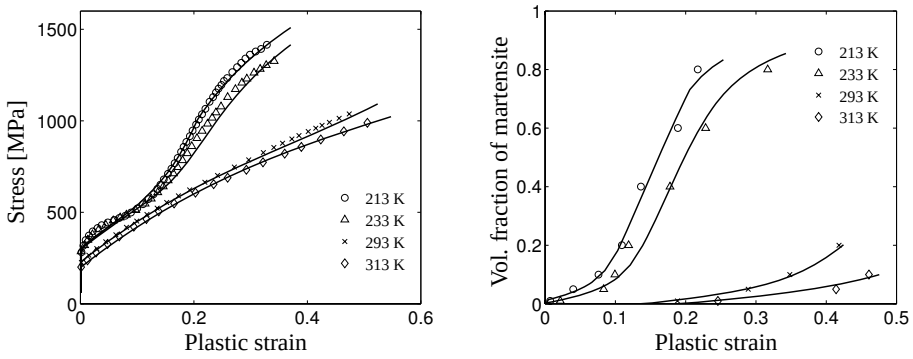

Figure 1: Left: Simulated stress-strain response (solid lines) compared with experimental results (symbols). Right: The volume fraction of martensite as a function of plastic strain, corresponding to the left graph. The experimental results are taken from uniaxial tension tests of AISI304 steel at different temperatures, cf. [5].

By considering a polycrystal with randomly oriented grains, a transformation surface can be established. Due to the symmetry of the austenitic fcc lattice, 24 different martensite variants are made possible. Considering a polycrystal and establishing a transformation condition for each one of these variants in each grain, a transformation surface is obtained after a homogenization of all grains. This surface shows close agreement with experimental findings. Using this crystallographically motivated surface as a guide, the phase transformation in the present model is based on a function h according to

$$h(\boldsymbol{\tau}, z, \theta) = K(z, \theta) \left[\left(3J_2 + \frac{3bJ_3}{J_2^{1/2}} \right)^{1/2} + \delta I_1 \right] - F_{trans}(z, \theta) = 0 \tag{1}$$

where b and δ are parameters to be fitted. $F_{trans}(z, \theta)$ is a barrier function that act as a threshold against transformation. By combining $K(z, \theta)$ and $F_{trans}(z, \theta)$, a calibration against experimental data is possible.

Figure 1 shows the model calibrated against experimental data found in [5] for AISI304 steel. The strong temperature dependence of the martensite evolution should be noted. Very little martensite is formed at higher temperatures whereas most of the austenite is transformed into martensite at lower temperatures.

Based on the above theory, a numerical implementation is preformed where it is seen that the present model only involves one additional equation as compared with standard J_2-plasticity with isotropic hardening. This renders a computational model that is robust and convenient in FE-based simulations.

Example

To illustrate the capabilities of the model and also the influence of a martensitic phase, consider a rod exposed to a tensile loading. The geometry is shown in Figure 2 and $r_0 = 3$ mm and $l_0 = 9$ mm is used in the simulations. To trigger necking, a small imperfection is introduced in the geometry whereby the "waist" of the rod is reduced by 0.03%.

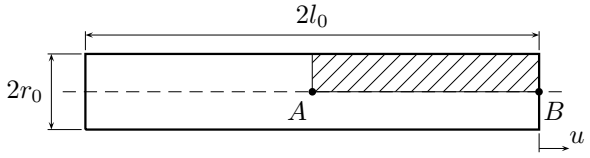

Figure 2: Geometry of the simulation model representing a cylindrical rod exposed to tensile loading. Taking advantage of the symmetry, only one fourth of the rod is actually analyzed (the hashed region). Points A and B are used for reference. The tensile load is applied by enforcing a displacement u of one end of the bar.

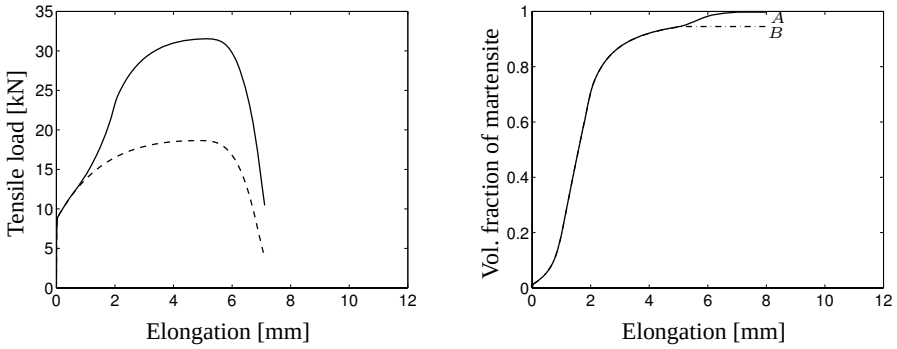

Figure 3: Simulated response of an axisymmetric bar exposed to tensile loading at $\theta = 213$ K. The left graph show the response both with phase transformation (solid lines) and without (dashed lines). The graph at the right show the corresponding evolution of martensite at the center end points of the simulated geometry, cf. Figure 2. The dash-dotted lines are related to the end point B of the rod and the solid lines are related to the center point A of the rod. Figure 4 shows the corresponding graphs at $\theta = 293$ K.

Figures 3 and 4 show load-displacement curves for the rod, with and without phase transformation. At the lower temperature of $\theta = 213$ K, the martensite phase evolves rapidly, cf. Figure 3. The localization of plastic deformation occurs almost at the same state of deformation, regardless of phase transformation. This is due to the rod being quite homogeneously transformed into martensite, which is seen in the right graph in Figure 3. However, the hardening is greatly pronounced in the presence of martensite. At room temperature, $\theta = 293$ K, the martensite evolves at a much lower rate, cf. Figure 4. The hardening behavior is hardly affected by the harder martensite phase, but the localization of deformation is markedly delayed. When localization is initiated, martensite forms and rapidly stabilizes the region of localization.

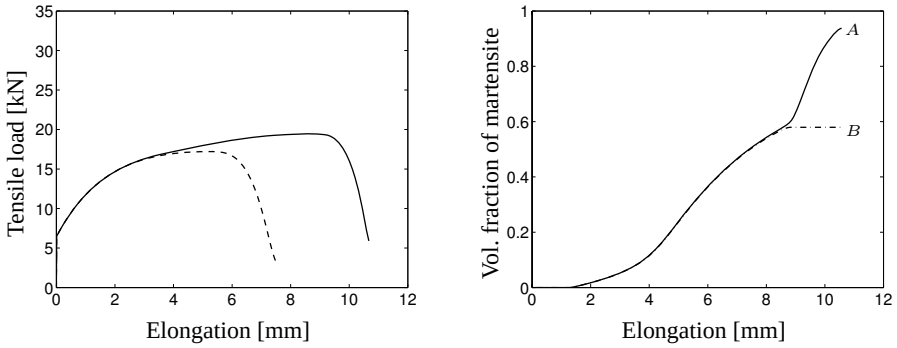

Figure 4: Simulated response of an axisymmetric bar exposed to tensile loading at $\theta = 293$ K.

References

[1] F. D. Fischer, E. R. Oberaigner, K. Tanaka, and F. Nishimura. Transformation induced plasticity, revised and updated formulation. *International Journal of Solids and Structures*, 35:2209–2227, 1998.

[2] H. Hallberg, P. Håkansson, and M. Ristinmaa. A constitutive model for the formation of martensite in austenitic steels under large strain plasticity. *Accepted for publication in the International Journal of Plasticity*, 2006.

[3] T. Iwamoto, T. Tsuta, and Y. Tomita. Investigation on deformation mode dependence of strain-induced martensitic transformation in trip steels and modelling of transformation kinetics. *International Journal of Mechanical Sciences*, 40(2-3):173–182, 1998.

[4] J. B. Leblond. Mathematical modelling of transformation plasticity in steels II: Coupling with strain hardening phenomena. *International Journal of Plasticity*, 5:573–591, 1989.

[5] M. O. Onyuna. *Deformation behaviour and martensitic transformations in metastable austenitic steels and low alloyed multiphase steels*. PhD thesis, Department of Materials Science and Technology, Freiberg University of Mining and Technology, 2003.

Continuum Mixture theory as an approach to Fluid-Structure Interaction

L. Strömberg
Fredrlg 38, se-38237 Nybro, previously Department of Solid Mech, KTH, Sweden
e-mail: lena_str@hotmail.com

Part I. Statics

Key words: Momentum supply, Weak formulation, Meta center stability

1 INTRODUCTION

The foundation of continuum mixture theory [1] is applied to fluid-structure models. Equations of motion and continuity are deduced for a two constituent mixture, and expressions for supply properties are suggested. The models are exemplified with hydrostatics.

The approach may be used as a complement to ordinary boundary condition, by considering an interaction with boundaries in a spatially distributed boundary layer, eg. viscous layers in flow. The principles and consequencies of regarding an entire construction as a mixture, will also be examined.

A coupling at the boundary may be considered a weak interaction, since it is present in the equation after a weak formulation, or an integration. A coupling in the equation is more of a strong interaction, and emanates from mixture modeling. (The coupling has similarities with the heat source factor and heat flux in the energy balance equation.)

In hydrostatics, a modification of Archimedes principle, gives a pointwise distributed uplift (buoyancy). For this buoyancy, a weak formulation is considered and a stability criterion at 'meso-level', is formulated. At macro-level, this is in analogy to meta center level stability for ships and off-shore structures.

2 STATIC MIXTURE MODEL

The constituents are assumed to be an ideal fluid, characterized by pressure p_f and density ρ_f, and a solid, with stress tensor $\mathbf{s}$, and density ρ_s. Neglecting inertia, the governing equations based on [1] read

$-\text{grad}\, p_f + \rho_f g + \text{div}\, P = 0$ (1)

$\text{div}\, \mathbf{s} + \rho_s g - \text{div}\, P = 0$ (2)

where g is gravity, and div P, is momentum supply.

3 APPLICATION IN HYDROSTATICS

Assuming that P is a linear function of p_f, and tr $\mathbf{s}$, makes it possible to solve (1) for P,

$P = c_1/(1- c_1)(\rho_f g\, y + c_2\, \text{tr}\, \mathbf{s})\mathbf{1}$ (3) and $p_f = 1/(1- c_1)(\rho_f g\, y + c_2\, \text{tr}\, \mathbf{s}) + C$ (4)

where c_1, c_2, C are material constants. Compared with classical hydrostatics, equation (4), is a modified pressure formula. Insertion of (3) into (2), will give an uplift, due to fluid content,

and a modified Poissons ratio.

To derive a potential, a weak form of equilibrium for a sub-body of the solid constituent is formulated. Assume a sub-body of solid partly submerged in fluid, with a cylindrical shape, subjected to forces as seen in Figure 1. Equilibrium (2) holds, with a reaction force from the anchor denoted by S, and at the upper part, P is zero.

With w being a weight function, the weak formulation, when $c_2=0$ reads

$\Pi=\text{Int}\,(w^T(\text{div}\,\mathbf{s} + \rho_s g - \text{div}\,P+S\delta(\text{location}))dV\,,\ \Pi=0$ (5)

When w is a virtual displacement, Π is known as a potential, [2]. Eq (5) is to hold for an arbitrary w, eg. a rigid body motion around fluid surface quantified by a small rotation an angle ϕ. Since diffusion is neglected, the entire mixture will rotate with the solid, to the configuration in Figure 1. Such a configuration is present, at a water surface with waves, or when air cavities.

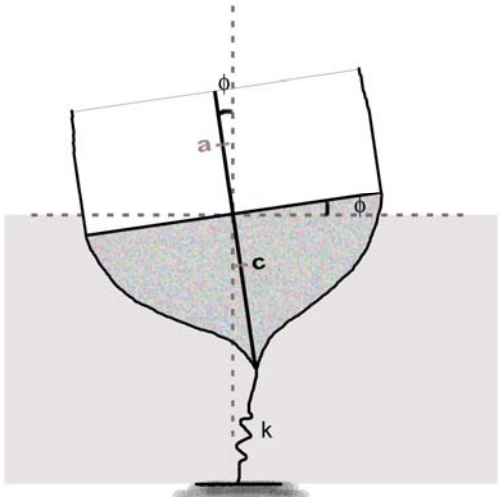

Figure 1. Rotational displacement of mixture

An integration by parts for P-term, gives, that uplift act at the upper fluid intersection surface, since this is the boundary of the mixture. Stability at equilibrium requires that the second differential of Π is positive, which gives the condition

$u\,\rho_f g\,\phi^2 I - u\,\rho_f g\,\phi^2 V c + kf(\phi,S) - \rho_s g\,\phi^2 (K+V)a > 0$ (6)

where u is a constitutive parameter for momentum supply P, at the boundary, a and c are the distance from origo to point a and c, K, V are the volumes above and submerged, I is the area-inertia moment for the boundary surface and f is a function of conditions for the anchorage. For k=0, equilibrium reads $\rho_s g\,(K+V) = u\,\rho_f g V$. Insertion in (6) gives the formula $a+c<I/V$, which, for u=1, is in analogy to meta center stability for a ship in water, or an aircraft on air. In mixture, as well as in traditional modeling, the density distribution may be a varying field, (since the constituent does not occupy the entire space), which alters the formula.

In classical traditional modeling, the solid and fluid are two different bodies, momentum supply P=0, and the coupling is at the boundary. In the weak formulation of the mixture modeling, the momentum supply will act at the boundary, altered by a factor u.

Generalisations could be done to

- Non-rigid body motion, strain implies a stress tensor, which give dependency on c_2
- anchorage force non-zero, ($S=k\phi^2$ or $k\phi$)
- friction at solid-fluid intersection.

4 CONCLUSIONS

By considering the fluid and structure as a mixture, an alternative approach to fluid-structure interaction was investigated. In mixture modeling, there are couplings also in the field equations, and not only at the boundaries. Model were applied to stability for floating objects.

Other areas where continuum mixture modeling is of interest are biomechanics, pressure-dependence on depth, density, temperature, salinity, and influence from measurement equipment.

5 REFERENCES

[1] Bowen, R.M.: *Theory of Mixtures.* Continuum Physics (1976) ed. by A.C. Eringen, Vol III, Academic Press.

[2] Magnusson. A.: *Branch identification in elastic stability analysis. pp5-10* Doctoral thesis. (2000) Lund University, Sweden.

Part II. Dynamics with relative motions

Key words: Diffusion, Weak formulation, Doppler effect, Aqua plane, Nonlinear simulation

1 INTRODUCTION

For a continuum mixture theory[1] featuring diffusion, equations for a two-constituent mixture will be summarised. Assuming constituent to be fluid, solid and gas, models in hydrodynamics are deduced. In applications of special relativity, a generalised Lorenz transformation appears. To describe Doppler-shift, we consider a constituent (fluid or gas) with velocity v_1 and density ρ_1, that transmits an acoustic wave, mixed with an acoustic medium at rest. Constituting the mixture to be an acoustic medium with sound/wave velocity c, a Doppler effect that depend on ratio of velocity and sound speed, as well as densities of the constituents are derived. For certain average values of densities, the classical relativistic Doppler formula will appear, as a special case.

At aqua-plane, vertical forces are due to gravity, buoyancy, and an uplift proportional to square of velocity, surface and density. Considering the angle to the water-surface as a degree of freedom, a weak form[2] of equation of motion will give a nonlinear equation. At linearisation, for different angles, a generalised format with eigen-frequency may be identified. For large speeds, behaviour is non-stable.

2 CONTINUUM MIXTURE MODEL

For a mixture of two constituents [1] with densities ρ_i and velocities $d_t x_i$, i=1,2, the density and velocity are defined as

$$\rho=\rho_1+\rho_2\ ,\ \rho d_t\mathbf{x} =\rho_1 d_t\mathbf{x}_1 +\rho_2 d_t\mathbf{x}_2 \tag{1}$$

The stress tensor for the mixture is

$$T_m=\mathbf{s}_1+\mathbf{s}_2-\rho_1\,\mathbf{u}_1\mathbf{u}_1{}^{T}-\rho_2\,\mathbf{u}_2\,\mathbf{u}_2{}^{T} \tag{2}$$

where $\mathbf{s}_i$ are stress tensors of the constituents, and $\mathbf{u}_i = d_t\mathbf{x}_i - d_t\mathbf{x}$ are the relative velocities.

3 APPLICATIONS

3.1 Induced Lorenz expression for relativistic frames/measures

Preliminaries: Constituent 1 has an absolute velocity v_1, and the stress tensor for the mixture is the pressure of an acoustic medium[3] with sound/(light) wave speed c, here

specified to ideal gas $p=\rho c^2$.

The first component of the stress tensor for constituent 1 will read (1),(2)

$-(\mathbf{s}_1)_{11}/c^2=(1-(v/c)^2(\rho^2{}_2/\rho\rho_1))\rho+(\mathbf{s}_2)_{11}/c^2$, where v is the velocity of the mixture.

An interpretation (for $(\mathbf{s}_2)_{11}=0$) is: If ρ is a measure/property in the frame of the mixture, then a corresponding measure in the frame 1 will be scaled by a ratio of v and c. This reminds of the Lorenz factor, but v is the absolute speed, and scaling will also depend of ratio of densities. Subsequently $(1-(v/c)^2(\rho^2{}_2/\rho\rho_1))$ will be known as the L-field, £. Here £=£(v).

£ may be expressed in absolute velocity for frame 1, or relative velocity between frame 1 and mixture $u=v-v_1$ by (1). For the relative velocity £=£(u)=$(1-(u/c)^2(\rho_1/\rho))$. If $\rho_2=0$, the velocity of the mixture equals the speed of frame 1, such that u=0, and £=1. This is since frame 1 constitutes the entire mixture. I.e. a non-trivial £ requires ρ_2 nonzero, and the classical Lorenz expression, may not be pointwise recovered. If ρ_1 and ρ_2 occupy different regions (as in examples of special relativity), an integration over volume give mean values that fulfil the classical Lorenz transformation.

3.2 Results for Doppler effect

We consider a mixture where constituent 1 and 2 not, necesarilly entirely, occupy the same region in space. *Preliminaries:* Constituent 1 has a constant absolute velocity v_1, and the stress tensor $s_1=-p_1(\rho_1)\mathbf{1}$, where p_1 and ρ_1 are the pressure and density of an acousic medium such that p_1, ρ_1 fulfil the wave equation, with sound velocity c_1-v_1 and $\rho_1=\exp(i\omega(t-x/(c_1-v_1)))$. For the mixture, close to 2: $T=-p\mathbf{1}$, where $p=p(\rho_2, ,)$ is the pressure of an acoustic medium with sound velocity c, and $\rho_2=\exp(i\omega(t-x/c))$. For constituent 2: $s_2=-p_2\mathbf{1}$.

Hereby, from (1)(2), $p_1 = p-(\rho_1\rho_2/\rho)v_1^2 -p_2$

By a quasi-weak formulation, properties of left hand side will be defined at the neighbourhood of 1, and properties of right hand side defined at the neighbourhood of 2, through integrating over volume with weighted average.

Differentiating twice with respect to time, and assuming that $d_t\rho_2>d_t\rho_1$ at 2 (thus defining location2), and vice versa, $d_t^2p= c^2d_t^2\rho_2$ from the wave equation for ideal gas, and $d_t^2(\rho_1\rho_2/\rho)=-\omega_2^2\rho_2 f(\rho_1,\rho_2)$, f being a function of the densities, it is achieved

$$\omega_1^2\rho_1c_1^2\,(1-(v_1/c_1))^2=\omega_2^2\rho_2c^2\,(1-f(\rho_1,\rho_2)(\,v_1/c)^2)-p_2$$

ω_2 is detected frequency at location2, and ω_1 is transmitted frequency at the location1.

For $c_1=c$ and the ‘average‘ values $\rho_1=\rho_2$ and $f(\rho_1,\rho_2)=1$ (since an integration over volume was presumed), and omitting p_2, the classical relativistic Doppler formula is recovered. The assumption of sound velocity c_1-v_1, is probably valid at a limited distance to the moving sound generator. When the function $f(\rho_1,\rho_2)$ vanishes, which is the case far from 1 or 2, the formula alters, which agrees with that the Doppler effect is more noticable, at close distance.

3.3 Aquaplane

For a boat on water, the uplift is due to relative velocity and buoyancy. Intersecting part of

boat and water is considered a mixture, such that (1)(2) holds.

At low depth, translation and buoyancy from pressure at depth is neglected. Vertical equilibrium (neglecting momentum supply and nondiagonal terms in s_1) then give

$m_1 g = \mathbf{e}_y^T \text{int}(\text{div}\ \mathbf{s}_1 dV) = e_y^T \text{int}(\mathbf{s}_1 \mathbf{n} dA) = s_{yy} A$, where A is projected area at water line, and m_1 is mass. At constant horisontal relative speed u, an angular periodic motion around equilibrium angle ϕ_e will be considered. The angle ϕ is defined positive CW, counted from ϕ_e, cf. Figure.

Guided by the expression (2), for the mixture, it is assumed that uplift is proportional to $\rho_1 u^2$. Hereby $s_{yy} = k\rho_1 u^2 = m_1 g/A$ which will be used in a dynamical analysis, where potential energy[2] is derived from equation of motion. Moment from uplift $\text{int}(\mathbf{x} \times \mathbf{s}_1 \mathbf{n} dA) = x_u s_{yy} A$, when s_{yy} is uniformly distributed, x_u denoting the center of uplift distribution.

Diffusion due to upward motion is neglected (in conjunction with assumption of low depth). Potential from gravity and uplift, give a linear model in a 1st approximation when uplift is determined from vertical equilibrium. Hereby $V = \phi^2 s_{yy} f(A, x_u, r_c)$ where f is a function and r_c is center of mass, and the Lagrangian T-V, where $T = J(d_t\phi)^2/2$, J being 2nd moment of inertia.

Nonlinear model.

In a refined model, higher order terms are considered, and in resulting non-linear model, the issue is what higher order terms to encount, and eventually, how to linearise. This may depend on if the goal is, to model severe event, to optimise a design for a special purpose, or to control the motion. Here, we will consider the (generalised) eigenfrequencies, the behaviour at turning points, and the case when the boat flip backwards, not returning to equilibrium.

For positive angles, since both $x_u(\phi)$ and projected area, $A(\phi)$, depend on angle, the uplift will increase of an higher order, which motivate a positive ϕ^3. (Refined small angle approx, giving negative contribution, is assumed less.)

Due to angular velocity, the horisontal velocity and then the uplift will change. Replacing s_{yy} in V, with $k\rho_1(u+\rho_2/\rho L(d_t\phi)\phi)^2$, L being the boat-length, give a dependence of $L(d_t\phi)\phi$, which give 'bi-nonlinearity'. For negative angles, the horisontal velocity component is increased at downward motion $d_t\phi > 0$, compared to that at the equilibrium angle, which increases the uplift. Therefore, at linearisation this will be included (in the potential energy) as $-(d_t\phi)^2\phi$, higher order term in ϕ is linearised at equilibrium angle.

Hereby, a normalised Hamiltonian to the Lagrangian will be $H = (d_t\phi)^2 + a_0\phi^2 + a_1\phi^3 - a_2\phi(d_t\phi)^2$

When damping is neglected, simulation is done for constant energy H, corresponding to initial velocity, that, if periodic motion, equals maximum velocity and determines eigenfrequency.

For largest a_1, the maximum positive angle will be small, and the acceleration is large at positive turning point, such that the negative velocity causes an 'escape from orbit' corresponding to a flip backwards. For moderate a_1, there is periodic motion, with larger maximum negative angle and slower acceleration and velocity at negative turning point, such that longer time 'is spent there'.

For smaller H and largest a_1, behaviour is stable periodic motion as seen for the innermost

circle.

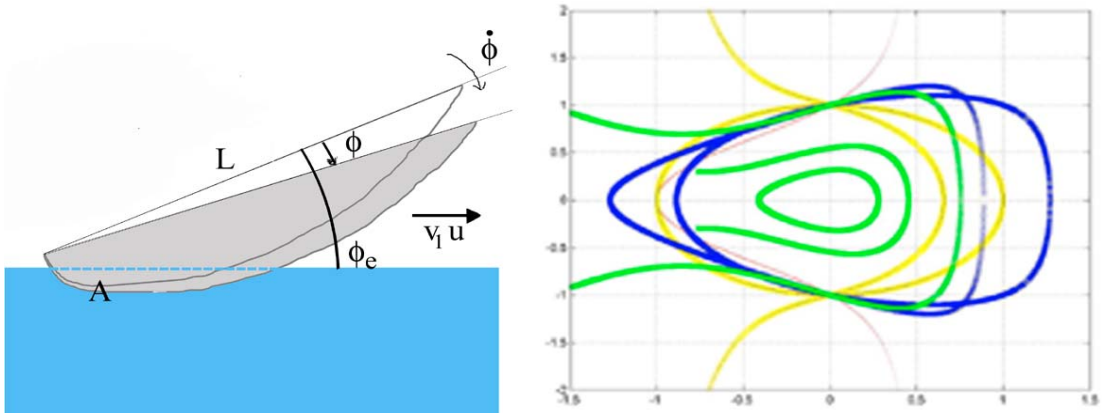

Figure. Phase portrait $d_t\phi$ versus ϕ for Hamiltonian H=1, and parameters $[a_0, a_1, a_2]$= [1,-0.3, 0.7], [1,0, 0], [1,0.3,1], [1,1,1], [1,2,-1], and H=0.3[1,1,1], H=0.1[1,1,1], from right at $(d_t\phi,\phi)$=(0,1.5), and diverging at ϕ=0.5; H=1[1,0, 2].

4 CONCLUSIONS

Within the framework of acoustic, when constituents and mixture fulfil the wave equation, characterised by sound speed, similarities with applications in special relativity, were notified. A derivation of a modified formula for Doppler effect, with a dependence of spatially distributed densities of constituents and mixture, were given.

At aqua-plane, a nonlinear equation of motion was derived. A simulation was done to show the qualitative behaviour depending on velocity, geometry and density.

The approach may also be used as a complement to ordinary boundary condition in fluid-structure interaction, by considering an interaction with boundaries in a spatially distributed boundary layer, eg. viscous layers in flow. In mixture modeling, there are couplings both in the field equations, and at the boundaries.

REFERENCES

[1] Bowen, R.M.: *Theory of Mixtures.* Continuum Physics (1976) ed. by A.C. Eringen, Vol III, Academic Press.
[2] Magnusson. A.: *Branch identification in elastic stability analysis. pp5-10* Doctoral thesis. (2000) Lund University, Sweden.
[3] Sorokin S.V: *Analysis of wave propagation in sandwich plates with and without heavy fluid loading.* J.of Sound and Vibr 271 (2004), 1039-1062.

Simulation of a Friction Stir Welding process using FE technique

Jonas Gagner and Aylin Ahadi

Division of Mechanics
Lund University, Lund Sweden
e–mail: aylin.ahadi@mek.lth.se

Summary

In this paper a three dimensional FE model of the friction stir welding (FSW) is presented and the FSW process is simulated. The model has been implemented in FE code Abaqus with user subroutines DLOAD, DFLUX and UMASFL. The material data used to describe the welded panels is from an aluminium alloy called AL-2024-T3 and the material is assumed to be isotropic with temperature dependent yield stress and elastic modulus. A sequentially coupled non-linear thermo-mechanical analysis was performed in order to study the temperature and stress distribution.

Introduction

FSW was invented and experimentally proven at The Welding Institute (TWI) in the beginning of the 90s and can be used for joining different materials and material combinations, if tool materials and shapes can operate at the forging temperature of the welded material. During the FSW process, the metal at high temperature, although not over the melting temperature, is exposed on powerful plastic deformation. The method is carried out by use of a rotating tool, which is forced down into the metal and carried along the welding direction, see Fig 1. In general, the tool comprises a shoulder and a probe. When the rotating tool is forced down to the metal, heat is generated due to friction. The tool also generates a significant amount of mechanical work under high pressure. The two plates to be welded are sheared together and a homogenous structure is formed. The crushing, stirring and forging action of the FSW tool produces a weld with a finer microstructure than the parent material. The result is a weld with the highest quality, free from pores and enclosures. Compared to other welding techniques where melting occurs, the FSW-method provides better mechanical properties of the weld, increased closeness and reduced deformation due to heat, because the material never reaches the melting temperature. Simulating the FSW process has been under way for some years now and plays an important part in the developing and improving work of this welding method. FSW process has been modeled using both Finite element and Finite difference techniques. In this paper a finite element model of the FSW process is presented and simulations are performed in FE code Abaqus.

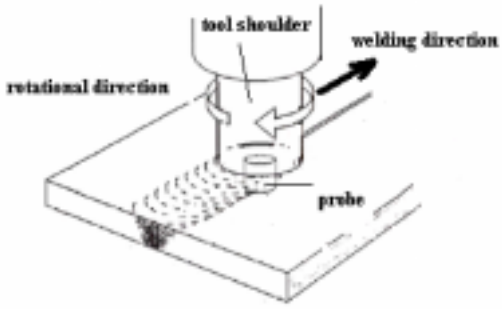

Figure 1: Illustration of the friction stir welding process.

Material properties

The material properties for aluminium alloy called AL-2024-T3 are used to model the welded plates. The material is modelled as an isotropic elasto-plastic continuum with kinematic hardening. Young's modulus, c.f. [4] and the yield strength, c.f. [3] are temperature dependent. Fig. 2

shows the influence of temperature on the yield strength and Young's modulus. The temperature effect on Poisson's ratio, ν, is very modest and the density, ρ, decreases about 4% when the temperature increases from room temperature to the melting point. Therefore, the Poisson's ratio and the density are assumed to be constants and they are set to 0,3 respectively 2770kg/m^3. Experimental data for the temperature effects on the thermal expansion coefficient, α, are fitted well as a linear approximation and varying from $2.43 \cdot 10^{-5}$ to $2.8 \cdot 10^{-5}$ over a temperature range between 20ºC to 500ºC, c.f. [3]. The conductivity and specific heat are set to 120W/mºK respectively 875J/kg·ºK.

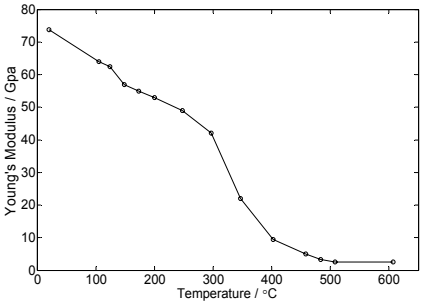

Temperature (°C)	Yield strength at 0% plastic strain (MPa)	Yield strength / Plastic strain (MPa / -)
24	345	483 / 0.17
100	331	455 / 0.16
149	310	379 / 0.11
204	138	186 / 0.23
260	62	76 / 0.55
316	41	52 / 0.75
371	28	34 / 1.00
400	21	25 / 1.00

Figure 2: The Young's modulus and the yield stress dependency on the temperature for AL-2024-T3.

FE-model

The model simulates a 105 mm friction stir weld of two 150×60×5.85 mm AA2024-T3 plates. A steel anvil with dimensions 240×240×25 mm is used as a backing plate. The tool shoulder radius is 9 mm and the tool probe radius is 3 mm. The weld starts 15 mm from one side and finishes 30 mm from the other side. The friction stir weld process involves three characteristic phases. The plunge period is a submerging of the tool into the AA2024-T3 plates with tool rotation speed of 600 rev/min and duration of 40 s. The dwell period is preheating at the start position with the same rotational speed and duration of 5 s. The weld period is longitudinal motion of the tool along the weld line with tool speed of 40 mm/min for the first 5 mm and then 80 mm/min for 100 mm. The temperature is measured using thermocouples at different locations in the plates and anvil. A dynamometer logged tool forces in three dimensions and the tool reaction torque. The finite element simulation is a sequentially coupled nonlinear thermo-mechanical analysis. The first step of the simulation is a nonlinear transient thermal analysis. The computed temperatures are then passed in to a nonlinear static mechanical large displacement analysis as a field variable. The tool is not included in the model as a physical body, but the effects of the tool are included in the thermal model as well as in the mechanical model.

The thermal model

The plates and the anvil are included in the thermal model. The AA2024-T3 plates are modelled as one single plate with the dimensions 150×120×5.85 mm. The plates are meshed as one single plate with 18000 8-node linear brick forced convection elements (DCC3D8) and the anvil is meshed with 12600 8-node linear brick elements (DC3D8). All free surfaces on the mesh is subjected to Newton's convection boundary condition $q_n = \alpha \cdot (\theta - \theta_\infty)$ where q_n is the heat flux per unit area in the direction of the outer unit normal vector, θ is the temperature on the surface of the plate or anvil, $\theta_\infty = 25$ °C is the room temperature and the convection coefficient $\alpha = 15$ W/(m^2°C). The conductive heat transfer between the plate and the anvil is modelled as $q_n = k(\bar{\theta}) \cdot (\theta_{plate} - \theta_{anvil})$ where the thermal conductance $k(\bar{\theta})$ is a function of the average temperature $\bar{\theta} = (\theta_{plate} + \theta_{anvil})/2$. The value of the thermal conductance was adopted from [4] and adjusted based on the experimentally measured temperatures. Heat is generated due to plastic deformation and friction. The total heat power is derived from the mechanical power. The mechanical power

is $P = \omega T + F_x v$, where ω the tool angular velocity is, T is the tool reaction torque, F_x is the tool reaction force in the direction of the joint line and v is the tool speed. The heat power that goes into the weld is $Q = \eta P$, where η is an efficiency factor. The efficiency factor takes account for the heat loss into the tool, radiation, vibrations, etc. An initial value of $\eta = 0.75$ was taken from [4], but the value was adjusted in the model, based on the experimentally measured temperatures.
The heat power generated at the shoulder is $Q_{shoulder} = \delta \cdot Q$ and the heat power generated at the probe is $Q_{probe} = (1-\delta) \cdot Q$. The fraction of heat power generated at the shoulder is denoted by δ. An initial value of $\delta = 0.75$ was taken from [4], but the value was adjusted in the model, based on the experimentally measured temperature distribution.
The heat generated at the shoulder is applied onto the area beneath the shoulder as a surface heat flux $q_{shoulder}$. The flux is assumed to have the form

$$q_{shoulder}(r) = \frac{3}{2\pi} \frac{Q_{shoulder}}{R_{shoulder,eff}^3 - R_{probe,eff}^3} r \quad , \; R_{probe,eff} < r \le R_{shoulder,eff} \tag{1}$$

where r is the distance from the tool centre, $R_{shoulder,eff}$ and $R_{probe,eff}$ is the effective shoulder radius and effective probe radius, respectively. The values are $R_{shoulder,eff} = 10$ mm and $R_{shoulder,eff} = 4$mm, in accordance with [4]. The heat generated at the probe is applied as an uniform body heat flux onto the elements corresponding to the volume of the probe. The body flux is,

$$q_{probe} = \frac{Q_{probe}}{\pi R_{probe,eff}^2 t} \tag{2}$$

where t is the plate thickness. The thermal loads are implemented in a user subroutine DFLUX. The mass flow was included in the model and was applied at a 1 mm thick layer below the effective shoulder and at the volume corresponding to the effective probe. The mass flow per unit area $\dot{m}$ was modelled as $\dot{m} = \rho \omega r$ where ρ is the density. The mass flow is implemented in a user subroutine UMASFL. The nonlinear equations are solved using a modified Newton method with asymmetric matrix storage and solution scheme. The trapezoidal rule is used for time integration.

The mechanical model

The anvil is not included in the mechanical model. The two plates are modelled as one single plate and meshed with 18000 8-node linear brick with reduced integration with hourglass control (C3D8R). The bottom of the plate is constrained from displacement in the z-direction by the backing plate and the clamped edges of the plate are constrained from displacement in the x- and y-direction. The forging force and the torque are applied as body forces to a top surface element layer with a thickness of 0.75 mm. The forging force is applied as

$$f_z = \frac{F_z}{\pi R_{shoulder,eff}^2 d} \quad , \; r < R_{shoulder,eff} \tag{3}$$

where F_z is the experimentally measured forging force and d is the thickness of the layer on which the body force is applied. The torque is divided into x- and y-components

$$f_x = \frac{3}{2\pi} \frac{T}{R_{shoulder,eff}^3 d} \frac{y}{r} \quad , \quad f_y = -\frac{3}{2\pi} \frac{T}{R_{shoulder,eff}^3 d} \frac{x}{r} \tag{4}$$

where T is the experimentally measured torque. The forces are described in a moving coordinate system (x, y) with its origin at the tool centre. The mechanical loads are implemented in a user subroutine DLOAD. The nonlinear equations are solved using the line search algorithm.

Results

The temperature at different locations in the plates and the anvil is measured and compared to experimental data in Fig 3. Fig 4 shows the distribution of the temperature and the von Misses stress in the plate halfway trough the weld.

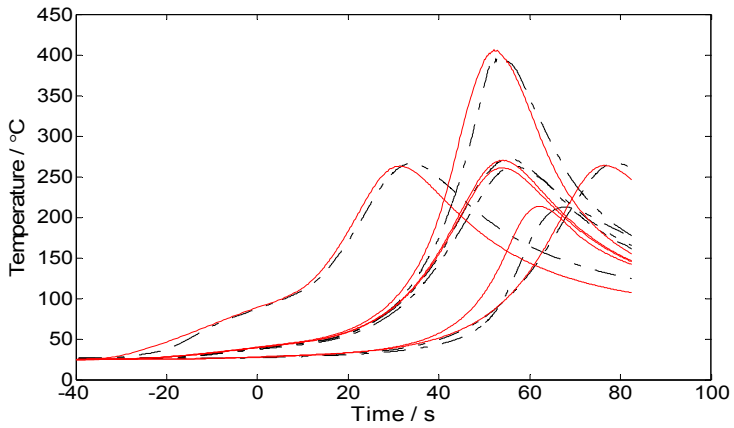

Figure 3: The temperature at different locations in the plates and the anvil. The black dash-dot lines are experimental data and the red solid lines are results from the FE thermal analysis.

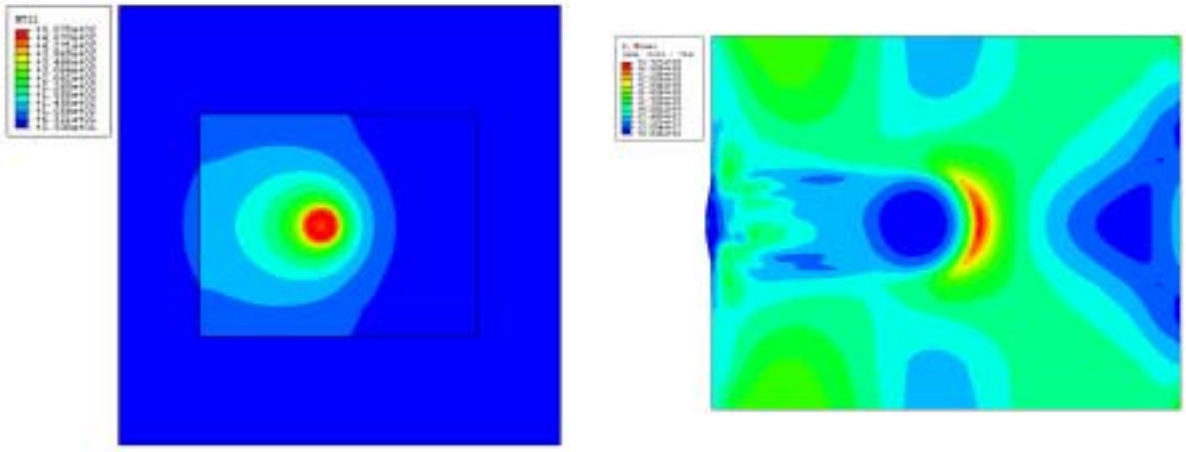

Figure 4: The temperature and von Misses stress distribution in the plate halfway trough the weld.

Concluding remarks

A FE model for the FSW process has been presented. The model includes the tool loads and takes into account the mass flow effects during the process. A simulation of the welding of two plates has been performed. The result from the temperature at different points on the plate have been compared to experimental data and showed good agreement.

References

[1] Cambridge University. (2002). FSW Benchmark. Accessed: http://www-materials.eng.cam.ac.uk/FSW_Benchmark/fsw-t_butt_6mm_2024-t3/fsw-t.html. [2006-09-24]

[2] ASM handbook, vol 2, Properties and selection:Nonferrous alloys and Special-Purpose Materials, USA, (1990).

[3] H. Schmidt, J. Hattel, J. Wert. An analytical model for the heat generation in friction stir welding. Modelling Simul. Mater. Sci. Eng., **12,** 143-157, (2004)

[4] Q. Shi, T. Dickerson, H.R. Shercliff. Thermo-Mechanical FE Modelling of Friction Stir Welding of AL-2024 Including Tool Load. Cambridge University Engineering Department, UK, (2003).

[5] J. Gagner. *FEM analysis of a Friction Stir Welding Process introducing mass flow effects*, Master thesis, Division of Mechanics, Lund University, (2006).